Investigating the regenerative potential of the neonatal mouse heart

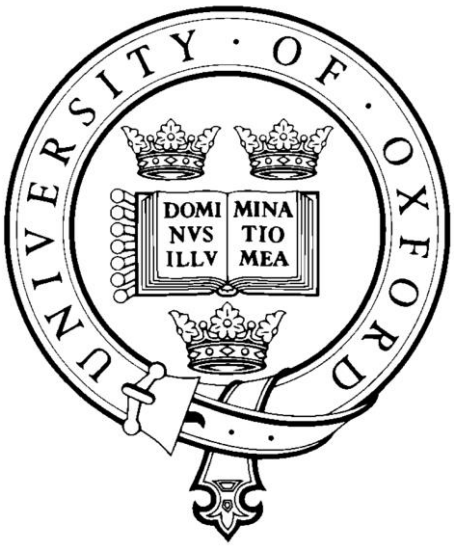

Mala Gunadasa-Rohling

Balliol College, University of Oxford
Department of Physiology, Anatomy & Genetics

A thesis submitted for the degree of
Doctor of Philosophy

Michaelmas Term 2024

ABSTRACT

After myocardial infarction (MI), the adult human heart is unable to regenerate lost tissue, leading to scarring, pathological remodelling and eventual progression to heart failure. There is currently no known "cure" other than the limited option of heart transplantation. The study of animal models that can intrinsically regenerate their heart offers potential insights into how to therapeutically target tissue restoration. Whilst regeneration is widely accepted for some amphibians and species of fish, mammalian heart regeneration is more controversial, with conflicting reports as to the extent and timing of recovery after different injury models. This thesis presents a significantly refined method for longitudinal magnetic resonance imaging of neonatal mouse hearts following coronary artery ligation to mimic heart attack. We document heart growth and development of the principal functional cardiac parameters. We confirm heart regeneration in individual animals injured on post-natal day 1 (P1) with restoration of tissue and resolution of injury, while those injured on P7 show the sustained adult injury response of fibrosis, scarring and impaired heart performance when imaged repeatedly up to 21 days after MI. This study resolves the controversy surrounding neonatal mouse heart regeneration and establishes a functional platform for live capture of the regenerative process and for the future testing of genetic or therapeutic interventions.

There are many factors that may contribute to the "closing of the regenerative window". Using the Fucci mouse model which demonstrates the different phases of the cardiomyocyte cell cycle by oscillating red/green fluorescent emissions, we quantify where cell cycle activity is occurring after injury in P1 and P7 pups compared to age-matched shams. The P1 surgery group showed strong activation of cell cycling around the area of the infarct damage in the left ventricle (LV) as well as in the intraventricular septum (IVS). In contrast, the P7 cohort showed very little activation in the LV damaged area or surroundings, but a surprising amount in the IVS and right ventricle (RV), regions remote to the site of injury. Differences were also apparent in the base, apex and atria. In addition, isolated cardiomyocytes (CM) from Fucci P1 and P7 mice allow real-time monitoring of the stages of cell division *in vitro*, where, by altering the cellular environment, differences in the responses of P1 and P7 myocytes to hypoxia (oxygen tension) and acidosis (pH) were monitored. During MI, these key factors are known to occur in parallel and affect cells via different but related mechanisms, and our model showed significantly different responses between the two cohorts.

Continuing the investigation into the changing environment of the developing heart, we tested pHLIP, a small biopeptide marker used in the cancer research field, to label acidic regions in the maturing myocardium. We injected pHLIP into mice of different ages, from P1 through to adult, to reveal areas of lower pH in the heart and document how these change during normal heart development. We saw acidic regions in the endocardium become more alkaline as the hearts age and the coronary vasculature matures into its adult pattern. We also tested pHLIP in an adult rat cryoinfarcted heart model to highlight acidity in the lesioned area.

Finally, we used immature and more mature human induced pluripotent stem cell-derived CMs (hiPSC-CM) to see if they behave like P1 and P7 CMs in a human model of heart injury. We compared these cell types in different combinations of hypoxia (atmospheric and chemically induced) and pH and noted different responses in cell contractile apparatus maturity and cell cycle activity.

We hope these investigations add further insights into why the regenerative window in mammals is time-limited, and closes after the first week of postnatal life in a mouse. If they could suggest potential mechanisms to extend the window into adult life where this ability would be extremely valuable, we may be able to mitigate some of the worst effects of heart failure after MI injury.

ACKNOWLEGEMENTS

The research for this thesis was undertaken in four different labs, each with their own specialist knowledge and expertise, and I would like to thank the supervisors and group members for their valuable assistance and welcoming me into their labs. First, I would like to thank Paul Riley for allowing me to undertake my doctoral studies while still working as his Senior Research Assistant performing heart surgeries for the group. I appreciate your faith and trust in giving me the massive neonatal MRI project, co-supervised by Jurgen Schneider. Thank you Jurgen and Mahon Maguire for making me feel at home at the BMRU, the 20 hr days of surgery and scanning, and for putting the words "eigenvalues" and "eigenvectors" back into my life, I hadn't realised I was missing them! Thanks also to Nicola Smart for being brave enough to take me on as a grad student and all your input and advice. The second part of my work was made possible by Pawel Swietach, a good friend before switching to supervisor mode. The Fucci cell assays and pHLIP research couldn't have happened without your magic macros...hoping we can switch back to just friends now that it's all over. Thanks to Damian Tyler for standing with me for the last section of work and Lisa Heather for sharing office and lab spaces. The biggest thank you has to go to Carolyn Carr for supporting me through all these research projects and supervising the completion of this work. You've been incredibly patient and helpful, and your amazingly wide range of knowledge covered everything in this thesis and so much more – it honestly couldn't have happened with you and I'm so grateful to have had you for the complex task of actually putting all the various projects together into a coherent thesis.

Another thank you goes to my assessors for their invaluable input into the thesis and suggestions on how to proceed to completion: Samira Lakhal-Littleton and Oliver Stone for both Transfer and Confirmation of Status examinations. Thanks again to Ollie (internal) and Dan Stuckey (external) for taking time to examine my thesis and discuss it at my viva. I hope it meets your expectations. Thank you also to my department Head, David Patterson, for permitting a staff member to also be a graduate student, and especially for assisting with fees. I'd also like to express my gratitude to Linacre and Balliol Colleges, I've been lucky to have been a part of both your communities – Thank you to Jane Hoverd (Linacre) and James Forder (Balliol) for offering me Junior Dean positions and providing room and board in Oxford.

There are many people that have helped me learn new procedures and techniques, without which this research couldn't have happened. From the Riley/Smart labs, thanks to Megan Masters for

teaching me the MI surgery, Susann Bruche for showing me many molecular biology techniques and to Joey Vieira for your wisdom on all things developmental biology. Thank you Tilly Mommersteeg for introducing me to a new animal research model, the zebrafish, and Sarah de Val for supporting some animal research costs. Additional appreciation goes to Denise Lynch, Katie McNeil and Tertia Softley for top-notch administrative support. From the Swietach group, thank you Alzbeta Hulikova, Carolina Garciarena, Johanna Michl, Wictoria Blaszczak and Mark Richards for both mentorship and friendship. And finally from the Carr/Heather/Tyler group, thanks to Ujang Purnama for teaching me the hiPSC-CM differentiation technique and to Marcos Castro Guarda for guiding me through RT-qPCR; thanks for lab management Claudia Montes Aparicio and Vicky Ball, especially for finding me space in your lab. Lastly, thanks to Jack Miller for all your help with statistics (which I will continue pretending to understand).

Special thanks to all my amazing college mates for accepting me without prejudice or judgement, I certainly never expected to make friends like you during this process but honestly don't know how I would have survived it without you. From Formal Dinners to Wine & Cheese: Sophie, Charlotte & Min for always giving me a spot, and Melissa, Tom, Nick & Ashwin for making it a party, thanks for the good times and the company. Cheers to Alister and Ollie (for friendship, peer support, burritos and espresso martinis); Pete & Zelim (best Junior Dean team ever); and Thomas (just for being there). Thanks to Claire, Michael & Matt (my lockdown family that continues to care and encourage from all over the globe) and to Gerardo & Eboni for being there from Day 1.

Finally, lots of love and thanks to my Mum, Dad and brother in Canada for your encouragement and support, I can't wait to visit.

This thesis is dedicated to my husband, Gerry, and our four beautiful children, Sara, Andrew, Victoria and Katy, who allowed their wife and mother to be absent for so long… it's time for me to come home.

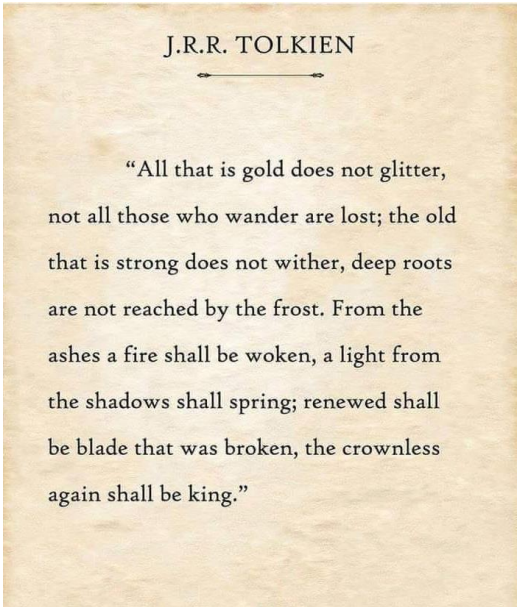

RESEARCH OUTCOMES

Published papers from this thesis

1. Magnetic Resonance Imaging of the Regenerating Neonatal Mouse Heart

M. Gunadasa-Rohling, M. Masters, M. L. Maguire, S. C. Smart, J. E. Schneider and P. R. Riley Circulation 2018 Vol. 138 Issue 21 Pages 2439-2441 (first author)

2. Alkaline nucleoplasm facilitates contractile gene expression in the mammalian heart

A. Hulikova, K. C. Park*, A. A. Loonat*, M. Gunadasa-Rohling*, M. K. Curtis, Y. J. Chung, et al. Basic Res Cardiol 2022 Vol. 117 Issue 1 Pages 17 (second author – joint)

3. Acidic environments trigger intracellular H+-sensing FAK proteins to re-balance sarcolemmal acid-base transporters and auto-regulate cardiomyocyte pH

A. D. Wilson, M. A. Richards, M. K. Curtis, M. Gunadasa-Rohling, S. Monterisi, A. A. Loonat, et al. Cardiovasc Res 2022 Vol. 118 Issue 14 Pages 2946-2959

National/International Conference & Seminar presentations

1. BHF CRM Annual Oxbridge Meeting (London) 2022 Jurgen Schneider (Neonate MRI)
2. BHF CRE Seminar (Oxford) Pawel Swietach (Fucci cells)
3. BHF CRM Annual Oxbridge Meeting (London) 2019 Paul Riley (Neonate MRI)
4. International Society for Magnetic Resonance in Medicine Imaging Conference (Singapore) 2018 Mahon Maguire (Neonate MRI)
5. BHF CRM Annual Oxbridge Meeting (London) 2022 Jurgen Schneider (Neonate MRI)

Prizes

Linacre College Studentship - Thomas Linacre Prize 2019

Linacre College Donmar Scholarship Research Prize 2020

Selected Poster presentations

1. European Developmental Biology Congress (EDBC), Spain 2019
2. Edinburgh BHF CRM Conference 2018
3. DPAG Development and Cell Biology Theme Annual Open Day 2018
4. Oxford Developmental Biology Symposium 2018
5. Glasgow BHF CRM Conference 2017

COVID STATEMENT

Chapter 3: Neonatal MRI

This chapter was not affected by COVID. All experiments took place before any restrictions.

Chapter 4: Fucci and pHLIP markers in heart slices

Loss of the Fucci strain of mice during the closure of Biomedical Services to students:

- All mice numbers had to be severely reduced to allow BMS staff to be furloughed during the pandemic closures. This meant we could only keep 2 cages of Fucci positive breeding males for this line. By the time we had access again, these mice were too old to breed successfully and we did not have the funds to restart this breeding line. Thus there were no new litters to use for fresh surgeries, so I had to rely on the stored samples.

Fucci signal fading due to imaging delays:

- The imaging of sections for the cell counting assay of the Fucci hearts after MI surgery and age-matched shams was interrupted due to COVID limitations which restricted access to equipment
- By the time access was reinstated, one of the two fluorescent signals had faded (mVenus green) and only mCherry red could be reliably counted. Attempts to enhance the green signal were unsuccessful. This limited the counting to only red G1 cells and relied on preliminary data to establish a correlation between the red and green cells. This also meant that imaging cell cycling in other cell types, as had been planned originally, was also abandoned.

pHLIP co-injections with hypoxia markers:

- The planned co-injection of pHLIP with pimodiazole to investigate whether regions of acidity coincided with hypoxia in the developing and injured heart was also not conducted due to lab closures and limited access to breeding facilities for CD1 mice. This limited the data results to acidity only without the correlation to hypoxia which would have been very valuable.

Adult rat cryoinfarct injury model series of experiments:

- The initial cryoinfarct study in adult rats was terminated early at 4 days post-injury as the date of closure of BMS was still undetermined at the time of surgery, and we had hoped that animals under procedure could be maintained until planned experimental endpoint. Unfortunately this turned out not to be the case and we had to cull and take samples at Day 4 after injections of pHLIP and Hoechst at Day 3.
- This reduced the number of surgeries for our final study as later surgeries were mostly designated for other lab members.

Chapter 5: Primary isolated Fucci CM and hiPSC-CM

Loss of the Fucci strain of mice during the closure of Biomedical Services to students:

- As above the loss of Fucci positive males to generate new litters of pups limited the availability of P1 and P7 litters so numbers of isolations were restricted. This affected the later experiments into the effect of acidity on P1 and P7, with P7 litters specifically being low in number: we were only able to do 2 isolations of P7 pups which we split into two groups to give us 3 sets.
- The final experiment which combined acidity and hypoxia together was only performed on 1 isolation of each age group before had to stop for COVID and we lost the line.

The hiPSC-CM experiments were not affected by COVID. All experiments took place after any restrictions.

TABLE OF CONTENTS

ABSTRACT i
ACKNOWLEGEMENTS iii
RESEARCH OUTCOMES v
Published papers from this thesis v
National/International Conference & Seminar presentations v
Prizes v
Selected Poster presentations v
COVID STATEMENT vi
Chapter 3: Neonatal MRI vi
Chapter 4: Fucci and pHLIP markers in heart slices vi
Chapter 5: Primary isolated Fucci CM and hiPSC-CM vii
TABLE OF CONTENTS viii
ABBREVIATIONS xiii
CHAPTER 1 1
1.1 HEART DISEASE AND FAILURE – WHY IS THIS A SIGNIFICANT PROBLEM? 2
1.1.1 Cardiovascular disease in the UK 2
1.1.2 Global effects of cardiovascular disease 3
1.1.3 Mitigating the effects of heart disease 4
1.2 MODELS OF HEART REGENERATION 5
1.2.1 NON-MAMMALIAN MODEL SYSTEMS 6
1.2.2 MAMMALIAN MODEL SYSTEMS, SMALL AND LARGE 9
1.2.3 IN VITRO MODEL SYSTEMS OF HEART DISEASE AND REGENERATION 13
1.3 HEART IMAGING TECHNIQUES IN PRE-CLINICAL RESEARCH STUDIES 14
1.4 HEART DEVELOPMENT & POINTS OF CONSIDERATION FOR REGENERATION 16
1.4.1 Early heart development 16
1.4.2 Later heart development – postnatal maturation in the mouse 17
1.5 THESIS AIMS AND RESEARCH SUMMARY 19
1.6 OUTLINE OF THE THESIS 20
CHAPTER 2 22
2.1 Animal models 23
2.1.1 Mice breeding and maintenance 23
2.1.2 Mouse strains and specific breeding strategies 24
2.1.3 Rats 24

2.2 Myocardial infarction surgery 25
2.2.1 Neonatal mice 25
2.2.2 Adult rat cryo-infarction 28
2.3 Tissue Collection and preparation 28
2.3.1 CD1 samples 28
2.3.2 Fucci neonate samples 29
2.3.3 pHLIP samples (neonate to adult mice and adult rats) 29
2.3.4 Cryosectioning 30
2.4 Immunofluorescent staining 30
2.4.1 Slide preparation 30
2.4.2 Background suppression 31
2.4.3 Blocking and primary antibodies 31
2.4.4 Secondary antibodies 31
2.4.5 Mounting slides 31
2.5 Imaging 33
2.5.1 Confocal imaging of tissue slices and cultured cells 33
2.5.2 Whole heart slice tiled images 33
2.6 Molecular biology 34
2.6.1 Genotyping mice strains 34
2.6.2 RNA extraction steps for qRT-PCR 36
2.7 Cell culture 39
2.7.1 Primary murine cardiomyocytes 39
2.7.2 Human induced pluripotent stem cells 39
2.8 Statistical methodology 41
CHAPTER 3 42
ABSTRACT 43
3.1 INTRODUCTION AND BACKGROUND 44
3.2 OVERALL AIM 49
3.3 METHOD DEVELOPMENT AND RESULTS 49
3.3.1 EXPERIMENTAL DESIGN 50
3.3.2 NEONATE MOUSE HUSBANDRY AND MAINTENANCE 50
3.3.3 IDENTIFICATION OF NEONATE PUPS 51
3.3.4 HARDWARE DESIGN 53
3.3.5 SOFTWARE DESIGN 54
3.3.6 MRI SCANNING 58

3.3.7 PRELIMINARY RESULTS INCLUDING CONFIRMATION OF SUCCESSFUL IMAGE RECONSTRUCTION AND FUNCTIONAL ANALYSIS BY THE SOFTWARE 61
3.3.8 BASELINE GROWTH AND DEVELOPMENT USING MRI SCANS OF THE SHAM SURGERY COHORT: CHANGES IN MASS AND CARDIAC FUNCTION OVER THE FIRST MONTH 65
3.3.9 FUNCTIONAL PARAMETERS OF THE HEART AFTER MYOCARDIAL INFARCTION INJURY OR SHAM FOR P1 VS P7 68
3.3.10 STUDY LIMITATIONS 72
3.4 DISCUSSION AND CONCLUSIONS 73
3.4.1 BASELINE GROWTH AND DEVELOPMENT OF FUNCTIONAL CARDIAC PARAMETERS: 74
3.4.2 CARDIAC FUNCTIONAL PARAMETERS AFTER MI INJURY OR SHAM SURGERY IN THE P1 VS P7 NEONATAL MOUSE: 76
3.4.3 LONGITUDINAL IMAGING AND FUNCTIONAL ANALYSIS OF NEONATAL MICE AFTER INJURY OR SHAM FOR P1 VS P7 76
3.5 FUTURE WORK 77
CHAPTER 4 79
ABSTRACT 80
4.1 INTRODUCTION AND BACKGROUND 81
4.1.1 CELL PROLIFERATION IN THE DEVELOPING AND REGENERATING MAMMALIAN HEART 81
4.1.2 FUCCI MOUSE MODEL TO VISUALISE CELL CYCLING IN THE MYOCARDIUM 82
4.1.3 INVESTIGATING AREAS OF ACIDITY IN DEVELOPING AND INJURED HEARTS USING PHLIP LABELLING TECHNOLOGY 86
4.2 AIMS 89
Aim 1: Areas of cell cycle activity in P1 vs P7 injured or sham hearts 90
Aim 2: Map areas of acidity and hypoxia in the developing mouse heart and after cryoinfarct injury in adult rats 90
4.3 METHOD DEVELOPMENT AND RESULTS 90
4.3.1 EXPERIMENTAL DESIGN (Part 1): INVESTIGATING AREAS OF CELL CYCLE ACTIVITY USING THE FUCCI MOUSE MODEL DURING DEVELOPMENT AND AFTER MI SURGERY 90
4.3.2 BREEDING AND GENOTYPING NEWBORN FUCCI PUPS 92
4.3.3 NEONATE MI SURGERY PROCEDURE FOR FUCCI PUPS 94
4.3.4 TISSUE STAINING OF FUCCI HEARTS 95
4.3.5 IMAGING OF FUCCI HEARTS 95
4.3.6 FUCCI IN NEONATAL HEARTS 96
4.3.7 FUCCI WITH ADDITIONAL CELL-SPECIFIC MARKERS 101
4.3.8 AREAS OF CELL CYCLE ACTIVITY AT P5 AND P11 WITH/WITHOUT MI SURGERY AT P1 AND P7 102
4.3.9 EXPERIMENTAL DESIGN (Part 2): INVESTIGATING AREAS OF ACIDITY USING pHLIP LABELLING TECHNOLOGY DURING DEVELOPMENT AND AFTER MI CRYOINFARCT SURGERY 106

4.3.10 IDENTIFYING ACIDIC REGIONS OF THE HEART USING pHLIP 107
4.3.11 pHLIP TISSUE COLLECTION SAMPLE PREPARATION 108
4.3.12 IMAGING OF pHLIP SECTIONS 108
4.3.13 TIME COURSE OF ACIDIC NICHES IN THE DEVELOPING MOUSE HEART 109
4.3.14 DATA ANALYSIS OF pHLIP SECTIONS 111
4.3.15 ACIDIC NICHES AFTER CRYO-INFARCT INJURY IN THE ADULT RAT HEART 115
4.3.16 IMMUNOFLUORESCENCE STAINING FOR CONTRACTILE PROTEINS IN ACIDIC MYOCARDIUM 118
4.3.17 STUDY LIMITATIONS 120
4.4 DISCUSSION AND CONCLUSIONS 121
4.4.1 CELL CYCLING VARIATIONS ACROSS THE HEART AFTER INJURY 121
4.4.2 USING pHLIP TO MAP AREAS OF ACIDITY ACROSS THE DEVELOPING AND INJURED MYOCARDIUM 124
4.5 FUTURE WORK 127
CHAPTER 5 128
ABSTRACT 129
5.1 INTRODUCTION AND BACKGROUND 130
5.1.1 CARDIOMYOCYTE CELL CYCLE AND DEVELOPMENT OF THE MYOCARDIUM 130
5.1.2 HUMAN INDUCED PLURIPOTENT STEM CELL CARDIOMYOCYTES 134
5.1.3 HYPOXIA AND ACIDITY IN CULTURED CELLS 137
5.2 OVERALL AIMS 139
5.2.1 P1 VS P7 CARDIOMYOCYTES IN CULTURE 139
5.2.2 hiPSC-CM RESPONSES TO HYPOXIA AND pH VARIATIONS 139
5.3 METHOD DEVELOPMENT AND RESULTS 140
5.3.1 EXPERIMENTAL DESIGN (Part 1): ISOLATED AND CULTURED CARDIOMYOCYTES FROM P1 AND P7 FUCCI MOUSE HEARTS 140
5.3.2 FUCCI CELL ISOLATION AND CULTURE FROM P1 AND P7 NEONATAL MOUSE PUPS 141
5.3.3 FUCCI CELL IMAGING AND ANALYSIS MACRO DEVELOPMENT 144
5.3.4 FUCCI ISOLATED CELLS: P1 VS P7 WITH NO TREATMENT (BASELINE) 146
5.3.5 FUCCI ISOLATED CELLS: P1 VS P7 – HYPOXIC ENVIRONMENT 149
5.3.6 FUCCI ISOLATED CELLS: P1 VS P7 CELLS - ACIDIC ENVIRONMENT 150
5.3.7 FUCCI ISOLATED CELLS: P1 VS P7 WITH ACIDIC MEDIA AND HYPOXIA 152
5.3.8 EXPERIMENTAL DESIGN (Part 2): Human induced pluripotent stem cell derived cardiomyocytes 155
5.3.9 hiPSC CULTURE AND MAINTENANCE 155
5.3.10 DIFFERENTIATION OF hiPSCs INTO CARDIOMYOCYTES 156

5.3.11 PREPARING THE CARDIOMYOCYTES FOR TESTING IN DIFFERENT CONDITIONS 157
5.3.12 hiPSC-CM: HYPOXIA VS NORMOXIA IMMUNOFLUORESCENT STAINING 158
5.3.13 FIBROBLAST CONTAMINATION OF hiPSC-CM CULTURES 163
5.3.14 HYPOXIA AND ACIDITY EFFECTS ON hiPSC-CM CULTURES EVALUATED BY qPCR 166
5.3.15 STUDY LIMITATIONS 170
5.4 DISCUSSION & CONCLUSIONS 170
5.4.1 FUCCI CELL ASSAYS 170
5.4.2 hiPSC-CM ASSAYS 174
5.4.3 SUMMARY DISCUSSION: HYPOXIA AND ACIDITY EFFECTS IN CULTURED CARDIOMYOCYTES 176
5.5 FUTURE WORK 178
CHAPTER 6 179
6.1 Longitudinal neonate MRI shows regeneration with tissue replacement and functional recovery after MI injury in P1 hearts but not in P7 180
6.2 P1 and P7 Fucci2 neonates show different areas and degrees of cell cycle activation across the myocardium after MI injury 181
6.3 pHLIP acidity marker in the developing heart and after adult injury 182
6.4 P1 and P7 Fucci isolated cells cultured in different environmental conditions 184
6.5 hiPSC-CM grown in different media and subjected to hypoxia and/or acidity 185
6.6 Concluding remarks 186
APPENDICES & SUPPLEMENTAL FIGURES 190
REFERENCES 211

ABBREVIATIONS

ACE (inhibitors)	Angiotensin-converting enzyme
ANOVA	Analysis of Variants (statistical test)
APC/C	Anaphase Promoting Complex/Cyclosome
ATP	Adenosine tri-phosphate
B27	defined media supplement of enzymes, proteins, vitamins and fatty acids
BHF	British Heart Foundation
BM	Body Mass
BMRU	Biomedical Magnetic Resonance (Imaging) Unit
BMS	Biomedical Services
BSA	Bovine serum albumin
C57Bl/6J	C57Bl/6J strain of mice
CD1	CD1 strain of mice
CHIPseq	Chromatin immunoprecipitation sequencing
CM	Cardiomyocyte
cMRI	Cine Magnetic Resonance Imaging
CRISPR	Clustered regularly interspaced short palindromic repeats
CT	Computerised Tomography
CVD	Cardiovascular disease
DAPI	4',6-Diamidino-2-phenylindole
DMEM	Dulbecco's Modified Eagle Medium
DMOG	Dimethyloxalylglycine
DMSO	Dimethyl sulfoxide
DNA	Deoxyribonucleic acid
DPBS	Dulbecco's Phosphate Buffered Saline
E8.0 (for example)	Embryonic day 8.0 (for example)
EC	Endocardial cell
ECG	Electrocardiogram
ECM	Extracellular matrix
EDV	End Diastolic Volume
ESV	End Systolic Volume
EF	Ejection Fraction
FB	Fibroblast

FBS	Foetal Bovine Serum
FGF	Functional Genomics Facility
FHF	First Heart Field
FUCCI	Fluorescent Ubiquitination-based Cell Cycle Indicator
G1 (or 2)	Growth 1 (or 2) (cell cycle phase)
Gem	Geminin – cell cycle control system protein
GO	Gene Ontology
GP	General practitioner
hiPSC	Human Induced Pluripotent Stem Cell
HR	Heart Rate
HS	Horse serum
IPSC	Induced Pluripotent Stem Cell
IVS	Intraventricular septum
LA	Left atrium
LAD	Left Anterior Descending (coronary artery)
LSM	Laser scanning microscope (confocal)
LV	Left ventricle
LVM	Left Ventricular Mass
LVM/BM	Left Ventricular Mass/Body Mass (ratio)
M	Mitosis (cell cycle phase)
M199	Medium 199
mAG	Monomeric Azami Green Fucci probe
MAT/Mat	Maturation media (cell culture)
MI	Myocardial Infarction
mKO	Monomeric Kusabira Orange Fucci probe
MRI	Magnetic Resonance Imaging
NCBI	National Centre for Biotechnology Information
NHP	Non-human primate
NHS	National Health Service (UK)
NIH	National Institutes of Health (USA)
NRVMs	Neonatal Rat Ventricular Myocytes
OCT	Optimal Cutting Temperature compound
ORC	Origin Recognition Complex
P/S	Penicillin/Streptomyocin antibiotic

P1, P5, etc.	Post Natal Day 1, 5, etc.
PBS	Phosphate buffered saline
PCR	Polymerase chain reaction
PFA	Paraformaldehyde
pH	negative log [H^+] (acidity measurement scale)
pHLIP	pH Low Insertion Peptide
PI	Post Injury
PBS	Phosphate Buffered Saline
PBST	Phosphate buffered saline with Triton X
PNS	Parasympathetic Nervous System
ProtK	Proteinase K
qPCR	quantitative PCR
RA	Right atrium
$Rb^{+/-}$	RPMI medium with B27 +/- insulin
RNA	Ribonucleic acid
RNAseq	Ribonucleic acid sequencing
rpm	revolutions per minute
RT	Room Temperature
RV	Right ventricle
S	Synthesis (cell cycle phase)
SCF	SKP1-CUL1-F-box protein ubiquitin ligase complex
SD	Sprague Dawley strain of rats
SHF	Second Heart Field
Skp1	S-phase kinase-associated protein 1
SMC	Smooth Muscle Cell
SV	Stroke Volume
TBE	Tris-borate-EDTA buffer
TE	Tris-EDTA buffer
Wnt	Wingless-related integration site (Wnt signalling pathway)

CHAPTER 1

Introduction

1.1 HEART DISEASE AND FAILURE – WHY IS THIS A SIGNIFICANT PROBLEM?

With ischaemic heart disease being a leading cause of morbidity and mortality worldwide, research into the mechanisms of cardiac repair and regeneration is being actively pursued with the aim of finding therapies that may have translations to the clinic. Human patients that suffer a myocardial infarction (MI), or "heart attack", are unable to replace the lost or damaged heart muscle with new functioning tissue. This loss constitutes billions of cardiomyocytes and can be up to 25% of heart tissue mass. Instead of replacing or regenerating this lost myocardium, a permanent, non-contractile fibrotic scar is laid down in its place to prevent heart rupture in the weakened area. The result is compensatory function and pathological remodelling of the remaining viable myocardium, with irreversible ventricular chamber dilation and thinning of the heart wall. This may ultimately lead to congestive heart failure.

1.1.1 Cardiovascular disease in the UK

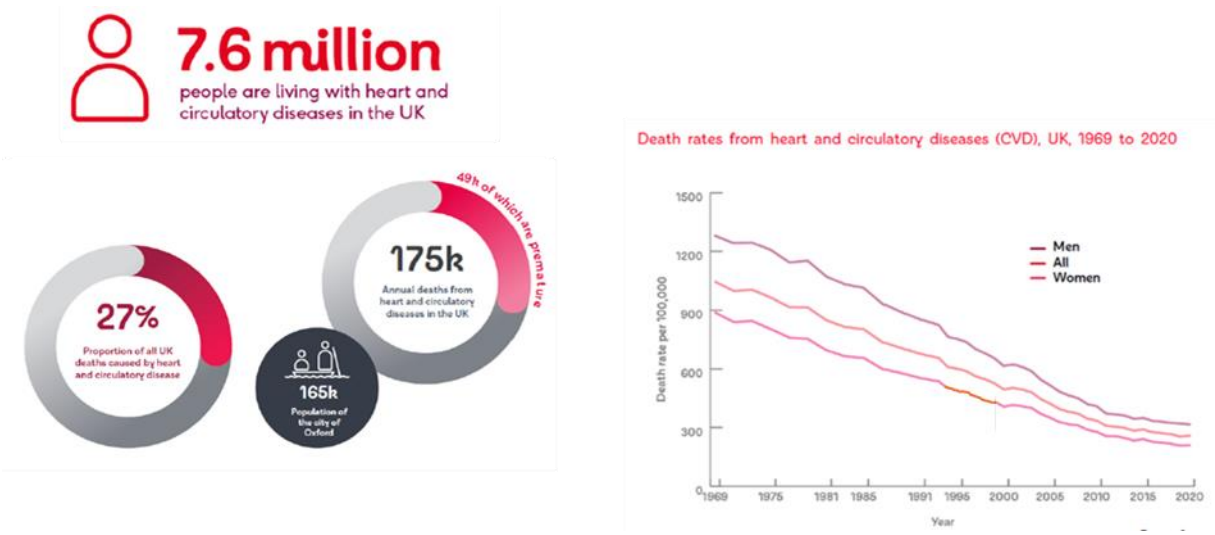

Figure 1: Statistics on heart and circulatory diseases in the UK, from the British Heart Foundation website, numbers updated for 2022 (left). The graph on the right shows how the death rate has dropped since 1969, although these figures are increasing slightly since the Covid-19 pandemic of 2020 with both men and women affected. From British Heart Foundation factsheet (UK CVD), September 2024.

Clinical advances in treatment of heart disease and especially timely interventions after MI have resulted in significantly fewer immediate mortalities (7 out of 10 people usually survive the initial injury, the death rate is now ¾ less than in 1969, see Figure 1) but that translates to many more people living with chronic heart disease for longer, with an increasing burden on health care

provision in many countries including the UK (BHF 2024). There are approximately twice the number of people living with heart disease than with cancer and neurodegenerative disease combined, and these people are 2-3 times more likely to have a stroke (Figure 2). An ageing and growing population adds to the burden, with a million more people estimated to be living with heart and circulatory diseases by 2030, and 2 million more by 2040. To give a local perspective to the numbers, today in the UK 480 people will die from heart or circulatory disease and ¼ of them will be younger than 75. Annually, this loss is more than the population of Oxford city.

Deaths from and numbers living with heart and circulatory diseases (CVD)

Nation	No. of People Dying from CVD (latest)	No. of People Under 75 Years Old Dying from CVD (latest)	Estimated Number of People Living with CVD (latest estimate)
England (2022)	142,638	39,112	6.4 million
Scotland (2023)	17,787	5,313	730,000
Wales (2022)	9,565	2,734	340,000
Northern Ireland (2022)	4,079	1,131	225,000
UK total (latest)	174,594	48,662	7.6 million

Figure 2: BHF analysis of official statistics – numbers are per year. Living with CVD estimates on latest health surveys with CVD fieldwork and GP patient data. From British Heart Foundation factsheet (UK CVD), September 2024.

1.1.2 Global effects of cardiovascular disease

An American Heart Association analytical study from 2020 estimated 36% of men and 47% of women aged over 45 that have heart disease or stroke will die within 5 years (Virani, Alonso et al. 2020, Huang, Huang et al. 2023). On a worldwide scale, it is obvious that CVD (cardiovascular disease) has a devastating effect as outlined in Figure 3. Of additional concern is that the burden falls disproportionately on regions that can least afford it with the age-standardised death rate in Micronesia over 10 times higher than that of Japan and San Marino as an example (BHF 2024).

GLOBAL HEART & CIRCULATORY DISEASE PREVALENCE & DEATHS (2021)				
	DISEASE PREVALENCE (million)		DEATHS (million)	
	2019	2021	2019	2021
N. AMERICA	46	50	1.1 (33%)	1
S. AMERICA	32	48	1 (28%)	1.1
EUROPE	99	115	4.1 (46%)	3.8
AFRICA	58	70	1.7 (19%)	1.8
ASIA & AUSTRALASIA	310	355	11 (36%)	12.5
WORLDWIDE	550	640	19 (34%)	19

Figure 3: Statistics for international prevalence of heart and circulatory disease and deaths around the world (2019 and 2021). Both the prevalence and death rate changes but in different directions depending on geography. Note the

% figures in the 2019 deaths column are % of total deaths (that data was unavailable for 2021). From British Heart Foundation factsheet (Global CVD), September 2024.

The health and social care cost for the NHS in England alone is estimated at £12 billion with wider economic costs nearly £28 billion per year (Gov.uk website, 2023). In the US, this figure tops $200 billion (Centres for Disease Control, 2021). These massive sums will only increase as the disease burden of an aging population combines with other factors such as increasing prevalence of Type II diabetes triggered by bad diet, sedentary lifestyles and obesity. The NIH alone invests $40 billion a year in medical research, $5 billion on heart disease, with more than three times that coming from other sources such as the medical products industry and various foundations, non-profit and patient groups (NIH, 2023; Nicholls 2018). In the UK, the medical research budget has dropped recently to approximately £1.6 billion.

1.1.3 Mitigating the effects of heart disease

These figures demonstrate the significant impact that ischaemic heart disease has on society. Along with the clinical interventions that are now available to mitigate the immediate effects of a heart attack (such as reperfusion through or around the blocked artery, with a balloon catheter and possibly a stent, and careful strategies to minimise reperfusion injury, use of thrombolytics and fibrinolytics), and longer term treatment of heart disease (with drugs such as beta blockers, calcium channel blockers, ACE inhibitors along with lifestyle modifications), research worldwide is aggressively pursuing more direct methods to reduce and eventually eliminate the impact. With the extremely limited option of organ transplant the only current "cure" for heart failure, other strategies need to be explored. One of these strategies is genuine regeneration of the dead or damaged myocardium by replacing it with new functioning cardiomyocytes that are fully integrated into the beating structure of the heart, without the need for further surgical procedures or pharmacological treatments. Some of the regenerative strategies being pursued in cardiovascular medicine include injection of stem cells, either directly or incorporated into various scaffolds, with the hope they will incorporate into the existing myocardium and either transdifferentiate into cardiomyocytes themselves or, through the release of targeted paracrine factors, promote the differentiation of other cardiac cell types such as fibroblasts into cardiomyocytes. In addition, they may possibly stimulate cell division and growth of existing cardiomyocytes. Developmental cues may be informative for regeneration by outlining how the heart first forms and which pathways, specific proteins, transcription factors, etc are essential to generating functional myocardium, and

suggesting which may be "temporarily turned back on" to facilitate growth of new tissue for repair (Davidson, Padro et al. 2021, Guo, Yang et al. 2023, Lawrence and Wilson 2024). In 2011, a landmark study by the Porrello group identified the first known example of mammalian heart regeneration in a study of the neonatal mouse pup (Porrello, Mahmoud et al. 2011). An array of models to investigate the potential of neonatal heart regeneration is available and these are discussed below to highlight developments in this field.

1.2 MODELS OF HEART REGENERATION

Various models of heart damage and disease have been studied over the last decades, especially with a view to facilitate regeneration of mammalian heart tissue and regain lost function after injury. Non-mammalian and mammalian systems are mentioned in brief here - for this thesis, the animal model of interest is the mouse (and to a much lesser extent, rat) and human induced pluripotent stem cells differentiated into cardiomyocytes in vitro.

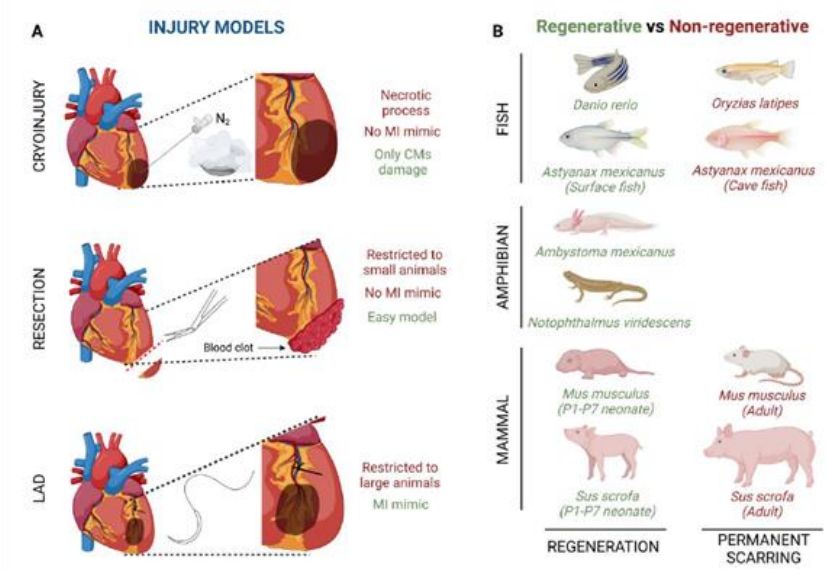

Figure 4: (A) Injury models of myocardial infarction and (B) interspecies comparisons of heart regenerative and non-regenerative capacity. *Taken from "Comparative analysis of heart regeneration: Searching for the key to heal the heart"* (Castillo-Casas, Cano-Carrillo et al. 2023)

1.2.1 NON-MAMMALIAN MODEL SYSTEMS

Amphibians

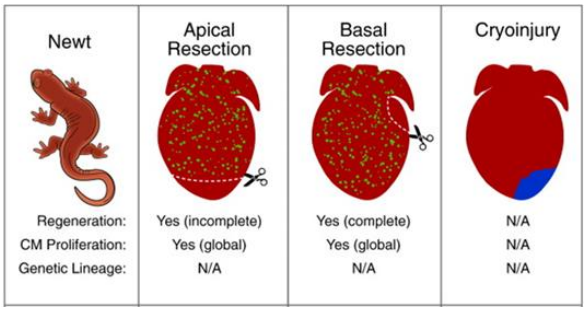

Figure 5: Newts and salamanders are one the earliest known examples of animal regeneration. Adapted from *"A neonatal blueprint for cardiac regeneration"* (Porrello and Olson 2014).

Regrowth of lizard tails that had been lost was first discussed in the 17th century, making it one of the original examples of regeneration. An age-dependency of tail regeneration in tadpoles and salamanders was noted in a treatise by Spallanzani in 1768. Moving forward, proliferation of cardiomyocytes was reported as early as the 1970s in the newt, and by the '90s proper studies detailed heart growth and regeneration in urodeles (Neff, Dent et al. 1996). They have remained a popular model that possesses a high degree of regenerative capacity (Godwin and Rosenthal 2014, Godwin, Debuque et al. 2017). With simulation from mitogens, cardiomyocytes from adult newts readily re-enter the cell cycle, dedifferentiate and either become multi-nucleated or properly divide into new CMs (there is heterogeneity in the response). This may happen via initial formation of a blastema, a region of dedifferentiated cells close to the wound area. These newt cells are extremely plastic and may even form other types of muscle or even cartilage and bone if they are transplanted elsewhere in the body (Ausoni and Sartore 2009, Zhang, Mignone et al. 2015). Other regenerative urodele amphibian models include the axolotl, with anuran amphibians such frogs and toads showing partial repair and scarring much like mammals (Jewhurst and McLaughlin 2015). Some years ago, studies were performed on isolated perfused frog (*Rana ridibunda*) hearts to determine the effects of $CoCl_2$, a hypoxia mimetic which stabilises the hypoxia-inducible factor HIF-1α. They saw increased activation of protective pathway proteins, including p38-mitogen-activated-protein (MAP) kinase, which may help adapt the cardiac tissue to low levels of oxygen (such as may occur during periods of winter hibernation) (Gaitanaki, Kalpachidou et al. 2007). However, they previously showed that complete hypoxia does not activate p38-MAPK (Aggeli, Gaitanaki et al. 2001). But $CoCl_2$ has side effects other than just mimicking hypoxia: $CoCl_2$ directly produces reactive oxygen species (ROS) (Moorhouse, Halliwell et al. 1985, Goldberg, Dunning et al. 1988,

Wang, Yokoi et al. 1993) so the interactions are complex. This same group has also looked at the effect of extracellular pH changes in this model, finding that alkalosis maximally activated the p38-MAPK pathway within 2 mins of perfusion while acidosis also activated it but at a lower level for a longer period (Stathopoulou, Gaitanaki et al. 2006).

Zebrafish (Danio rerio)

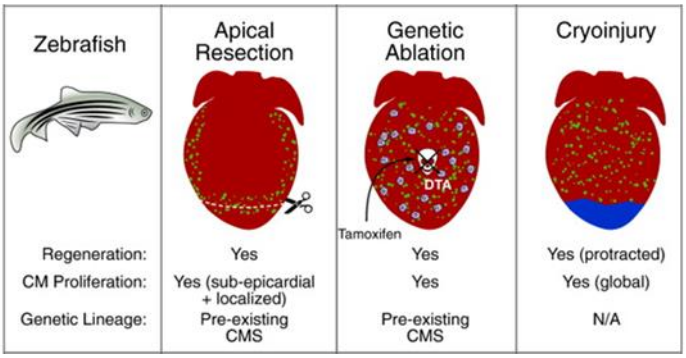

Figure 6: A widely used non-mammalian model system is the zebrafish. Studies show extensive regeneration of damaged tissues including the heart with functional recovery after different types of injury. It has been shown that the major source of new cardiomyocytes is proliferation of existing cardiomyocytes. Adapted from *"A neonatal blueprint for cardiac regeneration"* (Porrello and Olson 2014).

The zebrafish is very widely studied in heart (and other organ) regeneration, from as early as 2002 (Poss, Wilson et al. 2002) to this day (Apaydin, Altaikyzy et al. 2023, Huang, Huang et al. 2023, Singh Angom, Wang et al. 2023, Bouwman, de Bakker et al. 2025). Various models of myocardial infarction such as tissue resection (where up to 20% of the tip of the ventricles is cut away) to cryoprobe induction of damage (leaving the dead tissue intact) and genetic ablation with the use of inducible models to selectively destroy a subset of cardiomyocytes are used to probe different aspects of tissue restoration and functional recovery (Marques, Lupi et al. 2019). Hearts from animals up to 2 years old recover very well from these types of injuries. The amount of time it takes for this recovery depends on the degree of the initial insult, for instance, larger amounts of tissue resection take considerably longer to recover, but "scar" tissue laid down to prevent blood loss immediately after resection or the dead tissue where the cryoprobe has impacted is eventually replaced with new, fully integrated and functional heart tissue. This "scar" tissue, composed mostly of fibrin with very little collagen deposition unlike a mammalian scar, forms after a massive erythrocyte clot which blocks the initial cut across the ventricle (Gonzalez-Rosa, Burns et al. 2017). In turn, this is replaced by new cardiac myofibrils originating from the epicardial edge of the heart. It was determined that these new cardiomyocytes originated from existing cardiomyocytes undergoing cell proliferation (Jopling, Sleep et al. 2010, Wang, Panakova et al. 2011, Gemberling, Bailey et al. 2013).

Besides the heart, the zebrafish can also regenerate its fins, kidney, spinal cord, retina and even its telencephalon, making it a very useful model for studying regenerative mechanisms in these other organs for possible insights into heart regeneration. CHIPseq data show that at least some regenerative response enhancers were common to fin and heart regeneration (Kang, Hu et al. 2016), and other studies show common pathways involved in fin, hair cell and liver regeneration (Gemberling, Bailey et al. 2013, Marques, Lupi et al. 2019).

Although this model has remarkable regenerative potential, there are limitations due to the substantial differences in heart morphology and the physiological environment the heart functions within when compared to mammals. The fish heart only has two chambers, one ventricle and one atrium and there is only a single circulatory system pumping fluid around the body under a lower pressure, whereas mammals have a four chambered heart with a double circulatory system – one going to the lungs for re-oxygenation and the other carrying this re-oxygenated blood systemically around the body and at higher pressures. This double system is far more complicated developmentally, and this may be a factor in the more challenging regenerative potential. Other differences include the fact that the fish heart operates under a much lower oxygen tension than the mammalian heart (Singleman and Holtzman 2012), and cardiomyocytes retain the ability to divide throughout the lifetime of the organism, conspicuously remaining mononucleated (Dimasi et.al 2023). There are significant genetic differences with only 62% of mouse protein-coding genes having a corresponding zebrafish orthologue (Giffen, Liu et al. 2019, Potts, Stockdale et al. 2021). Thus, discoveries in this model may have limited applicability to the treatment of human diseases. Despite these limitations, a very interesting cross-species study bridging the gap between fish and mice by Chen et al. injected decellularised zebrafish extracellular matrix (zECM) into an injured adult mouse heart. They found mouse CM re-entering the cell cycle and proliferating, with cardiac functional recovery and even some tissue regeneration. Comparing the ECM between zebrafish and mouse (mECM) showed significant differences in composition: mECM contained a lot of collagen, while zECM had more elastin and fibronectin, as well as fibrinogens, fibrillin and periostin (Chen, Wang et al. 2016). A recent study comparing CM in the border zones of injured zebrafish and mice showed differentially expressed gene Hmga1 activated regenerative programs by clearing repressive histone marks (H3K27me3) in the fish but this did not happen in the mice. When this gene was overexpressed in mouse border zone CMs, it increased proliferation and functional recovery (Bouwman, de Bakker et al. 2025). Ectopic application of Hmga1 in neonatal rat ventricular myocytes (NRVMs) also increased their proliferation.

Cavefish (Astyanax mexicanus) and medaka (Oryzias latipes)

Another useful teleost fish model is that of the Mexican cavefish, *Astyanax mexicanus*, because this provides us with an interspecies comparative model: two members of the same family, "surface fish" and "cavefish", have drastically different responses to heart damage. The surface fish regenerate their hearts like zebrafish, but cavefish are groups that ended up stranded deep in riverbank caves and over time lost their eyes, pigmentation, slowed their metabolism to survive in a nutrient poor environment, and importantly, they also lost the ability to regenerate damaged myocardium (Stockdale, Lemieux et al. 2018, Tang, Guo et al. 2018, Koth, Wang et al. 2020, Nguyen, Gooijers et al. 2023, Carey, Hollins et al. 2024). This is much like another teleost fish, medaka, *Oryzias latipes*, which also does not regenerate. It is useful to study these closely related, age-matched examples to compare more directly why, where and what the differences might be to cause this disparate response to the same stimuli. RNAseq data comparing medaka and zebrafish show that one of the major differences is in the immune response to heart resection injury: the medaka response is much less, with macrophage infiltration delayed and fewer in number but neutrophils persisting longer. Experimentally manipulating this response to make it more robust improved the regenerative response of the medaka, and made it more like that of the zebrafish, with increased cardiomyocyte proliferation, neovascularisation and scar resolution (Potts, Stockdale et al. 2021, Carey, Hollins et al. 2024, Bouwman, de Bakker et al. 2025)

1.2.2 MAMMALIAN MODEL SYSTEMS, SMALL AND LARGE

Small mammalian models of heart disease and regeneration are arguably the best, most versatile model available to investigate basic mechanisms of myocardial damage and test potential therapies (Camacho, Fan et al. 2016). Rodent models are relatively inexpensive and easy to work with and have established protocols for handling, surgery and disease representations that are internationally recognised, with a large body of peer-reviewed publications to facilitate further research (Lam and Sadek 2018, Fine 2019, Price, Vieira et al. 2019, Weinberger 2019, Bouwman, de Bakker et al. 2025). However, as good as rodent models are, some differences do exist between them and the ultimate goal of understanding what happens in the human heart, and the larger animal models such as dogs, sheep, pigs and non-human primates bridge this gap (Camacho, Fan et al. 2016). They have organ systems which are more like ours, not only in size but with important physiological responses to surgical manipulation and treatment regimes. However, they also have a longer gestation period, become sexually mature later, and require more resources for

maintenance, so by necessity are used in far fewer numbers than rodents or non-mammalian models.

Small model - Mouse:

Mice have been used extensively to study heart disease. They can be genetically manipulated to provide a range of variants that embody desired research characteristics such as up- or down-regulation of certain proteins or entire pathways, expression of specific markers, and can mimic many disease situations (Guo, Yang et al. 2023). Advanced genetic engineering technologies such as CRISPR, Cut&Run, etc are making such models more accurate and prevalent, further enhancing their usefulness for research (Liu and Olson 2022). Practically, mice have a short gestation period, reach sexual maturity in 3-4 weeks and may be bred from 6-8 weeks old, reliably producing large litters that retain the desired traits into the next generation. Most importantly, the majority of genes and metabolic pathways are common to mice and men, conferring biological and physiological similarities between the two systems, and thus are very useful for basic research into mechanisms of disease as well as normal growth and development (Weinberger 2019, Guo, Yang et al. 2023).

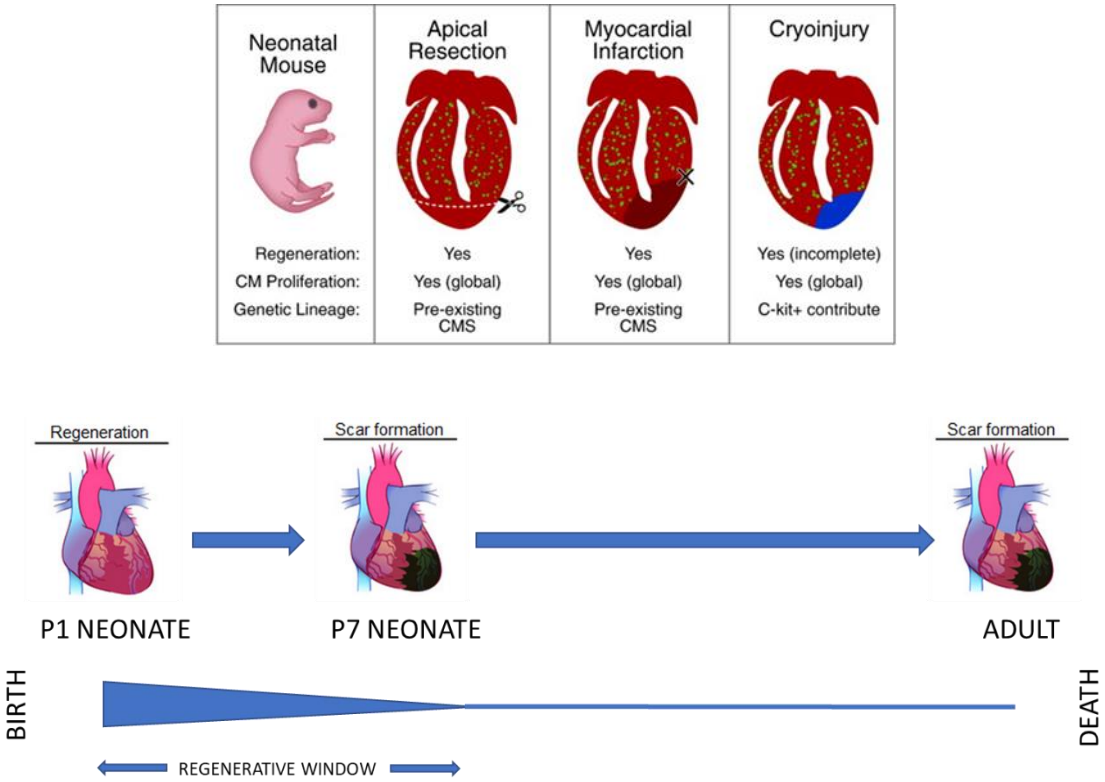

Figure 7: Neonatal mouse as a regenerating mammalian model of recovery after heart damage. Top: various injury protocols have been used to monitor regenerative abilities in mice from 1 to 10 days old. Bottom: It has been shown that a P1 pup can recover from MI injury with minimal tissue damage and full functional recovery whereas a P7 pup shows the adult response of permanent injury with progression to heart failure. This is called the "regenerative window". Adapted from *"A neonatal blueprint for cardiac regeneration"* (Porrello and Olson 2014).

Mouse models of heart regeneration have been popular since the Porrello study in 2011 (Porrello, Mahmoud et al. 2011). They showed neonate heart regeneration for the first time with an apical resection protocol performed on P1 pups: the injured area (they removed approximately 15% of the apical tip of the heart) is initially plugged by a large blood clot which is resolved within 21 days, being replaced with functional, normal myocardial tissue. The events leading to regeneration were very similar to those observed in the zebrafish, from clot formation, epicardial activation, inflammatory cell recruitment to the injury, to CM proliferation and functional recovery. This regenerative response was lost by P7, coinciding with CM loss of proliferative capacity. Later studies used the more clinically applicable model of myocardial infarction which is the leading cause of heart failure in humans (Haubner, Adamowicz-Brice et al. 2012, Mahmoud, Porrello et al. 2014). These studies induced infarction by LAD ligation. Cryoinjury has a different mechanism of action, and the recovery process differs somewhat, but if done early it can still result in nearly complete regeneration (Jesty, Steffey et al. 2012). This is comprehensively reviewed by Lam & Sadek where they compare methods of injury as well as extent of initial damage and note any resulting regeneration (Lam and Sadek 2018).

Isolated primary murine cardiomyocytes are also widely used to study various physiological cellular properties, despite adult cells not lasting more than a day or two after enzymatic dissociation. Embryonic to neonate mouse cells may be cultured for a week or longer and are often used to test small molecule and drug interactions *in vitro*. However, some significant differences may appear in response to certain drugs between mouse and human models, and next phase testing in larger animal systems is always necessary. The mouse model is discussed further in each research chapter, with an emphasis on LAD ligation-induced MI injury and cell cycling activity under various conditions and how these effect myocardial regeneration.

Small model - Rat:

Rats are also used for heart disease models and have similar but not identical responses to surgical manipulation as mice. They too are amenable laboratory test subjects with comparable husbandry requirements but with far fewer genetically altered strains available, although this is slowly changing. Historically, rat hearts were widely used in ex vivo organ studies, particularly on reverse perfusion Langendorff systems. Neonatal rat ventricular myocytes (NRVMs), like those from neonatal mice, are regularly used for primary culture assays. Rats have also been used in LAD ligation models of MI where P1 neonatal rats were injured and showed regeneration with minimal scarring and functional recovery three weeks later (these rats underwent echocardiography at 1 day

and 1,2,3 weeks after surgery). When LAD was performed on adult rats in this same study, they saw significant adverse effects of thinning LV wall and LV dilation with reduced ejection fraction (Wang, Paulsen et al. 2020).

Large model - Sheep:

In sheep, like other large mammals, cardiomyocyte proliferation is mostly complete just prior to birth with only 1% of cardiomyocytes still active in the cell cycle (Jonker, Louey et al. 2015). Binucleation starts about 2/3 of the way through the 152 day pregnancy, and cell hypertrophy also begins before birth, so both mechanisms of hyperplasia and hypertrophy contribute to the increase in heart size towards the end of gestation. It is interesting that there is a significant degree of cardiomyocyte apoptosis in the six weeks immediately after birth, so there is an adjustment in cell number before the final allocation is reached, but because of the hypertrophy the remaining cells are much larger. Nevertheless, there have been reports of normal function one month after MI injury in foetal sheep hearts (Allukian, Xu et al. 2013, Zgheib, Allukian et al. 2014) although this was at 65 to 76 days gestation, prior to the age where cardiomyocyte cell cycling declines (Jonker, Louey et al. 2015).

Large model – Pigs:

Gestation in pigs is approximately 115 days, slightly shorter than that of sheep, but similarly most CM have withdrawn from the cell cycle by birth, but with some cycling cells remaining up to 30 days. However, this mostly results in binucleation rather than proliferation of new cells. CM are fully mature within six months when bi- or multinucleation (up to 32 nuclei per CM has been observed) is nearly complete, cells are hypertrophied with mature sarcomeres and cell cycle arrest (Velayutham, Alfieri et al. 2020). The pig has recently become a validated large animal model for basic and clinical heart research that also demonstrates neonatal regeneration after MI (Ye, D'Agostino et al. 2018, Price, Vieira et al. 2019, Spannbauer, Mester-Tonczar et al. 2020, Velayutham and Yutzey 2022, Nguyen, Rosa-Garrido et al. 2024).

Large model – Non-human primates (NHPs):

Less is known about regeneration after injury or CM regulation in this category of research animals than the previously mentioned ones, no doubt due to the difficult ethical considerations and complexity of working with primates as well as the high cost. NHPs are usually rhesus monkeys (macaques) but may include chimpanzees, baboons or even gorillas. These last three species have

CM that become multinucleated by approximately four years old but the macaques remain binucleated (Rumyantsev 1991). Problems with NHP heart research include high mortality after MI ischaemia-reperfusion test surgeries, and the need for strong immunosuppression after cell or tissue grafting, however, some promising work is being done with injecting stem cell progenitors into NHPs (Blin, Nury et al. 2010, Steinhauser and Lee 2011, Cheng, Hsieh et al. 2023).

Large model – Human:

Finally, the most relevant model system of all is the human heart, but the few studies directly using this model are limited and contradictory. One area that seems well studied is human cardiomyocytes. In humans, binucleated CMs appear at about 30 weeks, or ¾ of the way through the full term of 40 weeks (Kim, Kim et al. 1992). At birth, 8% of LV and 12% of RV (right ventricle) CM are binucleated, increasing to 56% and 42% respectively one year later (Schmid and Pfitzer 1985). Another study claims CM remain 74% mononucleated up to 26 years of age with only 25.5% binucleated. Regardless, the cardiomyocytes are terminally differentiated and these nuclei are definitely polyploid no matter how many exist in a cell, and thus the cell is unable to divide (Olivetti 1996). Some studies state limited proliferation (~0.04%) of neonatal CM may occur up to 1 year after birth but this is insufficient for any degree of damage repair. A 2013 study detected mitosis in 0.012% and cytokinesis in 0.003% of CM at 1 year but this was gone by 20 years (Mollova, Bersell et al. 2013), however often cited papers by Bergmann report an annual turnover of 1% up to 25 years of age, dropping to 0.3% by 75 years (Bergmann, Bhardwaj et al. 2009, Bergmann, Zdunek et al. 2015). Other studies have noted proliferation in 3 month old hearts (Amir 2008; Huttenback 2001; Silva 2012; Ye 2016). There is some suggestion that a degree of regeneration can occur in the unloaded heart. In patients fitted with a left ventricular device (LVAD), "reverse remodelling" may occur, and on occasion this is sufficient for the LVAD to be removed (Ihnat, Zimmerman et al. 2011, Miller, Lancaster et al. 2015). This suggests that when the workload on the heart is removed, the potential for cardiac regeneration may return. Indeed, work from the Sadek group showed that prolonged mechanical unloading induced adult human cardiomyocyte proliferation (Canseco, Kimura et al. 2015).

1.2.3 IN VITRO MODEL SYSTEMS OF HEART DISEASE AND REGENERATION

In vitro cardiac models are essential systems for many research groups as they enable the use of controlled environments to examine many aspects of cardiac physiology, from subcellular

molecular assays to whole hearts. Drawbacks of the cellular systems include loss of cell-cell communications and the multifaceted interactions of different cell types that are present in more complex models. Cell culture of isolated CM provides the most tractable systems but primary cells, the most useful model, are short-lived while transformed cell lines begin to diverge from true cardiac physiology. Tissue explants are useful intermediate cultures between cells and whole heart, with myocardial slices once again becoming popular as a valuable model retaining some of the intrinsic structure of the heart (Camelliti, Al-Saud et al. 2011, Ou, Jacobson et al. 2019, Watson, Terracciano et al. 2019). Whole hearts perfused on a Langendorff system (sometimes referred to as "ex vivo") where the excised heart is hung from a cannula inserted into the aorta, through which flow media and buffers to maintain tissue function are still regularly used for some aspects of physiological research (Bell, Mocanu et al. 2011, Yeo, Tse et al. 2017, Baark, Waters et al. 2024). The use of human stem cells in cardiac research provides an in vitro model that is highly relevant to basic and clinical studies. In particular, induced pluripotent stem cell-derived cardiomyocytes cultured in 2D or in engineered heart tissue constitute a vast body of current research (Eschenhagen, Ridders et al. 2022, Dark, Cosson et al. 2023, Clancy and Santana 2024). The use of hiPSC-CMs is discussed further in research chapter 5.

1.3 HEART IMAGING TECHNIQUES IN PRE-CLINICAL RESEARCH STUDIES

Non-invasive imaging plays an important role in preclinical cardiovascular research, allowing for the study of heart structure and function in rodent models without the need for terminal procedures. Several advanced imaging modalities have been adapted for small animal use, each offering unique strengths suited to specific research questions (Khan 2016, Lindsey, Kassiri et al. 2018).

High-frequency echocardiography is a widely used technique due to its real-time imaging capabilities and high temporal resolution (Zhou, Foster et al. 2004, Schoen 2021). Using ultrasound frequencies between 20–70 MHz, this method provides detailed visualisation of cardiac anatomy and function. It is non-invasive and fast, therefore regularly used in rodent heart studies, although results can be somewhat operator-dependent and offer limited soft tissue contrast compared to other modalities as no contrast agents are administered (Baudouy, Michiels et al. 2017, Ouyang, Xu et al. 2024). Transthoracic echo is the most commonly used method where the probe is placed on the shaved chest of the animal and measurements of left ventricle dimensions, wall thickness, ejection fraction and fractional shortening may be recorded. Using Doppler ultrasound,

echocardiography is used to measure the flow of blood through the mitral valve and thereby to determine diastolic function. In contrast to MRI, echocardiography requires manual placement of the ultrasound probe which means it is not possible to accurately image the full heart and approximations are required to measure volumes. This can lead to errors when the heart morphology is distorted such as after myocardial infarction (Stuckey, Carr et al. 2008, Roberts, Price et al. 2017). Interestingly, the use of anaesthesia for echocardiographic imaging in mice may be optional. Some studies have attempted it on conscious but carefully restrained mice that have been acclimatised to the experimental setup so that the slowing influence of anaesthesia on heart rate and other changes to cardiac function can be avoided (Yang, Liu et al. 1999). However, this would require significant modifications to the experimental protocol and would not be practical for neonate imaging.

Micro-computed tomography (micro-CT) provides high-resolution, three-dimensional anatomical imaging, particularly valuable for visualising cardiac structures and vasculature when contrast agents (barium- and iodine-based as well as gadolinium liposomes) are used. Though it delivers excellent temporal and spatial detail which enables high-throughput studies, its use is limited by radiation exposure and relatively poor soft tissue contrast in the absence of contrast enhancement (Badea, Hedlund et al. 2007, Clark and Badea 2021).

Nuclear imaging techniques such as micro-positron emission tomography (micro-PET) and single photon emission computed tomography (micro-SPECT) offer insights into cardiac perfusion, metabolism, and cell viability through the use of radiotracers. These modalities are particularly useful in studying ischemia, infarction, and metabolic alterations in disease models. However, their spatial resolution is lower than that of MRI or CT, and their use requires access to radiochemistry facilities and involves exposure to ionizing radiation (Tian, Smith et al. 2009, Thackeray and Bengel 2016).

Cardiac magnetic resonance imaging (MRI) is considered the gold standard for detailed structural and functional assessment (Ruff, Wiesmann et al. 1998, French 2008, Böhm 2022). It offers high spatial resolution and superior soft tissue contrast, enabling precise measurements of ventricular volumes, ejection fraction, myocardial strain, and tissue characterisation such as fibrosis if late gadolinium enhancement is added to the imaging protocol (Chen, Zheng et al. 2024). While highly informative and reproducible, cardiac MRI in rodents is time-intensive, costly, and requires

anaesthesia and specialised equipment. This imaging method was chosen for the basis of this thesis, and is discussed further in the first research chapter.

Together these imaging techniques provide a comprehensive toolkit for investigating cardiovascular biology, physiology and pathology in rodent models, and the choice of modality should be determined by the study's requirements and/or restraints.

1.4 HEART DEVELOPMENT & POINTS OF CONSIDERATION FOR REGENERATION

Heart development is studied to inform research into processes that may provide insight into regeneration of the diseased and/or damaged adult heart.

1.4.1 Early heart development

The complicated process of heart development begins very early, with the heart being one of the first organs to function in the developing embryo (Figure 8). In humans, the earliest heartbeats can be detected 5-6 weeks after fertilisation and a functional, albeit immature, heart and vascular system develops by 8 weeks (Doyle, Lohr et al. 2015, Aguilar-Sanchez, Michael et al. 2018, Tan and Lewandowski 2020).

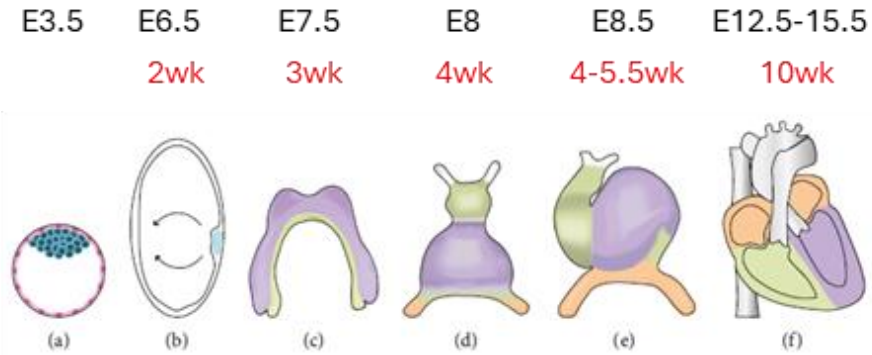

Figure 8: Summary of mouse heart development with approximate human timeline (shown in red). (a) blastocyst; (b) gastrulating embryo showing mesoderm (arrows); (c) first and second heart field myocardial progenitor cells migrate to the form the cardiac crescent; (d) the cardiac crescent fuses at the midline forming a tube; (e) looping positions the tube areas where the chambers will develop; (f) septation and development of cardiac valves produces 4 distinct chambers. *Adapted from "Cardiac stem cells in the post-natal heart: Lessons from development",* (Aguilar-Sanchez, Michael et al. 2018) *(mouse); "h*iPSC-*CM as a model for heart development and congenital heart disease"* (Doyle, Lohr et al. 2015)(human).

A mouse heartbeat can be seen at embryonic day 8.0 (E8.0), even before the organ is fully developed (Tyser, Miranda et al. 2016). Early heart development begins with primitive streak mesoderm providing myocardial progenitor cells. These first and second heart field cells, along with cells from the proepicardium and cranial neural crest, migrate to form a simple cardiac tube. This tube elongates and loops over and around itself as more cells are added. The final configuration of 4 chambers results from septation of this expanded tube with cardiac valves controlling the direction and timing of blood flow through the heart and body (Wessels and Sedmera 2003, de Boer, van den Berg et al. 2012, Sylva, van den Hoff et al. 2014, Doppler, Lange et al. 2017). After this initial period of organ development, the immature heart grows via hyperplasia, the proliferation and division of existing cardiomyocytes. In large mammals, at birth or even shortly before birth, this switches to hypertrophic growth where the size of each cardiomyocyte increases and cell cycle activity is much reduced (Bergmann, Bhardwaj et al. 2009, Jonker, Louey et al. 2015). In rodents, this occurs towards the end of the first postnatal week (Porrello, Mahmoud et al. 2011, Porrello and Olson 2014, Galdos, Guo et al. 2017). It is important to note that cardiomyocytes constitute 70-85% of total heart volume, and that there are other cell types present right from the beginning: in the ventricles, only 50% (by cell number) of the myocardium is composed of functional beating cardiomyocytes, and this drops to 30% in the atria, a region that does not need to pump as strongly as the ventricles. Fibroblasts and endothelial cells make up the remainder, with a few immune and smooth muscle cells present in small amounts (Zhou and Pu 2016, Quaife-Ryan, Sim et al. 2017).

1.4.2 Later heart development – postnatal maturation in the mouse

The neonatal heart undergoes many developmental changes during the first few weeks after birth, a period that extends for months in humans. Growth and maturation continue as the organ adjusts to the increasing demands of life outside the womb, with sudden changes in blood pressure, oxygen levels and nutrient sources. Human development is reviewed elsewhere (Sylva, van den Hoff et al. 2014, Buijtendijk, Barnett et al. 2020). Here we briefly discuss a few selected points illustrating the main changes between P1 to P7 in response to these and other environmental factors in our model organism, the mouse. This time period corresponds to the "regenerative window" during which different degrees of cardiovascular tissue recovery and regeneration occur following myocardial infarction and other types of injury.

Oxygen levels

A foetus develops in a relatively hypoxic environment in utero, which transitions abruptly at birth to a normoxic, oxygen-rich environment. It has been suggested that this is a major factor in triggering cell cycle arrest (Puente 2014; Nakada 2017). Rodent lungs are not fully mature at birth and thus they are mildly hypoxic for 3-7 days after, allowing a degree of cardiomyocyte proliferation (Lock 2013; Pringle 1986). Note that in sheep and humans, CM exit the cell cycle when oxygen levels are low, from 20-35mmHg which happens during late gestation (Duan 2017; Soothill 1986), but pigs retain some proliferative ability immediately after birth (Velayutham 2020; Yin 2020). Thus oxygen has an effect but may not be the main factor in this switch, and it definitely has different effects in different species.

Metabolism

Rapid growth of the neonatal heart is needed to supply a growing body with more nutrients. The heart itself also requires a lot of energy for continuous beating, nearly 6kg of ATP per day. In combination with the sudden switch from the hypoxic womb to the high oxygen tension after birth, this pushes changes in metabolism such as more reliance on oxidative phosphorylation over glycolysis. Immature cardiomyocytes use glucose as their main energy source and produce ATP anaerobically, however only a small amount of ATP can be generated from one molecule of glucose, so it is relatively inefficient. After birth, fatty acids, which are now abundant in the bloodstream due to suckling (they do not cross the placenta well so levels are low in utero (Piquereau and Ventura-Clapier 2018)), are broken down via beta-oxidation to produce acetyl-CoA (a 2-carbon molecule, 2C) which joins oxaloacetate (4C) to produce citrate (6C) and start the citric acid (Krebs) cycle. The enzymatic chain reactions of this cycle release ATP directly but also generate the electron carriers NADH and $FADH_2$ (3 and 1 molecule respectively) and 3 hydrogen ions (H^+) which proceed to the electron transport chain where the vast majority of ATP is formed (Dimasi, Darby et al. 2023). This part of the energy production process is dependent on oxygen, so happens only in aerobic conditions (Zheng 2012). This increase in oxidative metabolism is associated with an increase in mitochondria in the first weeks after birth, which in turn is associated with the generation of reactive oxygen species. ROS-induced DNA damage has been linked to the decreased proliferation of cardiomyocytes in the postnatal heart (Puente, Kimura et al. 2014).

Cell composition

Cardiomyocytes and other cells such as fibroblasts, endothelial, epicardial, vascular smooth muscle, neural crest and immune cells are the major cell types constituting heart tissue, and their relative populations change significantly in number and character during development and postnatally (Grandi, Navedo et al. 2023). They all have pivotal roles in the correct development and maturation of the heart and problems can lead to heart defects or lethality. Studies vary in their reported percentages of each cell type but a couple of key papers in murine and human hearts say it contains 60% endothelial cells and less than 20% fibroblasts, with cardiomyocytes making up only 25-35% (Pinto, Ilinykh et al. 2016, Gunthel, Barnett et al. 2018). One particularly interesting reference examined how cardiac cell types formed locally organised "cellular communities" which changed during human heart development. Combining single-cell RNA sequencing with multiplexed fluorescence in situ hybridisation, they revealed a diverse range of cell populations, many with their own sub-populations, across the heart which spatially organise into zones ("neighbourhoods") to form cardiac structures (Farah, Hu et al. 2024). An in-depth discussion of cell types is beyond the remit of this thesis.

Cardiomyocyte cell cycle activity

This is covered in depth in the research chapters 4 and 5.

1.5 THESIS AIMS AND RESEARCH SUMMARY

Aim 1: Show conclusively that early neonatal hearts regenerate using a modified MRI protocol (Research Chapter 1)

When we began this project, there was still considerable controversy over the recently discovered phenomenon of mammalian heart regeneration, including its extent and timeframe. Previous studies used the standard approach of sacrificing specimens at certain times after MI surgery in P1 and P7 neonatal mice and using histology to show that P1 pups regenerated damaged tissue and regained heart function whereas P7 pups did not, instead showing the adult response of scarring, permanent myocardial damage and reduced heart function. We wanted to prove regeneration occurred by following the same animal through three weeks of post-surgery monitoring by repeated MRI scanning at Days 4, 7, 14, and 21, sacrificing only at the experimental endpoint. This also allowed mapping of developing functional parameters in previously unknown detail by using

the sham cohorts. To do this required considerable modifications to the adult mouse MRI protocols with new hardware and a faster, retrospectively gated scanning software. This work was published in Circulation (2018, first author), and was presented at several conferences.

Aim 2: Use Fucci mice to examine cell cycle activity, comparing P1 to P7. Determine if this changes after MI injury as a prelude to regeneration. Also see if we can map areas of changing pH in the developing heart and if these can be shown to reoccur after injury (Research Chapter 2)

Previous studies have examined the areas immediately surrounding the damaged tissue after MI for evidence of changes in cell cycle activity, however, we could not find any which examined the entire four-chambered section of the heart, including regions remote to the injury site as well as the atria, and directly compared the regenerative with the reparative situation. Using the Fucci mouse model to identify cell cycling in the heart, we identified differences between cycling cell areas in the P1 and P7 heart after injury. The second aim was to see if we could apply the use of a tissue acidity marker, pHLIP (pH Low Insertion Peptide) previously used in the cancer research field, to map changes in acidity across the developing mouse heart from P1 through to adult and also to confirm that this shows a drop in pH in the immediate injury area after myocardial damage.

Aim 3: Modulate the environment of isolated P1 and P7 Fucci mouse CM to monitor changes in cell cycle activity due to hypoxia and acidity. Test if hiPSC-CM respond in a similar manner. (Research Chapter 3)

The first two chapters used the neonate MI injury model to investigate differences between P1 and P7 CM. This chapter used isolated P1 and P7 Fucci neonate CMs cultured under controlled environmental conditions to see how cell cycling was affected by direct manipulation of pH and hypoxia. These cells were imaged over a week of culture. We also differentiated IMR90 induced pluripotent stem cells into CM and cultured them in similar conditions. We stained the cells for cell cycling and contractile protein markers, and used RT-qPCR to monitor differences in response to these changes.

1.6 OUTLINE OF THE THESIS

Chapter 1 is the general introduction to the topic of heart disease and why it is a significant problem in the UK and around the world. It also briefly discusses some of the models used to study this problem and offers a summary of heart development used to guide these studies. Chapter 2

outlines the general materials and methods used throughout the thesis. Research chapters 3, 4 and 5 include novel materials, methods and specific experimental protocols and experimental results. These three research chapters, being somewhat distinct, have their own introductions and results discussion sections. Finally, in chapter 6, the main findings are very briefly summarised. Publications from this thesis are included in the appendices along with detailed research protocols and supplementary information.

CHAPTER 2

General Methods

Much of this thesis was the development and testing of new, custom protocols to investigate different parameters of heart growth and response to injury. These are detailed in the Method Development and Results sections of the research chapters. We also used several standard laboratory procedures which are outlined below.

2.1 Animal models

2.1.1 Mice breeding and maintenance

All mice were housed in dedicated animal care facilities at the University of Oxford with controlled temperature, humidity, light and noise levels (12 hour light/dark cycle, 20°C, 50% humidity). Food (regular mouse chow) and water were available ad libitum. Four to six animals of the same sex were kept in a cage, unless it was for breeding purposes (see below).

Breeding was done as pairs or trios (two females to one male), and plug checking was done every morning to estimate date of delivery in order to prepare for P1 and P7 procedures. The males were removed from the breeding cages after plugging (designated as embryonic day E0.5) or shortly before birth, and pups were weaned approximately 18-21 days after birth. Further details for specific breeding strategies for genetically modified strains are detailed below. All adult mice were routinely ear-clipped for identification and/or genotyping. Fucci litters were genotyped at P1-P3 by fluorescence emission which is described in Chapter 4. Pups were not clipped or individually identified, except for the MRI study which is outlined in Chapter 3.

All tissue samples were harvested by approved Schedule 1 methods. Mice were sacrificed by age-appropriate cervical dislocation (adults) or hindbrain destruction methods (neonates), with death confirmed by immediate cessation of circulation. The chest cavity was opened and the heart and immediate tissue dissected out as quickly as possible and removed into ice-cold PBS. After rinsing away blood and trimming as required, hearts were either fixed in PFA, snap frozen in liquid nitrogen or enzymatically digested for subsequent experimentation or storage. Rats were given a weight-dependent dose of sodium pentobarbital before cervical dislocation.

All animal procedures were done under licence from the Home Office by BMS trained staff, with breeding, injections and the neonatal mouse LAD myocardial infarction surgery performed by

myself (personal licence I7597E689) and the rat cryoinfarct surgery performed by Carolyn Carr under UK Home Office project licences PPL30/2987 (Paul Riley), PPL PF8462746 (Nicola Smart), PPL30-3322 (Carolyn Carr), and PP1224162 (Sarah de Val), compliant with the UK Animals Scientific Procedures Act 1986 Amendments Regulations 2012 incorporating the EU directive 2010/63/EU and approved by the local Biological Services Ethical Review Process.

2.1.2 Mouse strains and specific breeding strategies

CD1 and C57Bl6/J

Wild type CD1 and C57Bl/6J mice (male/female) were initially obtained from commercial breeders (Harlan or Charles River Laboratories, UK) and maintained as above. If pups or a local colony were required, breeding was done with one male paired with one or two females, at a minimum age of 8 – 12 and maximum of 32 weeks.

Fucci2-R26Rp

This line was a generous gift to the Riley Group from Professor Shankar Srinivas. Fucci positive males (heterozygous for R26Rp-Fucci-2 on a C57BL/6 background) were bred with wild type C57BL/6 females to maintain the Fucci line. The males are heterozygous for the Fucci construct as being homozygous is lethal during development or very shortly after birth, only these males were kept for future studs. For the experimental litters, they were mated with wild type CD1 females as these dams are less prone to cannibalisation and neglect after surgical interventions with their litters (see neonate MI surgery below), and Fucci heterozygous positive males and females were used for the studies.

2.1.3 Rats

Male Sprague Dawley rats aged 6-8 weeks were obtained from commercial breeders for the cryo-infarct surgery model. They were also housed communally, maximum 4 rats per cage, in dedicated animal care facilities for the duration of the studies.

2.2 Myocardial infarction surgery

2.2.1 Neonatal mice

Surgery preparation and anaesthesia

All surgeries were performed under aseptic conditions. Pups aged P1 or P7 from CD1 mothers were used as these dams are more tolerant of the interference with their pups, being less prone to maternal neglect or cannibalisation after the surgery or removal/subsequent return of their litters. The surgery area was thoroughly cleaned with 70% ethanol and disinfectant. A frozen ice block was taped down and covered with a sterile surgical drape, positioned asymmetrically with an area on one side for tools and equipment for immediate access as it was essential for these pup surgeries to be completed as quickly as possible once the pup was anaesthetised – the aim is to take no longer than 10 minutes per pup.

The entire litter was removed from the breeding cage and placed in the warming chamber (set to 28-32°C), lined with fresh tissue paper and containing a few small pots with soiled cage litter. A few pellets of mouse droppings were removed and placed into warm water to soften, to be used to bathe the pups at the end of the procedure.

A pup was removed from the warming chamber and placed into the anaesthesia induction chamber (pre-filled with 4% isoflurane carried by 2L/min 100% medical oxygen) until akinesia, usually from 1 to 2 minutes depending on pup age. The pup was wrapped in moist tissue and buried in crushed ice for another 2 to 4 minutes to fully anaesthetise by hypothermia and induce cardiorespiratory arrest. As soon as they showed no signs of response to touch or toe pinch, they were taped down on their back onto the ice pack. The left side of the pup was taped down first, securing the limbs and gently pulling the skin and underlying muscles downwards on that side. Then the right side was taped down, with a small push upwards of the body to present the chest clearly (this also separated the ribs to allow easier access to the heart). Additional tape was applied across the head and lower half of the body, leaving only the surgery site exposed. This was cleaned with a sterile cotton bud dipped in Hibiscrub™ (4% chlorhexidine gluconate diluted 1:5 with sterile saline as the undiluted solution is too harsh for neonate skin). See Figure 9 for surgery preparation.

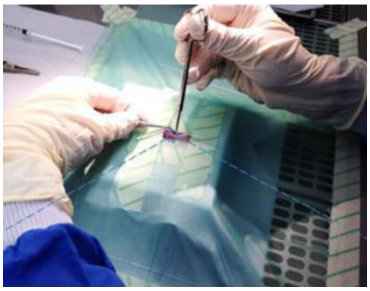

Figure 9: Neonatal mouse prepped for surgery under sterile conditions.

LAD ligation procedure

A small incision was made horizontally in the skin across the lower left chest. The chest cavity was carefully punctured with sharp pointed forceps and opened between two lower ribs on the left side. Blunt curved forceps were gently inserted to keep the chest open, being careful to avoid touching the lungs or heart underneath. Because of the hypothermia-induced arrest, the heartbeat should be very slow or non-existent which is essential for this procedure. The heart was extruded from the thoracic cavity by applying gentle pressure upwards from below the diaphragm and leftwards on the right side of the chest – the entire heart can be made to "pop out" but usually only the lower half can be squeezed through the ribs without too much trauma (Figure 10).

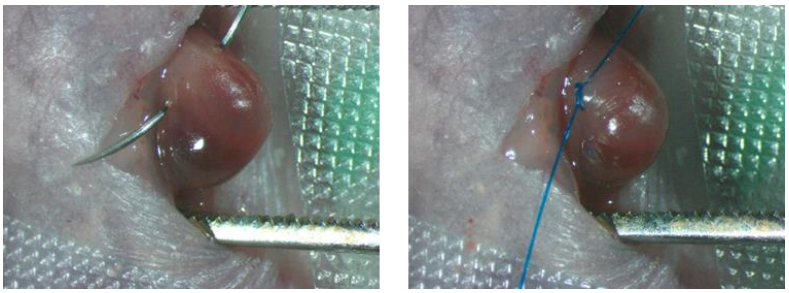

Figure 10: The neonatal mouse heart is extruded from the chest cavity and the LAD artery is permanently ligated.

The left anterior descending artery was ligated by placing a Prolene 7-0 suture through the left ventricle wall under the LAD and securing it tightly enough to block blood flow below the suture but taking care not to slice right through the tissue. For the sham surgeries, this suture was only passed through the heart without ligating. The heart was then carefully repositioned within the chest, the ribs sewn back together and the skin sutured closed. Topical local anaesthetic Marcain™ (bupivacaine hydrochloride) was applied to the wound area with a cotton bud.

Figure 11: Suturing ribs and sewing skin to close wound.

Surgery recovery

After skin closure, the pup was removed from the ice-block and warmed rapidly in front of a heat lamp, moving it continuously to keep an even temperature with care being taken not to overheat any particular area. To aid recovery and minimise any post operative pain, a small dose of isoflurane with extra oxygen was administered (0.5% isoflurane in 0.5L/min oxygen flow) via a tube held close over the face. Additional physical stimulation was provided by holding an active littermate in close proximity, which helped greatly in getting the pup to respond and awaken after anaesthesia. Recovery could be seen when the pup gave a first big gasp, and then resumed regular steady breathing. It was then moved away from the heat source gradually as breathing and movement increased. When the pup was fully recovered as observed by noting regular breathing, strong wriggling movements and a healthy pink skin colour, it was placed back in the recovery chamber with the rest of the litter until all the procedures were completed.

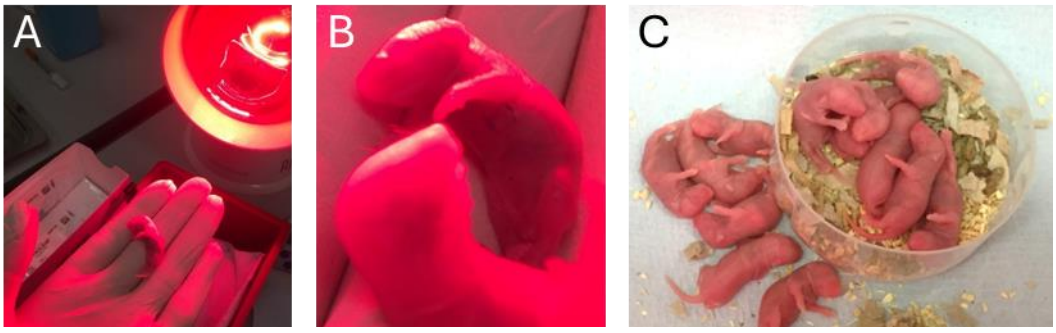

Figure 12: Recovery of neonate with an infrared heat lamp: (A) Rapid and even heat is applied to the chilled pup after surgical procedure (B) An active healthy littermate is provided to stimulate recovery (C) The pups that have recovered well (in the cup) are pink and wriggling resembling the unoperated ones outside the cup.

Healthy, properly recovered pups regained their original pink colour and were warm to the touch. A pup that subsequently becomes unwell due to a complication such as incomplete rib closure or heart failure may start turning grey and stop moving, and any that show such symptoms needed to be culled immediately. When the entire litter had undergone surgery, they were all coated with

the softened and mashed faeces mixed with water to disguise any lingering surgical and handling odours, and returned *en masse* to the mother. This final step is vital to reduce cannibalism by the dam. A quick and discreet check of the litter may be done the next day, but it is best not to disturb them for at least 48 hours to keep maternal stress to a minimum.

2.2.2 Adult rat cryo-infarction

Male 6-week-old Sprague–Dawley rats were divided into two groups (cryoinjury or sham surgery). Rats were anesthetized via isoflurane in oxygen (4% for induction, 2% for maintenance) and intubated for ventilation. Rats were maintained on a heated pad with monitoring of temperature, pulse oxygenation and electrocardiogram. Following a left thoracotomy and removal of the pericardium, the heart was stabilized by a loose stitch through the apex and myocardial infarction was induced by cryo-injury, via the placement of a 9 mm aluminium probe cooled to 77 K onto the anterio-apical surface of the left ventricle for 15s. The chest was closed in layers and the animal allowed to recover. In sham-operated rats, thoracotomy and cardiac exteriorisation were performed before the chest was closed. Animals were provided with pre- and post-operative analgesia, in the form of buprenorphine, meloxicam, and with lidocaine to prevent arrhythmia. Rat cryo-infarct procedures were performed by Professor Carolyn Carr with my assistance with preparation and recovery.

2.3 Tissue Collection and preparation

2.3.1 CD1 samples

Hearts were removed as described above, cleaned, trimmed (surface fat and excess blood vessels removed but both atria retained) and placed in labelled 7ml Bijou tubes containing ice-cold fixative 4% PFA and left at 4°C overnight. They were thoroughly rinsed in several washes of PBS and transferred to a solution of 30% sucrose in PBS at 4°C overnight. A final step used a 1:1 mix of 30% sucrose and Tissue Tek optimal cutting temperature compound (OCT) for a minimum of 2 hours at RT. After these dehydration steps, they were transferred to 100% OCT in plastic embedding moulds (15w x15h x 5d mm) (see Figure 13: 7ml Bijou tubes were used for sample collection and fixation before embedding in OCT in histology moulds. and carefully oriented in

preparation for cryosectioning. The hearts could then be frozen and stored at -80°C until needed for cryosectioning.


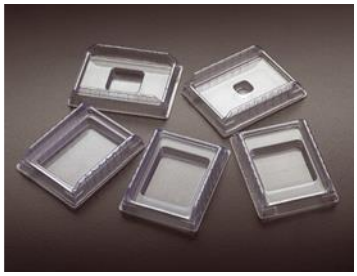

Figure 13: 7ml Bijou tubes were used for sample collection and fixation before embedding in OCT in histology moulds.

2.3.2 Fucci neonate samples

For the slice assay, 4 days after MI or sham surgery, neonatal hearts were removed and fixed in 2% PFA for 4 hours and then put through the sucrose and OCT protocols as for the CD1 adult hearts. They were embedded in 7x7x5 mm moulds and frozen at -80°C. From each pup, a tail snip was also taken and placed into a matched labelled Eppendorf tube for genotyping (this was done only for the first few litters in this project, to confirm the fluorescent torch method of instantaneous genotyping). For the isolated cell culture studies, neonate P1 and P7 hearts were removed and immediately digested in an enzyme mixture as described in Chapter 5.

2.3.3 pHLIP samples (neonate to adult mice and adult rats)

For the mice and rats injected with pHLIP, hearts and kidneys were removed and placed into ice cold PBS and rinsed to remove as much blood as possible. Heart samples will keep beating for a while after removal and this helps to release most of the blood within the ventricles, they can also be gently squeezed to eject all the remaining blood, switching between two or three fresh pots of clean PBS until it is fully clear (it's important to clear the excess blood as it interferes with pHLIP imaging). Organs were blotted dry and placed directly into appropriately sized moulds of chilled OCT, positioned for sectioning and then placed into crushed dry ice to freeze. These frozen blocks were then stored at -80°C. Note that pHLIP samples for direct imaging were not fixed.

2.3.4 Cryosectioning

Cryosections were cut using a Bright OTF Cryostat. Hearts in OCT blocks were usually positioned to present a four-chambered (long axis) view and sections were cut away from the block until all chambers were visible (the central section of the heart). When this area was reached, the sections were picked up onto glass slides (VWR Premium Superfrost, catalogue #48311-703), keeping them shielded from light as much as possible to preserve fluorescence. pHLIP samples for direct imaging were cut at 25µm (maximum thickness on this cryostat), while CD1, Fucci and pHLIP samples for immunofluorescence were cut at 8-10µm. Slides were stored at -20°C for direct imaging or staining within a few days or at -80°C for longer term storage.

SLIDE 1	SLIDE 2	SLIDE 3	SLIDE 4	SLIDE 5	SLIDE 6	SLIDE 7	SLIDE 8	SLIDE 9	SLIDE 10
1	2	3	4	5	6	7	8	9	10
11	12	13	14	15	16	17	18	19	20
21	22	23	24	25	26	27	28	29	30
31	32	33	34	35	36	37	38	39	40
41	42	43	44	45	46	47	48	49	50

Figure 14: Sections for staining were collected onto slides in such a pattern as neighbouring sections were on different slides to permit use at different times or with different combinations of antibodies. We used blocks of 10 slides

2.4 Immunofluorescent staining

2.4.1 Slide preparation

For staining, slides were removed from the freezer and left to dry for 10 minutes at RT. They were rinsed in PBS to remove the OCT embedding material and then permeabilised in 0.5% Triton X-100 in PBS (PBST) for 10 minutes at RT. They were rinsed again in PBS, and using a Q-Tip, carefully blotted dry between and around individual sections to allow encircling with an ImmEdge hydrophobic barrier pen (Vector Laboratories) if different antibody stainings were to be performed on the same slide (this also saves greatly on the volume of antibody needed).

2.4.2 Background suppression

Cardiac sections are notorious for having background autofluorescence and there are techniques to suppress or at least reduce this and minimise interference from desired image signal. We used TrueBlack to suppress green autofluorescence. 20x TrueBlack was diluted to 1x in 70% ethanol and vortexed to mix well. At least 100 µl was needed per section, and applied for 2-5 minutes. The sections were rinsed well (at least 3 times) with PBST to remove all traces of TrueBlack.

2.4.3 Blocking and primary antibodies

Sections were blocked with 10% goat or donkey serum and 1% bovine serum albumin (BSA) in PBST for at least 1 hour at RT, using the serum species that the secondary antibody was raised in to minimise background staining. The blocked sections were transferred to a humidified chamber and primary antibody diluted in blocking solution (1:50 – 1:1000, see table below) was applied and left overnight at 4°C.

2.4.4 Secondary antibodies

The following day, the slides were rinsed 3 times with PBST to remove primary antibodies. Alexa Fluor secondary antibodies diluted in the block solution (1:200) were added for 1 hour at RT, followed by rinsing for 5 minutes in PBST, followed by two more 5 minute rinses in PBS.

2.4.5 Mounting slides

If nuclear staining was desired, DAPI (4',6-Diamidino-2-phenylindole, dihydrochloride) diluted in block to 0.1µg/ml was applied for 3-5 minutes at RT, and rinsed off 3 times as per the 2° antibody. The slides were blotted to remove as much liquid as possible and mounting medium of 50:50 glycerol:PBS (or a commercial alternative such as Vectorshield) was applied. A coverslip was placed over the entire slide (lowered from one direction to avoid trapping bubbles around the sections), pressed down gently with tissue to remove excess and wiped clean before sealing with nail polish. The slides were kept at 4°C if imaging within a day or two, or -20°C for long term storage.

Primary Antibodies

Antibody	Raised in	Supplier	Catalogue #	Dilution
α-Actinin	mouse	Abcam	ab9465	1:50
mCherry	rat	Invitrogen	M11217	1:100
mVenus	chicken	Abcam	ab13970	1:100
Geminin	Mouse	Santa Cruz	SC-74456	1:50
Cdt1	Rabbit	Cell Signalling Tech	8064S	1:50
PDGFRa	Rabbit	Abcam	ab16868	1:200
Vimentin	Rabbit	Cell Signalling Tech	D21H3 5741S	1:100
a-SMA	Mouse	Sigma	F3777	1:200
Wt1	Rabbit	abcam	ab89901	1:100
Pecam	rat	BD	553370	1:50
phalloidin	Mouse	Invitrogen	A12379	1:500
Ki-67	rat	Invitrogen	14-5698-82	1:100
TNNI3	rabbit	Proteintech	21652-1-AP	1:100
TNNI1	rabbit	Proteintech	16102-1-AP	1:100
TNNT2	mouse	Invitrogen	MA5-12960	1:40
Crip2	rabbit	Novus	NBP 2-59094	1:100

Secondary Antibodies

Antibody	Supplier	Dilution
Alexa-Fluor goat α-chicken 488	Invitrogen	1:200
Alexa-Fluor goat α-mouse 488	Invitrogen	1:200
Alexa-Fluor donkey α-rat 546	Invitrogen	1:200
Alexa-Fluor chicken α-rat 546	Invitrogen	1:200
Alexa-Fluor goat α-mouse 555	Invitrogen	1:200
Alexa-Fluor donkey α-rabbit 555	Invitrogen	1:200
Alexa-Fluor goat α-mouse 647	Invitrogen	1:200
Alexa-Fluor goat α-rabbit 647	Invitrogen	1:200
Alexa-Fluor donkey α-rabbit 647	Invitrogen	1:200

2.5 Imaging

2.5.1 Confocal imaging of tissue slices and cultured cells

Fucci imaging was done on a Zeiss LSM 700 confocal microscope at 512 x 512 pixel resolution, 8 bits/pixel with an EC Plan-Neofluar 40x/1.30 Oil M27 objective lens. Confocal pinhole size was set to 74 μm. Three channels (red G1, green S/G2/M and blue Hoechst) were imaged sequentially with the details as below:

IMAGING	DISPLAY COLOUR	LASER WAVELENGTH	FILTER
Channel 1	Blue	405 nm	SP 490
Channel 2	Green	488 nm	BP 490 - 555
Channel 3	Red	555 nm	LP 560

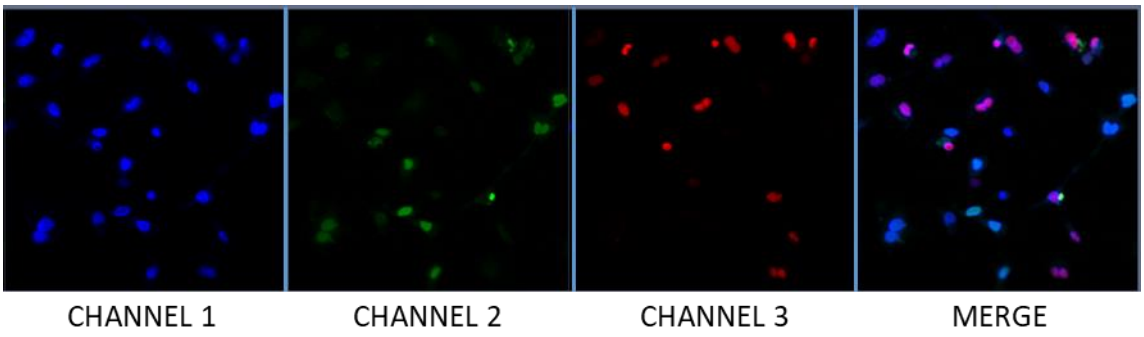

Figure 15: Confocal Fucci imaging in 3 channels (1: DAPI; 2: mVenus; 3: mCherry), with merged image. P1 section, magnification x400, zoom x2.

2.5.2 Whole heart slice tiled images

Each tissue section was imaged on a Leica DM6000 upright microscope with a Leica CTR 600 control system that had a motorised stage (OptoGrid Structured Illumination Microscopy Motorised Firmware 1.4, Excelitas Technologies), illuminated by a CoolLED pE-300 Lite system and captured by a Hamamatsu C10600-10B ORCA-R2 camera. Multiple images in an X-Y plane across the section were stitched together into a composite tiled image of the whole slice using Volocity 6.4.0 (Quorum Technologies) software. This allows both an overview of the whole slice and retains the ability to zoom in for details, down to cellular resolution (Figure 16).

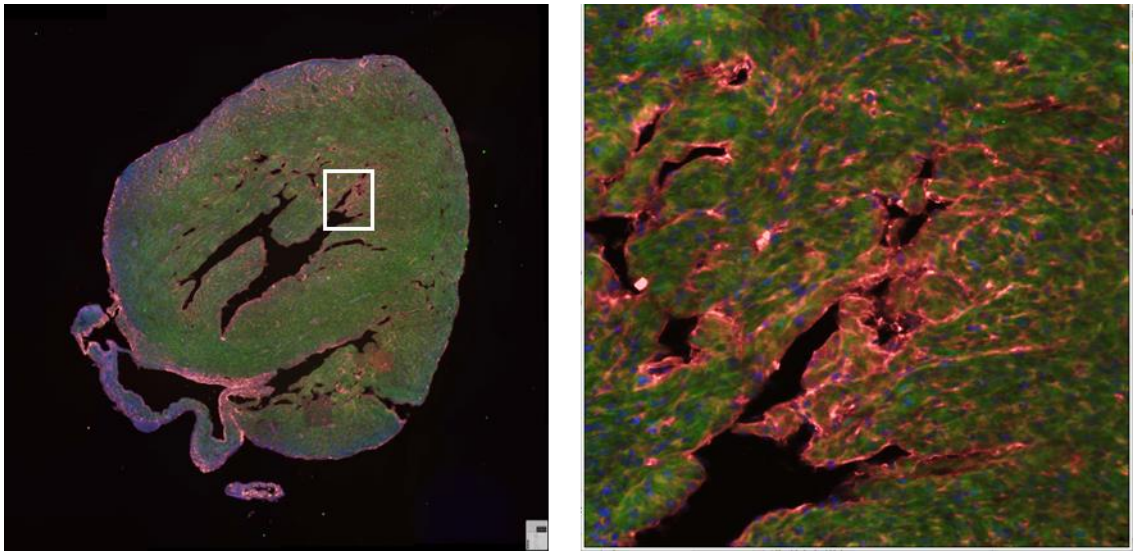

Figure 16: Tiled image (left) from a P1 mouse control heart slice. An image is taken on 4 (blue, green, red, far red) channels before the stage is moved to the location of the next image. This happens in a grid pattern across the entire area of interest with a set amount of overlap in both horizontal and vertical directions (in this case we used 15% overlap for all our tiled images). These individual images (here there were 1248 images) were then stitched together to create this tile. The right image shows a zoomed in view of the white square, showing the level of detail – cellular resolution is possible.

More details on this imaging and data analysis are in the research chapters that use the Fucci mouse model and the investigation of acidic niches in the mouse/rat heart using pHLIP labelling.

2.6 Molecular biology

2.6.1 Genotyping mice strains

Genotyping of adult mice was performed on ear clip biopsies removed for mouse identification. This was not feasible for pups and so a tail tip was taken at time of sacrifice. These samples are placed into prelabelled 1.7mL Eppendorf tubes which may be stored at -20°C until needed. Fucci neonates up to P3 could be genotyped by a light torch and goggles method which prevented unnecessary surgeries or tissue collection from Fucci negative pups.

DNA extraction

The tissue sample was incubated overnight at 55°C in 500µL of lysis buffer with Proteinase K (1mL lysis buffer : 1 µL 10mg/ml ProtK). The following day, 500µL isopropanol was added to each tissue sample and mixed for 30 mins at RT. The sample was centrifuged for 15 mins at 4°C at maximum speed (13000 rpm), and the supernatant decanted. The sample was washed with 1mL

70% ethanol, vortexed briefly, then centrifuged for 5 mins at 4°C at maximum speed, and the supernatant discarded. The sample was centrifuged again as before and any remaining supernatant removed with a P200 pipette. The pellet was resuspended in 100uL TE buffer and could be stored at 4°C until the next step.

Solution	Ingredients
Lysis buffer	100mM Tris pH 8.5, 5mM EDTA, 0.2% SDS, 200mM NaCl
Tris-EDTA (TE) buffer	10mM Tris pH 8.0, 1mM EDTA
Tris-borate-EDTA (TBE) buffer	40mM Tris pH 8.0, 20mM Boric acid, 1mM EDTA

DNA primers

Samples were stored at 4°C, placed in a 37°C heated bath for 30 mins to dissolve the pellet of extracted DNA. To make working stocks from the concentrated primer stored at -80°C, 2µL of the concentrate was mixed with 98µL dH_2O (1:50 dilution). This may be stored at -20°C for regular use. The working stock was mixed with enough PCR mix for all the samples plus the necessary controls using 22µL dH_2O, 1µL of forward primer working stock, 1µL of reverse primer working stock (total = 24 µL) per sample, with extra to allow for pipetting loss. Samples were aliquoted into labelled PCR tubes (illustra PuRe Taq Ready-To-Go PCR Beads, GE Healthcare).

FUCCI PRIMERS:	
ATGGTGAGCAAGGGCGAGGAG	mVenus-S
CTTGTACAGCTCGTCCATGCCG	mVenus-AS
GCTTCAAGGTGCACATGGAG	mCherry-S
CATGAACTGAGGGGACAGGA	mCherry-AS

Note that for Fucci2 genotyping, both sets of primers need to be run concurrently.

PCR DNA amplification

To each PCR tube with primer mix, 2µL of sample DNA solution was added (total volume = 26 µL), the tubes were covered and placed into the thermocycler (96-well Veriti thermal cycler, Applied Biosystems) with selection of the appropriate program for the gene of interest (the Fucci2 program is listed below). The amplified DNA can be stored at 4°C until needed .

FUCCI2			
Stage	**Temp C**	**Time**	**Cycles**
1	96	02:00	1
2	96	00:30	35
	65	00:30	
	72	00:30	
3	4	HOLD	1

Preparing and running the genotyping gel

Agarose (1.5g, Sigma) was added to 100mL TBE buffer (1.5% weight by volume gel), mixed gently and microwaved on high power for 2 minutes to fully dissolve. GelRed (10µL, VWR) was added to allow UV visualisation of DNA, and the liquid poured into a gel frame and left to set (at least 30mins). The gel was placed into an electrophoresis tank filled with TBE buffer. After adding Orange DNA Gel loading buffer (5µL, Life Technologies) to each amplified DNA sample, 15µL of this mixture was added to each well. The gel was run at 140V for 37 minutes and PCR products were visualised on the gel using a UV light box.

2.6.2 RNA extraction steps for qRT-PCR

RNA extraction from whole cell lysate

Cell samples were stored at -80°C for future RNA extraction in a known volume of Trizol. Using the RNeasy Mini Kit (Qiagen) to extract RNA, an equal volume of 70% ethanol was added to each sample, mixed gently, loaded into RNeasy mini spin columns with 2ml collection tubes (700 µL max volume each time – repeat if necessary) and spun for 15 seconds at 10,000 g. After discarding the flowthrough, the membrane was washed with 700µL Buffer RW1, centrifuged as before, and the flowthrough discarded. Then 500 µL Buffer RPE was added to the column, which was centrifuged as before, and the flowthrough discarded. This step was repeated with a 2 minute centrifuge, and then the column was moved to a fresh 2mL collection tube and centrifuged again for 1 minute to dry the membrane. Finally, the spin column was moved to a 1.5mL collection tube and 30 µL RNase-free water added directly onto the membrane. The tube was centrifuged for 1 minute to elute the RNA. The RNA yield and purity was assessed using the NanoDrop spectrophotometer following manufacturer's instructions. The ratio of the absorbances at 260/280 should be approximately 2.0 for acceptable RNA purity.

Complementary DNA (cDNA) synthesis

We used the High Capacity cDNA Reverse Transcription Kit to convert our RNA into DNA for amplification. Using the RNA quantification values from above, the volume of sample needed to get 1ng of RNA in 10 µL volume was calculated for each sample, to give a consistent RNA amount in each PCR tube. A master mix was made:

Master mix for cDNA	**amount µL/sample**
10X RT Buffer	2.0
25X dNTP Mix	0.8
10X Random Primers	2.0
Multiscribe Reverse Transcriptase	1.0
Nuclease-free water	4.2
TOTAL	10.0

10 µL master mix was added to 10 µL diluted RNA to give a final volume of 20 µL which was analysed in the thermocycler (SensoQuest Basic Thermal Labcycler, SenoQuestGeneFlow) with this program: 10 min at 25°C, 120 min at 37°C, 5 min at 85°C. This cDNA can be stored at -20°C until needed.

Primer design

We used the NCBI Primer-Blast website (www.ncbi.nlm.nih.gov/tools/primer-blast/) to design the primers for our qRT-PCR experiments. The parameters we needed to optimise for SYBR Green reactions included: GC content of 50-60%; primers ending in G or C; melting temperature of 65-75°C; primer length of approximately 20 nucleotides; flanking the exon-exon border of the gene to avoid genomic DNA amplification. Some primers were from other researchers in our group or published papers, but all were independently validated before use.

PRIMERS USED WITH hiPSC-CMs			
Housekeeping	UBC	F	CCTGGTGCTCCGTCTTAGAG
		R	TTTCCCAGCAAAGATCAACC
Myosin Heavy Chain 6	MYH6	F	TCCTGCGGCCCAGATTCTTC
		R	TCTTCCTTGTCATCGGGCAC
Myosin Heavy Chain 7	MYH7	F	AAGGTCAAGGCCTACAAGCG
		R	CCAGGGCTGAGCAGATCAA
Troponin T2	TNNT2	F	GACAGAGCGGAAAAGTGGGA
		R	CTCCTTGGCCTTCTCCCTC

Cell cycle Cyclin D2	CCND2	F	TCATTGAGCACATCTTGCGC
		R	TCACAGGTCGATATCCCGCA
Cell cycle Cyclin D1	CCND1	F	ATCAAGTGTGACCCGGACTG
		R	CTTGGGGTCCATGTTCTGCT
Cell cycle Cyclin E1	CCNE1	F	AGAGGAAGGCAAACGTGACC
		R	TTATTGTCCCAAGGCTGGCT
Cell cycle Cyclin A2	CCNA2	F	GGTACTGAAGTCCGGGAACC
		R	GAAGATCCTTAAGGGGTGCAA
Cell cycle Cyclin B1	CCNB1	F	CATGGTGCACTTTCCTCCTT
		R	AGGTAATGTTGTAGAGTTGGTGTCC
Cell cycle Aurora kinase A	AURKA	F	TCTTGGAAGACTTGGGTCCTT
		R	TCAAATATCCCCGCACTCTG
Cell cycle Cyclin CDC7	CDC7	F	GATCTCTTGGAGACGGCGAC
		R	AGATGCAAAATGCCAGGGTT

Quantitative real-time PCR

We used an Applied Biosystems StepOnePlus Real-Time PCR system (Applied Biosystems, ThermoFisher) for performing the qPCR reaction, using SYBR Green for detection. Reactions were run in triplicate wherever possible but sometimes duplicate on a MicroAmp Fast Optical 96-well plate (ThermoFisher). A master mix was made using Power SYBR Green PCR Master Mix #4367659:

Master mix for RT-qPCR	**amount µL/sample**
Power SYBR Green Master mix	7.0
Forward primer	0.7
Reverse primer	0.7

The plate layout was designed to include gene(s) of interest and housekeeping controls for each sample. 7 µL of Master mix and 3 µL of cDNA sample were added to each well (total volume = 10 µL) and the plate sealed with cover film (MicroAmp Optical Adhesive Film, Applied Biosystems), pressing down firmly to avoid evaporation during heating cycles. The plate was spun briefly and placed in the qPCR machine. We used a two-step method with 40 cycles.

Stage	**Temp C**	**Time (s)**
Holding	95	600
Cycling (denaturation)	95/60	15
Melt curve (annealing/extension)	60	30

Data analysis of qPCR: $\Delta\Delta C_T$ calculation method

Data were analysed using the standard $\Delta\Delta C_T$ method (Livak and Schmittgen 2001) to calculate relative amounts of mRNA to a housekeeping gene that should not be affected by the different experimental conditions. The data was plotted to show fold change $2^{-\Delta\Delta CT}$. C_T is the cycle threshold value where the fluorescent signal detected using SYBR Green reagent first exceeds the background signal, and this varies between experimental samples. The method is outlined below:

1. Calculate the average Ct value per target gene and housekeeping gene
2. Calculate ΔCt = Ct [target gene] - Ct [housekeeping gene]
3. Calculate ΔΔCT: ΔΔCT = ΔCT [experimental group] – ΔCT [control group]
4. Calculate the relative fold change: $2^{-\Delta\Delta CT}$
5. Use relative fold change for statistical analyses

2.7 Cell culture

2.7.1 Primary murine cardiomyocytes

Standard cell culture techniques were followed for all aspects of these cultures after enzymatic digestion to isolate CM from dissected heart tissue.

2.7.2 Human induced pluripotent stem cells

The hiPSC-CMs were differentiated from the foetal lung fibroblast cell line IMR90. We induced differentiation using timed Wnt activation based on the protocol of Lian et.al 2013, followed by metabolic selection to remove contaminating fibroblasts and then procedures to induce selective maturation before treatments to induce hypoxia and/or acidity (detailed in Chapter 5). Standard stem cell culture techniques used to prepare for these treatments are listed below.

Thawing, plating and growing IMR90 hiPSC aliquots for culture

Frozen IMR90 cell aliquots (1mL) were removed from liquid nitrogen storage, thawed and added to 9mL PBS to neutralise the 10% DMSO in FBS cryoprotectant, and centrifuged at 1500rpm for 4 mins at RT. The supernatant was discarded and the cell pellet resuspended in 1mL mTeSR media. 2µL Rock Inhibitor (Y-27632) and another 1mL mTeSR media was added and mixed gently. This

2mL of cell mix was then plated onto a single well of a 6-well cell culture plate (pre-coated with Matrigel) and left to settle for 10mins before moving to the incubator for culture.

Culturing IMR90 hiPSCs

The cells were cultured in mTeSR medium in a standard tissue culture incubator at 37°C, 5% CO_2 with 20% oxygen and humidity provided by free water in the bottom tray. They were checked daily and the medium was replaced with fresh mTeSR until the cells were confluent (85-95% well area covered in cells).

Splitting IMR90 hiPSC cells when confluent

This single confluent well was split into six wells: the old media was removed and cells rinsed with DPBS. 1mL ReLeSR was added and incubated for 1 min at RT. Then 800µL was removed, the plate moved to the incubator for 6 mins. The remaining ReLeSR was then carefully removed so as not to disturb the cells, 1mL of mTeSR was added and the cells dislodged by gently pipetting up and down to lift the cells. This was removed to a 50mL falcon tube, which was topped up to 12mL mTeSR. After mixing, this was aliquoted into 6 wells for further culturing. When this plate was confluent, this process was repeated by splitting the cells into 15 wells (2 full plates of 6 wells each which were used for experiments and 3 wells of another plate for continued culture of IMR90 hiPSCs.

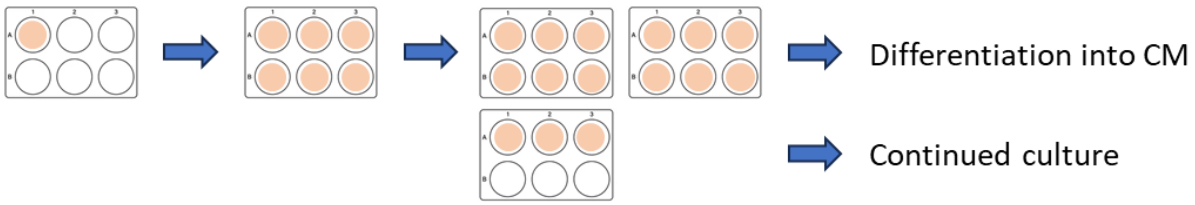

Figure 17: Splitting hIPSC for experiments and further culture. A frozen vial of low-passage stem cells is thawed and plated into one well of a 6-well culture plate. When this is confluent, it is split into 6 wells which in turn is split into 15 wells: 2 full plates are used for experiments while the last half plate is cultured on or frozen and stored for future use.

Freezing IMR90 hiPSC aliquots for storage

The media was removed from the well, which was washed with 2ml of PBS without calcium or magnesium. 1ml TrypLE was added to each well, incubated for 10mins at 37°C, before adding 4ml DPBS. The cells were harvested by gentle trituration, and an aliquot was counted for viable cells using Trypan Blue. The cells were centrifuged at 300g (1500rpm) for 4-5mins, and the

supernatant was discarded. The pellet was resuspended in CryoStor to give 5 million cells in each 1ml freezer vial. The vials were placed into an isopropanol freezing chamber and frozen at -80°C overnight before being transferred to long term liquid nitrogen storage.

hiPSC-CM experimental harvest

After these preparations, the media was removed and the wells rinsed with ice-cold PBS. For the qPCR experiments, Trizol was added (volume noted), and the cells scraped down into labelled eppendorfs and flash frozen in liquid nitrogen for RNA extraction later. For the immunostaining experiments, the cells on the coverslips were fixed with ice-cold 4% PFA, rinsed with PBS and stored at 4°C under fresh PBS in sealed plates until staining.

2.8 Statistical methodology

Most statistical analyses were performed in GraphPad Prism software, which was also used to plot the results. For two experimental groups, tests used to compare values included two-tailed unpaired student T test or Mann Whitney depending if the data distribution was considered normal or not. For more experimental groups, we used one- or two-way ANOVA, some with multiple comparisons. A p-value of less than 0.05 was considered statistically significant. More complex analyses were performed by Professors Carolyn Carr and Jack Miller.

CHAPTER 3
(Research Chapter 1)
Neonatal MRI

INVESTIGATING THE INTRINSIC CAPACITY FOR MYOCARDIAL REGENERATION IN THE NEONATAL MOUSE

ABSTRACT

The adult mammalian heart lacks the ability to regenerate damaged tissues post-ischaemic injury, leading to non-contractile fibrotic scarring and impaired function. However, it has been proposed that neonatal mice possess a limited "regenerative window" during the first few days of life. This study aimed to investigate myocardial regeneration in neonatal mice using longitudinal, non-invasive functional cardiac MRI. Two cohorts of neonatal mice, at postnatal day 1 and 7 (P1 and P7), underwent myocardial infarction (MI) or sham surgery and were scanned at baseline (before surgery), and on days 4, 7, 14, and 21 post-surgery. Modifications to existing rodent-scanning MRI protocols were necessary to accommodate the small size of neonatal mice hearts, including custom-designed cradles, heating pads and physiological monitoring equipment and accelerated imaging techniques.

Results showed that the P1 cohort exhibited minimal injury at Day 21 with restored function, indicating potential myocardial regeneration, while the P7 cohort displayed significant scarring and ventricular remodelling, similar to adult hearts post-MI. Longitudinal imaging allowed for repeated scans of the same specimen, providing insights into the progression of heart injury or recovery. Key findings included a significant increase in end-diastolic volume (EDV) and end-systolic volume (ESV) and significant decrease in ejection fraction (EF) with the P7 MI injury group compared to the age-matched shams. EDV, ESV and EF in the P1 MI cohort matched the sham cohort for the study duration. Heart rate exhibited a non-linear pattern, with a notable dip around P14-15 for both cohorts with or without injury, potentially linked to developmental changes.

This study successfully demonstrated the feasibility of using MRI to monitor myocardial regeneration in neonatal mice, highlighting the regenerative capacity of the P1 heart and the reparative response of the P7 heart. The findings provide a foundation for studying these dynamic processes longitudinally which would facilitate future research into enhancing regenerative therapies for heart injury. Further development of MRI techniques and analysis software is needed to improve accessibility and efficiency for routine use in research and clinical settings.

3.1 INTRODUCTION AND BACKGROUND

The adult mammalian heart is unable to generate tissues that are damaged after ischaemic injury, and even if a small number of new muscle cells may be formed by division of existing cardiomyocytes, it is not sufficient to restore any degree of lost function (Anversa, Leri et al. 2006, Bergmann, Bhardwaj et al. 2009, De Falco, Cobellis et al. 2009, Bergmann, Zdunek et al. 2012, Bergmann 2019). Instead, a non-contractile fibrotic scar is laid down to prevent immediate ventricle rupture. However, it has been postulated that the neonatal mouse heart can regenerate following myocardial infarction (MI) injury, but only if this injury happens during the first few days of life – an age limited "regenerative window" (Porrello, Mahmoud et al. 2011). This has generated significant controversy and debate, especially about the timing and extent of this regeneration – a comprehensive analysis of heart regeneration studies may be found in these references: (Anversa, Leri et al. 2006, Lam and Sadek 2018, Huang, Huang et al. 2023). Prior to our study, the only "proof" of neonatal regeneration to date had been several histological studies taking specimens at fixed times after injury, a method which necessarily precluded longitudinal assessment of an individual and also did not provide any functional insights. As expected, this led to differences in results from different groups, as there was no verifiable way to establish the extent of initial injury (in fact whether any actual injury had or had not occurred), thus whether or not any regeneration or repair had taken place. As far as we were aware, there had not been any attempts to use any biomarker assays such as troponin T to check for cardiac injury in neonatal mice although it has been suggested that this may be a clinically viable procedure in young paediatric patients and is regularly used to quantify extent of heart injury or disease in adult rodents and humans (Clark, Newland et al. 2004, Clark 2006).

Magnetic resonance imaging (MRI) has long been established as the method of choice for non-invasive functional imaging of the diseased and healthy heart in humans and adult rodents. MRI is a radiation-free technique (unlike CT) to visualise tissues deep within a patient, exploiting the differences in magnetic resonance properties between tissue types, including whether they may be injured or not, to obtain a clear and detailed image which is invaluable for clinical diagnosis of heart disease. It can clearly distinguish muscle, fat, water and blood without the need for additional contrast agents, although these may be used in certain circumstances to distinguish between viable and damaged tissue. It has excellent spatial resolution and can scan in any desired plane, and can also provide "movies" (cine MRI) of the beating heart with very high temporal and spatial resolution (Karamitsos and Neubauer 2011, Dall'Armellina, Piechnik et al. 2012). With this single

method of imaging, we can gain insight into ventricular and valvular function in both normal and diseased states, cardiomyopathies due to ischaemia and other causes as well as congenital heart disease (Shah, Chryssos et al. 2009, Karamitsos and Neubauer 2011, Saleh, Sharp et al. 2012).

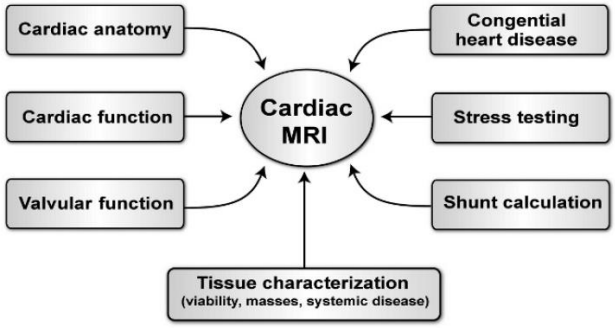

Figure 18: Uses of Magnetic Resonance Imaging in the study of the heart. From *"*Magnetic resonance imaging: a wealth of cardiovascular information*"* 2009 (Shah, Chryssos et al. 2009).

In this chapter we aimed to use MRI to follow changes in the neonatal heart post MI. Although protocols for imaging the adult mouse heart were well established (Wiesmann, Ruff et al. 2000, Lau, Miller et al. 2017, Lau, Miller et al. 2017, Lewis, Miller et al. 2018), in order to obtain images from the much smaller neonatal mouse heart, there needed to be modifications to the scanning protocol, and these are detailed in the sections on hardware and software design later in this chapter. These modifications were informed by earlier work in Professor Schneider's group on imaging live adult zebrafish hearts after cryoinjury with recovery, where scanning equipment needed to be miniaturised and imaging time minimised (Koth, Maguire et al. 2017).

Traditionally, histological studies have been the basis to determine the extent of heart regeneration in mammals as well as other non-mammalian species such as zebrafish and salamanders (Huang, Sievers et al. 2006). To show that the reported complete (or nearly complete) early neonatal mouse heart regeneration was reproducible in our labs, we performed a series of surgeries on P1 and P7 pups and examined histological sections of these hearts post injury. We wanted to confirm injury in both cohorts by examining tissue architecture and collagen deposition (indicating scar formation) after MI surgery. Four days after injury, short axis sections of P1 hearts, located below the plane where the LAD was ligated, were stained with Masson's Trichrome. Areas of collagen deposition were seen as blue-purple tissue and compromised tissue in the ventricles where the regular muscle arrangements were disturbed are highlighted in Figure 19. This confirmed initial injury after MI was visible with histology 4 days post surgery, the time of the first planned MRI scan.

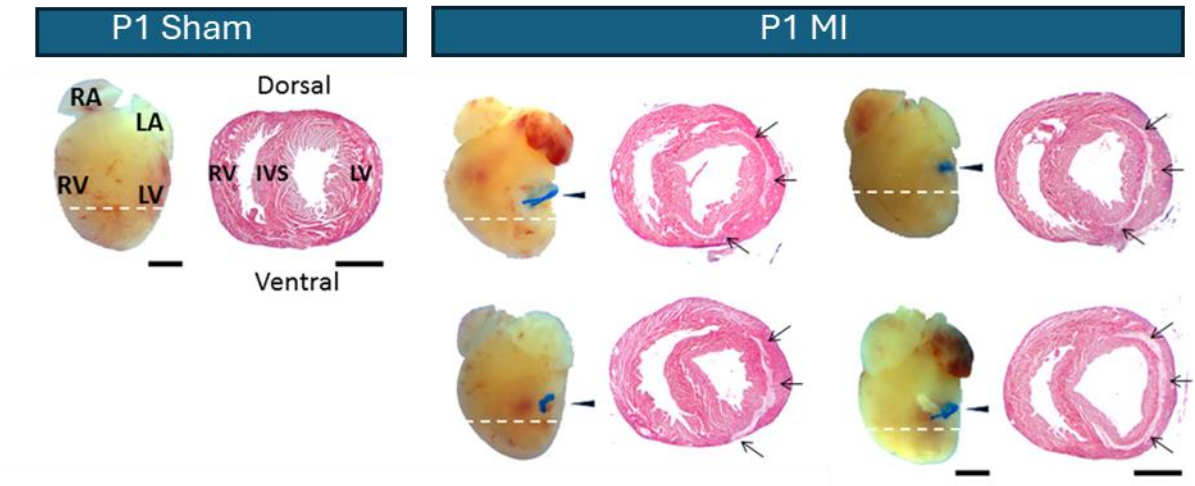

Figure 19: Histological assessment of hearts from preliminary cine-MRI study 4 days post-injury at P1 confirms initial injury after MI. Ventricular short-axis slices (approximate location shown by the dashed line) from 1 sham and 4 MI hearts were stained with Masson's trichrome. The compromised left ventricle anatomy in the MI hearts is highlighted by the black arrows. Arrowheads indicate suture placement. MI = myocardial infarction; RA = right atria; RV = right ventricle; LA = left atria; LV = left ventricle; IVS = inter-ventricular septum. Scale = 1mm. (Modified from Masters, M. DPhil thesis 2016 and BioRxiv preprint Gunadasa-Rohling et al, doi: https://doi.org/10.1101/329474)

This was repeated for MI on P7 pups, and we quantified the amount of infarcted LV tissue at Day 4 for both P1 and P7 cohorts (Figure 20 A, B). To check injury at the experimental endpoint, we performed histology on Day 21 samples as well. This confirmed that the P1 cohort showed very little injury at day 21, despite hearts stained earlier showing comparable, albeit smaller, infarct sizes to those seen in the P7 cohort. In contrast, the P7 cohort showed the expected scarring and ventricular remodelling at day 21 as seen after injury in an adult heart (Figure 20 C, D).

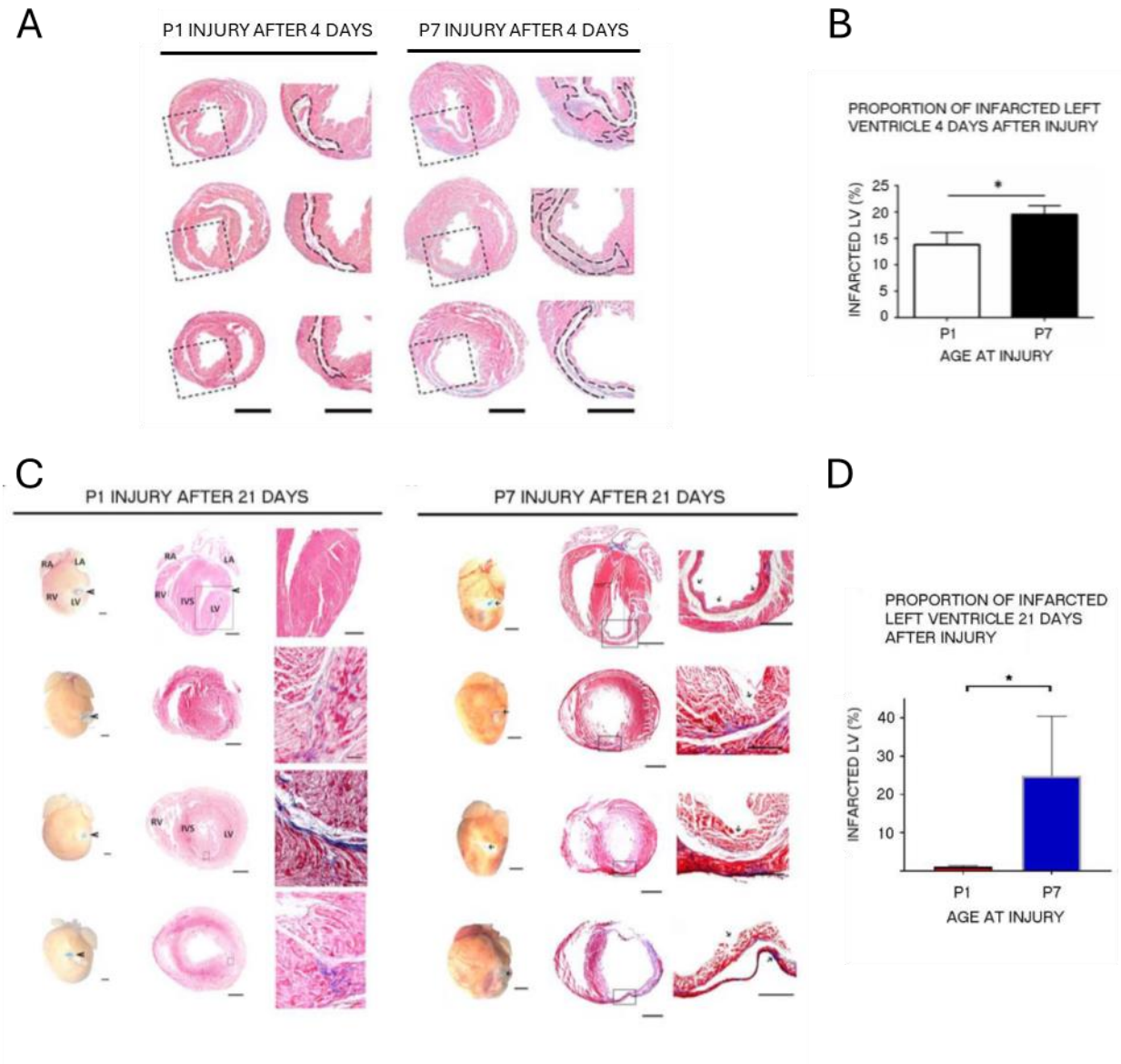

Figure 20: (A) H&E staining of representative sections from mid-infarct region from P1 and P7 hearts 4 days post injury. Boxed regions indicate zoomed images, shown adjacent, with dashed regions indicating infarct borders. Scale bars = 1mm. (B) The proportion of infarcted left ventricle (LV) was quantified as a percentage of total LV myocardial area over multiple sections from hearts injured on P1 (n=7) and P7 (n=3). (*p < 0.05, Mann-Whitney test). (C) Top row of long axis slices of P1 and P7 hearts removed at Day 21 post MI surgery (arrowheads indicate suture placement of blue thread) to compare regenerative ability of early versus late neonatal myocardium. The P1 heart (left) remains thick and healthy while the P7 (right) shows ventricular remodelling and thinning of the heart wall (arrows). Collagen scar tissue shows as areas of blue-purple (Masson's trichrome staining). Other P1 and P7 MI hearts with sections shown in short axis view (rows 2-4) further illustrate the damaged ventricular wall with collagen deposition and thinning evident for the P7 cohort. Scale bars: Top row: P1 whole heart, LA slice and magnification = 500µm; P7 whole heart and LA slice = 500µm, magnification = 100µm. Rows 2-4: P1 scale bars: whole heart and SA sections = 500µm; magnification = 50µm. P7 whole heart and SA sections = 500µm; magnification = 50µm. (D) The proportion of infarcted left ventricle at Day 21 is quantified for P1 and P7 hearts: *p<0.05. Mann Whitney test, n=4 for both groups (Modified from Masters, M. DPhil thesis 2016 and BioRxiv preprint Gunadasa-Rohling et al, doi: https://doi.org/10.1101/329474)

Finally, longitudinal histology from sham and surgery mice taken from Day 4 to 21 showed different degrees of injury over time. Figure 21 shows short axis sections from P1 and P7 hearts at Days 4, 7, 14 and 21 post surgery. The blue-purple area of collagen visible in the P1 heart at Day 7 after MI is not seen in later Days 14 and 21 slices (taken from different specimens). Only

very small areas of collagen scar tissue remain. Assuming there were similar levels of initial injury in all these animals, then the apparent recovery of the damaged areas is indicative of myocardial regeneration. The P7 sections look very different. There were extensive areas of thinned ventricle wall clearly visible starting from the mice sacrificed at Day 7 which increased as time passed. The walls at Day 14 and 21 included areas that were extensively stained blue-purple for collagen scarred areas with very little healthy myocardium left.

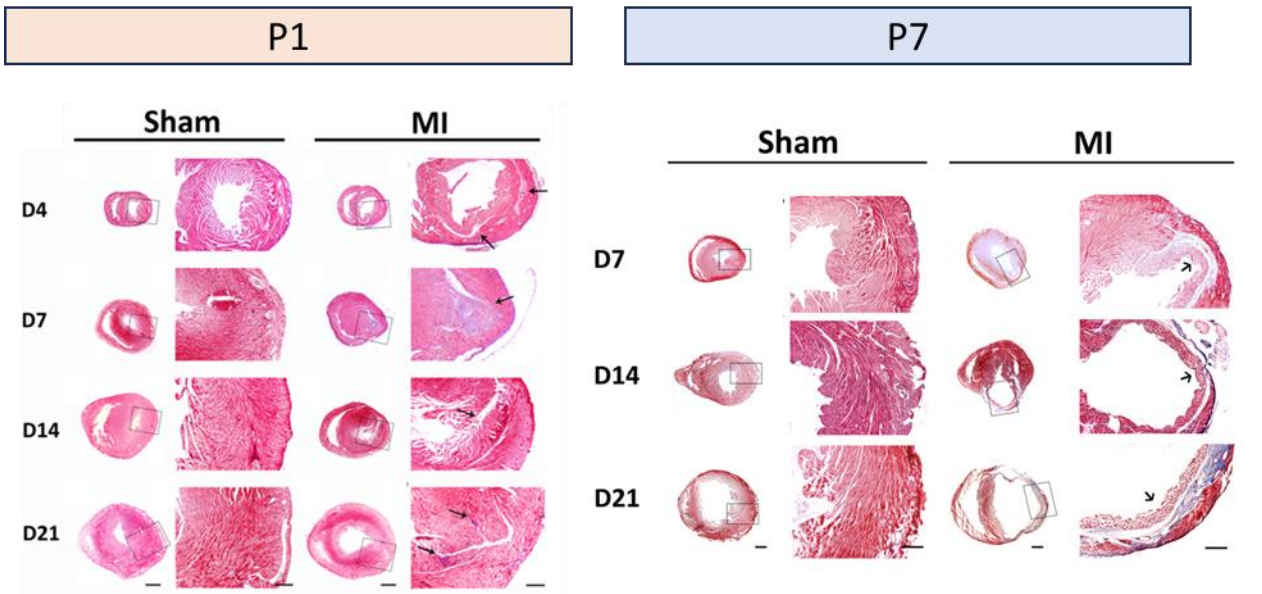

Figure 21: Short axis slices of P1 (left) and P7 (right) mouse hearts comparing injury and sham at Days 4, 7, 14 and 21. For the P1 hearts after MI, the tissue is healthy and thick with minimal scar tissue visible (blue-purple areas) after surgery at Day 21, comparable to the shams. For the P7 hearts, the difference between sham and injury is obvious with areas of remodelled and thinned ventricle walls clearly presented. Extensive scarring (blue-purple areas) can be seen from Day 14 while the damaged, thinning wall is present one week after surgery (shown in top MI slice) and is also evident at Day 4 (not shown). Scale bars: P1: short axis section = 250um; magnified sections = 100um; P7: short axis section = 100um; magnified sections = 250um. (Modified from Masters, M. DPhil thesis 2016 and BioRxiv preprint Gunadasa-Rohling et al, doi: https://doi.org/10.1101/329474)

These figures showed that the published histology on heart slices from P1 and P7 neonatal hearts after MI surgery could be successfully replicated in our lab and with our techniques. This laid the foundation upon which to build this new study using longitudinal non-invasive imaging to attempt proof of regeneration in the same specimen after checking for actual injury.

At the time of this study, for anything as small as a neonatal mouse pup, only limited work had been attempted to assess cardiac function in three-day old mice and this was in a terminal study (Wiesmann, Ruff et al. 2000). This chapter presents the first successful study of cardiac cine imaging of neonatal mice from as early as one day after birth (P1) using retrospectively gated, accelerated MRI with full recovery and repeated scans of the same specimen, up to five times in three weeks. High resolution imaging allowed left ventricular functional parameter analysis on

two cohorts, P1 and P7, both split into two groups (with and without MI surgery), to compare the regenerative P1 heart with the reparative P7 heart. This study demonstrates that cardiac functional MR imaging with recovery in newborn mice is feasible and it also facilitates the investigation and monitoring of the processes of myocardial regeneration during the early first days of life. This work was published in *Circulation* in November 2018 (Gunadasa-Rohling, Masters et al. 2018), paper included in Appendix 1.

3.2 OVERALL AIM

The aim of the work in this chapter was to use functional cardiac MRI in neonatal mice to show that neonatal mammals retained some regenerative ability in their heart muscle similar to that seen in some other species such as amphibians and teleost fish, but that this was lost shortly after birth. Working with Professor Jurgen Schneider and Dr Mahon Maguire of the Oxford Biomedical Magnetic Resonance imaging Unit (BMRU), we wanted to set up early neonate cardiac functional imaging with recovery as a novel platform to monitor heart regeneration in real time.

3.3 METHOD DEVELOPMENT AND RESULTS

The surgical techniques required for neonatal mouse MI were already established within our group and the method is outlined in Chapter 2 General Methods. However, some modifications were required to adapt the technique for this project. Although I had been doing neonatal mouse surgeries for some time, the pups were always studied as a batch and there was no need to identify individuals within the litter. In order to monitor each pup's progression from baseline through to injury or potential recovery, I had to devise a method of labelling each young neonate that would last through the 21 days of the procedure. There were also some minor adjustments made to the pre- and post-surgery protocol to incorporate the MRI scan, but by far the biggest innovations required to perform these experiments were the modifications to the MRI scanning procedure, with significant advances in new hardware and software essential to adapt to the small size of the neonatal pup and our intention to ensure full recovery of the animal after each scan. These technical modifications were performed by Professor Jurgen Schneider and Dr Mahon Maguire

and their team in a collaboration with our lab group prior to my starting this experiment, but I was involved with the final developmental iterations and testing of the analysis software.

3.3.1 EXPERIMENTAL DESIGN

Two cohorts of pups, one at P1 and the other at P7, underwent myocardial infarct surgery using the Left Anterior Descending (LAD) coronary artery ligation model with a permanent suture, or sham surgery with no permanent injury. Each cohort would be scanned five times at Baseline, Day 4 post injury/sham which would confirm presence or absence of a visible functional injury, followed up by scans at Days 7, 14 and the experimental endpoint of Day 21 at which point the mouse was to be sacrificed and tissue samples taken. An outline of the experiment is shown below:

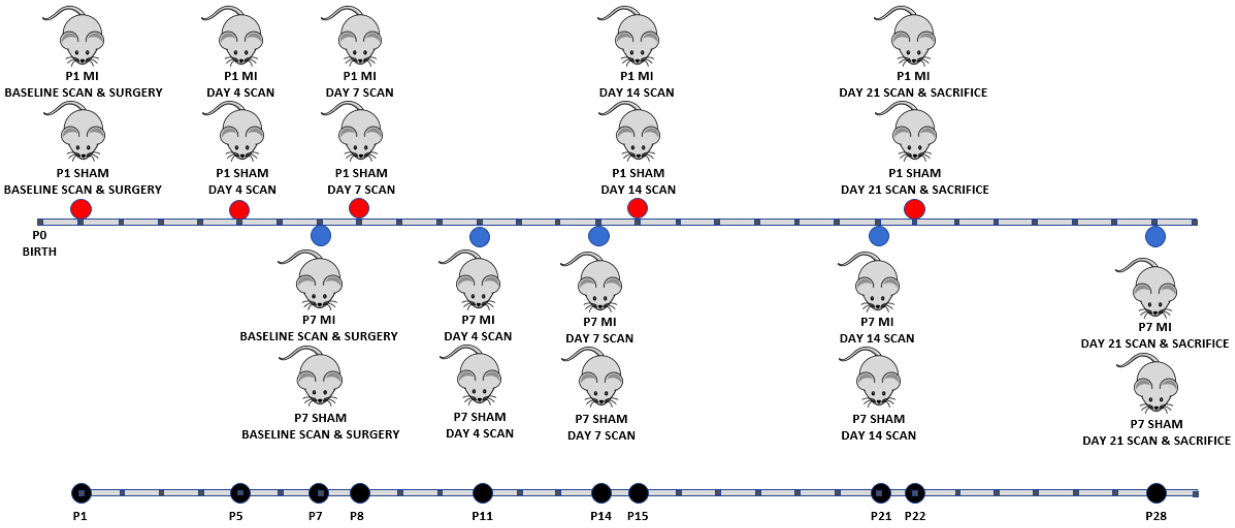

Figure 22: Experimental design for P1 and P7 neonate mouse pup surgery and MRI scanning. The P1 cohort is the top set (red dots), with the P7 cohort intercalated as shown (blue dots). The bottom line illustrates the time points that we collected scan data (black dots).

3.3.2 NEONATE MOUSE HUSBANDRY AND MAINTENANCE

For this study it was necessary to generate sufficient pups at P1 and P7 for the experiments and to mitigate any potential cannibalism due to the stress on the mother from pups being removed from the cage and then returned after surgery or imaging. We initially set up breeding trios (one male and two females) for which the cage bedding was changed regularly until a few days before

the anticipated birth of a litter. At that time, the male was removed from the cage, and the pregnant females separated into individual cages to litter down, splitting the used cage bedding between them. This bedding was then not changed until the pups were at least 10-12 days old which greatly reduced the occurrence of pup cannibalism as the soiled litter helped to mask the smells from the handling, surgery and anaesthetic that lingered on their skin. The P1 cohort remained with their mothers for the duration of the study (21 days), while the P7 cohort were weaned and divided into new cages of males and females at approximately 21 days.

3.3.3 IDENTIFICATION OF NEONATE PUPS

As our experimental plan required repeated measurements from the same neonate mouse pup, we had to explore methods of permanently identifying each individual pup within the litter. For the first few days after birth, their ears are very small and flattened tight against the head making ear notching impossible, and we did not have the option of skin tattooing on our project license. After consultation with the animal care staff and confirming with the vet, we decided to label them with a permanent marker. As permanent marker pens such as Sharpie™ are routinely used on adult mice and rats (usually to mark their tails) with no adverse affects (Wang 2005), we wanted to extend this to neonate labelling, a process which, to that date, had not been documented in the literature.

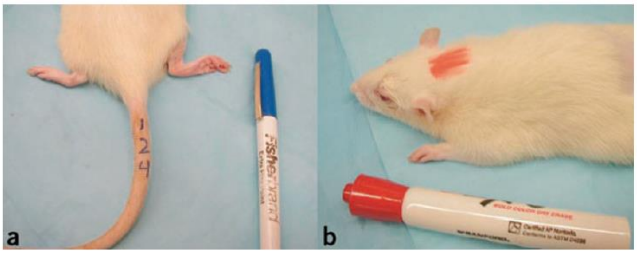

Figure 23: Common methods of rodent identification include (a) tail and (b) fur marking with a permanent marker pen. This is routinely done for short term adult mouse and rat labelling, when it's not necessary to use more permanently ear clipping. From A Primer on Rodent Identification, (Wang 2005).

Careful and regular monitoring of a litter of "test" pups was authorised, which involved regular checking for the first few days. The marker pen did not seem to irritate or injure the pup's delicate skin and also caused no distress to the mother, but unfortunately it was quite quickly removed due to grooming by the mother and the high rate of skin turnover in a newborn pup from growth and abrasion against littermates, nesting mother, and cage bedding. The markings on our test litter were not very legible by the next morning. We needed to re-mark the pups 2 or 3 times a day in

order to keep them clearly labelled. In addition to a large number on the pup's back, we marked around the top of the limbs and tails using a number code (Figure 24) to increase the chance of the identification holding over an extended time period (these areas seemed slightly less accessible to being rubbed off or groomed away by the mother). This marking system was well tolerated by the CD1 strain of mice that generally has very competent and low-stress mothers with robust pups – we had no losses attributable to the increased researcher handling or labelling.

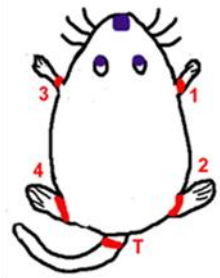

Mark 1	Right forelimb
Mark 2	Right hindlimb
Mark 3	Left forelimb
Mark 4	Left hindlimb
Mark T	Tail

Combination of marks to identify pups:			
Pup 1 = 1	Pup 6 = 3 & 4	Pup 11 = T & 3	Pup 16 = T & 3 & 4
Pup 2 = 2	Pup 7 = 1 & 3	Pup 12 = T &4	
Pup 3 = 3	Pup 8 = 2 & 4	Pup 13 = T & 2 & 4	
Pup 4 = 4	Pup 9 = T & 1	Pup 14 = T & 1 & 3	
Pup 5 = 1 & 2	Pup 10 = T & 2	Pup 15 = T & 1 & 2	

Figure 24: Labelling of individual neonate pups. Each pup had to be remarked repeatedly to avoid losing track of each particular specimen until they were old enough to be permanently ear notched.

The P1 litters were permanently ear notched at the time of the Day 14 MRI scan, and the P7 litters were notched with their Day 7 scan. This method of pup labelling was used throughout this study.

3.3.4 HARDWARE DESIGN

This study was performed at the BMRU and used their MRI facilities. The system comprised a 9.4T magnet, 400MHz scanner from Agilent Technologies, with a horizontal bore (210mm), a VNMRS DirectDriveTM console, and a shielded gradient system (inner diameter 60 mm, gradient strength 1 T/m, rise time 130 μs). Since the standard animal cradles for adult mice were too big to securely position a neonate, a set of new cradles was designed to accommodate the growing mouse pups (Table 1). These were 3D printed using acrylonitrile butadiene styrene on an HP Designjet printer - sizes are detailed below and a neonate positioned in a fitted cradle is shown in Figure 25.

Table 1: Hardware parameter modifications for neonatal mouse MR imaging equipment. Inner and outer cradle diameters are listed.

MOUSE AGE	RF COIL DIAMETER	CRADLE DIAMETER	FIELD OF VIEW	SLICE THICKNESS
P1 – P7	20 mm	12.5 mm – 16.5 mm	15 mm^2	0.5 mm
P8 – P14	28 mm	18 mm – 22 mm	20 mm^2	0.7 mm
P14 – P28	33 mm	26 mm – 36 mm	20 mm^2	0.7 mm

Several nose cones were made to fit snugly over the pup's face to deliver the mixture of isoflurane in oxygen anaesthetic gas. A custom-made air-heated blanket (ambient air flow rate 4.0 L/min) was pre-calibrated to yield a surface temperature of approximately 36°C and was placed over the back of the pups to maintain body temperature during the scan. A miniature pressure pad, made from polyurethane foam and polyvinylchloride film fixed to a polythene tube, was placed beneath the pups and connected to a commercial pressure transducer (RS Components) to acquire respiratory and heart rate signals of the pups while in the magnet. The experimental setup with a pup in situ is shown in Figure 25 with a representative physiological monitoring trace.

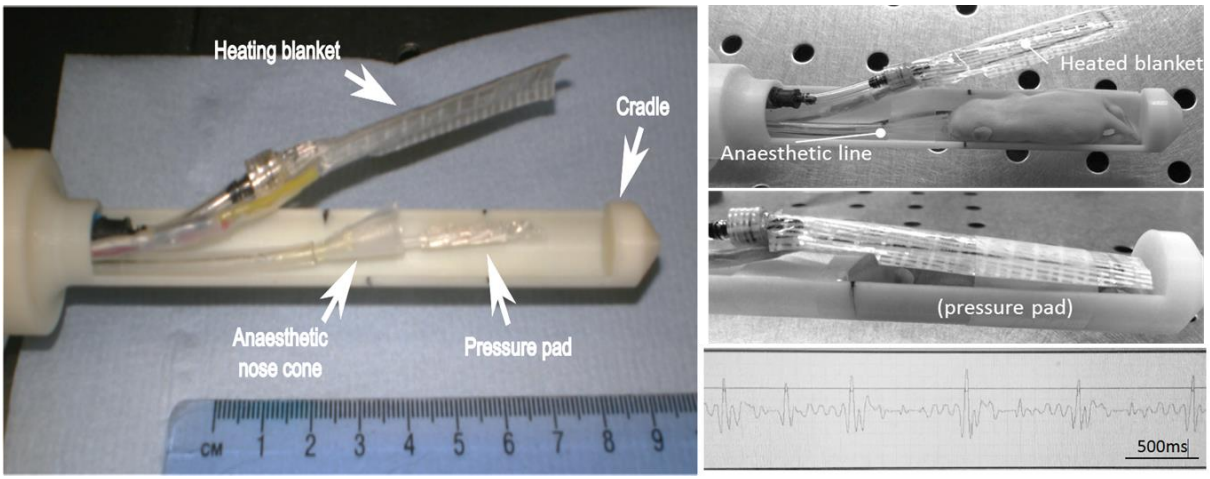

Figure 25: Custom designed hardware for MRI scanning of neonatal mice. Left: the neonate cradle with pressure pad, anaesthetic nose cone and heating blanket. Right: the pup was positioned in the cradle with the pressure pad underneath the diaphragm for physiological monitoring. The anaesthetic line with nose cone delivered isoflurane carried in oxygen. A heated blanket covering the animal maintained physiological temperature, and it was all secured by surgical tape to prevent movement. Heart rate and respiration (shown in the lower right graph) were continually checked for the duration of the scan. The mouse shown is 7 days old (approximately 3cm from nose to base of tail) in an 18mm cradle. Hardware design and assembly was done by Dr. Mahon Maguire and Prof Jurgen Schneider.

3.3.5 SOFTWARE DESIGN

To minimise the time the pups would be away from the mother (a vital factor in pup survival) a protocol was developed using compressed sensing and retrospective gating (see our bioRxiv paper Gunadasa-Rohling et al. https://doi.org/10.1101/329474). The accelerated imaging (2x compressed sensing) protocol greatly condensed the total scan time by reducing the number of data points taken ("undersampling") assuming they do not change too much across small areas, and then reconstructing the missing sample points by mathematical algorithms later off line (Wech, Lemke et al. 2011, Koth, Maguire et al. 2017). The Wech study determined that you could undersample by a factor of three and not compromise the spatio-temporal resolution or the accuracy of the functional cardiac parameters but we decided two times was enough for our experimental requirements. The retrospective gating enabled these scans to proceed without requiring clear signals from the pressure transducer. The motion of the heart was detected directly from non-triggered MR data and generated a so-called "navigator signal" which was then used to gate the cine-MR image reconstruction (Hiba, Richard et al. 2006). This synchronised the timing of the MRI images with the cardiac cycle to remove motion artefacts and clearly show one complete heartbeat cycle from diastole through systole and back.

The navigator signal was analysed such that the cardiac cycle (one complete heartbeat) was sectioned into 20 frames. Data reconstruction was performed offline using a custom written software package "bmru_itools" developed inhouse by Prof. Schneider's team, using Interactive Data Language "IDL" version 8.3 from Harris Geospatial. One of the first successful reconstructions is shown in Figure 26.

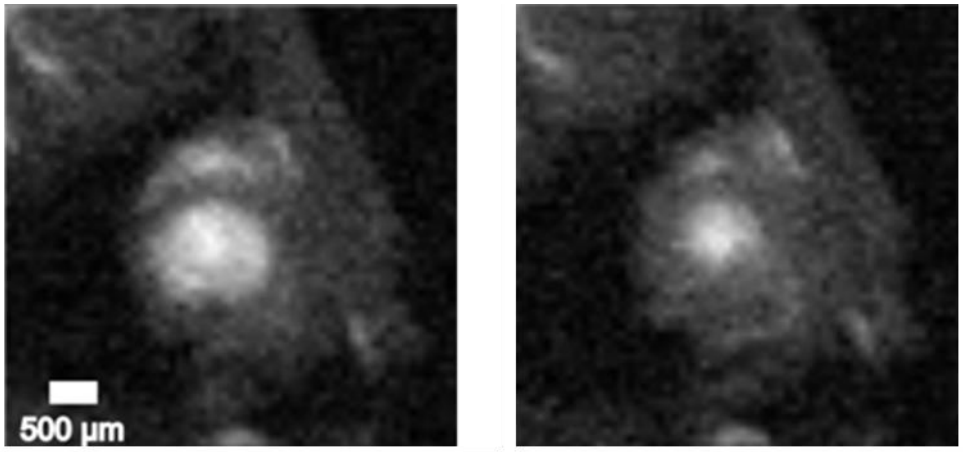

Figure 26: Frames from a representative retrospectively gated cine image of an uninjured P1 mouse from a pilot study. This was the first time as far as we are aware that this has been visualised in such a young pup. These frames are end diastole (left) and end systole (right).

The software interface used to generate the images is shown in Figure 27. The input signal deduced from the retrospective gating is shown in Figure 27A. By adjusting parameters shown Figure 27D and continually reconstructing the images, a clear image with a full range of motion across diastole and systole could be visualised. The ECG trace (Figure 27B) was shown separately from the respiratory trace (Figure 27C) and both needed to be adjusted individually – when the parameters had been set correctly, the peak or trough amplitude points from A coincided visually with those calculated by the software (see the blue triangles in Figure 27B, C, E and F).

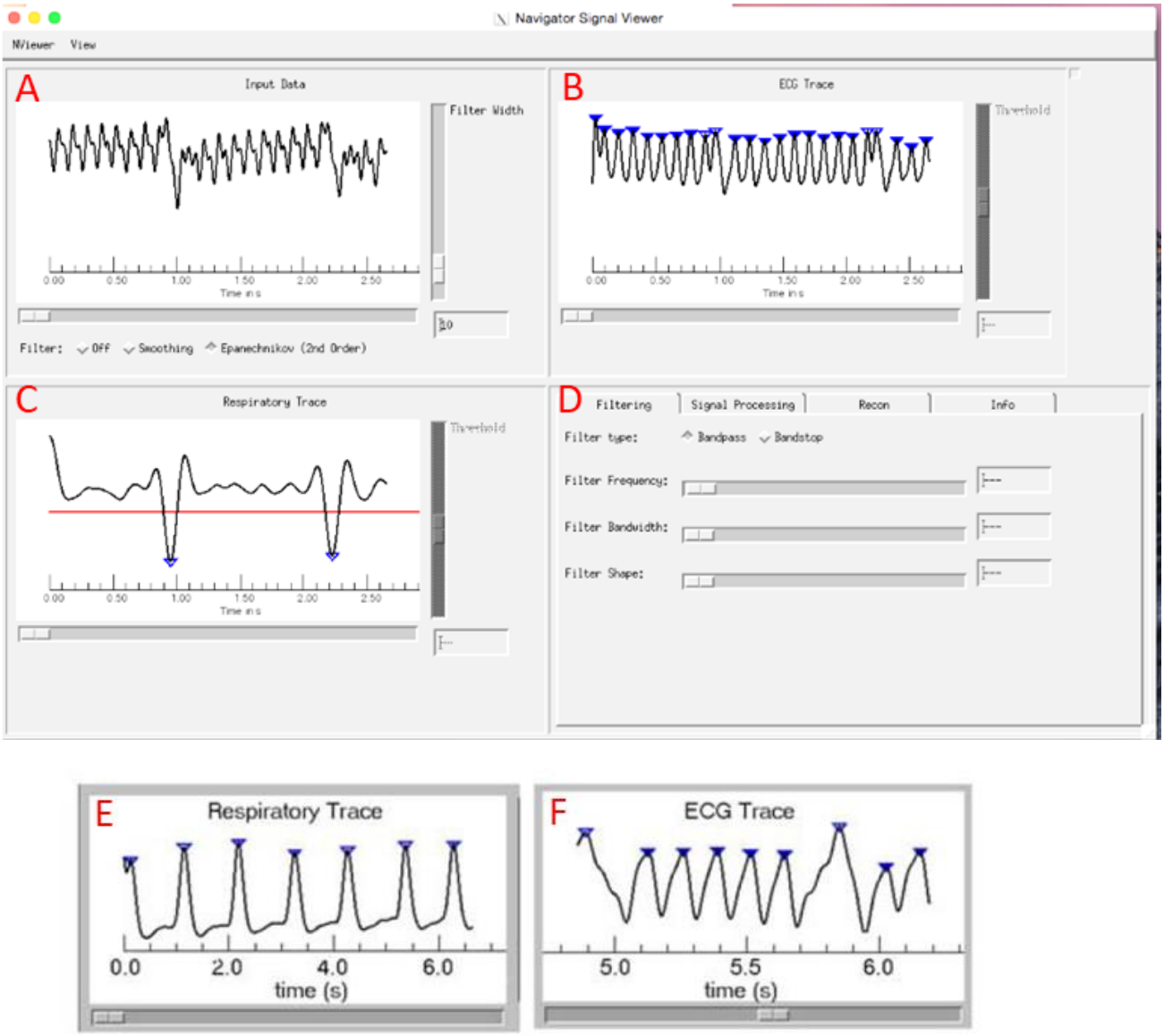

Figure 27: Extraction of ECG and respiratory traces from the navigator signal. (A): The navigator signal is shown in the upper left of this screenshot from the analysis program. (B-C): It is broken down into its two components, the ECG showing the heartbeat (upper right), and the respiratory signal (middle left). (D): A range of parameters are manually adjusted and the image reconstructed until the best visualisation of a complete cardiac cycle is achieved. (E-F): Another window showing more details of the respiratory and ECG traces.

When the image was as clear as possible, the frames that occurred at diastole (maximum ventricle dilation – largest internal volume) and systole (maximum ventricle contraction – smallest internal volume) were selected by visual examination. The outer and inner walls of the ventricle were manually outlined (Figure 28).

This process was repeated for every slice through the heart. When all the slices had been analysed, the programme output the calculated values of EDV and ESV for each slice, and then EF, SV and LVM for the entire heart (see Figure 29).

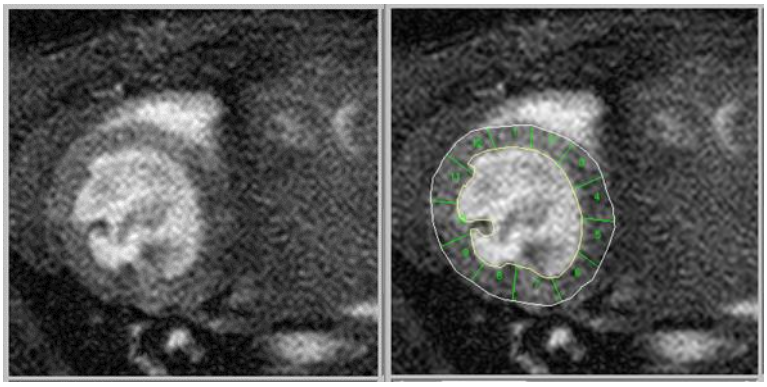

Figure 28: An example of a short axis cine MRI slice that has been optimised (left) and subsequently manually segmented (right).

Problems with the new analysis software took time to resolve and delayed this work beyond the pilot "proof of concept" stage for some time. We could not check the scans as we were working or do any preliminary analysis during the four weeks of the study itself as the software was still not fully developed but we had to proceed due to constraints on magnet booking time and animal housing and breeding issues. Some of the main problems resulted in an obvious lack of motion across an entire heartbeat for some scans despite extensive tweaking of the navigator signal, and some slices not being able to be visualised at all thus rendering that heart data incomplete. With careful notes of the steps, the values input and the results output, I was able to feedback results to Professor Schneider and Dr Maguire so that they could modify the software. After several rounds of this beta testing and quality control of the programme, we were finally certain the results were robust and reproducible. The final images were much more crisp and clear, with a full range of motion throughout the cardiac cycle. All the slices of any single heart could be opened in the programming environment, visualised and segmented as above so that EDV and ESV could be measured accurately. Then a last module reconstructed the whole heart and calculated the cardiac function values of EF, SV and LVM/BM. The final output of the scan analysis software is shown in Figure 29.

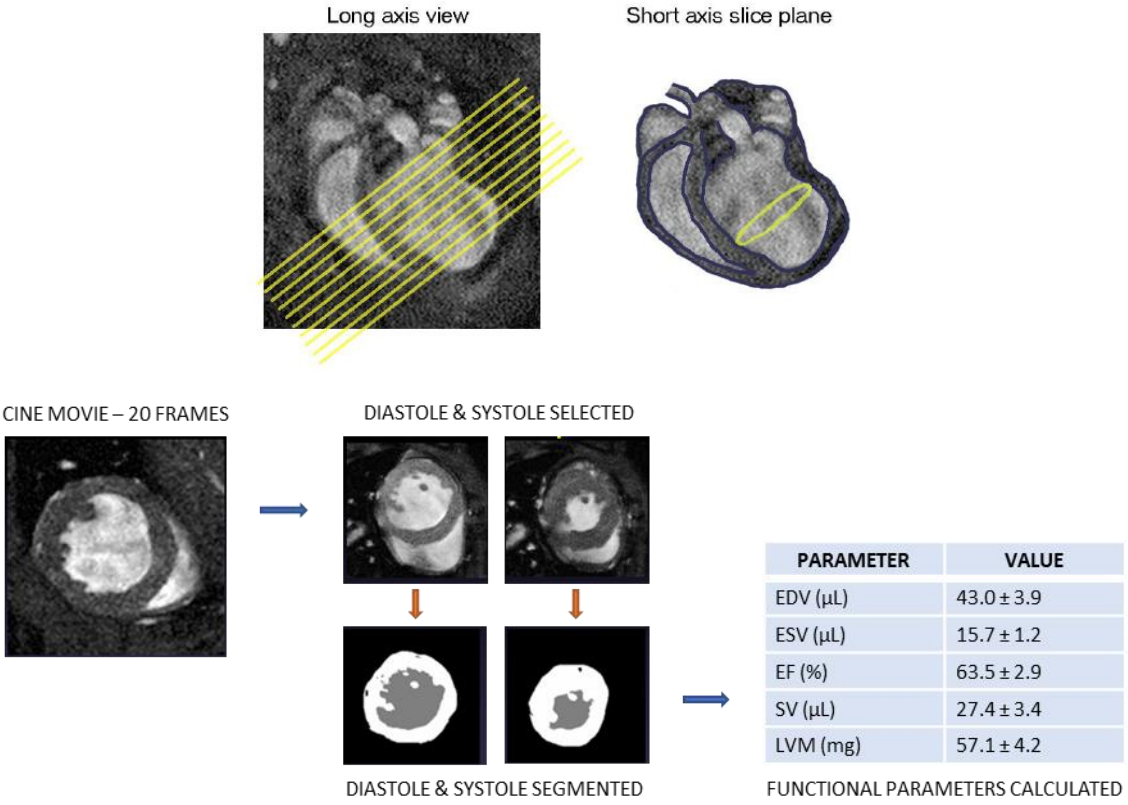

PARAMETER	VALUE
EDV (µL)	43.0 ± 3.9
ESV (µL)	15.7 ± 1.2
EF (%)	63.5 ± 2.9
SV (µL)	27.4 ± 3.4
LVM (mg)	57.1 ± 4.2

Figure 29: Top row: 8 – 12 short axis slices, 0.5 – 0.7mm thick, were acquired from the base to the apex to cover the whole of the left ventricle Bottom row: Outline of data analysis procedure: the frames that occur at diastole (maximum ventricle dilation – largest internal volume) and systole (maximum ventricle contraction – smallest internal volume) were selected by visual examination. The outer and inner walls of the ventricle were manually outlined and the software calculated the values of EDV, ESV, EF, SV and LVM. This was repeated for all the slices from base to apex and summed up (example values shown above with ± standard deviation).

3.3.6 MRI SCANNING

Scanning Preparation

On the morning of each scan, all pups from the litter to be scanned that day were removed from the mother and placed together in a heated enclosure at 32°C. The pup to be scanned was taken out and checked carefully for any signs of distress or weakness before being placed in the induction chamber. Anaesthesia was induced using 4% isoflurane carried in 100% oxygen at 2.0 L/min flow rate. The pup was checked for identification (remarking the skin if necessary for the younger pups) and weighed before positioning belly down in the appropriate sized cradle, with their nose inserted into the size-matched nose cone. Anaesthesia was maintained at 1.5% - 2.0% isoflurane at 1.5 L/min oxygen flow throughout the scan. The pup was carefully positioned on top of the pressure pad and covered by the air blanket. The whole setup was secured with surgical tape to prevent

movement, and inserted into the bore of the scanner. Physiological measurements and temperature were continuously monitored throughout the scan.

Neonate MRI scanning procedure

After scouting for the short-axis orientation of the heart using a fast, spoiled 2D gradient echo sequence (TE/TR = 1.15/5 ms, flip angle 15°, number of averages 8, slice thickness 0.5/0.7 mm, field-of-view (FOV) 15 x 15 mm^2 to 25 x 25 mm^2), B0-maps were acquired (TE/TE/TR = 0.86/ 0.75/5 ms, flip angle 15°, number of averages 4, slab thickness 11.2 to 15.0 mm, field-of-view (FOV) 20 x 20 x 15 mm^3 to 25 x 25 x 20 mm^3) to allow for automated shimming of a 3D volume across the cardiac region of mouse. Retrospectively gated, compressed sensing (CS) accelerated multi-frame imaging ('cine-MRI') was performed covering the heart from base to apex in a contiguous stack of short-axis slices (TE/TR = 1.86/4.6 ms, flip angle 10°, number of averages 1, number of frames 50, number of repetitions 6, slice thickness 0.5/0.7 mm, number of slices 8 - 12, field-of-view (FOV) 15 x 15 mm^2 / 20 x 20 mm^2). Each repetition was two-fold under sampled in phase-encoding direction and corresponding sampling patterns were generated as reported previously (Cassidy, Schneider et al. 2004). All imaging was performed without prospective cardiac and respiratory gating.

The total imaging time including animal preparation ranged from 35 – 45 minutes, depending on the age of the pup and therefore the size of the heart as this determined the number of image slices necessary to scan the entirety of the heart (8 – 12 slices, with a thickness of 0.5 – 0.7 mm each). Image contrast and resolution were sufficient for manual segmentation and derivation of functional parameters.

Post scanning recovery procedure

Once the scan was completed, the pup was removed from the cradle and one of the following steps was taken:

(a) If this was the first baseline scan of the pup at either P1 or P7, it was moved to the surgery area of the room and underwent the MI LAD ligation or sham procedure. The pup was first allowed to partially recover from the anaesthetic for 10-15 mins depending on the imaging duration. Whilst still under the influence of residual isoflurane, it was wrapped in moist paper towel and placed on crushed ice for 1 (P1) or 2 minutes (P7) to induce a surgical plane of anaesthesia by hypothermia. The pup was then taped down onto the

prepared ice block and the myocardial infarction or sham surgery was performed. We found that it was critical to recovery after surgery that most of the isoflurane was allowed to be expelled from the pup before the additional hypothermia step or the anaesthesia would be too deep and it would not survive.

(b) If this was scan 2 – 4, the pup was allowed to recover under a heat lamp and then moved to the warming chamber with its littermates. Upon completion of all scans on a litter, the pups were covered with a mash of warmed, moistened faeces collected from their home cage (to disguise external odours and thereby facilitate maternal acceptance) and collectively returned to the dam.

(c) For scan 5, the final scan of the project, the pup was culled by cervical dislocation with its heart immediately removed into 4% PFA for fixation overnight. They were individually labelled with their identification codes and stored for potential future histology.

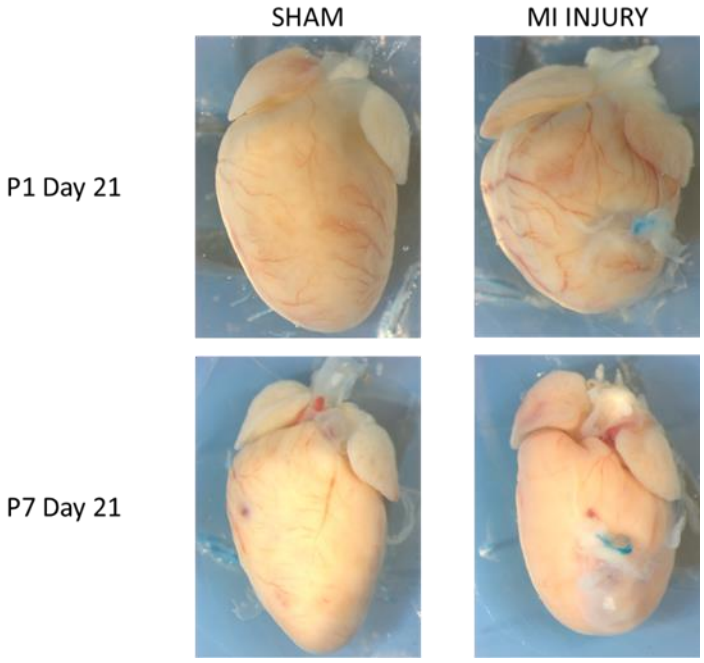

Figure 30: Example hearts from P1 and P7 pups with/without MI injury removed for examination and prospective histology at Day 21, the experimental endpoint of our neonate MRI study. The injury is clearly visible in the P7 heart but no obvious damage is present for the P1 heart. Note these photographs are not the same scale.

3.3.7 PRELIMINARY RESULTS INCLUDING CONFIRMATION OF SUCCESSFUL IMAGE RECONSTRUCTION AND FUNCTIONAL ANALYSIS BY THE SOFTWARE

As mentioned above, at the end of the five MRI scans (Day 21 of this study) each pup was sacrificed by the approved Schedule 1 procedure and the hearts removed for further analysis (Figure 30). Even before sectioning and staining, the injury in the P7 heart was clearly visible as a thinning and damaged area below the blue suture thread. The area around the suture in the P1 heart was still heathy, thick and vascularised, and looked like it functioned normally.

Because we were still developing and testing the software during the scanning process, we decided to do a preliminary evaluation of the data by looking at the key study timepoints of Baseline (Day 0), first scan (Day 4) and experimental endpoint (Day 21) for both P1 and P7. This partial data set was also used for the final development of the image analysis software modules, and we did several iterations of testing, image reconstruction and checking of the output functional parameters to confirm the results were physiologically sensible before continuing.

Previous work in our laboratory had confirmed injury by akinesis of the ventricle wall after P1 MI by cine-MRI at Day 7 post injury, which was reinforced by histology. The pup was scanned at baseline before surgery and again at Day 7 after which it was immediately euthanised and the heart removed for sectioning and staining (Figure 31).

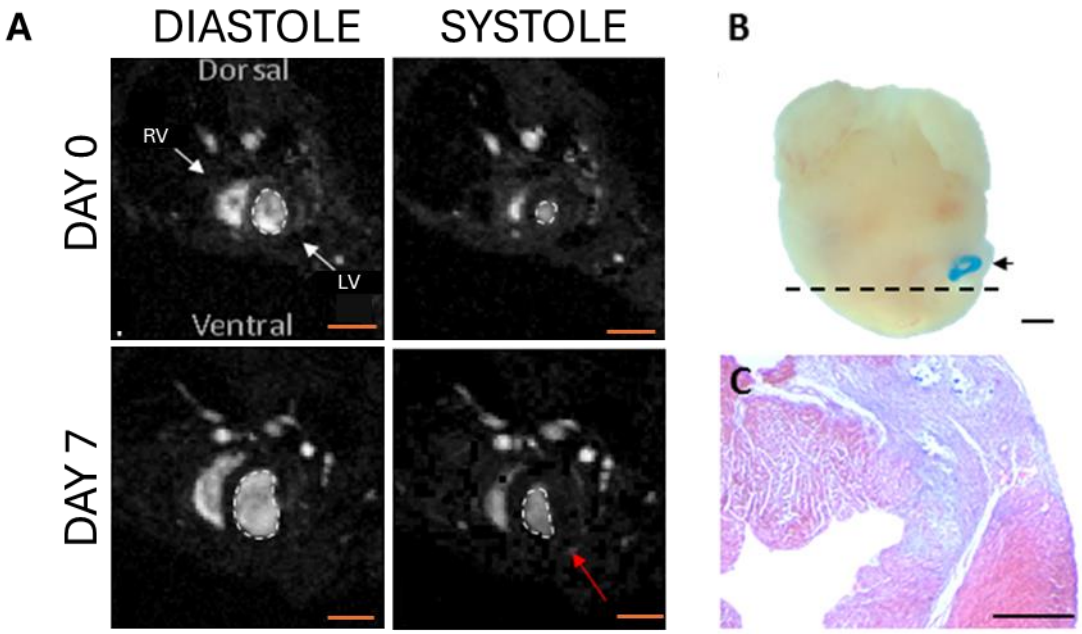

Figure 31: Infarct visualisation by lack of wall motion and histology at Day 7 post MI surgery on a P1 neonate. (A) MRI images of hearts in diastole and systole before (D0) and 7 days post-MI (D7). The area of reduced contraction (akinesis) of anterior left ventricle (LV) on D7 in systole (red arrow). Dashed line outlines luminal borders of the LV. (B) Whole heart ex vivo with the blue suture visible. The dashed line indicates plane of transverse sectioning in (C) Masson's trichrome staining of the anterior LV wall with significant collagen deposition (blue staining) and similar morphology to that seen by MRI (A). Scale A = 1mm; B and C = 500μm. (Modified from Masters, M. DPhil thesis 2016).

Looking at mid-ventricular slices from the new cine image movies we could see similar areas of akinesia for both the P1 and P7 surgery groups at Day 4, but with a clear difference after 21 days post surgery between the two cohorts. Note that only samples that had clear akinesia around the wound site at Day 4 which is indicative of myocardial damage were taken for further analysis and contributed to the final results of this study. The cine image frames from diastole and systole shown in Figure 32 clearly illustrates these differences.

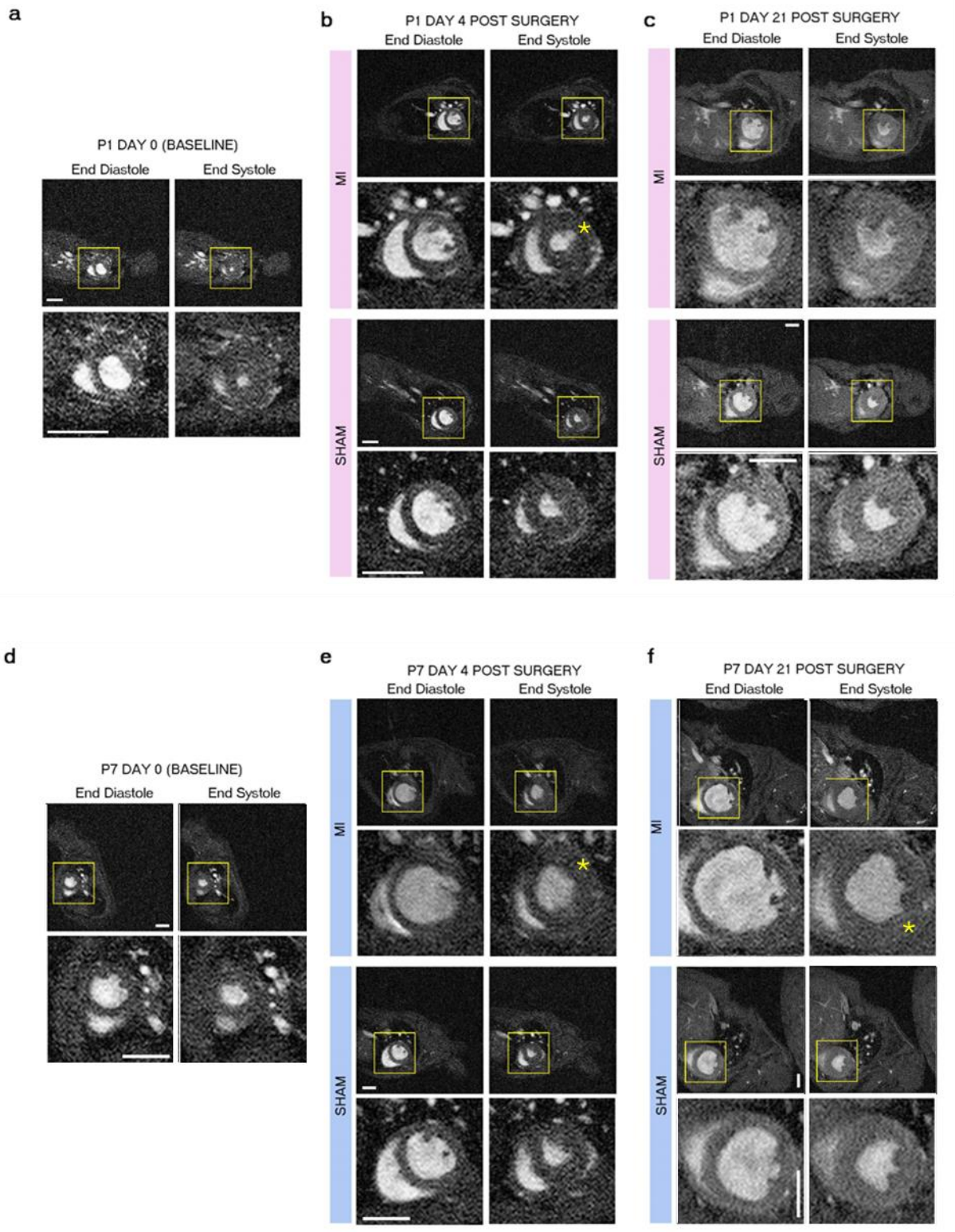

Figure 32: Cine MRI images of P1 and P7 mid-ventricular short axis sections with frames capturing diastole and systole shown for Day 0 (Baseline scan), Day 4 and Day 21 (Endpoint). The top images (a-c, pink bars) are from the P1 cohort with frames after MI compared with Sham directly below; and the same for the P7 cohort (d-f, blue bars) in the bottom half of this panel. It is clearly visible that the P7 after MI has enlarged diastole and systole volumes compared to the age-matched sham, whilst the P1 examples are very similar to each other. Areas of akinesis are labelled by a yellow asterisk in the magnified MI systole images. All scale bars = 2mm

Analysis of these preliminary scans (Figure 33) gave us a quick overview of the entire project and justified the time investment in doing the complete set of analyses shown in the following sections. Enlarged volumes at diastole and systole for the injured P7 cohort at day 21 were manifest in reduced ejection fraction, while this was not evident for the P1 cohort.

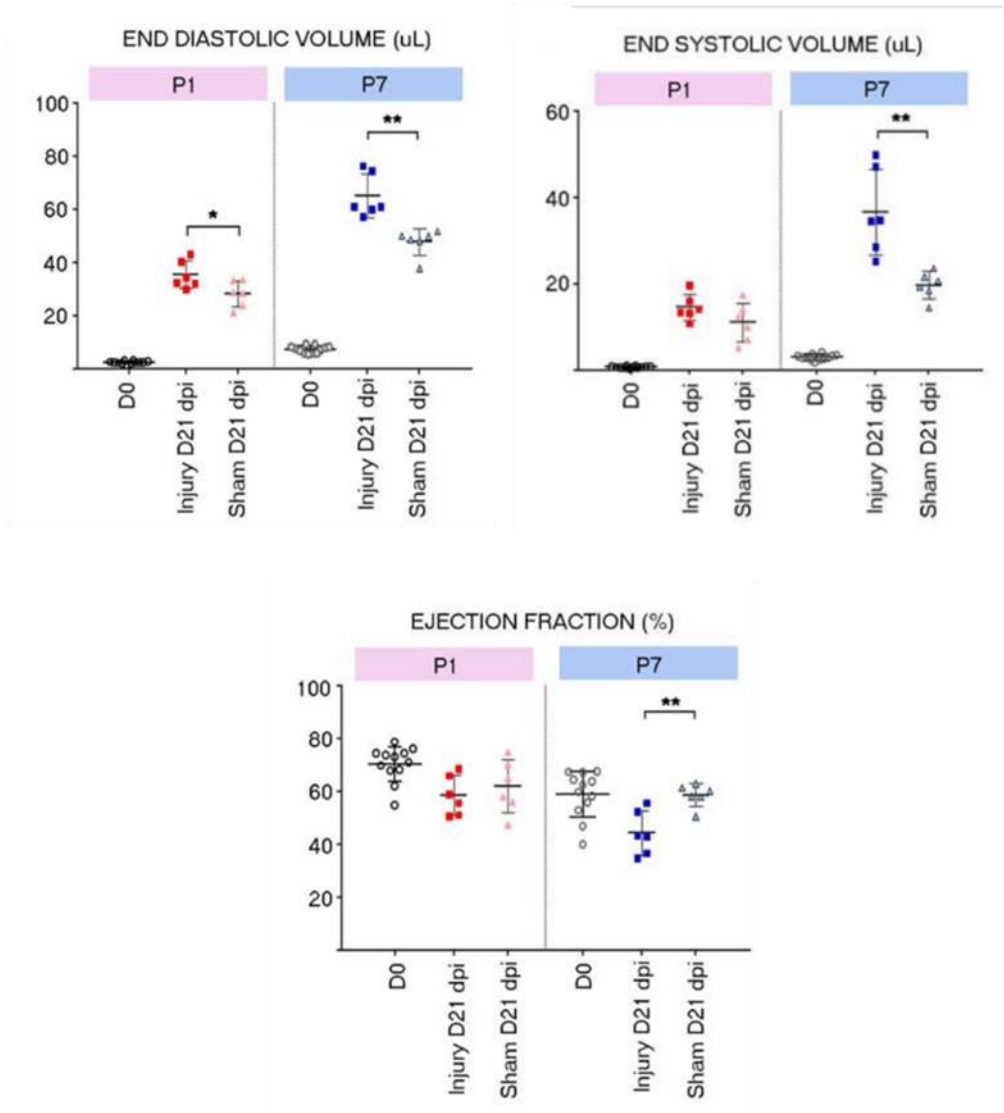

Figure 33: Preliminary results from the analysis of P1 and P7 data at the experimental endpoint of Day 21 post surgery. Top row shows EDV and ESV and the bottom is the calculated EF. (Student's t test, *p<0.05; **p<0.01, n=6 for all groups)

3.3.8 BASELINE GROWTH AND DEVELOPMENT USING MRI SCANS OF THE SHAM SURGERY COHORT: CHANGES IN MASS AND CARDIAC FUNCTION OVER THE FIRST MONTH

One of the aims of this project was to document the normal growth of the neonatal mouse heart and to monitor the development of its functional parameters using the data from the sham control groups of both P1 and P7 cohorts. The scans took place at Day 0 (baseline), Day 4, Day 7, Day 14, and Day 21, which correspond to pup ages P1, P5, P7, P8, P11, P14, P15 and P21, P22 and P28, and we obtained data for the following time points (Figure 34):

	P1	P7
Baseline	P1	P7
Day 4	P5	P11
Day 7	P8	P14
Day 14	P15	P21
Day 21	P22	P28

Figure 34: Taken from the experimental plan illustrating when we had MRI scan data for the sham pups. Both P1 and P7 cohorts are included, giving us a total of 10 dates.

We were interested in the relative growth of the left ventricle as a ratio of total body mass, heartbeat rate as well as ejection fraction, none of which had been recorded for P1 pups or followed through maturation for the first four weeks of life. These results are shown in Table 2 and Figure 35.

Table 2: Growth and development of cardiac function in uninjured hearts from P1 – P28.

	P1		P7		P1		P7	
	BODY MASS		BODY MASS		LVM /BM		LVM /BM	
	Mean	SD	Mean	SD	Mean	SD	Mean	SD
D1 - P1	1.91	0.15			0.25	0.04		
D4 - P5	3.55	0.19			0.22	0.03		
D1 - P7			4.76	0.58			0.30	0.05
D7 - P8	4.65	0.45			0.24	0.05		
D4 - P11			7.58	0.57			0.29	0.03
D7 - P14			9.33	0.64			0.28	0.02
D14 - P15	6.88	0.94			0.31	0.05		
D14 - P21			14.02	1.12			0.30	0.03
D21 - P22	13.00	1.99			0.33	0.03		
D21 - P28			23.16	2.19			0.27	0.02
	P1		P7		P1		P7	
	HEART RATE		HEART RATE		EJECTION FRACTION		EJECTION FRACTION	
	Mean	SD	Mean	SD	Mean	SD	Mean	SD
D1 - P1	407.17	18.56			71.92	2.47		
D4 - P5	475.80	24.83			64.52	7.28		
D1 - P7			389.67	58.60			58.13	7.23
D7 - P8	400.40	21.67			65.10	2.61		
D4 - P11			411.83	26.77			63.25	8.14
D7 - P14			336.33	60.14			60.28	9.48
D14 - P15	279.00	28.91			61.79	8.95		
D14 - P21			444.00	32.96			62.42	4.60
D21 - P22	461.50	14.58			62.20	10.01		
D21 - P28			474.17	22.27			58.84	4.29

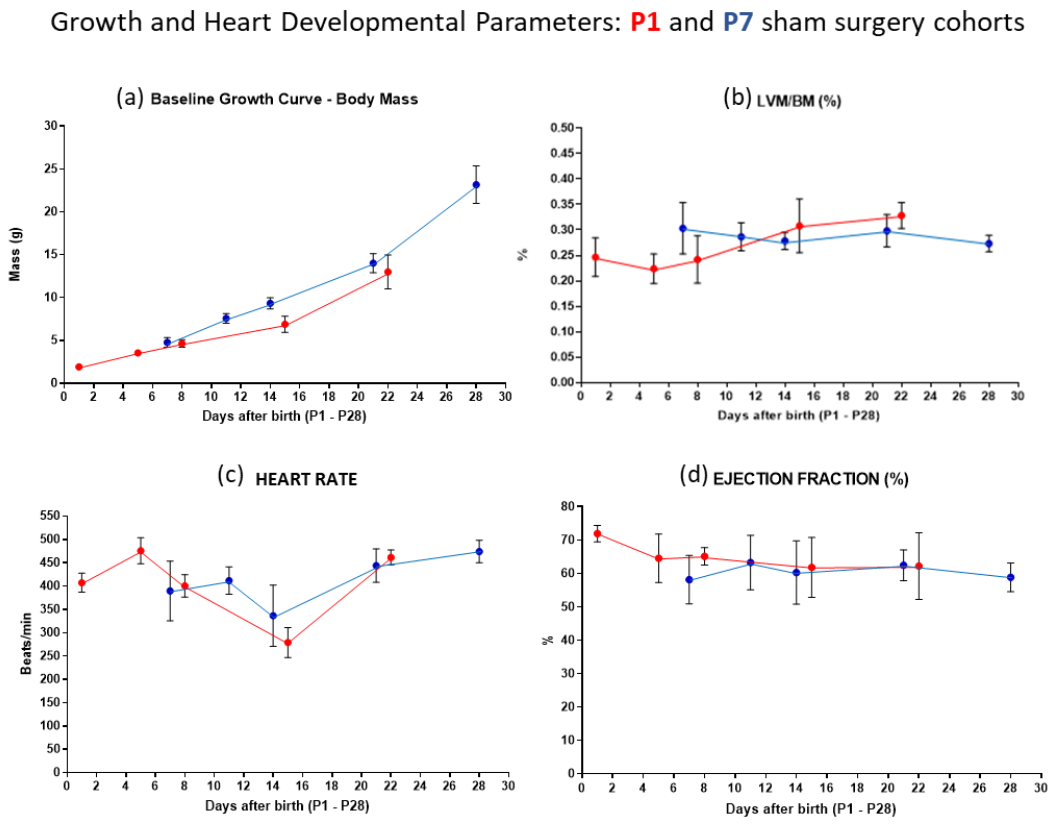

Figure 35: Development of (a) body mass (BM), (b) left ventricular mass to body mass ratio (LVM/BM), (c) heart rate (HR) and (d) ejection fraction (EF) in sham control animals (RED LINES are the P1 cohort; BLUE LINES are the P7 cohort) over the study duration of 28 days; n=6 for all groups. Apart from the body mass, the other values are calculated from the analysis of the MRI scans.

Body mass:

Body mass increased linearly from birth to approximately P21 after which the rate of growth increased. At the end of the study, we noticed that the P7 cohort seemed to outweigh the P1 group at similar time points (P14-15 and P21-22), with a significant difference of nearly 2.5g between them at day 14-15 (P7 cohort @ P14 = 9.33±0.64; P1 cohort @ P15 = 6.88±0.94, p <0.005; see Figure 35(a) and Figure 36(a)).

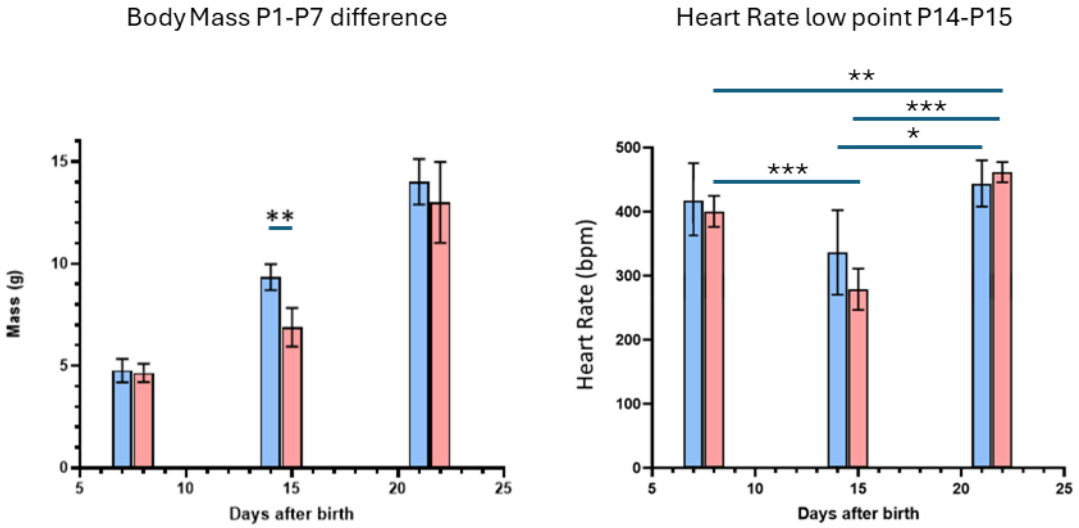

Figure 36: **BLUE** columns are the P7 cohort; PINK columns are the P1 cohort. Left: Body mass difference between the P1 and P7 cohort at a similar age – P14 and P15: The P7 cohort weighed almost 2.5g more than the P1 cohort which had received 3 doses of anaesthesia by this age. Note that body weight increased significantly with time in both groups but this is not shown on this graph for clarity. Right: the low point in heart rates shown for both the P1 and P7 cohorts at this same age – this dip is observed for both sham cohorts as well as the injury cohorts at this age (*P7 between Day 14 and Day 21; ***P1 between Day 8 and Day 15 and between Day 15 and Day 22; **P1 between Day 8 and Day 22. Mixed effects analysis with Tukey post-hoc for both graphs. See also Figure 19).

Left ventricular mass index:

The left ventricular mass index was calculated by quantifying the volume of the left ventricular wall from the MRI scans multiplied by the specific gravity of heart muscle, 1.05 g/ml, which was normalised to body mass:

$$\frac{LVM}{BM}index = \frac{\left[LV\ volume\ (ml) * 1.05\ (\frac{g}{ml})\right]}{body\ mass\ (g)}$$

The LVM/BM of the P1 group increased gradually such that the value at P21 was higher than that in the first week of life. There was no change in LVM/BM with time in the P7 group.

Heart rate:

In the P1 group, the heart rate increased from P1 (407 ± 18.56 bpm) to P5 (476 ± 24.83 bpm) before decreasing to 400 ± 21.67 at P8 and reaching a low of 279 ± 28.91 at P15. A week later at P22 it was restored to 462 ± 14.58, close to the expected adult value. The data from the P7 cohort was more variable (see Table 3) but showed a similar dip at P14 which again significantly increased at P21 and P28. This very non-linear, almost sinusoidal set of values was consistent between the two age groups, both with and without MI surgery, and entirely unexpected.

Ejection fraction:

We recorded an EF of 71.9 ± 2.2% at P1, to our knowledge the earliest measurement of cardiac function in the neonatal mouse by MRI. Falling to 64.5 ± 6.5% after 4 days, it only reduced to the expected adult value of 60% after two weeks. This was not significantly higher than the EF at time points after surgery but was significantly higher than that in the baseline scan of the P7 mouse.

3.3.9 FUNCTIONAL PARAMETERS OF THE HEART AFTER MYOCARDIAL INFARCTION INJURY OR SHAM FOR P1 VS P7

After a successful surgery, the result of myocardial infarction damage was clearly visible in the first MRI scan (Day 4) for both the P1 and P7 cohorts. Due to surgical variation amongst the pups, only animals that showed clear infarct damage at this time, visible by a region of akinesis in the left ventricular wall in the area where the suture was placed, were selected for further scan analysis at the experimental timepoints. The grouped results for EDV, ESV, EF, SV, HR and LVM/BM for each of our four conditions: (1) P1 with MI injury; (2) P1 with sham injury; (3) P7 with MI injury; (4) P7 with sham injury are graphed in the Circulation paper (included in Appendix 1, with a table of values in Appendix 2 and graphed in Supplemental Figure S1).. This initial analysis was a one-way ANOVA with Sidak's multiple comparisons to measure how the MI cohort differed from the age-matched sham cohort at each timepoint for each of the parameters of interest listed above. Another way to show these results which emphasises the significance of our aim to follow each pup individually is the longitudinal data illustrated by a subset of data for three neonatal pups from

each group, and is shown in Supplemental Figure S2. Finally, a post-hoc two-way ANOVA with repeated measures was performed to examine changes over time for each group and between groups, revealing further insights into how these two cohorts of mice, the regenerative P1 group and the reparative P7 group are affected by surgery with these results shown in Table 3 and Figure 18 below.

Table 3: A two-way ANOVA with repeated measures was performed, analysing for the effect of time and MI. P values are present for each group, with $p < 0.05$ highlighted in bold here

	Interaction between treatment and time	time	Infarct v sham	Repeated measure
EDV P1	P=0.1140	**P<0.0001**	**P=0.0423**	P=0.1858
EDV P7	**P=0.0017**	**P<0.0001**	**P=0.0009**	**P=0.0014**
ESV P1	P=0.8327	**P<0.0001**	P=0.2155	P=0.4193
ESV P7	**P<0.0001**	**P<0.0001**	**P=0.0037**	**P<0.0001**
SV P1	**P=0.0267**	**P<0.0001**	P=0.0737	**P=0.0124**
SV P7	P=0.7566	**P<0.0001**	P=0.5198	P=0.0894
EF P1	P=0.8331	P=0.6913	P=0.7128	P=0.7410
EF P7	P=0.2685	P=0.2706	**P=0.0102**	**P<0.0001**
HR P1	P=0.7899	**P<0.0001**	P=0.5395	P=0.7780
HR P7	P=0.6243	**P<0.0001**	P=0.5330	P=0.7828
LVM/BM P1	P=0.7346	**P<0.0001**	P=0.6490	**P=0.0185**
LVM/BM P7	P=0.1790	P=0.1458	**P<0.0001**	P=0.6111

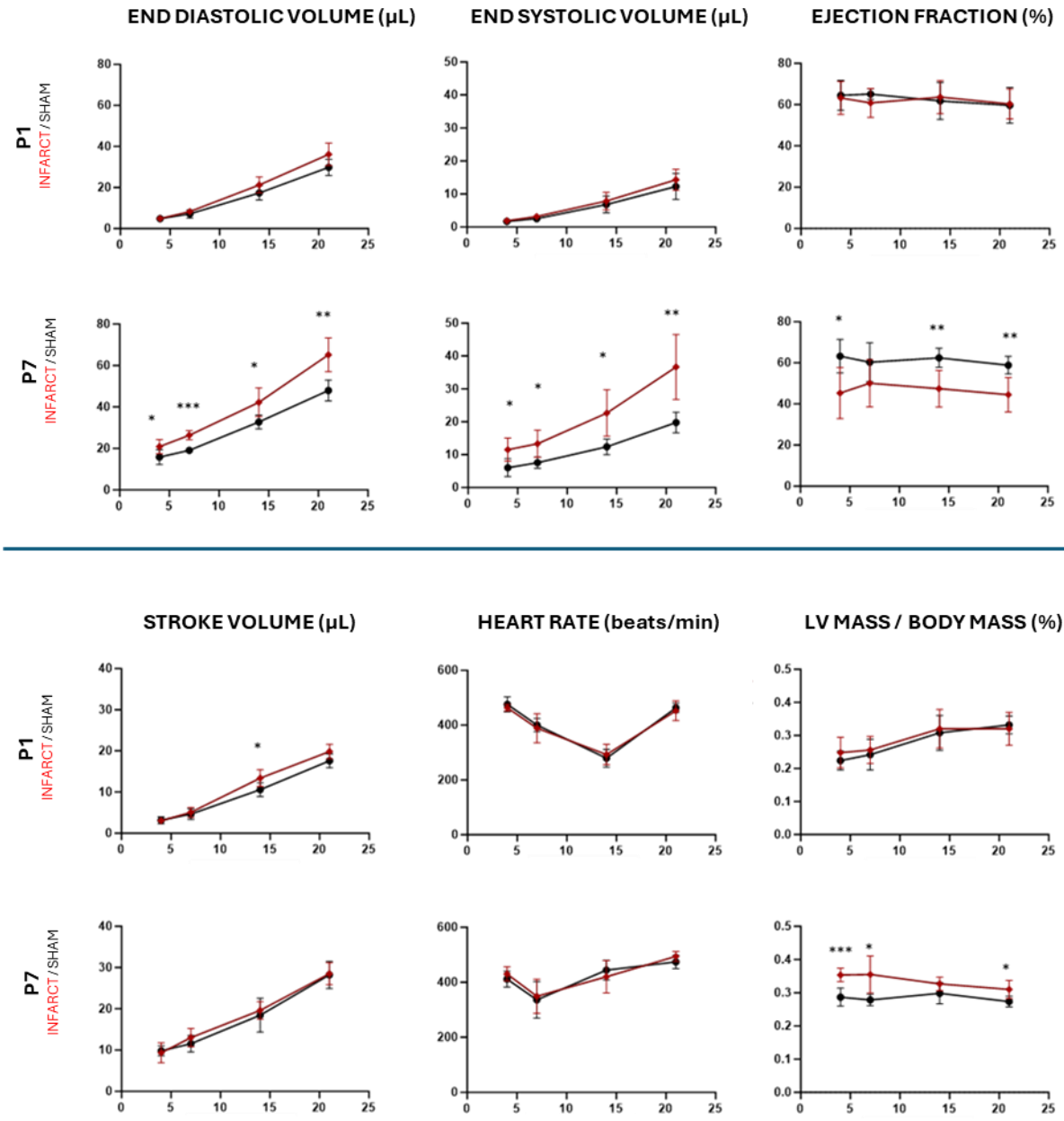

Figure 37: Post-hoc two-way ANOVA analysis of functional parameters over time for MI vs sham groups of P1 and P7 cohorts. The difference between the groups becomes evident over time for the P7 cohort ventricular volumes and ejection fraction, while P1 MI and sham cohort groups remain similar. See Table 3 and results text for full discussion. *, **,*** indicate significance at each point; n = 6 for all groups.

This analysis (Figure 37 and Table 3) reveals further insights into how these two cohorts of mice, the regenerative P1 group and the reparative P7 group are affected by surgery and time. EDV and ESV increase for all four groups driven by growth of the animal over three weeks, but we can see that with the EDV and ESV for the P7 MI group, this is significantly faster than the P7 sham. Even though the EF does not change over time, it is also significantly lower in the P7 MI than in the P7 sham group. Repeated measure analysis indicated a significant effect on EDV, ESV and EF in the P7 hearts but not the P1 hearts, showing that the increase seen in the infarcted P7 hearts

over time was greater than that in the sham hearts. SV increases as the heart grows larger as expected and is maintained even after injury. The HR of both cohorts are also consistent and show the dip at P14/15 mentioned previously (more on this parameter below). The LVM/BM ratio increases for both P1 groups together but the P7 MI group is higher than the P7 sham indicative of injury-induced hypertrophy.

Finally, this analysis allows us to directly compare the data at the same time points for all these four groups (Figure 38). Very strongly significant differences are evident between the P1 and P7 MI groups at age 7/8, 14/15 and 21/22 days with increases in EDV and ESV with a corresponding reduction in EF. When we examined the heart rate of these four different groups for the duration of this experiment, we did not see any significant differences between the injury and age-matched sham animals for either the P1 or P7 cohorts. However, these data support the finding in the analysis of the sham animals, showing a decrease in heart rate around P15 (day 14 and day 7 post MI in P1 and P7 groups, respectively) such that the heart rate at that time point is significantly lower than that at 21 days post-op in all groups.

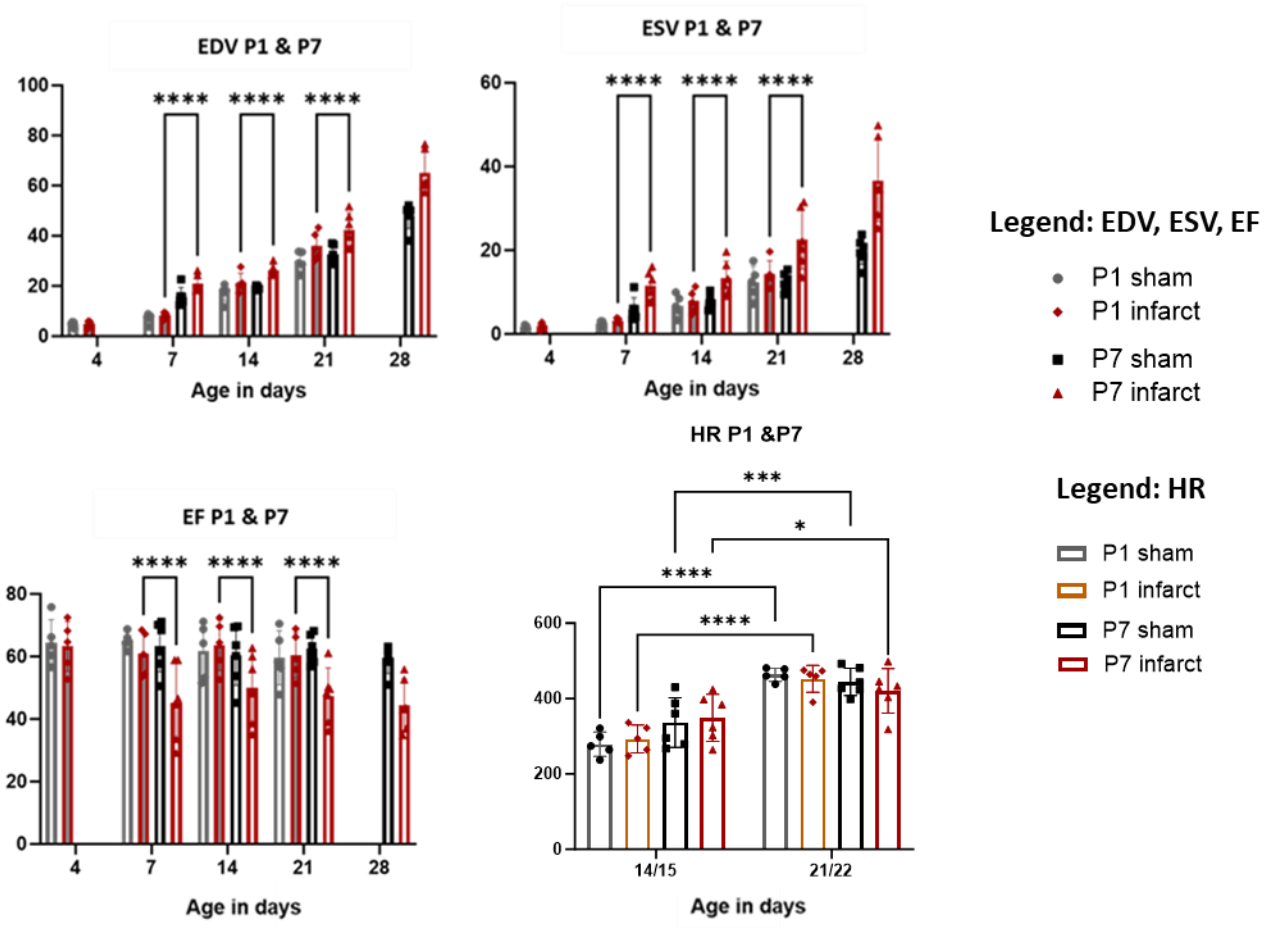

Figure 38: Two-way ANOVA analysis allows direct comparison between P1 and P7 cohorts at nearly equivalent ages (7/8, 14/15 and 21/22 days). The increased EDV and ESV and reduced EF in the P7 infarct group can be clearly

seen. Although there is no difference in heart rate at any one timepoint between the groups, the drop in the heart rate for all groups at age 14/15 days is statistically lower than a week later as shown here (it is also lower than the week before although this is not included in this plot, see Figure 17).

3.3.10 STUDY LIMITATIONS

There are a number of limitations to the work presented in this chapter.

There is no histology to back up the data from the MRI study. In the pilot studies, histological sections were taken from a set of animals after surgery to validate the reproducibility of the infarct protocol. In addition, sections were taken to show that hearts injured at P1 did not show damage after 21 days in contrast to those injured at P7 (BioRxiv preprint Gunadasa-Rohling et al, doi: https://doi.org/10.1101/329474). Histological analysis of the hearts in this MRI study would have provided further validation of the functional changes we saw.

There was no measurement of the infarct scar in the MR images. This could have been done using delayed enhancement after administration of gadolinium or by measuring the akinetic region of the tissue. In the pilot study the feasibility of experiments using late gadolinium enhancement (LGE) on neonatal mice post MI injury was explored, however the results of IP delivery or uptake were inconclusive. These studies did show clear areas of akinetic wall movement after MI which were not observed in the sham cohorts, and subsequent histology immediately after the day 7 post injury MRI scan confirmed collagen deposition in the anterior LV wall, indicating the feasibility of MRI to visualise infarct injury by wall motion measurements (Masters, M DPhil thesis 2015). As our experiments were time-sensitive, we did not try LGE for this regeneration study and relied on observed akinesis at the Day 4 scan. However, quantifying the size of the akinetic region on the images would have provided useful additional data from our study.

Poor apical image quality in some MRI scans may have reduced the accuracy of measurements in the differences in the diastole and systole ventricle size, leading to possible errors in measuring EDV and ESV for these extreme slices. However, this error would be minimal in comparison to the larger and much clearer differences in the remainder of the scans, rendering this uncertainty not significant and not affecting the overall volumes to a major extent.

Due to the larger mass of the P7 neonate, there is the possibility that the internal body temperature during surgery may have been higher than that of the P1, and this may have been a cause of the increased damage to the P7 hearts. However, we took the increased mass into account during the hypothermia induction procedure and left the P7 cohort buried in ice for several minutes longer than the P1. Although we did not measure heart rate directly during surgery, there was no observable difference in heart rate or respiratory function between the P1 and P7 pups, and no additional bleeding in either cohort. An infrared camera to measure body temperature could be used to check this during surgery but it would still be difficult to record the important core temperatures, and would cause potential delays to completion of the surgical procedure which is time-sensitive in neonates.

Finally, this study could only confirm restoration of function by MRI after MI injury in P1 mice which was not observed in P7 mice. The use of LGE in the images would have been a useful indicator of tissue damage in the akinetic regions. Without that, it is possible that the myocardium was stunned during the surgery in the P1 mice, rather than fully ischaemic, and therefore recovered more rapidly (Kloner 2020). Nevertheless, a large body of work in this field has confirmed the presence of a postnatal regenerative window after MI in the mammalian heart as first shown in 2011 (Porrello, Mahmoud et al. 2011), and indicated by a consensus statement regarding myocardial regeneration in 2017 (Eschenhagen, Bolli et al. 2017).

3.4 DISCUSSION AND CONCLUSIONS

This project formed part of an ongoing collaboration between Professor Riley's group that has the experience with adult murine myocardial infarction models and the technical expertise of Professor Schneider's group in the analysis of functional cardiac parameters by magnetic resonance imaging and the engineering and development of new protocols for MRI scanning. The Riley group had recently started performing MI surgery on neonatal mouse pups, and the aim was to adapt the established protocols for adult murine MRI to facilitate early longitudinal scanning of newborn mouse pups, with and without MI surgery, from right after birth. We wanted to show how the functional parameters of the heart develop over the first four weeks of life, and importantly, how these are affected by myocardial infarction surgery, and prove conclusively that complete (or near complete) regeneration can occur after MI at P1 but not at P7.

3.4.1 BASELINE GROWTH AND DEVELOPMENT OF FUNCTIONAL CARDIAC PARAMETERS:

Having developed the technology to image the neonatal mouse heart, we were able to measure the functional parameters of the uninjured heart over the first month of age (10 time points from P1 to P28) and to determine if there might be an adverse effect of repeated anaesthesia on the neonatal mice. These factors had not been documented in the literature from such an early time point.

Body mass and LVM/BM index:

As expected, we found that body mass increased approximately linearly from birth to Day 21 after which the rate of growth increased. This was attributed to the fact that the mouse pups were weaned at 21 days post birth. What was interesting was the significant difference in mass between the P1 and P7 cohorts at P14-15 (and higher P7 weights at P21-22). Repeated administration of anaesthesia early in development may have a negative effect on body growth and may have contributed to this difference in weights as the P1 cohort had already received three doses of anaesthesia lasting approximately 40 minutes each by the end of their first week of life (P1, P5, P7). A study into the effect of repeated doses of isoflurane, for 3 hours at P3, P5 and P7, on brain development in neonatal mice saw neuroapoptosis and behavioural changes but no difference in body weight (Maloney, Yuede et al. 2019). A similar study into 30 minutes exposure at P7, P8 and P9 or P15, P16 and P17 saw only mild behavioural alterations and no loss of body weight (Rosenholm, Paro et al. 2017). Both these studies were done on C57BL/6 mice whereas our study used CD1 pups which are physically larger in size from an early age. We can suggest that because CD1 pups grow larger and faster (Jensen, Porsgaard et al. 2016), they might be more susceptible to the potential negative effects of anaesthesia on their very early growth rates and thus account for our observed body mass differences. Despite the lower body mass observed for the P1 cohort, we found that the LVM/BM ratio for the first week of life was also lower in the first week than that after 2 weeks. Wiesmann et al, who assessed animals from P3, also reported an increase with age (Wiesmann, Ruff et al. 2000). It is interesting that the LVM/BM ratio in the P1 cohort matched that in the P7 cohort by day 14/15 despite the significant difference in body weight at that age. Our study adds important new data for the first week to the knowledge base.

Heart rate

At baseline, the heart rate of the P1 pup was lower than expected but increased by P5. We believe this may have been the effect of the isoflurane anaesthesia used during the MRI scan and the

increasing tolerance to it as the pup matured. It would be interesting to know the P1 heartrate without anaesthesia but this would be technically difficult to measure. It has been well documented in human infants that HR decreases from neonate to infant and toddler and continues to decrease into adulthood (data from a Great Ormond Street Hospital report 2013) but a comprehensive review in the Lancet shows an increase in HR from birth to a small peak at 1 month of age before decreasing into later childhood (Fleming, Thompson et al. 2011). However, it is known that general anaesthesia suppresses the rodent heart rate (Lukasik and Gillies 2003, Berry, Thedens et al. 2009) and that in very young paediatric patients this effect is more prominent in the immediate neonatal period than in older infants (Saikia and Mahanta 2019). There are also changes in neural activity during this time such as changes in the developing sympathetic and parasympathetic nervous systems that innervate the heart and influence heart rate during the immediate neonatal period. One of the most interesting findings from this study was the nonlinearity of the neonatal heartbeat rate during this first month. Both the P1 and P7 cohorts showed a clear decrease in heart rate at P14 – 15, to almost half its previous rate, before increasing to the adult rate of approximately 450 beats per minute. This decrease was also echoed in both the P1 and P7 cohorts after MI injury, strengthening the observation. The decrease in heart rate at around P15 coincides with a surge in T3 thyroid hormone which has been thought to induce cardiomyocyte proliferation (Walsh, Ponten et al. 2010, Naqvi, Li et al. 2014, Alkass, Panula et al. 2015). This hormone burst can increase cardiomyocyte numbers by up to 40% and it's not unreasonable to suggest this rapid change in cell number may result in a transient decrease in heart rate. However, the literature also disputes this sudden increase in CM numbers at this time by suggesting there is only an increase in CM ploidy rather than complete cell division (Alkass, Panula et al. 2015). Nonetheless, we have shown a clear decrease in heart rate at this time in both injured and non-injured models. This novel finding would benefit from being revisited in another study using longitudinal neonate MRI from P1 for at least a month and correlating cell cycling with hormonal measurements and other cell activity.

Ejection fraction

The high ejection fraction of the P1 mouse heart, 71.9 ± 2.2%, is another novel finding of this study. Falling to 64.5 ± 6.5% after 4 days, it continued to drop to the expected adult value of approximately 60% after two weeks. This differed from the P7 cohort, which was at this adult value from the first scan onwards. The results for the P7 cohort matched an earlier study which did not observe any change in EF with physiological growth (Wiesmann, Ruff et al. 2000). Other rodent studies found that the EF increased in the first 4 days, briefly decreased at day 7 and then

increased to the adult value gradually over 21 days.(Wu and Wu 2009) – this was done in rats and the animals were only anaesthetised and scanned once and then sacrificed.

This study of the developing functional parameters of the neonatal mouse pup heart during its first month of life has raised some very interesting and novel findings which could provide insight to the significant physiological changes that are occurring during this critical time, as well as the effect of prolonged early anaesthesia on cardiac development and function. This illustrates the value in our experimental model which allows imaging of very early timepoints so we may capture and analyse these initial events.

3.4.2 CARDIAC FUNCTIONAL PARAMETERS AFTER MI INJURY OR SHAM SURGERY IN THE P1 VS P7 NEONATAL MOUSE:

The EDV and ESV of the P7 injury cohort was larger than the age-matched shams at every timepoint of the study, including at the first measurement 4 days post injury. This suggests ventricular remodelling (here it is increased dilation) in an attempt to compensate for the damage sustained to the heart from this infarction injury. With our model of neonate MRI, we can see the evolution of the injury in the P7 cohort while the P1 cohort does not differ significantly at the end point and there was also no difference immediately after injury. EF was maintained at the level of approximately 60%, as previously reported in the literature for neonatal mice. The heart physiologically compensates for damage to maintain the vital parameter of SV for as long as possible. As discussed at length above, the HR unexpectedly appears as a sinusoidal curve with a "low point" around P14-15 for both P1 and P7 age groups and also for both injury and sham pups. And finally, the LVM/BM response for the P7 injury group is increased over the P7 sham group probably due to oedema in the first days after the surgical damage. It then drops as cardiomyocytes are lost and the infarct area thins. The P1 injury group shows an increase in line with the P1 shams.

3.4.3 LONGITUDINAL IMAGING AND FUNCTIONAL ANALYSIS OF NEONATAL MICE AFTER INJURY OR SHAM FOR P1 VS P7

The non-invasive nature of MRI facilitated one of the most valuable results of this project - the ability to monitor the same animal repeatedly over an extended period of time and follow the

development of the damage and malfunction or see recovery after injury as it happens week by week. The enlarged ventricles at diastole and reduced contraction at maximum systole of the P7 injury group are clear indications of cardiac remodelling in an attempt to compensate for the damaged non-contractile area of myocardium that has been permanently weakened and scarred. This is not observed for the P1 injury group where both EDV and ESV remain in line with those of the shams but with a possible small increase at the very end of the study. This shows that even at Day 21, regeneration may not be 100% complete as some previous histological studies indicate, but that a small degree of damage still remains for some individuals (Konfino, Landa et al. 2015). This may be due to variation of initial injury size, with the larger infarcts having the greater impact on regeneration times. This may have fully resolved had the study continued monitoring the animals past three weeks, but unfortunately we were unable to do this at this time due to project licence limitations.

Longitudinal MRI with full recovery has not been reported for any mice as young as one day after birth prior to this work, and the results conclusively define that there is indeed a regenerative window for young mammals and indicate this is over after seven days. Building on this, any number of therapies or interventions may be tested to limit the regenerative ability of the P1 group or, more importantly, enhance that of the older P7 group.

3.5 FUTURE WORK

Although this work was performed a few years ago, the further development of this experimental technique was delayed due to the move of Professor Schneider's research group to a new Clinical Imaging facility at the University of Leeds and the difficulties with the pandemic lockdowns. These results were first presented at a conference in 2019 after publication of the paper in 2018 and again recently in October 2022, where future work to progress this procedure was discussed. Despite the successful results of this study with the novel adaptations of MRI techniques to scan very small hearts, there were some issues raised that need to be addressed to make this process more accessible to other researchers and suitable for routine use in the lab and clinic. One major issue was the post-scanning analysis which was very time-consuming and required a high level of training. Also, increased scanning speed, higher scan resolution and the ability to quantify extent of injury during the scan would be valuable. Additional hardware development including an electrode to derive ECG signals directly from very small organisms, more advanced use of

respiratory signals and better fitting MRI cradles would be beneficial. A grant proposal was submitted to the BHF in 2022 to address these concerns (notes from the application are listed in Appendix 3).

CHAPTER 4
(Research Chapter 2)
Fucci & pHLIP Slices

FURTHER INVESTIGATIONS OF THE MOUSE MYOCARDIUM DURING THE REGENERATIVE WINDOW: LOCALISING AREAS OF CELL CYCLE ACTIVITY AND ACIDITY DURING DEVELOPMENT AND INJURY

ABSTRACT

The neonatal mouse heart exhibits a unique regenerative capacity during the first week of life, with injury at postnatal day 1 (P1) leading to functional recovery, while injury at P7 results in permanent scarring and reduced cardiac function. This study aimed to investigate two key aspects of heart development and injury response during this regenerative window: (1) spatial and temporal variations in cell cycle activity and (2) the presence of acidic niches in the myocardium. Using the Fucci2 (Fluorescent Ubiquitin Cell Cycle Indicator) mouse model, which enables visualisation of cell cycle phases via two oscillating fluorescent markers, we mapped cell cycling activity across 21 regions of the heart at P5 and P11 following myocardial infarction (MI) or sham surgery at P1 and P7. Additionally, we used pHLIP (pH Low Insertion Peptide), a novel peptide marker for acidic tissue, to identify regions of acidity in developing mouse hearts (P1, P7, P21 and adult) and adult rat hearts after cryoinfarct injury.

Fucci imaging revealed significantly higher cell cycling activity in P5 compared to P11 hearts post-MI, with P1-injured hearts showing widespread activation across the left ventricle and interventricular septum (IVS). In contrast, P7-injured hearts exhibited less cell cycle activity overall, with small changes seen primarily in the IVS and right ventricle. pHLIP imaging demonstrated distinct acidic niches in the endocardial regions and atria of P1 and P7 hearts, which had largely dissipated by P21 and were absent in adult hearts. In adult rat hearts, cryoinfarct injury induced an initial diffuse response across the entire myocardium, including the epicardium and atria, which later localised to label acidity at the damaged myocardium. This correlated with reduced expression of contractile proteins such as Crip2 and Tnnt2.

This study provides novel insights into cell cycle activity and extracellular acidity across the myocardium during development and after injury, and establishes pHLIP as a valuable tool for investigating tissue acidity in cardiac development and disease. Future work integrating hypoxia markers and advanced imaging techniques could further elucidate the mechanisms underlying heart regeneration and repair.

4.1 INTRODUCTION AND BACKGROUND

Having demonstrated the regenerative capacity of the P1 neonatal mouse heart and the existence of a one-week long regenerative window, we wanted to explore some aspects of the differences between P1 and P7 hearts that may be involved in the different results after injury at these timepoints. We were interested in possible reasons for why P1 could regenerate and recover complete (or nearly complete) cardiac function and P7 injury ends in permanently reduced heart function. As outlined previously, many factors change, some dramatically, during this first week of life. While this is an intense area of research, we chose to focus on identifying regions of cell cycling over the whole heart, rather than just at the site of injury, four days after myocardial infarction injury at P1 and P7. In addition, we monitored regions of acidity in the developing and injured rodent heart using a small peptide pH marker from the cancer research field to see if we could identify any differences that may also contribute to the changes in regenerative potential.

4.1.1 CELL PROLIFERATION IN THE DEVELOPING AND REGENERATING MAMMALIAN HEART

From previous studies of the regenerating zebrafish heart, it has been determined that the majority of new cardiomyocytes that contribute to repair after injury are derived from pre-existing cardiomyocytes rather than some other stem cell or progenitor pool, either endogenous or recruited from elsewhere in the body (Jopling, Sleep et al. 2010, Leone, Magadum et al. 2015, Foglia and Poss 2016, Galdos, Guo et al. 2017). Also, for the normal growth and development of the fish heart, it was this division of existing cardiomyocytes that made up the final number of beating cells. Similarly, in mammals, myocyte proliferation is believed to underlie regeneration of injured neonatal mouse hearts, where new cardiomyocytes are generated by cell division of existing cardiomyocytes, rather than alternative sources such as differentiation of resident or incoming stem cells (i.e. originating from blood-borne bone marrow stem cells) or trans-differentiation of another resident cardiac cell population (i.e. epicardial cells, endothelial cells or fibroblasts) (Riley and Smart 2011, Smart, Bollini et al. 2011, Simoes and Riley 2018, Gladka, Johansen et al. 2023).

However, some of these resident or infiltrating cell populations may contribute to the division of existing cardiomyocytes by providing paracrine signals (Bargehr, Ong et al. 2019, Huang, Huang et al. 2023). Epicardial cells can differentiate into various cell types including fibroblasts, smooth muscle cells and endothelial cells, all of which are essential for tissue repair. They also secrete

paracrine factors and support regeneration by reactivating developmental pathways. Endothelial cells contribute to neovascularisation after injury, increasing vessel density in the border zone to enhance perfusion and limit further cardiomyocyte loss. They also regulate inflammatory cell recruitment and can transition into mesenchymal cells to support vessel maturation. Pericytes stabilise and help mature new blood vessels during angiogenesis. They can also contribute to fibrosis and may potentially, in limited cases, generate new cardiomyocytes. Fibroblasts proliferate and convert into myofibroblasts post-MI, producing extracellular matrix to form a collagen scar that maintains heart integrity. They also phagocytose apoptotic cells, modulate inflammation, and interact with other cells to promote angiogenesis and repair. In addition, resident immune cells such as macrophages play critical roles in clearing necrotic cells, recruiting inflammatory cells, and supporting angiogenesis. They also have an important role in scar formation and resolution and are involved with cardiomyocyte regeneration. These integrated actions ensure progression from inflammation to scar formation in adults or regeneration in neonates, maintaining heart function after injury (Riley and Smart 2011, Smart, Bollini et al. 2011, Gray, Toor et al. 2018, Simoes, Cahill et al. 2020, Simoes and Riley 2022).

We hypothesised that there may be a difference in the number, type and/or location of proliferating cell populations in regenerative P1 versus reparative P7 injury settings. As far as we were aware, an attempt to comprehensively map this across the neonatal heart had not been undertaken, and we decided it would be a useful exercise to map the spatio-temporal changes in cycling cardiomyocytes in the first instance, and then to also investigate other cell populations within the heart such as fibroblasts, endothelial cells and the migrating cells from the epicardium.

4.1.2 FUCCI MOUSE MODEL TO VISUALISE CELL CYCLING IN THE MYOCARDIUM

The Fucci (Fluorescent Ubiquitin Cell Cycle Indicator) strain of mice enables study of cell cycle phases by real-time imaging of live cells in culture (studied in Chapter 5) or fixed cells in sections of heart tissue. Nuclei in these mice emit red (mCherry, in G1) or green (mVenus, in S/G2/M) fluorescence (Sakaue-Sawano, Kurokawa et al. 2008, Sakaue-Sawano, Ohtawa et al. 2008, Sakaue-Sawano, Hoshida et al. 2013). For a brief time, at the transition from the G1 to the S phase of the cell cycle, these emissions overlap and a yellow nucleus may be seen. Cells that are not actively cycling, i.e. quiescent or senescent, will be non-fluorescent. This is illustrated in the inner circle of

Figure 39 which compares the colours expressed by Fucci cells during cell cycling with those from a range of other markers (Easwaran, Leonhardt et al. 2005, Alvarez, Wang et al. 2019):

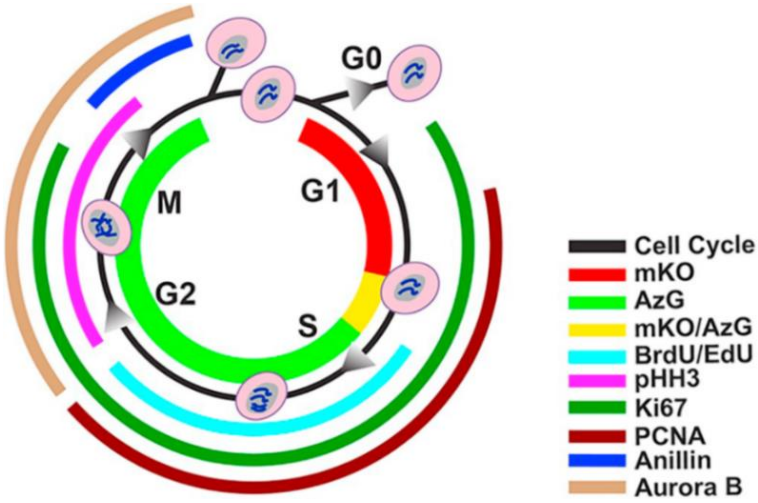

Figure 39: Markers of cell cycle division and status: Fucci fluorescence mKO (red) presents in G1 phase, and AzG (green) presents during S/G2/M phases, where during the G1/S transition both fluorescence (mKO/AzG) present simultaneously and merge into a yellow colour. BrdU or Edu, both thymidine analogues incorporate into DNA during synthesis (cyan). Phosphorylated Histone 3 (pHH3) is responsible for chromatin condensation and is thus present during G2 through M phase (magenta). Nuclear antigen Ki67 is present from G1 to M phase (emerald). PCNA is present between G1 and G2 phase in response to DNA synthesis (burgundy). Anillin plays a role in creating the cleavage furrow formation and begins to accumulate in late G2 through late M phase (blue). Aurora B plays a role in mitosis, present from G2 through M phase (sand). From *"*Cardiomyocyte cell cycle dynamics and proliferation revealed through cardiac-specific transgenesis of fluorescent ubiquitinated cell cycle indicator (Fucci)*"* (Alvarez, Wang et al. 2019).

How Fucci works

The cell cycle is predominantly regulated by transcriptional control of cyclin genes and post-translational mechanisms of cyclin-dependent kinases and inhibitors (Gavet and Pines 2010), but another important factor is ubiquitin-mediated proteolysis of key proteins. APC/C (Anaphase Promoting Complex/Cyclosome) and SCF (Skp-Cullin-F-box) are two related multi-subunit protein complexes that catalyse the ubiquitination of proteins destined for proteasomal degradation. Primarily, APC/C promotes the onset of anaphase at the mitotic check point by marking securin (a protein that holds sister chromatids together) with ubiquitin, leading to its destruction by the proteasome and triggering separation of the chromosomes by the enzyme separase. It also targets cyclins A and B, thereby inactivating most cyclin-dependent kinases which then leads to dephosphorylation of other cell cycle proteins (including Geminin which is important for the Fucci mechanism as detailed below) and results in the completion of M phase. APC/C remains active during G1, keeping cyclin levels low until the start of the next division cycle. At that time, the second complex, SCF, is activated. It marks some G1 regulatory proteins and also some cyclin-Cdk inhibitors (CKIs) for destruction which allows for activation of S-Cdk and the

start of DNA replication (Peters 1998). Regulation of APC/C activity is dependent on association with two subunits – Cdc20 in mid-mitosis and then Cdh1 from late-mitosis through to G1. SCF is both a direct substrate of, and also a feedback inhibitor of, APC and these two complexes alternate reciprocally throughout the cell cycle.

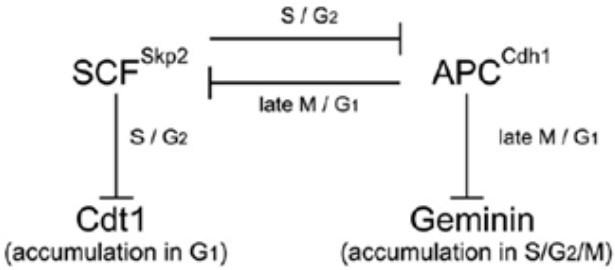

Figure 40: Cell-cycle regulation by SCF-Skp2 and APC-Cdh1 maintains bi-stability between G1 and S/G2/M phases. From "Visualizing spatiotemporal dynamics of multicellular cell-cycle progression" (Sakaue-Sawano, Kurokawa et al. 2008).

Fucci technology is based on the ubiquitin-mediated proteolysis of two antiphase oscillating proteins that regulate the mammalian cell cycle: Cdt1 and Geminin. Cdt1 is a protein associated with the ORC (Origin Recognition Complex) which is assembled at various locations on the DNA molecule and is involved with licensing the start of DNA replication once during the cell cycle. It accumulates in the nucleus from late mitosis to the end of G1, at which point it is either marked for destruction by the SCF complex or bound and inhibited by geminin. This allows the ORC to release the DNA helicases in both directions of the DNA strand at the start of S phase and initiate DNA replication. Geminin is a Cdt1 inhibitor which accumulates during S/G2/M phases preventing another round of DNA duplication, and it is destroyed by APC/C in late mitosis. This allows Cdt1 to build up again and restart the cycle (Caillat and Perrakis 2012, Alberts 2015).

Development of Fucci mouse models

The first Fucci probes were based on the CAG promotor and emitted orange (mKO2 - monomeric Kusabira Orange 2) and green (mAzG – monomeric Azami Green) fluorescence during G1 and S/G2/M cell cycle phases respectively. mKO2 was fused to the ubiquitylation domain of human Cdt1 hCdt1 (30/120) and mAG was fused to human Geminin hGem (1/110). The CAG promotor is not uniformly expressed in all tissues, and it was tricky to maintain both probes independently. This model was replaced by the Fucci2 probes which emit brighter, more contrasting red (mCherry) and green (mVenus) signals which are based on the Rosa26 promotor (Figure 41). This R26p-Fucci2 line also has both phase probes on the same transgene to guarantee co-inheritance

and is more uniformly expressed in almost all body tissues (Abe, Sakaue-Sawano et al. 2013). Using the Fucci2 mouse model, we can determine where exactly cell cycling activity is occurring and co-staining will help determine which cell types are involved.

An interesting addition to the Fucci model systems is the development of the Fucci-Tg mouse which expresses Fucci in cardiomyocytes only, driven by the α-MHC (α-Myosin Heavy Chain) promoter. This model was shown by immunostaining and Western Blotting to express mKO2 and AG only in heart tissue and not lung, liver, spleen, stomach or bladder. Within slices of heart, co-staining with tropomyosin (CM), von Willebrand Factor (endothelial) and vimentin (fibroblast) markers confirmed CM specificity. Very interestingly, they showed that mature cardiomyocytes expressed both mKO2 and AzG, remaining poised at the G1/S transition phase rather than undergoing a full mitotic exit (Alvarez, Wang et al. 2019).

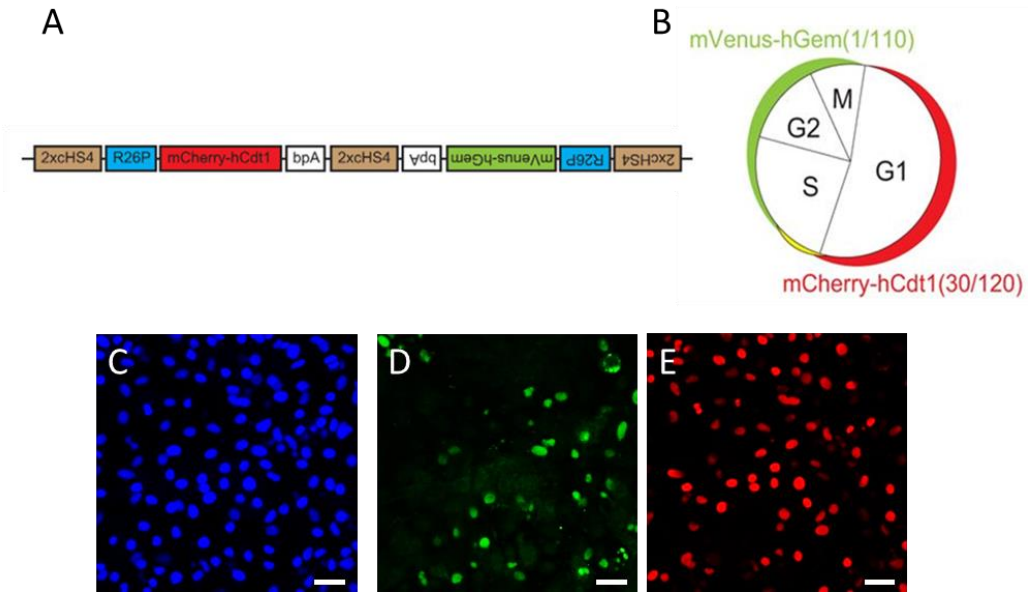

Figure 41: (A) The Fucci2 fluorescent probes, mCherry-hCdt1 and mVenus-hGem, on the Rosa26 promotor. (B) Red mCherry signal is visible in nuclei in the G1 phase while green mVenus signal is present during S, G2 and early M phases. A brief overlap of these signal is present at the start of S phase as shown by the yellow signal. Finally, there is a period of no fluorescence at the end of mitosis when the nuclear membrane has been broken down and just before Cdt1 begins to accumulate again at the start of the next cycle. (C-E) Red and green fluorescent nuclei in a slice of P1 Fucci2 mouse heart tissue visualised by 3-channel imaging; All nuclei are stained with blue DAPI for visualisation. Scale bar = 50μm.

4.1.3 INVESTIGATING AREAS OF ACIDITY IN DEVELOPING AND INJURED HEARTS USING PHLIP LABELLING TECHNOLOGY

This research chapter will also test a marker for acidic tissue, pHLIP, in mice of different ages. Developed for the cancer research field where it is used to label acidic lymph nodes and the core of solid tumours, I believe this was the first time it was used in the context of heart development and regeneration. We aimed to see differences in the location and extent of acidic regions as the heart matures from P1 to adulthood, to provide further insights into the closing of the regenerative window. Acidic tissue has also been reported after injury or disease and we wanted to test pHLIP labelling in a rat heart cryoinfarction model.

What is pHLIP?

pHLIP is a short peptide (22-37 amino acids) derived from bacteriorhodopsin C with two new end sequences attached. At neutral and high pH (low acidity), it exists in an aqueous solution or very loosely bound to the surface of a lipid bilayer. In a low pH (high acidity) environment, the peptide quickly inserts into any nearby membrane with very high affinity. This is accomplished by the protonation of two aspartic acid residues within the central transmembrane region of the peptide which makes it more hydrophobic. This triggers the folding into an α-helix configuration and subsequent insertion into the membrane, with the C-terminus of the peptide entering the cell, while the N-terminus remains outside along the surface (Hunt, Rath et al. 1997). The pHLIP association with membranes at low pH (≤5.0) is approximately 20x that at high pH (≥8.0). This process is very stable and does not seem to harm the cell in any way, normal physiological processes continue unchanged ((Andreev, Dupuy et al. 2007, Andreev, Engelman et al. 2009, Anderson, Moshnikova et al. 2016). If a target drug is attached to the pHLIP C-terminus, in acidic regions the peptide can act as a "nano-syringe" and inject the drug into the underlying membrane - this has been exploited to deliver otherwise cell-impermeable cargo into a cell ((Andreev, Engelman et al. 2009, Andreev, Engelman et al. 2014, DuPont, Visca et al. 2022). For imaging, fluorescent markers may also be attached to either end of the pHLIP molecule (Shan 2004, Macholl, Morrison et al. 2012, Wyatt, Moshnikova et al. 2018).

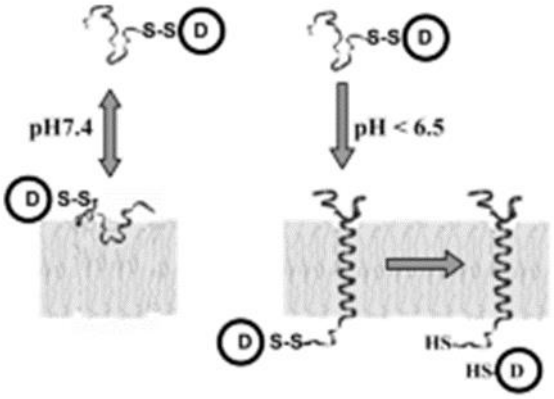

Figure 42: Insertion of pHLIP across a biological membrane. At pH > 7.0 - 7.2, pHLIP sits loosely on lipid bilayer surface; at pH < 7.0 - 6.5, it inserts into the membrane. From Reshetnyak et.al Translocation of molecules into cells by pH-dependent insertion of a transmembrane helix (Reshetnyak, Andreev et al. 2006).

Acidity in development

Acidic and hypoxic niches are a normal part of mammalian development and are assumed to be present in the early stages of heart formation and maturation. Embryonic and foetal hypoxia has been studied extensively (Compernolle, Brusselmans et al. 2003, Semenza 2007, Menendez-Montes, Escobar et al. 2016), but acidity during these time periods is less well researched. Although they often coexist and may be closely linked, hypoxia and acidity have different effects on cell function and organ development as well as operating via different molecular pathways. A defining factor in the growth of the heart is the development of the coronary vasculature, both for distribution of nutrients and oxygen and for clearance of waste products such as excess acids extruded from metabolically active cardiomyocytes (Sharma, Chang et al. 2017, Majesky 2018, Lupu, De Val et al. 2020). During the mid-gestation stage, coronary vessels form an initial vascular plexus covering the outer surface of the heart, which is extensively remodelled until birth. At this time, the heart muscle has areas of more mature compact myocardium with an established blood vessel network on the outer portions of the heart, with an inner layer of trabecular myocardium facing and lining the ventricles. This region of trabecular myocardium remains less vascularised than the outer areas, instead utilising finger-like projections directly into the ventricle for nutrient and gas exchange with the encompassed blood (Daiou, Petalidou et al. 2022). Postnatal growth of the heart involves compaction of this trabecular layer with formation of a new subset of coronary vessels to supply the endocardial regions. These new vessels are thought to originate from trapped endocardial cells which go on to form the vascular endothelial cells of the blood vessel walls (Tian, Hu et al. 2014, Fukuda, Aharonov et al. 2019). During the neonatal period, this network expands

three- to four-fold, mostly by contribution from the endocardium, and continues to develop with more new vessels forming until the fully mature adult coronary vasculature is established.

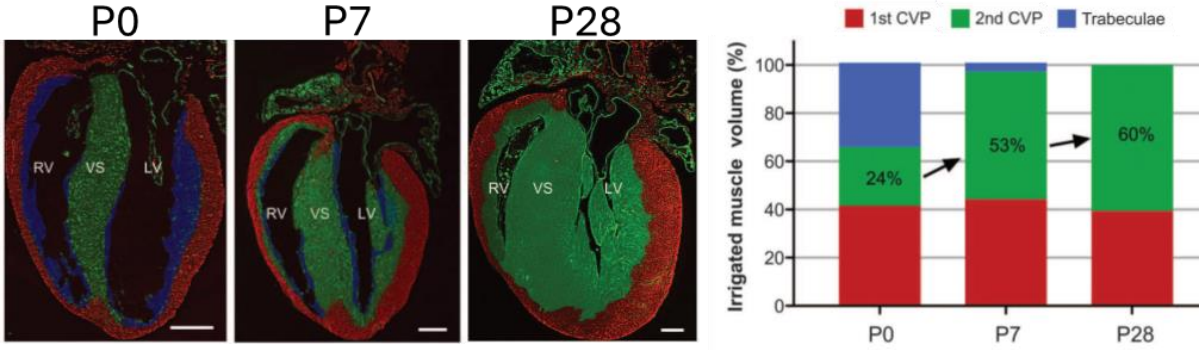

Figure 43: Compaction of the inner ventricular area of a developing mouse heart. Two distinct coronary vascular plexi (CVP) form as the trabeculated endocardial region (labelled here in blue) condenses to form the second CVP. Adapted from "Vessel formation. De novo formation of a distinct coronary vascular population in neonatal heart" (Tian, Hu et al. 2014).

Acidity in disease

It has been known for some time that tissues can have elevated levels of extracellular acidity in certain pathological states such as cancer, stroke, inflammation (Andreev, Dupuy et al. 2007, Andreev, Engelman et al. 2009, Vavere, Biddlecombe et al. 2009) and ischaemia, including myocardial ischaemia (Garlick, Radda et al. 1979, Cobbe and Poole-Wilson 1980, Sosunov, Anyukhovsky et al. 2013). In many of these cases, there are co-morbidities such as low blood supply and hypoxia, leading to a change in cell metabolism to favour anaerobic glycolysis. This increases the production of acidic protons from carbonic and lactic acids which need to be extruded from the cell by transmembrane protein pumps to maintain normal physiological functions within the cell. Unlike healthy tissue, reduced blood circulation around diseased tissues allows these acidic protons to accumulate, thus dropping the local pH just outside the cell membranes (extracellular pH) to a lower value than the intracellular pH (Gerweck and Seetharaman 1996, Andreev, Engelman et al. 2014). In hypertrophic disease conditions, myocardial tissue reverts to a more foetal metabolic profile characterised by increased glucose use and decreased fatty acid oxidation, potentially as a mechanism to improve oxygen efficiency for ATP synthesis which is important in an ischaemic environment (Kolwicz, Purohit et al. 2013). Specifically, acidic regions appear after myocardial infarction injury in an adult heart due to an increase in anaerobic respiration and reduced vascular clearance in the damaged tissue (Garlick, Radda et al. 1979, Kemi, Arbo et al. 2006).

pHLIP in the heart and other organs

After injection, pHLIP circulates through the bloodstream to reach most body tissues including the heart. By using pHLIP labelled with a fluorescent probe, Sosunov et.al. showed that ischaemic heart tissue damaged after MI induced by LAD ligation could be targeted in vivo and imaged directly, thereby showing the potential for pHLIP to transport therapeutic drugs or small molecules specifically to this area (Sosunov, Anyukhovsky et al. 2013). It accumulates in the kidney, marking the renal cortex area as acidic due to the metabolism of small proteins which release acid byproducts into the local extracellular environment (Andreev, Dupuy et al. 2007). A recent study using pHLIP to study acidic stroke lesions implies it can cross the blood-brain barrier (Ye, Jo et al. 2024). It does not accumulate to any significant level in tissues such as liver or lung, therefore we chose to collect kidney tissue as the control for our new heart developmental study.

Acidity and Contractile proteins in the heart

Muscle contraction is highly sensitive to cytoplasmic pH, with low pH levels limiting contraction by reducing Ca^{+2} binding to troponin and also affecting electrical signalling in the CM sarcolemma (Vaughan-Jones, Spitzer et al. 2009). It has also been shown that low pH is a limiting factor in the formation of the contractile proteins which provide the pumping action of the heart. (Cobbe and Poole-Wilson 1980, Kemi, Arbo et al. 2006). A study in our lab determined that alkaline conditions were conducive to expression of contractile genes with transcriptomics noting striated muscle contraction as having a highly ranked GO term in response to acidic conditions. This was confirmed by proteomics, and amongst other contractile proteins, the scaffolding protein Crip2 was identified as one that was reduced in an acidic environment (Hulikova, Park et al. 2022). In monolayer cultures of NRVMs, we saw that Crip2 and troponin staining was reduced in acidic media of pH 6.4 over alkaline media of pH 7.4 (see Figure 74 later in this chapter), and we wanted to use pHLIP to see if areas of acidic myocardium had less contractile proteins than undamaged areas after cryoinfarct injury in adult rat hearts. We also wanted to look at the distribution of contractile proteins in the developing mouse heart.

4.2 AIMS

In this chapter we examined two aspects of the developmental changes that occur during the first week after birth: (1) changes in cell cycle activity across the entire heart and (2) changes in the

extracellular environment of the cardiac tissue in terms of acidity and hypoxia. Since these aspects may be affected by ischaemic injury, we wanted to investigate how neonatal hearts responded after MI surgery.

Aim 1: Areas of cell cycle activity in P1 vs P7 injured or sham hearts

Using the Fucci2 mouse model, we wanted to characterise the areas of cell cycle activity in neonate hearts after MI or sham surgery to determine if there is a difference between the younger (P1) regenerative hearts and the older (P7) reparative hearts. We thought there might be differences not only in the number of dividing cells, especially cardiomyocytes, but also their location within the heart itself. *Note that due to Covid limitations, the additional experiments in this chapter to determine cell type by immunofluorescent co-staining with specific cell markers had to be abandoned.*

Aim 2: Map areas of acidity and hypoxia in the developing mouse heart and after cryoinfarct injury in adult rats

Using the novel marker, pHLIP, we wanted to see if it could be used to show that there were areas of acidity in heart tissue during development and also in adult heart tissue after ischaemic injury. We aimed to use pHLIP in conjunction with pimodiazole which is a known marker for hypoxia, to see if regions of hypoxia and acidity coincided. *Again, due to Covid restrictions, the hypoxia experiments in this chapter had to be abandoned.*

4.3 METHOD DEVELOPMENT AND RESULTS

4.3.1 EXPERIMENTAL DESIGN (Part 1): INVESTIGATING AREAS OF CELL CYCLE ACTIVITY USING THE FUCCI MOUSE MODEL DURING DEVELOPMENT AND AFTER MI SURGERY

To quantify proliferating cell populations through the regenerative window in intact and injured neonatal mice, the experimental design was planned as illustrated in Figure 44 below. The tissue harvest point of four days post injury/sham was chosen here to match the first MRI scan after injury in the previous study. This is when the mouse has recovered from the initial acute affects of surgery and it has been shown to be the peak of the inflammatory response (Simoes and Riley 2022). It is also the time when the injured ventricle wall is most prone to rupture in the adult

mouse model of MI (Nahrendorf, Swirski et al. 2007). There were 4 groups of mice: P1-MI, P1-sham, P7-MI, P7-sham as for the MRI experiments. After 4 days the animals were sacrificed and hearts harvested and prepared for IF staining.

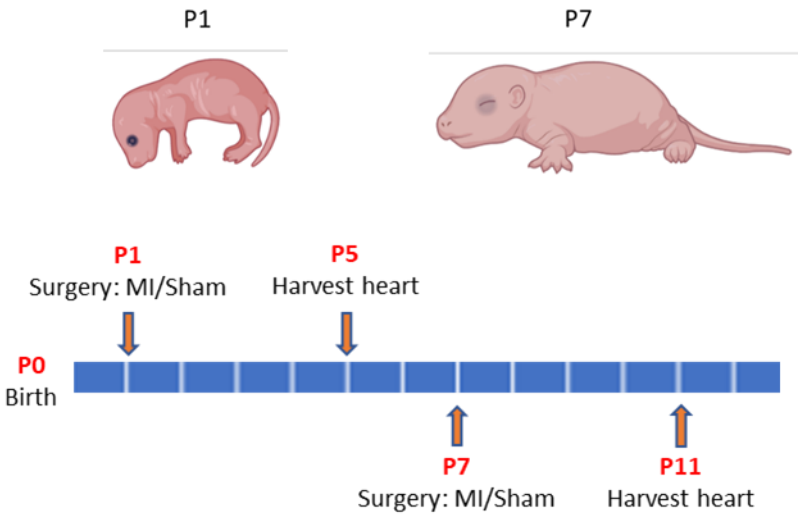

Figure 44: Experimental design for detecting areas of cell cycling activity and differences between P1 and P7 four days after injury. Slices of heart tissue were collected at P5 and P11 from the injury and sham groups. Cycling cells were counted in situ by imaging the red and green Fucci cell cycle indicators.

The Fucci mouse model clearly shows cells that are actively cycling, that is in S, G2 or M phase, with green nuclei, and those in G1 with red nuclei. Counting where these coloured nuclei appeared across a longitudinal section of a heart would give us an overview of areas of proliferating cells. All nuclei were to be stained with DAPI, and they should have inherent red or green fluorescence from the inserted Fucci gene.

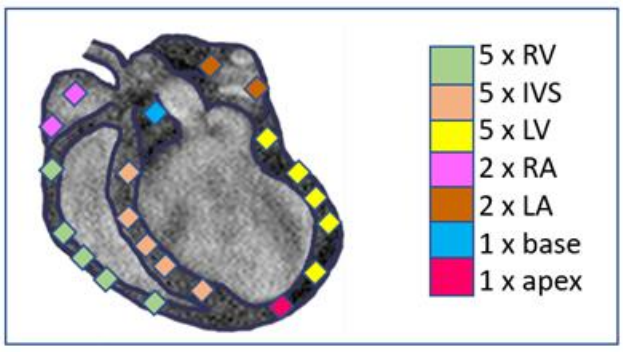

Figure 45: Areas of the heart across a long axis (four-chamber) section where the cells were to be counted. A total of 21 images were taken for each slice: 5 from each ventricle wall, 2 in each atria and one each at the base and apex. We counted 3 complete slices through the middle area of each heart, 1 through the midsection, 1 dorsal and 1 more ventral but all with 4 full chambers.

We took 5 images along the length of the right and left ventricular outside walls, as well as the intraventricular septum (Figure 45). They were chosen to be midway from base to apex, designated LVM for the Left Ventricular Middle – this was the area where the myocardial infarct injury by LAD ligation suture would be positioned; close to this point above (left ventricular upper 1, LVU1) and below (left ventricular lower 1, LVL1); and then more remote above and below the midpoint (LVU2, LVL2). Corresponding names were assigned to the five points along the RV wall and IVS. This is detailed in Figure 46 below.

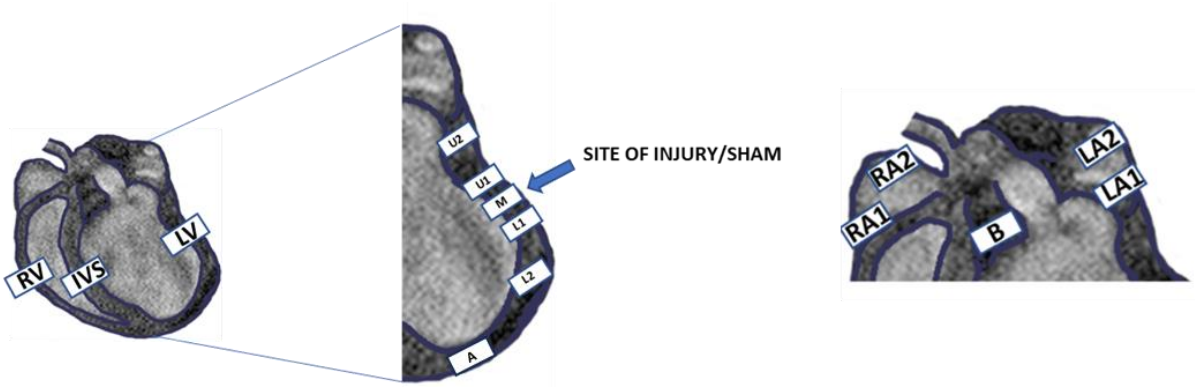

Figure 46: Labelling points along the heart walls for cell counting. The mid-ventricular section is where the permanent ligation suture is placed for the MI samples, or where the needle is passed through the heart but not ligated for the sham samples. The points immediately above and below are in the border zone of the injury, and the final two points are considered remote. There are two points in each atrium (one towards the tip and the other more midpoint) and one at the base and apex.

In addition to the ventricle walls, there were two points counted for each atrium, one on the outer tip and one more central, designated RA1 and RA2 for the right atrium, and similarly for the left. And finally, a point at the base of the heart centrally between the atria and avoiding the great vessels of the outflow tract and one at the bottom tip of the heart, the apex (also Figure 46). We wanted to check three long axis slices per heart, one through the midsection, one more dorsal and one more ventral but all within the complete four chamber view of the heart.

4.3.2 BREEDING AND GENOTYPING NEWBORN FUCCI PUPS

For these studies, Fucci pups were generated by mating Fucci positive males with wildtype CD1 females as outlined in Chapter 2 General Methods - Mice. When the pups are very young (P0 – P3) they can be easily identified as Fucci positive or negative using a bright LED light and filter system. We used a NightSea™ Dual Fluorescent Protein torch with royal blue and green LEDs for excitation of green and red fluorescent proteins respectively, and a set of barrier filter goggles

(Figure 47). The goggles reject the reflected light and transmit only the fluorescence with high contrast. While the Fucci positive pups were not bright enough to actually fluoresce green or red, they could be clearly identified by their bright silver colour when the combination of blue light with yellow goggles was used. The Fucci negative pups were, in comparison, a dull grey, almost invisible in a darkened room. The first few litters were confirmed by using PCR genotyping with tail clips (see General Methods – Genotyping and Figure 48) run with two gels for each of the mCherry and mVenus bands, but subsequent litters were done with the torch only to avoid doing unnecessary surgeries on negative mice. All pups shown as Fucci positive by this light & filter goggles method were indeed positive as shown by fluorescent cell imaging after experimental use, making this a very useful method of "instant" and non-invasive genotyping. As far as I'm aware, this was the first time that this system was used for identifying Fucci positive pups although it is used for GFP pups (which usually have a much brighter green fluorescence). Adult Fucci samples were genotyped by PCR genotyping (sample gel in Figure 48).

RB-GO – Royal Blue, Green Only	440 – 460nm	500 – 560nm bandpass
GR – Green	510 – 540nm	600nm longpass

Figure 47: The NightSea™ Dual Fluorescent Protein torch and goggles used for quick and accurate identification of Fucci positive or negative neonatal pups without the need for genotyping.

Since the pups are a cross between black Fucci+ C57 males and white wildtype CD1 females, they are born a mixture of black and white pups. Even at P1, the skin is a slightly different colour, and these need to be separated before checking genotype using the method outlined above as they show under the fluorescent torch slightly differently. On a day when four litters were born, giving a total of 54 pups, I did a tally of the outcome:

GENOTYPE	BLACK PUP	WHITE PUP	TOTAL	FATE
FUCCI (+)	13	13	26	KEEP
FUCCI (-)	22	6	28	CULL
TOTALS	35	19	54	

From the 35 "black" pups, 13 were Fucci positive (37%), while from the "white" group, 13 out of 19 (68%) were positive. While this was an interesting observation, I did not investigate it further.

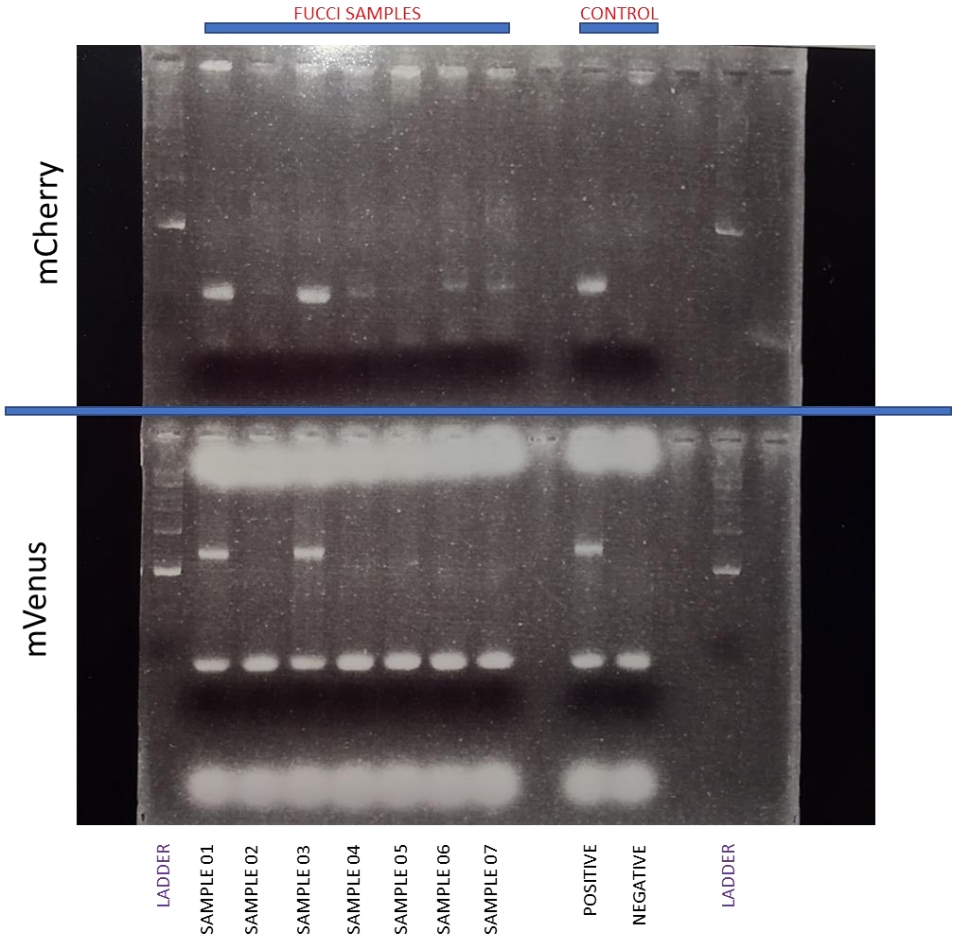

Figure 48: Sample of Fucci genotyping gel. Run with 7 Fucci pup samples (columns labelled Sample 01-07) with positive and negative controls, flanked by 2 ladders. In this Fucci litter only two pups were positive for mCherry (top half of gel) and mVenus (bottom half of gel) – samples 01 and 03. The rest (samples 02, 04, 05, 06, and 07) were negative. The primers are detailed in General Methods – Genotyping.

4.3.3 NEONATE MI SURGERY PROCEDURE FOR FUCCI PUPS

Fucci-positive pups were split into two groups: one for MI surgery, the second for sham surgery. The rest of the MI surgery procedure was as outlined in Chapter 2: General Methods – Neonate Surgery. Over the course of several litters, it was noted that pups with the Fucci transgene did not seem to be any different in their response to the MI surgery at P1 or P7 in terms of survival compared with those that were Fucci negative (some of which also underwent surgery for control/spare hearts).

4.3.4 TISSUE STAINING OF FUCCI HEARTS

Due to the inherent fluorescence of Fucci samples with two colours (red for mCherry, green for mVenus), the choice of secondary antibody stain colours for any other markers was limited. All sections were stained with DAPI to label cell nuclei (see Figure 41 and Figure 51). To enhance detection of the Fucci signal, we usually used antibodies for mCherry and mVenus or GFP. This was optional for the mCherry signal, which was very bright, but was almost always necessary for the green signal which was usually much fainter and also blended significantly with the green autofluorescence of cardiac tissue, making the green nuclei difficult to distinguish from background (see Figure 56). This was exacerbated if the Fucci samples were stored for more than a few weeks before imaging – the mVenus signal faded very quickly. The only additional imaging channel available was Far Red and this was used for all cell markers. TrueBlack staining was used to suppress or at least reduce the green autofluorescence of cardiac tissue but we found this only had limited effectiveness whilst adding extra time to the protocol and exposing the slice to more light, thus reducing the inherent signal, so we did not continue with it. The standard tissue staining protocol was followed (see General Methods – Immunofluorescent staining).

4.3.5 IMAGING OF FUCCI HEARTS

Fucci imaging was done on a Zeiss LSM 700 confocal microscope using three channels for the cell counting assay (presented in the next chapter of this thesis) (DAPI, mVenus, mCherry - Figure 49) with a fourth added if we were investigating cell type. We also imaged complete slices of Fucci hearts on a Leica DM600 upright microscope with a motorised stage and Leica CTR 600 control system which took multiple images in an X-Y plane grid and stitched them together into a composite image using Volocity software. These tiled images give an overview of the heart at high resolution which can be zoomed in to view details with good resolution if desired, unlike a lower magnification image of the whole heart (see Figure 50). The damaged myocardium at P11 after MI injury at P7 is clearly visible in the slice, with dramatic thinning of the left ventricular free wall and apex of the heart. The P5 heart after injury at P1 shows a section of torn myocardium where the suture was placed but the tissue surrounding it is still thick and healthy. Sample tiled images (that have been co-stained with vimentin or PDGFRα) are shown in Figure 50. Imaging details are outlined in General Methods – Imaging.

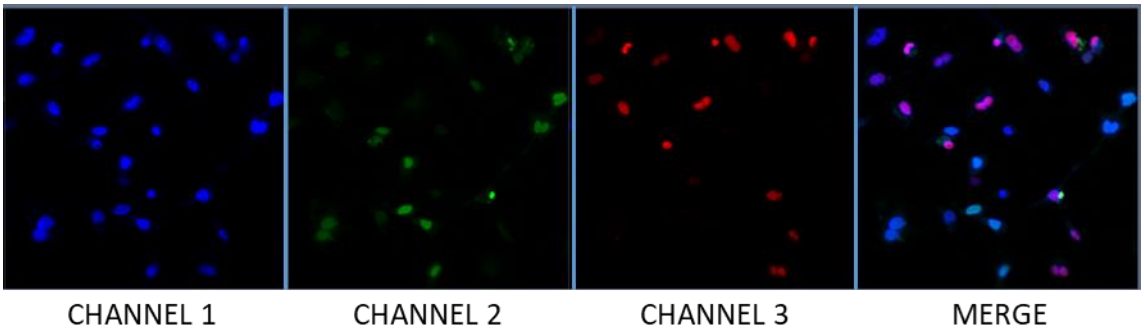

Figure 49: Confocal Fucci imaging in 3 channels (1: DAPI; 2: mVenus; 3: mCherry), with merged image. P1 section, magnification x400, zoom x2.

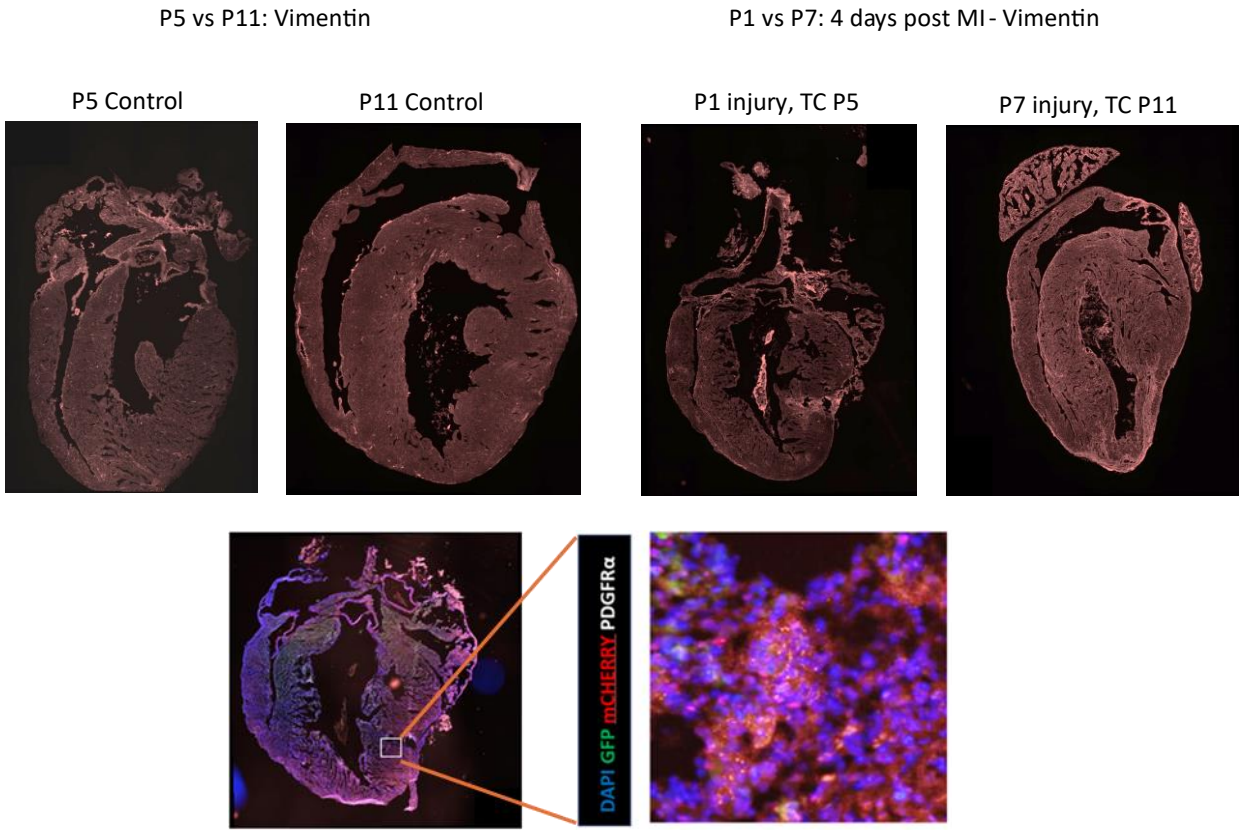

Figure 50: Tiled images of complete Fucci pup heart sections. P5 and P11 hearts are shown with and without MI surgery at P1 or P7 (TC = tissue collection). These have been co-stained with vimentin to show fibroblasts and fibrotic scar damage. Bottom row: another tiled image from the P5 injury heart slice and zoomed in area (white square) stained with PDGFRα showing cellular resolution. Note these images are not to scale.

4.3.6 FUCCI IN NEONATAL HEARTS

To establish a protocol for consistent imaging of Fucci in neonatal hearts, the hearts were prepared using our standard protocol and co-stained with DAPI. The first images of Fucci labelled cell nuclei in our neonatal mouse heart are shown in Figure 51 below. As this was very fresh tissue,

the red and green nuclei are clearly visible and non-overlapping, with almost all cell nuclei fluorescing with one or the other indicator.

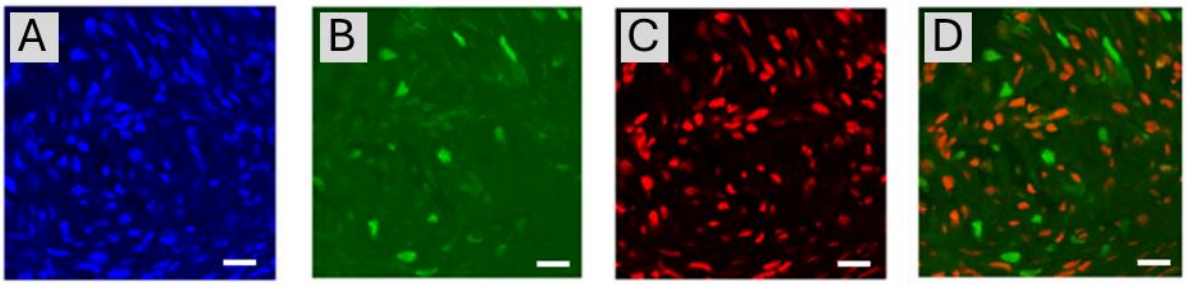

Figure 51: Preliminary 3 channel confocal images of a P5 uninjured Fucci2 mouse heart section without any additional antibody staining other than a DAPI nuclear stain (blue) shown in (A). The green S/G2/M (B) and red G1 (C) cells are clearly visible, with the two combined Fucci fluorescences overlayed in (D). Scale bar = 50µm.

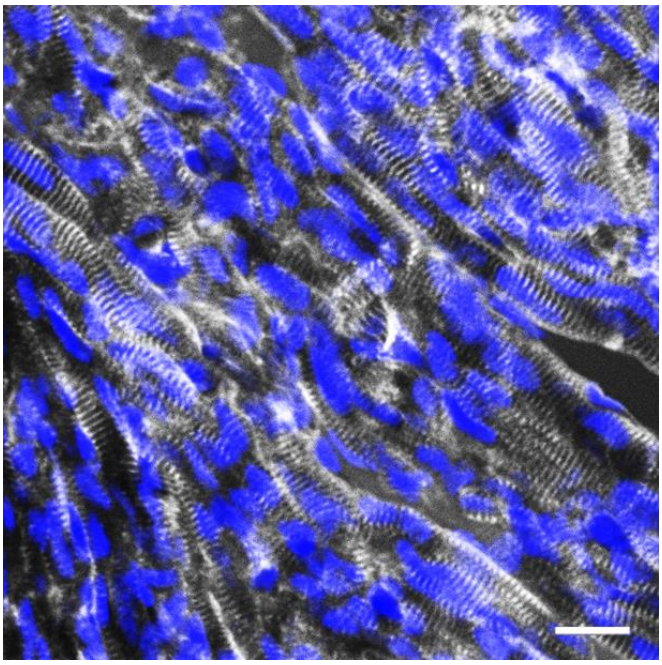

Figure 52: A slice of P5 mouse myocardium stained with a-Actinin (sarcomere labelling in grey) and DAPI (nuclei in blue) showing the arrangement of cardiomyocytes within the tissue. Scale bar = 50µm.

Staining the cardiomyocytes in a P5 heart (Figure 52) showed that the nuclei varied in size, shape and orientation. It was clear that manually counting the nuclei in all these cells would be laborious (see Figure 53), so we wanted to automate the process as much as possible. Several attempts were made to use existing cell counting modules either written for ImageJ or with some modifications to our in-house Matlab macros. Unfortunately, because of the non-circular and irregular nature of the cardiomyocyte nuclei, mostly due to variable cell orientation within the slice (Figure 52), this was not as straightforward as we had hoped. I manually counted cells for a few sample images

(Figure 53) to provide a control for various automated counting paradigms but none proved satisfactory, so we decided to use a more involved method of "semi-automated" counting using standard modules available in Image J (Figure 54).

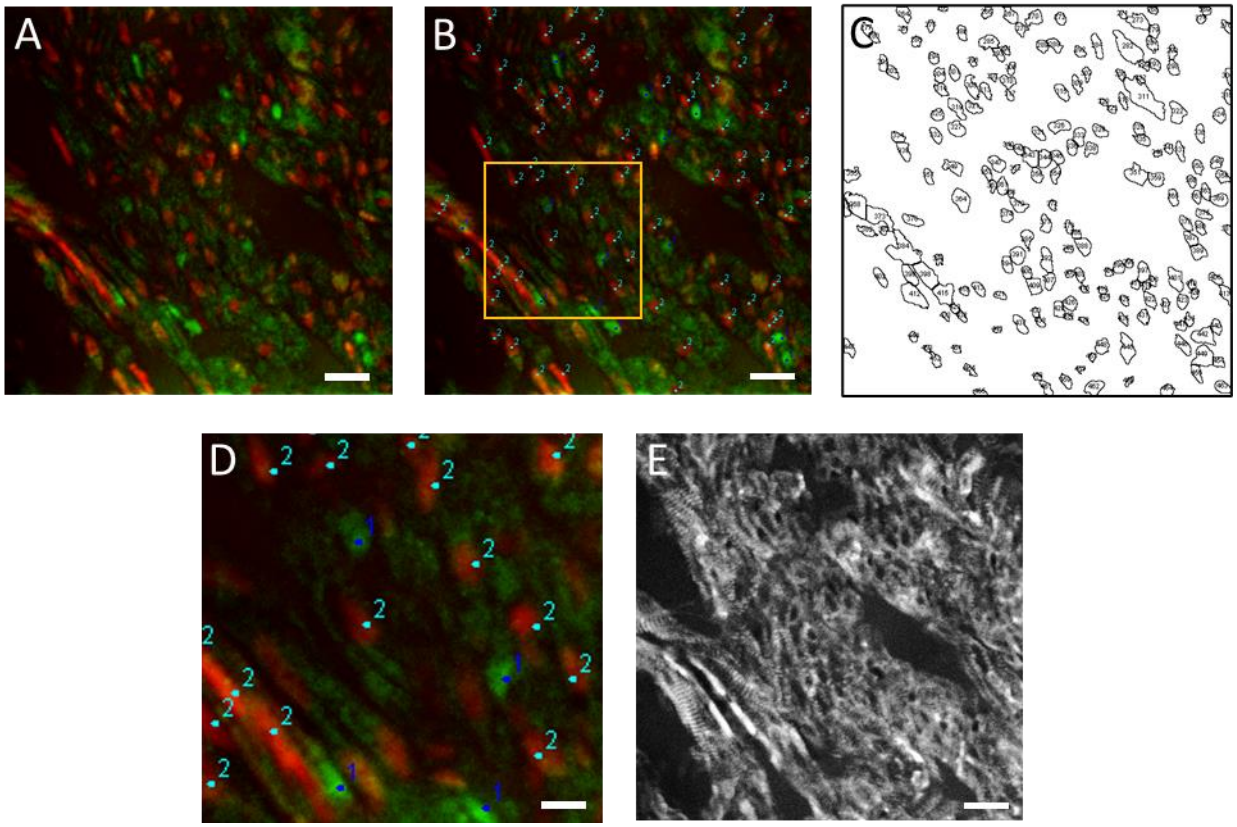

Figure 53: Manual cell counting of red and green cardiomyocyte nuclei. (A) Original image; (B) Manually marked green nuclei S/G2/M labelled "1"; red nuclei G1 labelled "2"; (C) ImageJ macro used to outline all nuclei using DAPI staining (not shown) as a mask; (D) close up of labelled nuclei in yellow box from (B); (E) α-actinin stain (grey) to show cardiomyocytes, the small "holes" are where the nuclei are located. Scale bars for A, B, C, E = 50μm; D = 15 μm.

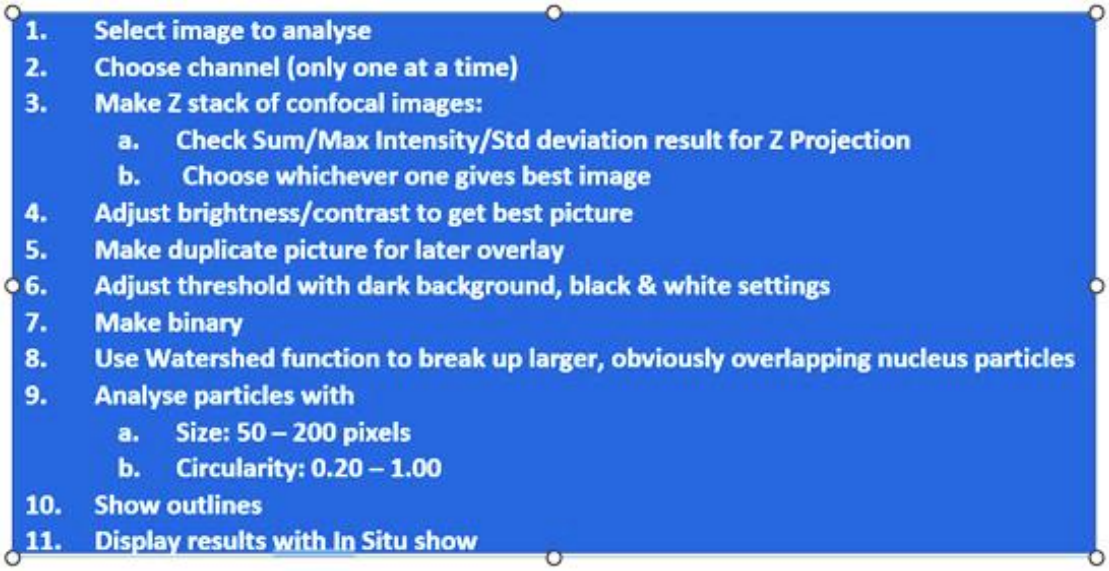

Figure 54: Protocol of "Semi-automated" cell nuclei counting using standard ImageJ modules.

This protocol generated outlined images as shown in Figure 55. These were overlaid with the duplicate optimised picture from Step 5 and any obvious missing nuclei were manually marked for counting with ImageJ's Cell Counter module. An example of the full process is presented in Figure 55 below for the DAPI (all nuclei) channel and for the red mCherry marked nuclei. However, this was more problematic for the green nuclei as there were fewer cells and the amount of autofluorescence in the green channel for cardiac tissue made it difficult to set image thresholds, so I resorted to manually marking and counting those nuclei (Figure 56).

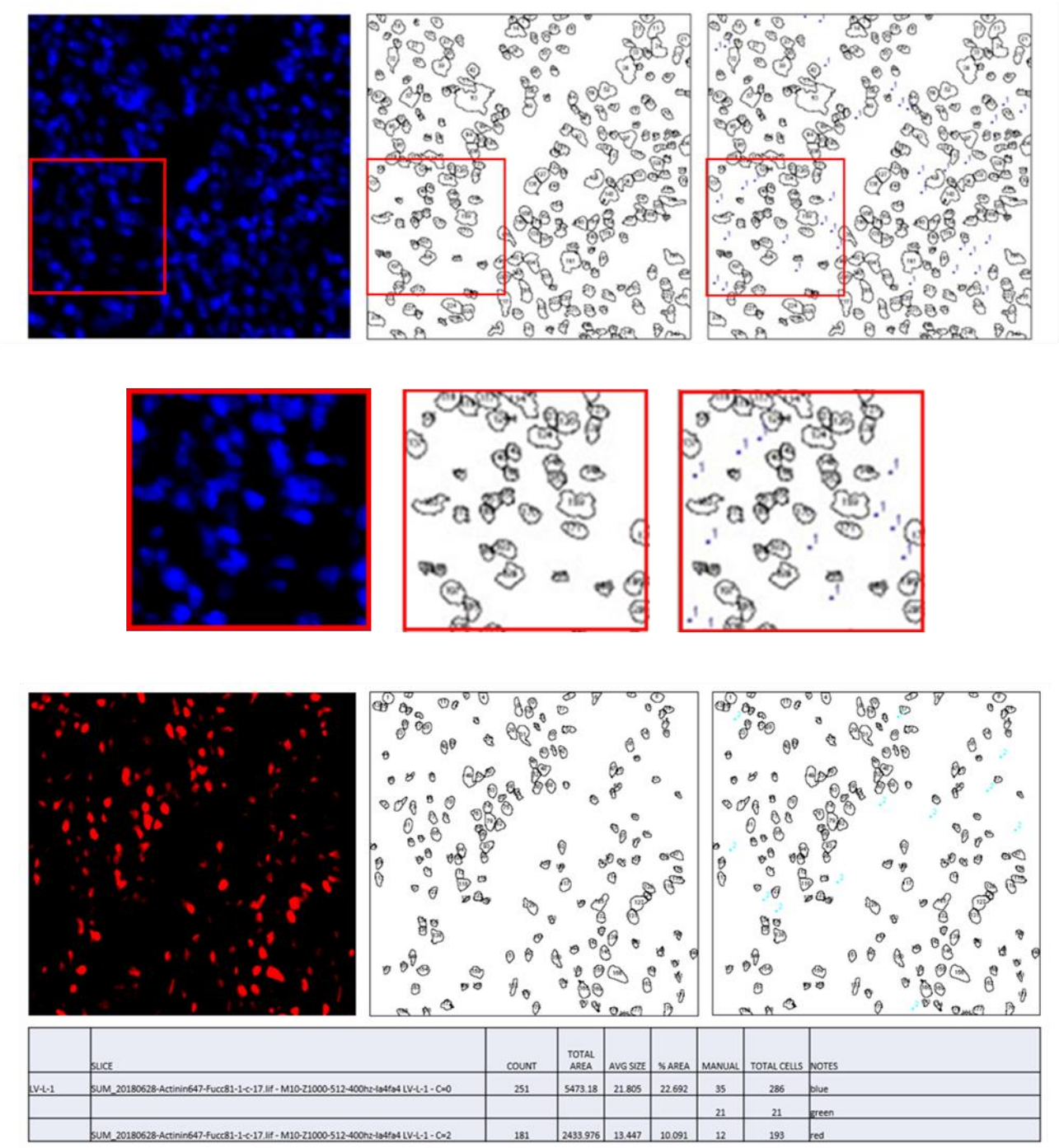

	SLICE	COUNT	TOTAL AREA	AVG SIZE	% AREA	MANUAL	TOTAL CELLS	NOTES
LV-L-1	SUM_20180628-Actinin647-Fucci81-1-c-17.lif - M10-Z1000-512-400hz-la4fa4 LV-L-1 - C=0	251	5473.18	21.805	22.692	35	286	blue
						21	21	green
	SUM_20180628-Actinin647-Fucci81-1-c-17.lif - M10-Z1000-512-400hz-la4fa4 LV-L-1 - C=2	181	2433.976	13.447	10.091	12	193	red

Figure 55: Semi-automated cell counting for the blue DAPI and red G1-mCherry channels. This was done by following the protocol outlined above. Top row: The first outlined image (centre column) was generated by ImageJ automatically and the second image was with the manual added additional cells using the overlay. Middle row: higher magnification of the squares in the outlined images showing the manually added extra cell counts marked by “1” and blue dots. The sum of these gave the total cell count. Bottom row: Same process for the red channel with added cells marked by “2” in the overlay on the right.

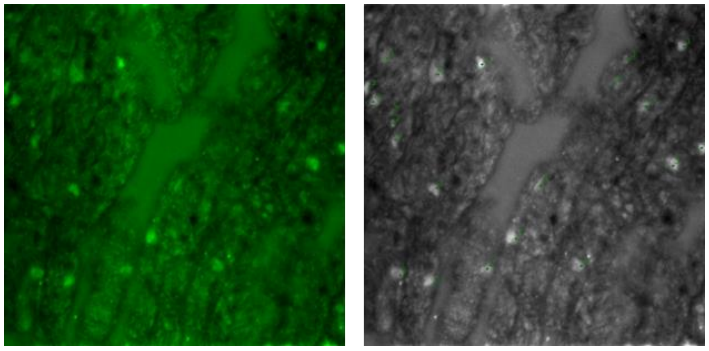

Figure 56: Autofluorescence meant that green S/G2/M nuclei had to be counted manually.

4.3.7 FUCCI WITH ADDITIONAL CELL-SPECIFIC MARKERS

Now that we had a protocol for cell nuclei counting, we added different cell type markers to the staining procedure. The first test was Fucci with the epicardial marker Wt1. The results were very clear and promising, with bright red and green Fucci signal and Wt1 in the far-red channel (imaged in grey) presenting along the epicardium on the outer edge of the ventricle wall (Figure 57).

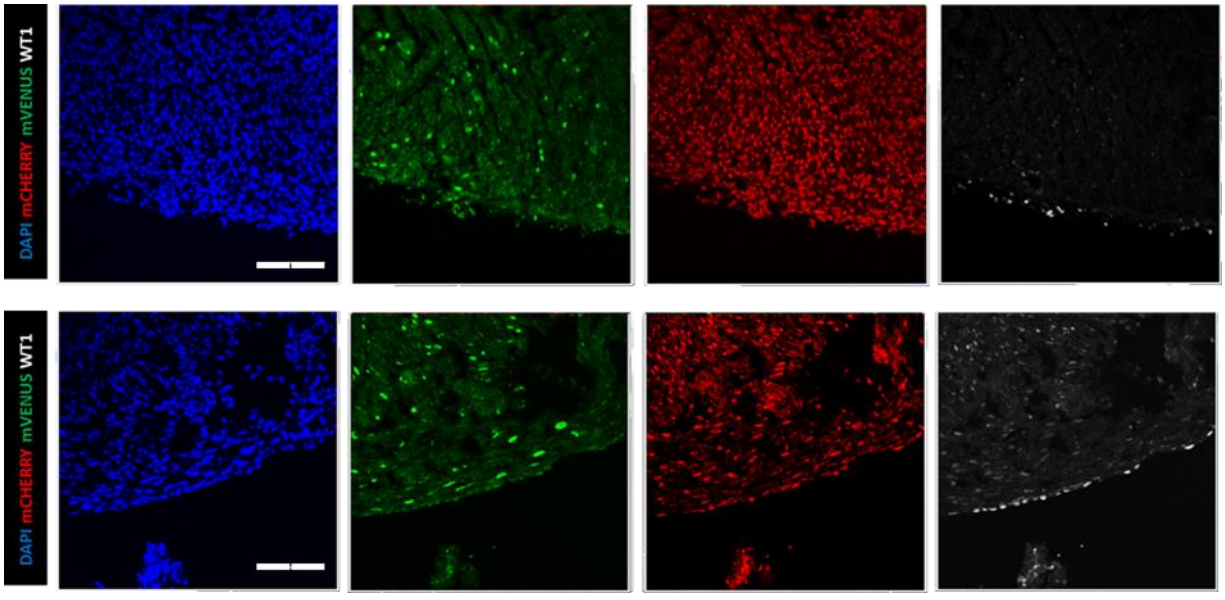

Figure 57: Fucci fluorescence co-stained with WT1 to mark epicardial cells. This is a P5 uninjured Fucci-positive mouse pup. Scale bar (shown in DAPI screen) = 100µm.

Other cell markers tested in preliminary experiments included vimentin and PDGFRα for fibroblasts, αSMA for smooth muscle and Pecam for endothelial cells. Unfortunately, due to

COVID restrictions, these experiments had to be abandoned and we proceeded with cardiomyocytes only.

4.3.8 AREAS OF CELL CYCLE ACTIVITY AT P5 AND P11 WITH/WITHOUT MI SURGERY AT P1 AND P7

Hearts were harvested after MI/sham surgery and prepared for imaging after fixation, sectioning and staining as outlined earlier. Nuclei were counted in the assigned sections from each region as per the experimental design. For the first sections counted, while the tissue was still fresh, all three channels for an image were counted, the ratios of red/blue (cells in G1 to total cell count), green/blue (cells in S/G2/M to total cell count) and green/red (actively dividing cells to total cells getting ready to divide or with potential to divide) were calculated, a sample is shown below for the ventricles of a P5 control heart slice:

	BLUE	GREEN	RED	G + R	%G/B	%R/B	%G+%R	%G/(%G+%R)	%R/(%G+%R)	total
RV-U-1	262	6	209	215	2.29	79.77	82.06	2.79	97.21	100.00
RV-M-1	355	10	227	237	2.82	63.94	66.76	4.22	95.78	100.00
RV-L-1	212	8	190	198	3.77	89.62	93.40	4.04	95.96	100.00
IVS-U-1	266	11	237	248	4.14	89.10	93.23	4.44	95.56	100.00
IVS-M-1	309	14	275	289	4.53	89.00	93.53	4.84	95.16	100.00
IVS-L-1	296	15	245	260	5.07	82.77	87.84	5.77	94.23	100.00
LV-U-1	258	14	215	229	5.43	83.33	88.76	6.11	93.89	100.00
LV-M-1	332	20	233	253	6.02	70.18	76.20	7.91	92.09	100.00
LV-L-1	286	21	193	214	7.34	67.48	74.83	9.81	90.19	100.00

Figure 58: Numbers and ratios of red/blue, green/blue and green/red cells across sections of a P5 control heart slice. The first 3 columns are raw counts of the blue (total # nuclei), green and red nuclei. The 4th column is the total of nuclei expressing either red or green, with columns 5 and 6 showing these as a ratio of total nuclei: note that this does not add up to 100 percent due to some unlabelled or uncounted nuclei in each area. RV: Right Ventricle; IVS: Intraventricular Septum; LV: Left Ventricle (all with 3 sections U=Upper, M=Middle, L=Lower).

Unfortunately, this cell counting assay was also interrupted by the COVID lockdowns. The green S/G2/M signal, which was already weaker than the red, had faded to below the limit of detection. Several attempts were made to enhance the signal with different antibodies, antigen retrieval, and background suppression techniques but green nuclei counts were unreliable. To compound the problem, we also lost the Fucci strain of mice due to a lapse in breeding so could not repeat surgery/sham procedures. The only option was to use the original samples but only assay the red fluorescent cells in G1 and make the assumption that a decrease in G1 cells reflects increased cell

cycling. This assumes that few cells were quiescent or senescent, which is supported by data from the initial fresh sections where the majority of cells were red, yellow or green (Figure 58).

Cell cycling in the infarcted heart

The data from the regions of the P5 and P11 hearts are shown in Figure 59 and Figure 60. Data analysis was complex as the data could be considered in a number of ways. There were three mice for each of the four conditions and three sections were taken from each region of each heart. This could be considered as three biological samples with three technical repeats for each region, as shown in Figure 45, but we were aware that variability between the technical repeats could be larger in some regions than in others and we did not want to lose that information by merely averaging these repeats. We shared the data with Professor Jack Miller who fitted the data using a linear mixed model with Satterthwaite's method where the random effects of this mixed model allowed per-heart variability while taking into account our multiple measurements of the same region. The model assessed 'cell count' as a function of three variables: MI/control, postnatal age, and the region of the heart. Interestingly, this more complex analysis of the data increased the number of significant differences found for each effect and in the post hoc analysis compared with that found using an ANOVA. The linear mixed model determined that age had a significant effect on the cell count holding everything else constant (**p=0.0059), the effect of MI/control was greater (***p = 9.62e-9), and the effect of region was the greatest (***p 2.2e-16). A post hoc analysis showed differences between most regions making it hard to draw conclusions. For comparisons between regions in P5 MI hearts there were 107 differences, and in P11 MI hearts there were 8. Interestingly, there were also 28 differences for P11 control hearts, of which 17 involved LVM1, but none for P5 control hearts.

The data are presented as bar charts showing the averaged data for each region in Figure 59, with statistical differences shown for P5 vs P11 with MI/control held constant (Figure 56A), or for control vs MI with postnatal age held constant (Figure 56B). Figure 60 shows the same data as violin plots for each region of the heart, indicating the distribution of the nine data points (three replicates from three hears) for each region. In each case the significances shown are the same. It is clear that there was significantly more cell cycling in the P5 MI heart than in the P11 MI heart or the P5 control heart, and this was in all regions of the left ventricle and the septum. Interestingly there was some cell cycling in the middle of the left ventricle of the P11 control heart when compared the P5 control. When comparing control and MI hearts at P5, there was also some cell

cycling in the right atrium and the base. The P11 MI heart showed more cell cycling than the P11 control in regions across the heart but to a significantly lower extent than that seen at P5. There were differences in the middle and lower right ventricle and septum, upper left ventricle and left atrium. The violin plots (Figure 60) also show that the data for the control hearts was fairly consistent in most regions but there was much more variability in the MI hearts. (Note that a simpler plot of the data from a preliminary analysis is shown in Supplemental Figure S3)

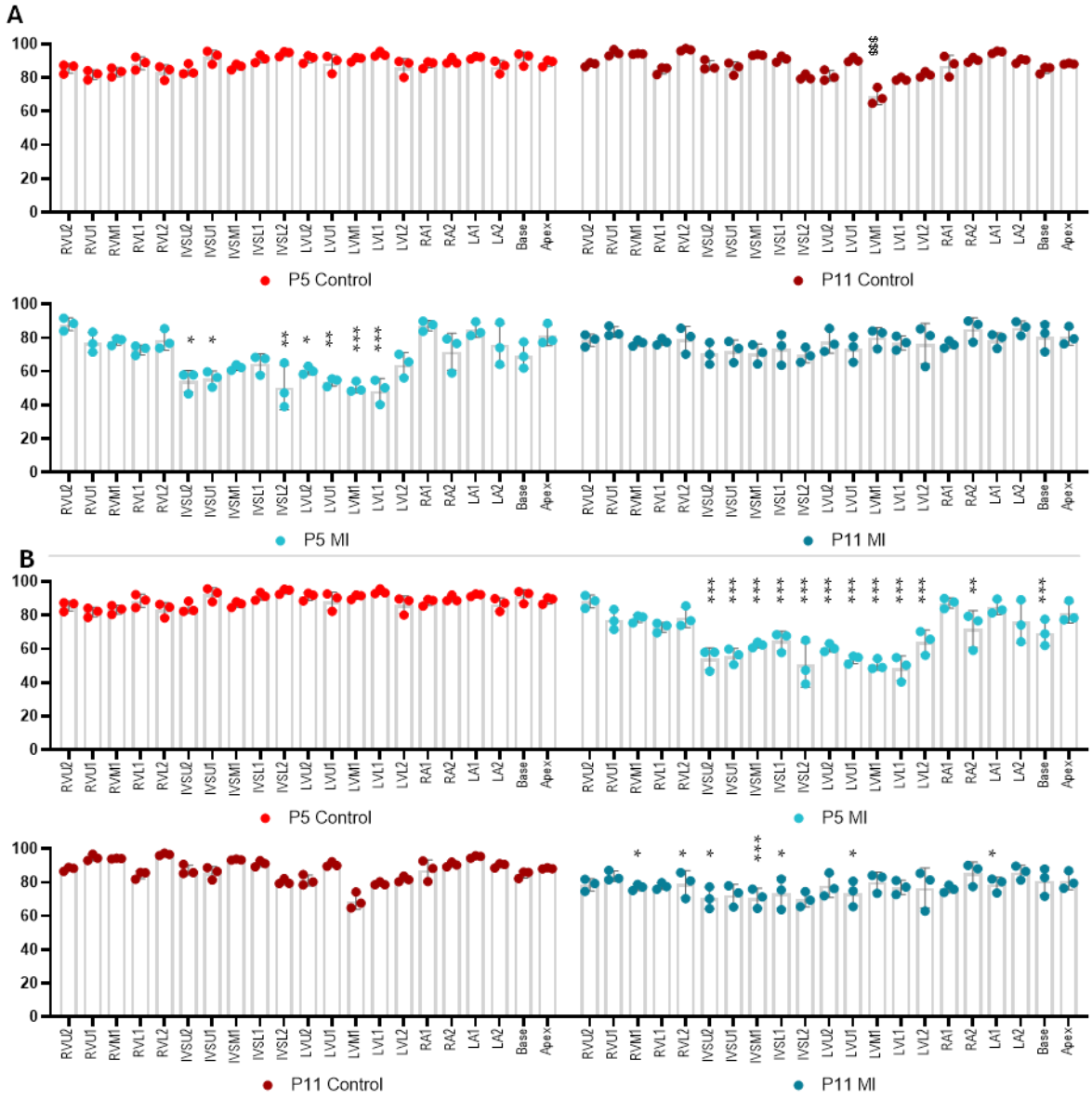

Figure 59: Cell cycling activity in the regions of the heart. N = 3 hearts in each group (data from 3 slices per region averaged heart), Type III Analysis of Variance with Satterthwaite's method, (A): showing differences between P5 and P11 in Control and MI *P < 0.05; **P < 0.01; ***P < 0.001 for MI P5 vs MI P11; $$$ P < 0.001 for Control P5 vs Control P11; (B): showing differences between Control and MI at P5 and P11; .*P < 0.05; **P < 0.01; ***P < 0.001 for MI P5 vs Control at each age.

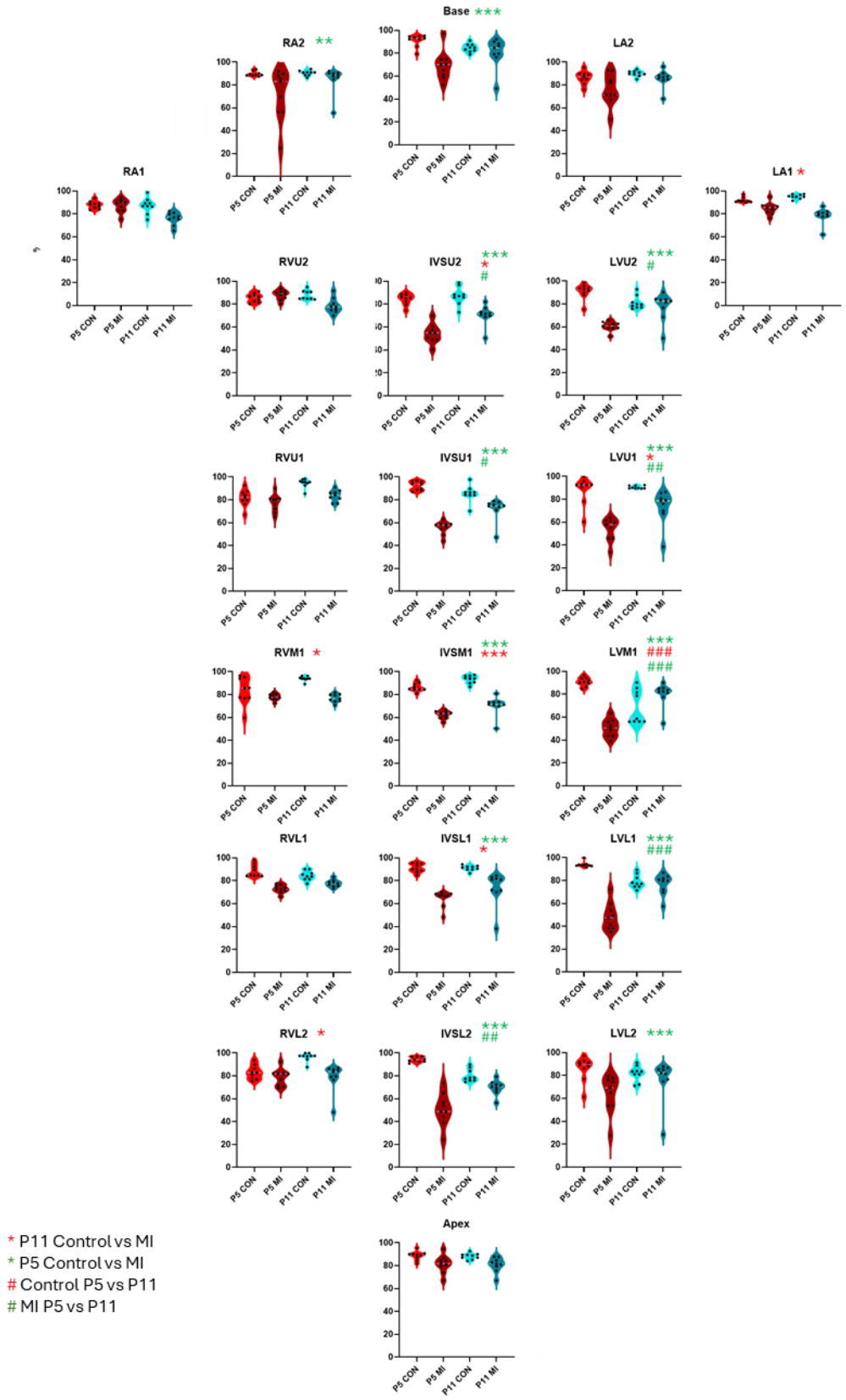

Figure 60: Violin plot showing cell cycling activity in the regions of the heart laid out in their appropriate locations. N = 3 hearts in each group, Type III Analysis of Variance with Satterthwaite's method, *P < 0.05; **P < 0.01; ***P < 0.001 for control vs MI at P5 (green) or P11 (red); # P < 0.05, ## P < 0.01, ### P < 0.001 for P5 vs P11 in controls (green) or MI (red).

Summary

An overview of these results is shown in Figure 61 below. The areas of greatest significant differences ($p < 0.001$ or less) between age-matched control and post-surgery hearts are mapped onto an illustration of a heart slice. It can be seen that more areas are strongly activated after MI injury at P1 than at P7 (11/21 vs 6/21) and interestingly, the remote regions respond more strongly after injury at P7 than areas close to the actual site of the suture.

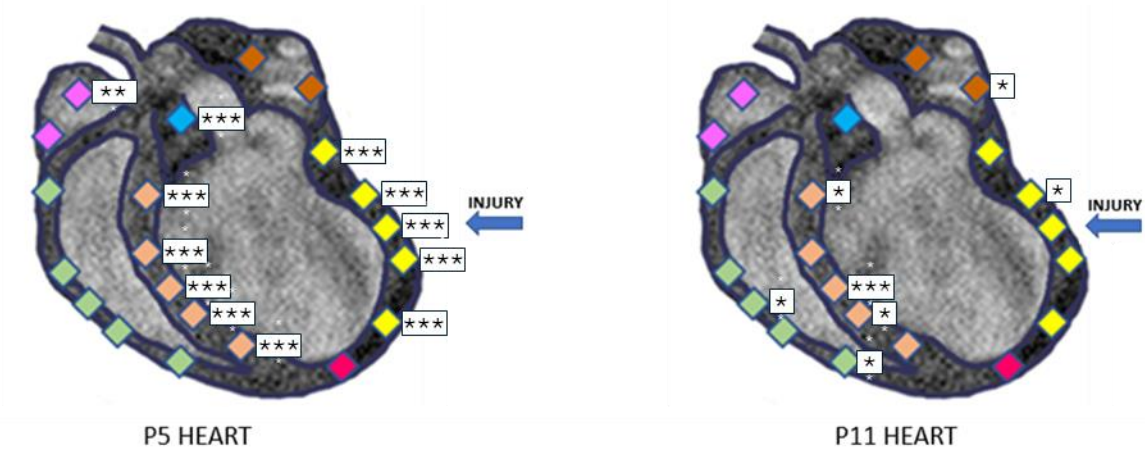

Figure 61: Summary graphic showing the different response to surgery at P1 and P7: regions of greatest cell cycling activity after MI injury in P5 and P11 hearts (4 DPI) when compared to age-matched shams. The P5 heart shows cell cycle activation along the left ventricle and intraventricular septum whereas the P11 heart has activation in more remote regions including the right ventricle and left atrium. The significance values are from Figs. 23 above where *P < 0.05 and ***P < 0.001 are mapped directly onto an outline of the heart indicating a significant difference between control and MI hearts at that age.

4.3.9 EXPERIMENTAL DESIGN (Part 2): INVESTIGATING AREAS OF ACIDITY USING pHLIP LABELLING TECHNOLOGY DURING DEVELOPMENT AND AFTER MI CRYOINFARCT SURGERY

We wanted to compare P1 and P7 mouse hearts for potential differences in amount and location of acidic tissue to see if this would add further information to the changes that occur during the regenerative window. This was to be extended to include P21 and adult mice to complete a developmental study of acidic regions of the heart (unfortunately we could not include P14 due to licence restrictions). The plan was to inject pHLIP into mice at these ages and harvest the heart and other control organs 24 hours later for sectioning, imaging and analysis. Wildtype CD1 mice were used to avoid any autofluorescence that would come from Fucci mice, even though our pHLIP was conjugated to Cy5.5 which is a far red marker and should not interfere with Fucci emissions. We also wanted to demonstrate acidity after myocardial infarction injury by cryo-probe

in adult Sprague Dawley rats followed 5 weeks later with pHLIP injections 24 hours prior to tissue harvest and processing as before. These experiments are outlined in Figure 62 below:

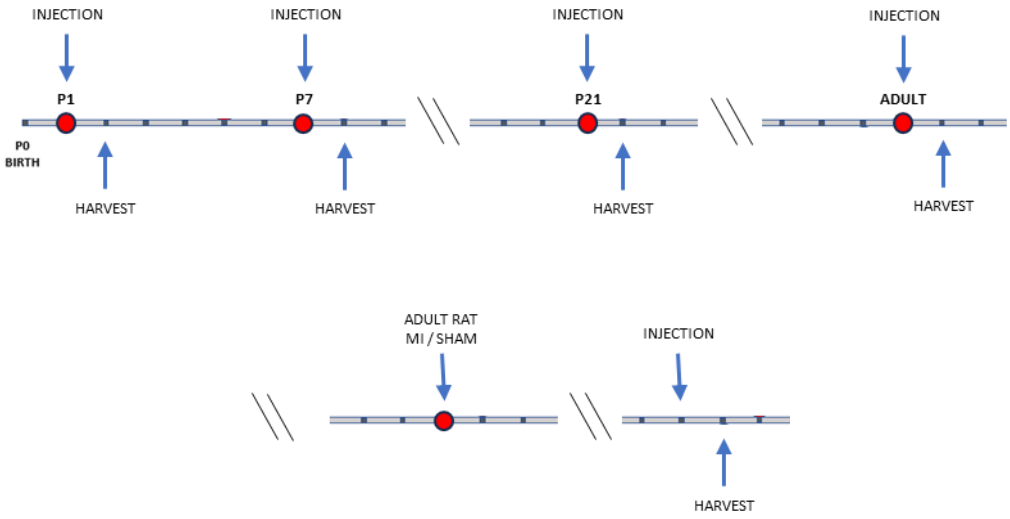

Figure 62: pHLIP experimental design: Top row: the developmental study of acidic regions of the mouse heart with timepoints at P1, P7, P21 and Adult with harvest 24hrs later (note this would be done on different mice). Bottom row: the cryo-infarction study with adult rats where pHLIP was injected 5 weeks after surgery and harvested 24 hours later.

4.3.10 IDENTIFYING ACIDIC REGIONS OF THE HEART USING pHLIP

We used CD1 mice for this study as we did for the neonate MRI study and based the dose on two earlier studies with adult female C3D2F1 or male C57B mice (Andreev, Dupuy et al. 2007, Sosunov, Anyukhovsky et al. 2013). Our group collaborated with this lab to obtain the pHLIP for this project. In their study with adult male C57B mice weighing 23 – 32g, they injected 80μM pHLIP in 100μL PBS (0.35 – 0.25 nmol/g) intravenously. As there was not a precedent for using pHLIP in neonatal mice we extrapolated down by body weight and chose to inject 20μL pHLIP solution of the same concentration. The average body weight of a P1 mouse was 2.18g (n = 17 from 3 litters) which would require an intravenous injection of 10 μL. However, this is not feasible in a neonatal mouse, so I did a subcutaneous injection of 20μL to account for the less direct route of delivery. This subcut injection volume of 20μL was also used routinely in other experimental procedures on neonatal mice so we felt it was a safe volume to start the experiments. However, the average P7 neonate pup weight was 6.59g (n = 14 from 3 litters), which meant we would need to either increase the volume of 80μM pHLIP solution injected or increase the concentration while keeping the volume consistent. We opted to do the latter and used a 3x concentrated solution. Adult CD1 mice weighed approximately 25g, and we tried 200 μL of 80 μM pHLIP in sterile PBS

intraperitoneally (IP) or subcutaneously, with overnight incubation or tail vein injections of 100 µL of pHLIP but with incubation of only 5 hours. Both IP and IV injections gave us clear bright pHLIP signal in the kidneys and very little in the heart as expected, however IV was more reproducible. Subcutaneous injection in adult mice produced very little signal in either heart or kidney.

For a control marker of perfusion across the entire heart tissue, we added Hoechst 33342 (10mg Hoechst/kg body weight) to the pHLIP solution. The Hoechst dye should label all areas that are exposed to the injected solution independently of tissue pH levels thus serving as a perfusion standard against which to measure pHLIP retention (Smith, Hill et al. 1988). The final doses and injection methods for pHLIP alone and pHLIP + Hoechst co-injection are summarised in Appendix 4.

4.3.11 pHLIP TISSUE COLLECTION SAMPLE PREPARATION

Following administration of the pHLIP solution and incubation *in vivo*, hearts and kidneys were removed after Schedule 1 as outlined in General Methods – Animal Models. Tissues were rinsed well in ice-cold PBS and snap frozen on powdered dry ice in a histology mould filled with chilled OCT, positioned for long axis cryosectioning. pHLIP imaging works best with very thick sections (the literature recommends 100µm), but the maximum our cryostat could cut was 25µm. Since the tissue was unfixed before cutting, these thicker sections also reliably gave complete, untorn sections of good structure. Rat heart and kidney tissue was harvested in the same way after cryo-infarct surgery.

4.3.12 IMAGING OF pHLIP SECTIONS

The pHLIP sections were initially imaged only for fluorescence in the Far Red channel as our pHLIP variant was pre-conjugated to Cy5.5 fluorophore dye (excitation 683nm/emission 703nm). After establishing dose protocols for each age group, we also imaged Hoechst-33342 (excitation 350nm/emission 461nm) on the DAPI channel for the quantification analysis. The slides were brought to room temperature and viewed directly without mounting media or coverslip as per our

collaborator's imaging protocols. Each tissue section was imaged and tiled using the Leica DM6000 upright microscope as detailed above for the Fucci slices. For analysis, this was done in 16-bit grayscale resolution with fixed illumination intensities and time exposures for both channels, imaged sequentially, keeping all other settings (electronic gain, contrast, pinhole, magnification and zoom) constant.

We re-imaged some of the earliest hearts injected and sectioned almost 4 months after their initial test images to determine how long pHLIP remained visible when stored frozen at either -80°C or -20°C. Unlike the Fucci samples, there was very little diminishing of the pHLIP signal, it remained clear and very bright in the same areas as before. As pHLIP is an unknown marker in the field of cardiac biology, it was important to test its viability and this confirmation of a consistent and long-lasting signal was an encouraging result.

4.3.13 TIME COURSE OF ACIDIC NICHES IN THE DEVELOPING MOUSE HEART

P1 and P7 neonate pHLIP test injections:

The first pHLIP injections were performed on a small group of P1 and P7 pups to test tolerance and any possible toxicity of the dye in neonatal animals since all previous work was in adults only. We found the pups had no adverse reactions after 24 hours, and the mothers continued to nurture the pups normally despite the large blue injection site on their necks. These pups also had an IP injection of Hoechst an hour before Schedule 1 which was also well tolerated. Pups which had no injections were used as a control. (These images are shown in Supplemental Figure S4)

Some of these first images from P1 and P7 pups are shown in Figure 63 (top and middle row). We could see regions of acidity clearly identified by increased intensity of the pHLIP signal: more acidic tissue at the inner endocardial regions lining the ventricles and across the atria. As expected, the kidney was very bright in the outer renal cortex and could serve as a reference control to confirm that pHLIP absorbance by body tissues was successful within 24 hours after a subcutaneous injection of dye. To check that this signal was due to the injected pHLIP being absorbed into tissues and distributed via the circulatory system, we put the un-injected control heart and kidney into a solution of pHLIP in PBS at pH 6.6 for 24 hours. As shown in Figure 63 (bottom row) the pattern of pHLIP signalling was very different: bright signals were located only

along the very edge of the tissue that had been in direct contact with the acidic buffer and had not penetrated the interior. The kidney had some small dots of signal where pHLIP had entered via the blood vessels exiting into the buffer. There was very little signal from Hoechst which also indicated limited perfusion.

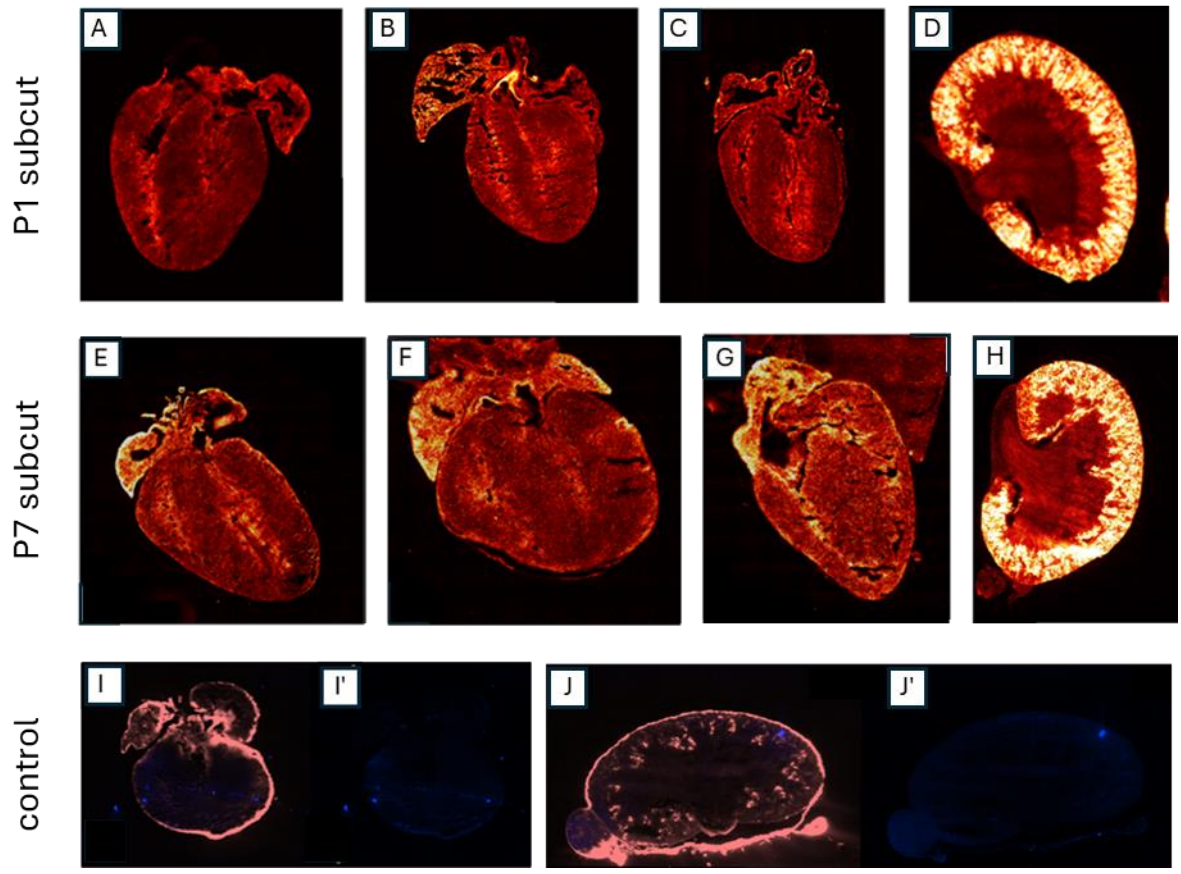

Figure 63: Three hearts and an example kidney labelled with pHLIP from P1 pups (top row A-D) and P7 pups (middle row E-H). These samples were collected 24 hours after subcutaneous injection of 20 µL of 80 µM or 240µM Cy5.5-labelled pHLIP dye respectively. Bottom Row: Control P1 heart (I, I') and kidney (J, J') placed into PBS acidified to pH 6.6 containing 80 µM pHLIP for 24hrs, imaged for pHLIP (I, J) and Hoechst (I', J').These images are not to scale but maximised for the image tiling software.

Adult mouse pHLIP test injections:

In adult mice, we compared heart and kidney tissues harvested 24 hours after a subcutaneous injection of 200µL of 80µM pHLIP with those from an intravenous injection of 100µL of 80µM pHLIP harvested after 5 hours.

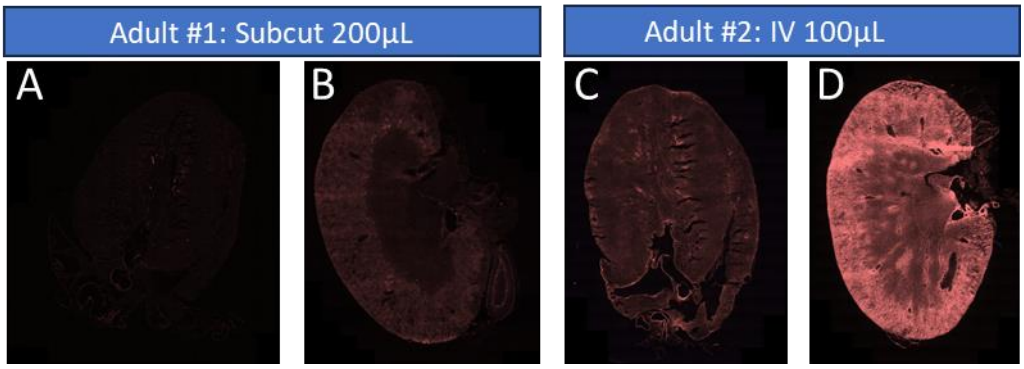

Figure 64: (A) Adult heart #1 injected subcutaneously with 200µL of 80µM pHLIP, harvested 24 hours later. (B) The corresponding kidney for control. As the kidney signal was low, the injections were repeated intravenously (C) Adult heart #2 with an IV injection of 100 µL of 80µM and (D) kidney. Here, the kidney signal was as bright as expected but the heart remained low in pHLIP signal suggesting neutral pH throughout the adult heart. We also tested 200µL of 80µM pHLIP for 24 hours with an intraperitoneal injection with results similar to the IV injection (not shown). As above, images not to scale.

After the sub-cut injection, the pHLIP signal was barely detectable (Figure 64: (A) Heart, (B) Kidney), whereas after IV injection the signal in the kidney was as bright as expected for an acidic tissue but that in the heart remained low, suggesting a neutral pH throughout the myocardium Figure 64: (C) Heart, (D) Kidney).

4.3.14 DATA ANALYSIS OF pHLIP SECTIONS

To get a dataset of different ages, pHLIP and Hoechst co-injection was performed in neonatal and adult hearts (P1: n=20, P7: n=9, P21: n=12, adult: n=13).

The intensity of Hoechst signal allowed us to see the penetrance and distribution of the pHLIP solution and could be used to normalise the signal from the pHLIP. It also indicated freezing and cutting artefacts in the tissue slices such as non-uniform thickness and folding of the section on the glass slide. Images of a P1 heart in Figure 65 show that the Hoechst signal was reasonably uniform across the tissue section but there were a few areas of high or low intensity.

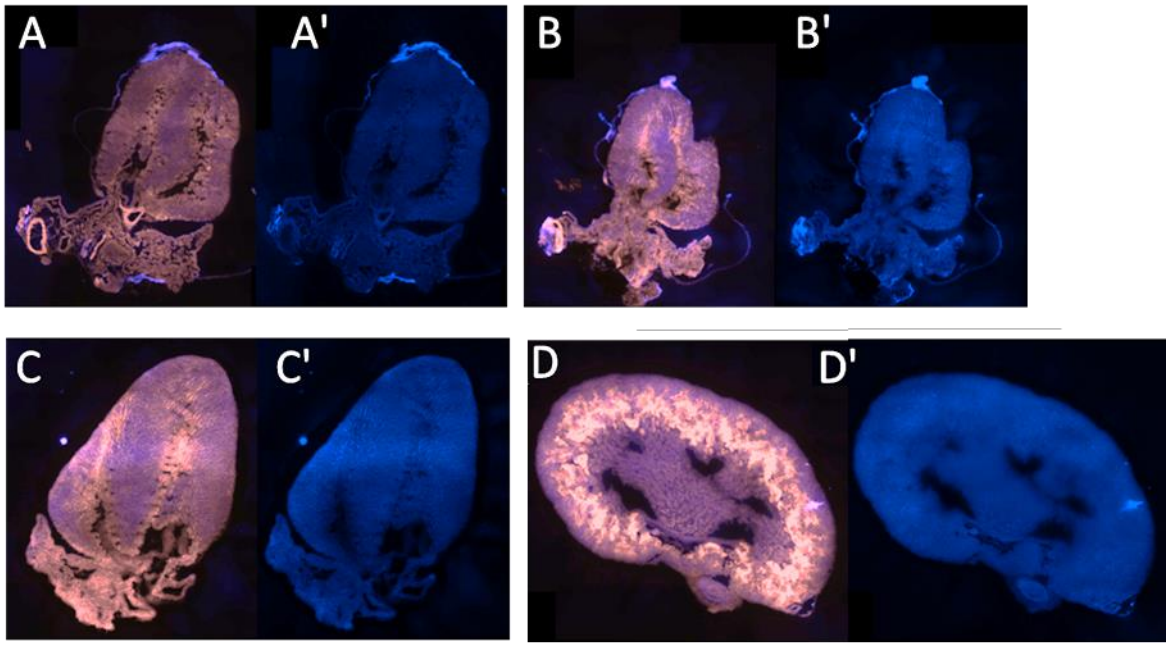

Figure 65: Preliminary images of pHLIP and Hoechst co-injected P1 hearts harvested after 24 hours (pHLIP and Hoechst signals merged A,B,C; Hoechst signal alone A',B',C'). An example kidney from one of these mice shows the intense acidity of the kidney cortex (pHLIP and Hoechst D, Hoechst alone D'). Note that these images are not to scale but maximised for the image tiling software.

To quantify these images, we used a combination of standard ImageJ modules with a custom written Matlab macro to calculate pixel ratios.

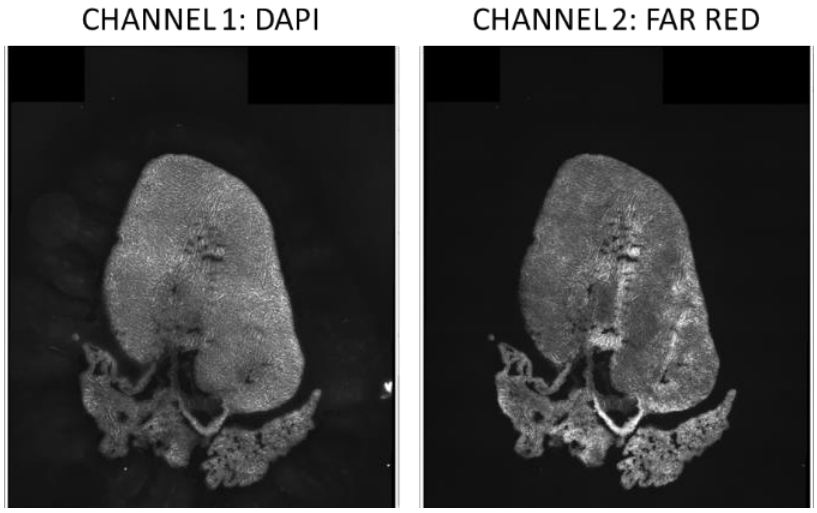

Figure 66: Two image channels for ratiometric analysis. Both channels (Channel 1: DAPI measuring Hoechst 3343 signal; Channel 2: Far Red measuring pHLIP signal) recorded signal in 16-bit grayscale and the relative intensities (for each pixel) were used to calculate pH (acidity) levels across the slice of tissue.

To prepare ratiometric maps, we paired 16-bit grayscale pHLIP and Hoechst images (Figure 66). The background intensity of both channels was subtracted and then pixelwise ratioing was applied to pixels above a set threshold defined as two standard deviations above background signal. This

value was colour mapped from blue to red based on intensity of the far red pHLIP signal over that of the blue Hoechst (Figure 67).

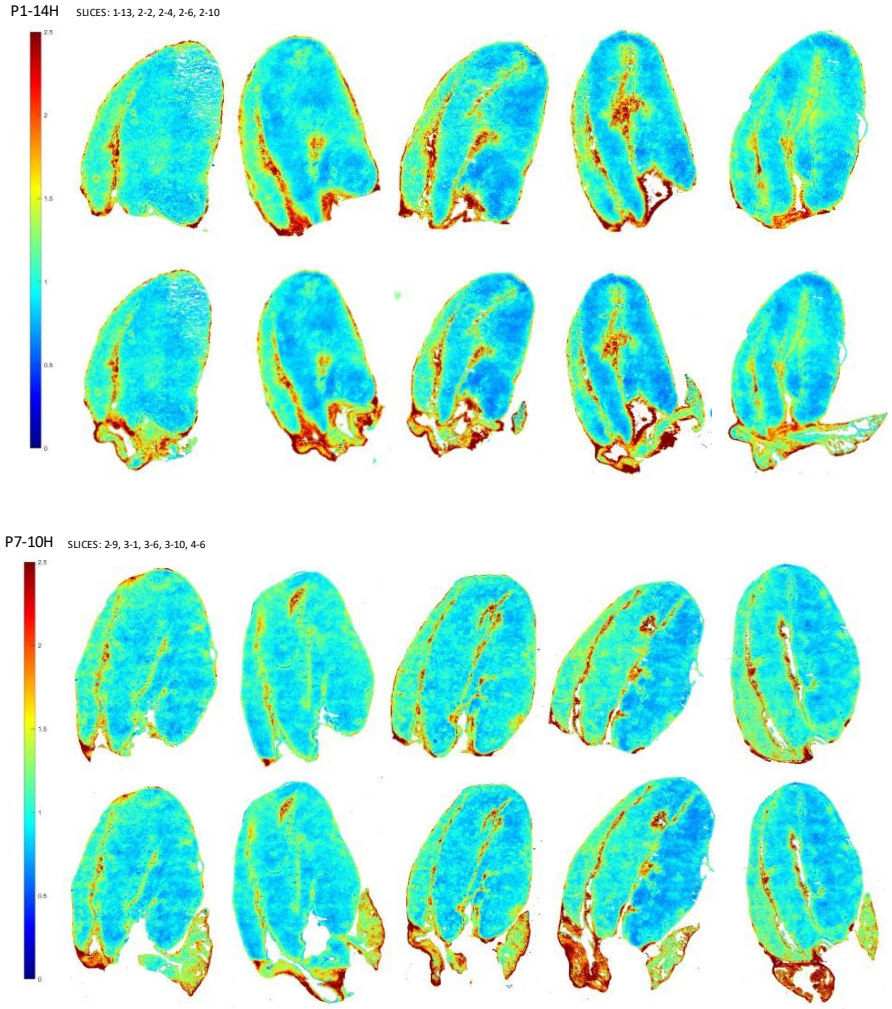

Figure 67: Image analysis via our ratiometric Matlab macro to show relative amounts of pHLIP (appearing yellow to red according to increasing intensity) to Hoechst 33342 perfusion marker. These are 10 slices through a single P1 heart (top) and P7 heart (bottom), with an intensity scale to the left.

Both P1 and P7 hearts showed a consistent acidic region along the endocardial walls and the atria. This signal was quantified in a histogram of relative intensities (Figure 68) summing pixel values from five mid-luminal slices per heart (for this analysis, we masked and only used the ventricle area, omitting the atria and major vessels): the areas that are acidic have a pHLIP/Hoechst ratio higher than one standard deviation over the balanced ratio of one (Figure 68).

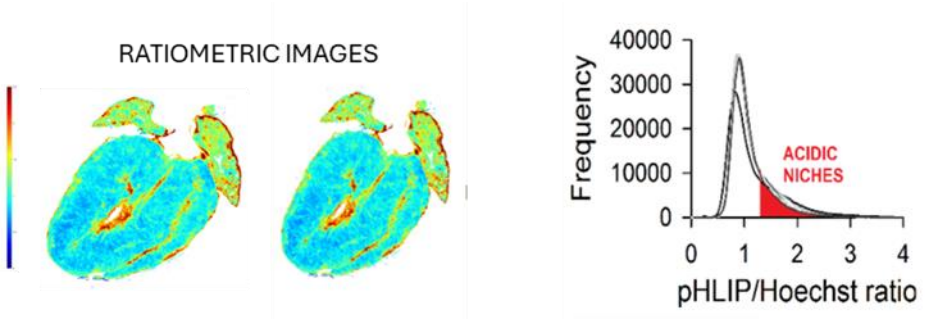

Figure 68: Ratiometric (pHLIP/Hoechst) histogram showing areas of increased pHLIP signal where acidic niches are present in this P7 heart (shown here in red,). Each of the lines is the histogram for a single slice (2 are shown here) Note that this frequency histogram only counts pixels within the ventricles (a masked area) and excludes the atria and great vessels even though the representative images (left) show the entire slice.

The P21 hearts still had a few small areas of acidity dispersed throughout the myocardium (Figure 69) but did not show the clearly acidic endocardial regions seen for the younger hearts. The adult hearts show no significant areas of pHLIP staining. More sample images from these hearts are in Supplemental Figure S-5.

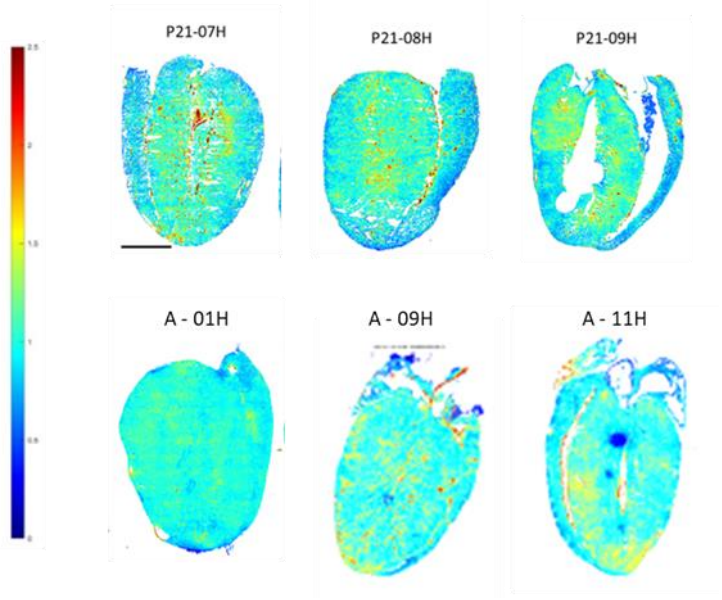

Figure 69: pHLIP ratiometric images for P21 (top row) and Adult (bottom row) hearts after 24 hours of incubation with pHLIP and Hoechst. Note that the endocardial regions are not showing extensive red unlike the younger hearts above.

Further analysis of the frequency histograms for neonate vs adult heart pHLIP/Hoechst ratio as shown below indicates the neonate curves are best fitted with three Gaussian distributions (bell curves). The skewed "tail" to the right is the amount of acidic over neutral tissue areas. The adult heart is evenly centred around the 1:1 ratio (Figure 70).

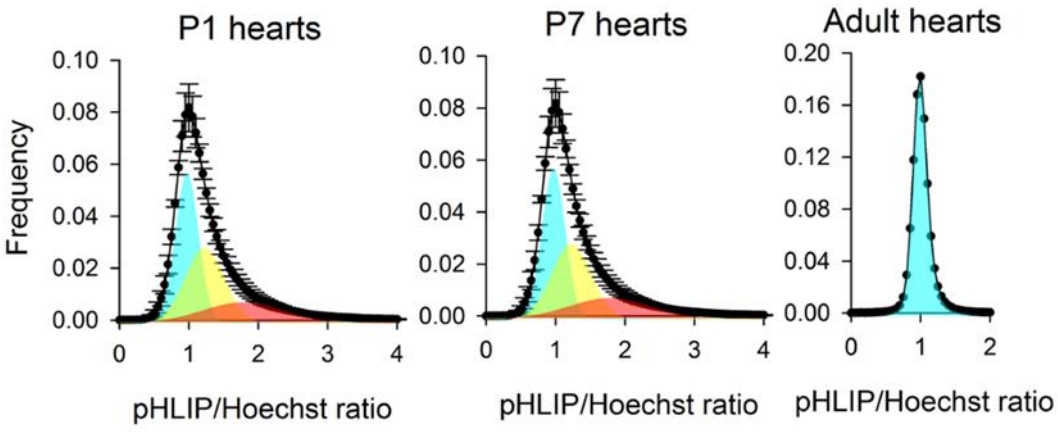

Figure 70: Frequency histograms of intensity ratio values of pHLIP/Hoechst for different ages of mouse heart. The P1 and P7 hearts are positively skewed (n=6 hearts per group included here from 20 and 9 samples respectively) while the adult hearts (one heart shown here from 13 samples) are not skewed and centre on a ratio of 1 meaning there are no areas where pHLIP signal is higher than anywhere else in the slice.

This study of acidic niches in the developing mouse heart was published in "Alkaline nucleoplasm facilitates contractile gene expression in the mammalian heart", Basic Research in Cardiology 2022 (Hulikova, Park et al. 2022).

4.3.15 ACIDIC NICHES AFTER CRYO-INFARCT INJURY IN THE ADULT RAT HEART

To investigate acidic regions in an adult rodent injury model, we used cryo-infarct in the rat. Cryoinjury differs from LAD ligation induced MI as it involves pressing a probe cooled in liquid nitrogen directly onto the left ventricle wall for approximately 15 seconds to induce cell death and scar formation. Cryoinjury induces "ischaemia-like" necrotic tissue damage and apoptotic cell death across 20-30% of the ventricle, and it is theoretically easier to produce injuries of consistent size and intensity, thus reducing surgical variability (Chablais, Veit et al. 2011). We wanted to see if pHLIP could show areas of acidity after injury to the myocardium in the same way as demonstrated by our colleagues in a mouse model of LAD ligation (Sosunov, Anyukhovsky et al. 2013). Cryoinjury was performed by Professor Carolyn Carr in male Sprague Dawley rats aged 6-8 weeks with tissue planned to be harvested 5 weeks after surgery. Dosage of pHLIP and Hoechst was adjusted from that used in the mouse, please refer to Appendix 4 for details.

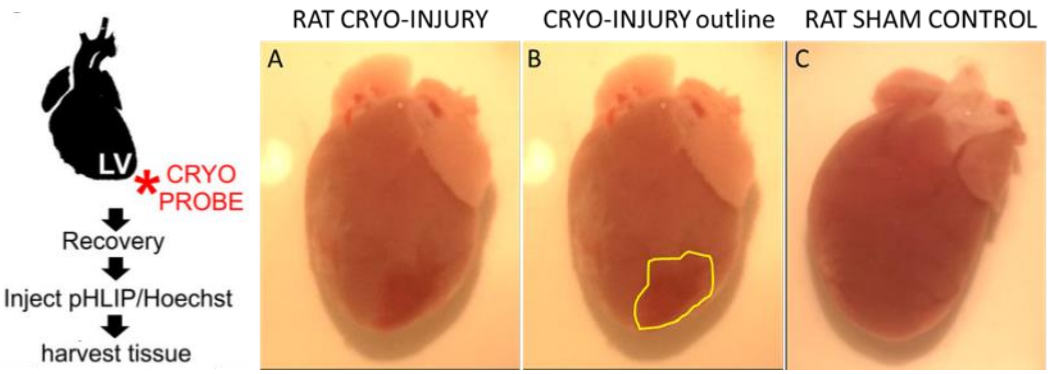

Figure 71: Adult rat cryo-infarct heart protocol – these images show samples 4 days post injury (A) A frozen cryo-probe was placed on the lower left ventricle and the area of damage is visible even after 4 days (B) damaged myocardium outlined in yellow (C) The uninjured matched control.

Unfortunately, due to an imminent COVID shutdown of all surgical procedures, we had to terminate the initial study after only 4 days, treating the animals with the weight appropriate dose of pHLIP and Hoechst administered intraperitoneally on Day 3 post surgery. The hearts were harvested on Day 4, sectioned, imaged and analysed to generate ratiometric images as for the mouse samples (Figure 72, top row). We saw regions of acidity corresponding with the area where the cryoprobe was placed on the tissue to cause the injury. We noted acidic regions within the atria as for the neonatal mouse pups. Also of interest is that it appears that the entire epicardium was labelled by pHLIP indicating global activation.

A second set of surgeries was harvested after 5 weeks, with a more advanced injury indicated by a large area of damaged myocardium and severe thinning of the ventricle wall (as well as reduced LV EF measured by MRI). The pHLIP signal shows regions of acidity around the injury site which extended through the ventricle and up the endocardial walls. The time-matched control sham surgery rats did not show these focussed acidic regions. The quantification of this second set (n=4 cryoinfarct, n=5 sham) and sample images are also presented in Figure 72, middle and bottom rows.

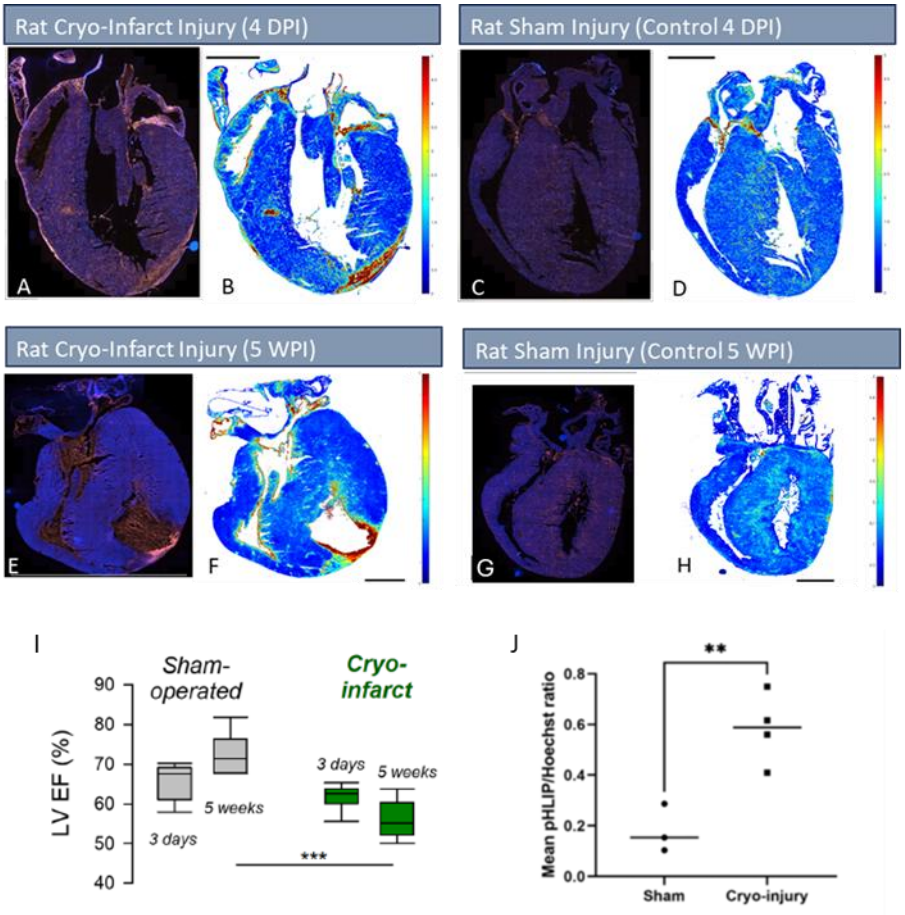

Figure 72: pHLIP imaging in adult rats after cryo-infarction injury. Top row: Samples collected 4 days post-surgery, with 400µL of 160 µM pHLIP injected intraperitoneally 24 hours prior to tissue harvest. The area of damaged myocardium and acidity in the injured heart (A) is clearly visible in both the original image and the ratiometric analysed image (B). The sham control heart does not have any regions of acidity marked by pHLIP (C, D); n=1 for each group. Middle row: Another set of surgeries on rat hearts was performed with MRI to monitor injury (n=6 for both groups). We saw pHLIP signal with a large cryo-infarct (E, F) and none in a sham injury (G, H) harvested five weeks after injury, with 400µL of 160 µM administered intravenously 5 hours prior to Schedule 1. (I) LV EF measured by MRI at 3 days and 5 weeks post injury/sham surgery. (J) The quantification of pHLIP/Hoechst ratio across myocardium of this second set of rat hearts after cryo-infarct (n=4) or sham surgery (n=3), t-test **$p < 0.01$.

A final set of cryo-infarct surgeries was harvested after two weeks with pHLIP injections. The hearts where an infarct region could be seen were used for immediate cellular dissociation by enzymatic digestion (experiments not included in this thesis) and the less damaged hearts and sham controls snap frozen and imaged as before. Interestingly, in these hearts that showed no visible damage, there still appeared to be an overall activation of an injury response (as has been suggested for other myocardial infarction models) and this showed as an increased acidity across the entire myocardium which was not evident for the sham animals. In work by others in the group, cardiac metabolism and acidosis were measured three days after cryoinjury using hyperpolarised ^{13}C imaging. This showed a diffuse build-up of lactate and a depletion of bicarbonate across a large part of the myocardium. In contrast, measurement of myocardial pH using hyperpolarised MR at five weeks after cryoinjury showed no difference between sham and infarcted hearts, suggesting

that the generalised acidosis seen by MR at three days and using pHLIP at two weeks had resolved by five weeks.

This study of acidic niches after cryo-infarct injury in the adult rat heart was published in "Acidic environments trigger intracellular H+-sensing FAK proteins to re-balance sarcolemmal acid-base transporters and auto-regulate cardiomyocyte pH", Cardiovascular Research 2022 (Wilson, Richards et al. 2022).

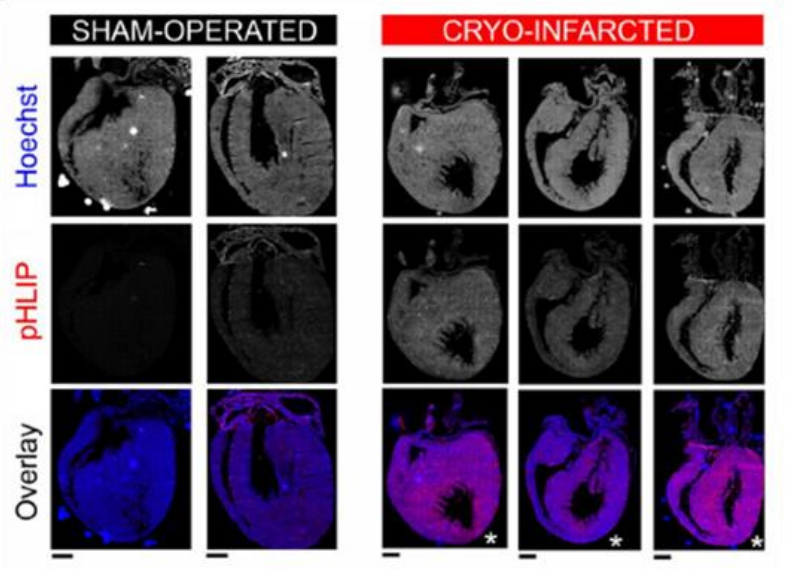

Figure 73: Cryo-infarcted adult rat hearts show overall activation and increased acidity even before acute thinning. These samples were harvested two weeks after infarct or sham injury, with 400µL of 160 µM pHLIP co-injected with Hoechst administered intravenously 5 hours prior to Schedule 1. Scale bar = 1.6mm. *Taken from our paper "Acidic environments trigger intracellular H+-sensing FAK proteins to re-balance sarcolemmal acid-base transporters and auto-regulate cardiomyocyte pH", Cardiovascular Research 2022* (Wilson, Richards et al. 2022).

4.3.16 IMMUNOFLUORESCENCE STAINING FOR CONTRACTILE PROTEINS IN ACIDIC MYOCARDIUM

Having identified acidic regions in the cryoinfarcted rat heart, we wanted to see if these areas contained reduced protein expression of contractile proteins. Work in our lab on isolated neonatal rat ventricular myocytes showed that cells cultured in acidic media of pH 6.4 had less Crip2 and Tnni1 than those cultured in normal pH 7.44 (see immunofluorescent antibody staining results in Figure 35 A-C). It is known that troponin subunits switch isoforms during heart development, from slow skeletal Tnni1 and Tnnt1 in embryonic myocardium to cardiac Tnni3 and Tnnt2 shortly after birth and into maturity. We also performed western blot and an ELISA assay for troponin

subunits Tnnt2, Tnni1 and Tnni3 over a range of pH values (6.4, 6.78, 7.05, 7.44) and saw clearly how these were affected (Figure 74 D-E).

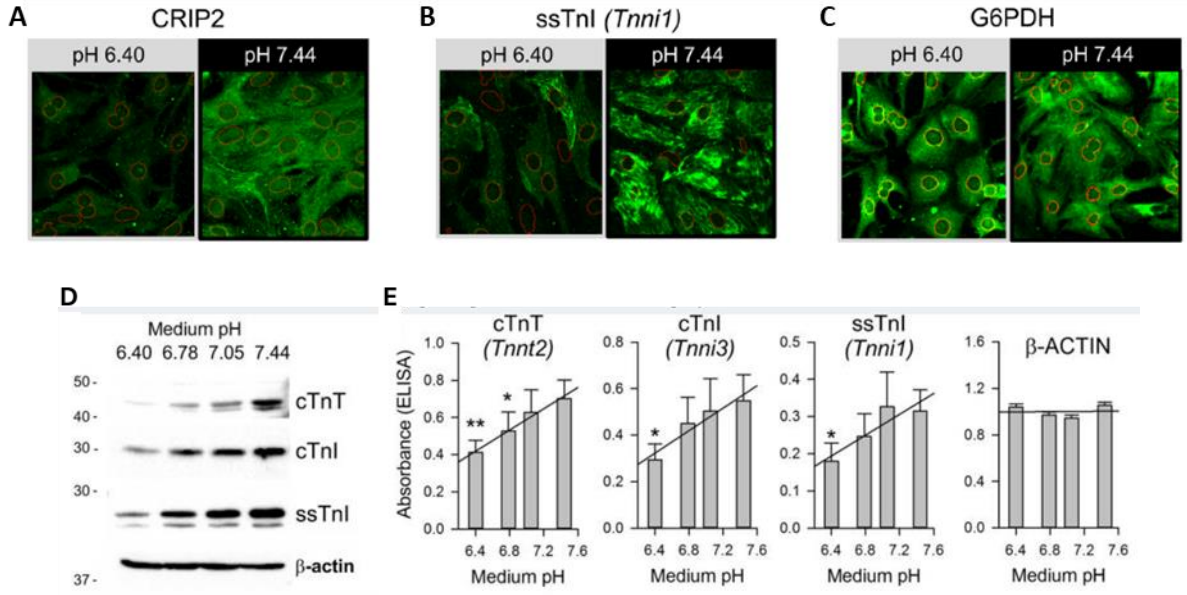

Figure 74: Top row: Immunofluorescent staining of NRVMs grown as a monolayer in acidic (pH 6.4) or alkaline (pH 7.4) cell culture media. (A) Crip2 and (B) Tnni1 show decreased expression in the acidic medium while (C) the control staining for G6PDH which is not affected by pH levels within this range is unaffected. Bottom row: (D) Western blots for troponin subunits cultured for 48hrs in 4 different pH media; (E) An ELISA assay testing these same conditions. This work was performed by Dr Alzbeta Hulikova and myself. Taken from our paper Hulikova, Park et al. 2022.

We wanted to check contractile proteins in sections of the cryoinfarcted adult rats. Antibody staining against Crip2 and Tnnt2 was performed on sections contiguous to where the pHLIP signal was recorded. As presented in Figure 75, in the damaged myocardium areas with high acidity there is no Crip2 or Tnnt2 present due to the loss of cardiomyocytes which have been replaced with fibrous scar tissue. Interestingly, it appears that in areas that are not labelled as acidic with pHLIP but are adjacent to the damaged areas, reduced Crip2 and Tnnt2 staining is indicated by reduced green fluorescent signal, i.e. the lower RV and IVS had less intense signal than mid/upper IVS and LV unaffected by injury. Looking at injured hearts, both Crip2 and Tnnt2 staining increases as the amount of damage and size of the infarcted area reduces.

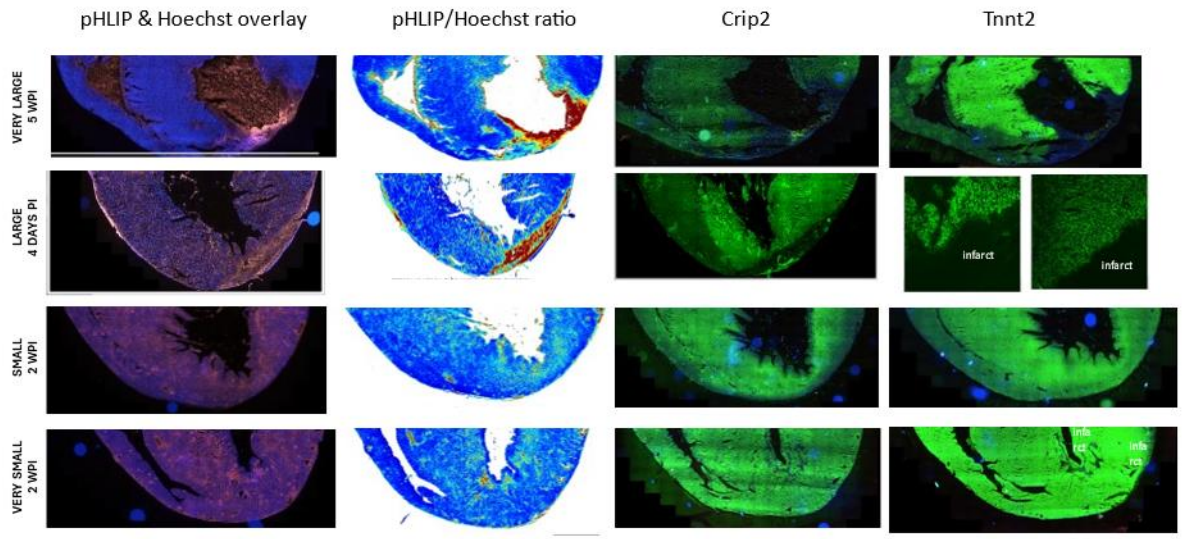

Figure 75: Immunofluorescent staining on four cryoinfarcted adult rat hearts with varying degrees of damage. Top row: a very large infarct after 5 weeks with an intense area of acidic labelling with pHLIP localised to the infarct. Here Crip2 staining is reduced only in the immediate injury area probably due to the loss of CM, whilst Tnnt2 shows less signal here as well as remotely into the IVS and RV. Second row: a large infarct after only 4 days showing an intense pHLIP signal where the injury occurred but also an overall diffuse acidic response across the myocardium. Here both Crip2 and Tnnt2 are absent in the infarct damaged area but also appears reduced remotely (Tnnt2 remote data not shown here). Third row: a lesser degree of damage by cryoinjury after 2 weeks still showing a diffuse acidic response and nonuniform Crip2 and Tnnt2 across the myocardium. Fourth row: the smallest cryoinjured heart without any thinning of the wall at 2 weeks shows uniform staining for both contractile proteins across the injury site and remote regions as demonstrated by equally intense green signal across the heart.

4.3.17 STUDY LIMITATIONS

There are a number of limitations to the work presented in this chapter.

The FUCCI mouse model we used was the R26p-Fucci2 mouse in which the Fucci probe is expressed in all cells and is not specific to cardiomyocytes. Using the Fucci-Tg mouse, which only expresses Fucci in cardiomyocytes, would have been more explicit in excluding other cell types but unfortunately we didn't have access to this line (it was in development at the time of our initial studies with Fucci2). In the pilot study we stained sections for vimentin and PDGFRα for fibroblasts, αSMA for smooth muscle, pecam for endothelial cells and Wt1. However, due to the red and green fluorescence of the FUCCI signal and the blue of DAPI, we were limited to using far red for any other antibodies. We used the co-stained sections as a training set and could distinguish cardiomyocytes in the tissue by size and morphology. Endothelial and smooth muscle cell nuclei lining blood vessels tend to be smaller than CM nuclei and lie in lines or as small circles of nuclei in a vessel cross-section; fibroblasts also have smaller nuclei and lie in groups around the

muscle fibres; epicardial cells lie outside the muscle bundles on the outer edge of the tissue section. Nevertheless, it is possible that some non-myocytes were included in the manual counting.

The disruption due to the Covid pandemic not only meant that we lost the breeding colony of Fucci mice and therefore had low numbers of animals in our study, but also that tissue we had already harvested no longer showed quantifiable green fluorescence. As a result, we could only quantify red nuclei and make the assumption that a decrease in the number of red nuclei implied that the cells had entered the cell cycle (as validated by using nuclei counts from the pilot studies with fresh tissue that had both red and green fluorescence in a Pearson's correlation statistical test). However, we accept that loss of the red fluorescence could also result if cells were in G0 or due to misidentification of the cell cycle by the CDT1 reporter (Grant, Kedziora et al. 2018).

When comparing tissue sections between hearts, variability in infarct size and position could lead to issues when assigning regions to infarct, border zone or remote data sets. However, as the neonatal mouse heart is small it was routine to take sections through the entire heart and regions for analysis were carefully selected based on the suture position and areas of visible tissue damage.

4.4 DISCUSSION AND CONCLUSIONS

4.4.1 CELL CYCLING VARIATIONS ACROSS THE HEART AFTER INJURY

From the first chapter we knew that P1 hearts can recover muscle mass and heart function after MI surgery while P7 proceeds to cell loss, permanent scarring and reduced function. In this chapter we wanted to see if we could map where cell recovery was occurring and annotate any differences between these two cohorts.

We used the R26p-Fucci2 mouse model to monitor cell cycling activity across the myocardium in neonatal pups that had MI ligation or sham surgery at either P1 or P7. At the experimental endpoint of 4 days post-surgery, we removed the hearts and prepared them for immunofluorescent staining and imaging. We imaged 21 areas spanning the lengths of the free ventricular walls and the interventricular septum, both atria and the base and apex of the heart to comprehensively map the regions close to the injury as well as those more remote. We counted cells marked by the

mCherry Fucci2 probe as G1 and correlated that the majority of the remaining cells would be in S/G2/M. Four days after MI, the P1-injured heart responded by having more areas of active cell cycling than the P7-injured one, and the location of these areas was also different.

Comparing the uninjured hearts at P5 and P11 showed no significant differences between these apart from an interesting peak in activity (shown by a drop in G1 labelled cells) in the LV mid-region of the P11 hearts. This occurs at a similar time-point to the dip in heart rate that we saw in the MRI study and may be related to the controversial increase in cell cycling activity at 2 weeks of age connected to the burst of thyroid hormone that has been reported in the literature, although this would require more investigation. After MI injury, these two cohorts differ significantly, with the P5 MI having more cell cycling activity across all 5 points of the LV and also 2 points in the IVS when compared to P11 MI. Compared with age-matched shams, the P5 MI group showed significantly more activity at all 5 points of both the LV and IVS as well as 1 point in the RA and the base. The RV, LA and apex were similar to the shams. Overall, the P11 MI cohort responded less strongly and in fewer regions: only 1 point in the LV had more activity than the sham. Interestingly, the IVS did show 3 points of increased cell cycling in addition to 2 points along the RV and LA which we did not see for the younger hearts, so while the response is less, it does extend more remotely.

A few other studies looked at a single point in each area at embryonic and neonatal timepoints. A 2014 study done by the Hashimoto group (Hashimoto, Yuasa et al. 2014) used the then newly developed Fucci-red (FucciG1-#596) and Fucci-green (FucciS/G2/M-#504) transgenic mice strains (both using the CAG promotor) to look at cycling cells in sections of embryonic E18.5 right ventricles to confirm that these Fucci markers were co-expressed with CMs stained with Nkx2.5. They proceeded to use this to look at developing CMs from mice at 8 ages (E11.5, E14.5, E18.5, P1, P3, P5, P7 and P9W (nine weeks old)) in 5 areas of myocardium: RA, LA, RV, LV and IVS. They noted that the percentage of CM in G1 increased from a low at E11.5 to a high of nearly 100% at P9W, with a slight dip at E18.5. Correspondingly, the S/G2/M ratios were highest at E11.5 (just over 20%) and dropped to nearly 0% by P9W. There was an interesting small peak of G1/S phase CMs at E18.5 in all 5 regions which matched the dip in G1 cells, and importantly, they did not observe any significant differences between these regions at any point in the study. Closer inspection of the developing RV myocardium from E11.5 to P1 showed statistical differences between the compact and trabecular layers at E11.5 and E14.5 but no difference by E18.5 or P1 of S/G2/M cardiomyocyte numbers - compact myocardium dropped from

approximately 50% to 5% at P1, while trabecular myocardium ranged from less than 20% at E11/5 to 10% at P1.

Another group (Hirai, Chen et al. 2016) looked at cell cycling across the myocardium during embryogenesis to early postnatal using Troponin T-Cre;CyclinA2-LacZ-EGFP mice. CyclinA2-GFP was expressed from mid-G1 to mid-M phases and the Tnt-Cre restricted it to CM. They chose this system over Fucci so the other fluorescent channels were free for other markers. They also used Volocity software to generate tiled images across the slice of IF stained myocardium and ImageJ to count cells. From E10.5 – 14.5, they saw CyclinA2-EGFP labelled cells in the ventricular compact zone but not the trabeculae, and that the rate of cycling activity gradually reduced over this time, and continued after birth to P10. They noted that immediately after birth (P0-P1) there was less cell cycle activity of CM in the RV relative to LV and IVS. They speculated this may be a result of reduced pressure experienced by the RV and may contribute to the difference in final size (thickness) between these walls. They were also interested in the speculated P15 proliferative burst of CM so used their model to investigate – their results showed no such burst occurred, that there was a steady decline in activity from P14 to P20 within the LV wall. This result corroborated their earlier review article which compared results from four studies and concluded that the observed burst was more likely due to increased cell cycle activity which resulted only in increased ploidy rather than actual numbers of cells (Hirai, Cattaneo et al. 2016).

A more recent study by the Soonpa group showed that certain strains of mice expressing a genetic variant of troponin (tnni3k) had increased S-phase activity in the remote myocardium and infarct border zone following MI ligation over mice that did not have this variant (Soonpaa, Reuter et al. 2023). This study retrospectively looked at four adult mice 2 weeks post injury and they noted the difference was not there in the infarct zone itself. They defined a border zone 1000μm wide, centred on the line demarking the injured myocardium with the healthy section, the infarct area was apical to this border zone and the remaining ventricular tissue in the LV, RV and IVS was the remote region. They used a non-infarcted heart as a control and, by counting nuclei, compared percentages of nuclei in the different zones of the injured vs control heart. They found that 48% of cells in the border zone survived after 2 weeks, and only 4% in the infarct zone. Therefore the increased S-phase activity did not seem to progress further to result in new cell generation.

Another recent study in the Fleischmann group found that after a very large infarct caused by cauterising the root of the left coronary artery (LCA) in the P1 mouse, there was an adaptive

response in the RV to compensate for the lesion injury to the LV (Hu, Malek Mohammadi et al. 2024). They saw prominent myocyte expansion and proliferation in the RV which lead to increased RV mass and preserved heart function. The LV also responded with CM division and binucleation as well as revascularisation. Interestingly, the large injury caused by LCA root cauterisation mostly affected the middle layer of the myocardium, leaving the inner and outer layers of myocardium along with the epicardium and endocardium intact. This response was gone by P3 and if they performed the same injury it lead to heart failure and death within a week.

These studies indicate that there is a growing interest in mapping cell cycle activity across the whole myocardium after adult MI injury. As far as I'm aware, our study was the first time this had been mapped so finely across the entire neonatal myocardium, and also after injury, comparing MI cohorts against control shams with the specific intention of noting differences between P1 regenerating and P7 repairing myocardium.

4.4.2 USING pHLIP TO MAP AREAS OF ACIDITY ACROSS THE DEVELOPING AND INJURED MYOCARDIUM

Continuing our study of the neonatal mouse heart, we injected a marker of acidic tissue into mice aged from P1 to adult to see if we could demonstrate areas of low pH in the developing myocardium. This small peptide marker, pHLIP, has been used in cancer research to reliably label acidic tumour tissue and we wanted to repurpose it for use in investigating heart development. It was conjugated to a fluorescent dye and whole slice tiled imaging was performed to map any labelled areas. First we tested pHLIP for any possible adverse effects after administration to neonatal mice as previously it has only been used in adult mice (Andreev, Dupuy et al. 2007) and found it was well tolerated by the pups as well as the nursing dams for the 24 hour test period. We determined that the dose of pHLIP needed to be adjusted for body weight, and that also the intensity of the signal was dependent on the injection method: subcutaneous injections needed more time than direct intravenous injections to reach all areas of the body, as determined by brightness of the heart (variable) and control kidney tissue (consistently bright).

We injected pHLIP into P1, P7, P21 and adult wildtype CD1 mice. After correcting for any possible differences in perfusion and post-harvest tissue processing, we saw that both P1 and P7 have distinct regions of acidity in the endocardial areas lining the ventricles as well as in the atria.

These have mostly dissipated by P21 and were completely absent in the adult hearts, confirmed by quantifying the pHLIP signal relative to the co-injected perfusion marker Hoechst 33342 and analysing the histogram of intensity level ratios. As far as we know, this developmental study of acidic niches in the heart is the first direct investigation of this aspect of heart physiology, although much research has been done in how acidity directly affects CM properties such as contractility and expression of sarcolemmal ion channel proteins. It corroborates the large body of developmental studies into hypoxic areas of the heart (as discussed in the introduction to this chapter). The inner myocardial walls are still highly trabeculated at birth, and compaction to form the mature endocardium occurs gradually, not yet complete by the end of the first week of life but complete by P28 (Tian, Hu et al. 2014). As this region remains less vascularised than the compacted areas of the myocardium, it is conceivable that the reduced perfusion would contribute to the buildup of acidity from metabolically active cells. A study by the Zhou group has shown that the majority of cycling cardiomyocytes in adult mice are located in the subendocardial layer of the left ventricle (Liu, Pu et al. 2021). They developed a CM-specific variation of their new method, "ProTracer", to label a cell cycle marker such as Ki-67 with a link to a reporter gene such as GFP. The system can be activated with a timed dose of tamoxifen which triggers the link and permanently marks TNNI3-expressing CM in the cell cycle with the fluorescent dye (Figure 76). They did not look at neonatal mice in this study, but it is interesting that the regions of cycling activity match those of our acidic niches in neonates. However, this may not be induced by increased acidity as the mature vascular perfusion in the adult inner myocardial wall (IMW) might be removing the metabolic output of these cycling CM unlike in the neonate situation.

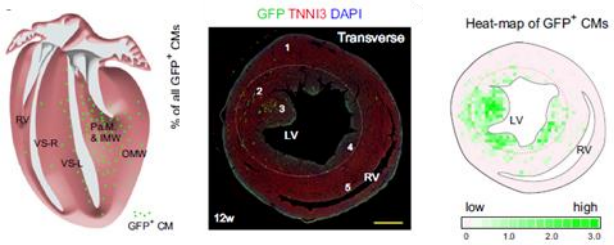

Figure 76: Cardiomyocyte specific ProTracer identifies CM cell cycle activity in an adult mouse heart. The IMW of the LV is labelled with TNNI3^{+}-GFP^{+}-Ki67^{+} cells indicating they are active in the cell cycle. From *"Cell proliferation fate* mapping reveals regional cardiomyocyte cell-*cycle activity in subendocardial muscle of left ventricle"* (Liu, Pu et al. 2021)

To map regions of acidity in an injury model, we injected pHLIP into adult rat hearts after cryoinfarct injury. If the injury was severe, we observed a bright pHLIP signal focussed at the damaged tissue where the cryoprobe impacted the myocardium as soon as 4 DPI, and we also saw a generalised response across the heart with the epicardium and atria being particularly bright.

Other studies (Riley and Smart 2009, Smart, Bollini et al. 2011, Leinonen, Emanuelov et al. 2013, Bollini, Vieira et al. 2014) noticed activation of the epicardium in the adult heart after injury with mobilisation of epicardial cells into the underlying myocardium and also suggested cell activation in the atria. Five weeks after major injury, the thinning infarcted area showed an intense transmural acidic signal which extended up into the lower endocardial regions, some signal remained in the atria but the epicardium was no longer labelled. With hearts that sustained a milder initial injury, we saw a general increased acidity across the myocardium up to two weeks post injury These regions were not present in the time, age and species matched sham control hearts. Previous work from our group has shown that the high[l-^{13}C] lactate signature in the rat heart at three and seven days post MI was associated with high numbers of activated monocytes and macrophages which are highly glycolytic (Lewis, Miller et al. 2018).

We examined the contractile proteins Crip2 and Troponin T2 in the cryoinjured adult rat myocardium in tissue slices adjacent to where the pHLIP slices were positioned. Tnnt2 is the predominant troponin isoform in mature cardiac muscle (Park, Gaze et al. 2017). This staining was done before we obtained the final results from the Fucci cell cycling counting study, so at that time we did not know about the cell cycle activation in the remote regions of the P7 mice hearts. The clearly labelled areas of reduced contractile proteins directly within the damaged myocardium and also in the areas remote to the injury seem to match the areas where there was increased cell cycling activity post MI ligation, i.e. the lower RV and IVS had less intense signal than mid/upper IVS and LV unaffected by injury. The series of hearts with injuries ranging from severe to mild showed this loss of contractile protein staining reducing in some areas of the slice, with the least damaged heart having an even distribution across the entire myocardium. Whilst this is a preliminary result, it does fit with other work from our group (Hulikova, Park et al. 2022), and it would be interesting to investigate this with a follow up study.

The attempts to stain the pHLIP labelled neonatal mouse hearts for these contractile proteins was unsuccessful in part due to the unfixed tissue being very difficult to section thinly enough to get both an even slice and antibody penetration, but it would have been interesting to see if there was less staining in the endocardial regions where the tissue is acidic.

The only other study using pHLIP to label the infarcted heart looked at the tissue immediately after coronary artery occlusion. They saw an increase in pHLIP signal in the area at risk as would be expected in an ischaemic region (Sosunov, Anyukhovsky et al. 2013). Cryoinfarct injury differs

from ligation in that it is more of a necrotic process and tends to affect CM more than other cardiac cell types so it was meaningful that acidity was also present in the cryo-damaged myocardium and could be labelled by this marker. To date, pHLIP has not been used in any other developmental studies.

Although this was a relatively simple counting and imaging assessment of cell cycling areas and regions of acidity, it adds valuable and unique insight into how the myocardium develops and responds to injury.

4.5 FUTURE WORK

As with the previous research chapter, more automation of the image analysis would be helpful to increase accuracy and efficiency of nuclei counting. This work would also benefit from the use of the newer Fucci mouse models that express red or green fluorescence only in cardiomyocytes (such as the Fucci-Tg strain where Fucci expression is driven by the α-MHC promotor) to avoid any discussion of other cell types. It would be interesting to overlap this with Fucci2 and add other cell markers as originally intended. More immediate tissue processing is also critical as the Fucci signal is not very robust over time. For the pHLIP study, valuable insights may be gained by the combination of this acidity marker with pimodiazole or similar for hypoxia, in fact co-injection of pHLIP and hypoxia markers into Fucci mice, with the use of RNAscope to look at cell cycling markers and contractile proteins (Atout, Shurrab et al. 2022), would make a very comprehensive study for a thesis.

CHAPTER 5
(Research Chapter 3)
Fucci CM & hiPSC-CM

ISOLATED NEONATAL FUCCI AND HUMAN INDUCED PLURIPOTENT STEM CELL CARDIOMYOCYTES AND THEIR RESPONSES TO HYPOXIA AND ACIDITY

ABSTRACT

Cardiomyocyte (CM) proliferation is critical for heart development and regeneration, yet adult mammalian CMs exhibit limited proliferative capacity. This study investigates the effects of hypoxia and acidity on CM cell cycling using neonatal Fucci mouse cardiomyocytes and human induced pluripotent stem cell-derived cardiomyocytes (hiPSC-CMs) at different maturation levels. Fucci-positive CMs were isolated from P1 and P7 mouse hearts and cultured under baseline, hypoxic (via DMOG), acidic (pH 6.6), and combined hypoxic-acidic conditions. hiPSC-CMs were differentiated and cultured in standard media (Rb+) or increasingly matured in fatty acid-enriched (Mat) media, then exposed to hypoxia (2% O2 or DMOG) and/or acidity (pH 6.4) for 12 to 24 hours.

Baseline Fucci assays revealed no significant differences in cell cycle activity between P1 and P7 CMs, likely due to selective loss of mature cells during isolation. However, under hypoxia, P1 CMs exhibited a marked increase in G1/S phase cells, suggesting cell cycle arrest at the restriction point, while P7 CMs showed a delayed and much less pronounced response. Acidic conditions similarly increased G1/S fractions in P1 CMs but had minimal effects on P7 cells. Combined hypoxia and acidity uniquely promoted P1 CM progression into S/G2/M phases, indicating potential for enhanced proliferation under these conditions.

hiPSC-CMs in Mat media displayed greater maturity, evidenced by increased α-actinin and troponin I3 expression, but were more sensitive to hypoxia, with reduced cell survival and MYH7 mRNA levels. Hypoxia and acidity reduced cell cycle marker expression (e.g., CCND2, CCNA2) in both Rb+ and Mat cultures, with DMOG-induced hypoxia showing distinct effects compared to atmospheric hypoxia. Fibroblast contamination was higher in Mat media under hypoxia, emphasizing the need for improved purification protocols.

These findings highlight the differential responses of neonatal and hiPSC-CMs to hypoxia and acidity, with implications for cardiac regeneration strategies. Future work should focus on refining isolation and culture methods, integrating advanced imaging systems, and exploring TNNT2-Fucci hiPSC-CMs to further elucidate CM cell cycle dynamics.

5.1 INTRODUCTION AND BACKGROUND

Studying cell cycling in whole or slices of heart after myocardial infarct surgery at P1 and P7 has some inherent limitations such as difficulty imaging the cells plus the variable nature of the surgical results, which is amplified in the neonate situation. In this final chapter, we wanted to look more precisely at how cardiomyocytes may respond to changes in hypoxia (oxygen tension) and acidosis (pH) after ischaemic injury. Using isolated primary CMs from regenerative P1 hearts and nonregenerative P7 hearts from Fucci mice, we aimed to monitor numbers of cells in each cell cycle phase over a week of culture in different but controlled environmental conditions. We also wanted to see if we could perform similar experiments in a human system of induced pluripotent stem cells that had been differentiated into cardiomyocytes with two distinct levels of maturity.

5.1.1 CARDIOMYOCYTE CELL CYCLE AND DEVELOPMENT OF THE MYOCARDIUM

Cardiomyocyte hyperplasia and hypertrophy

Historically, cardiomyocytes were assumed to be nonproliferative when mature explaining why the adult myocardium does not regenerate to replace lost and damaged CM after injury. Immature CM divide readily and contribute to the growth of the myocardium, a process known as hyperplasia (these early cells have matched periods of karyokinesis (nuclear division) and cytokinesis (cytoplasmic division) resulting in true cell division) but when mature this growth becomes hypertrophic with each cell becoming larger but generally exiting the traditional cell cycle – reviewed in (Ahuja, Sdek et al. 2007) . Recent studies have challenged this hypothesis, saying small numbers of CM maintain their ability to proliferate when mature or possibly go through a phase of dedifferentiation which promotes disorganisation of sarcomeric structures which in turn permits proliferation (Kubin, Poling et al. 2011), although at a very low rate reported to be <1% and decreasing further with age (Bergmann, Bhardwaj et al. 2009, Bergmann, Zdunek et al. 2015, Li and Izpisua Belmonte 2016, Doppler, Lange et al. 2017, Lazar, Sadek et al. 2017). This population of cells retains embryonic or neonatal features such as smaller size, mononucleation and lower levels of oxidative DNA damage (Kimura, Xiao et al. 2015). This recent discovery, that even a small number of cells may be capable of productive cell division, has prompted the increased interest in CM cell cycling in the mature myocardium as a potential aid to heart regeneration.

Foetal CM and other cardiac progenitors are initially derived from cardiac mesoderm during early cardiogenesis, with both populations contributing to CM numbers. However, by E10.5 - E12.5 noncardiomyocytes stop converting to CM and the final numbers at birth are mostly due to hyperplasia of these existing CM with contributions from the second heart field to the outflow tract, right ventricle and parts of the atria (Rumyantsev 1991, Li, Lv et al. 2019) as described in Chapter 1: Introduction "Heart Development". Some cell types such as neurons migrate within tissues as they mature but a time-lapse imaging study using living slices of Fucci G1-#596 and Fucci S/G2/M-#504 myocardium, aged E14.5 and P1, showed that proliferating CM did not move within the slice but stayed in place. Fucci positive CM nuclei were targeted and imaged every 30-60 minutes, and their movement tracked using Imaris software, showing very little cell movement (Hashimoto, Yuasa et al. 2015).

Cardiomyocyte cell cycle and variants

The cell cycle is traditionally divided into four phases, G1 (growth or gap phase 1), S (where DNA synthesis and chromosome duplication occurs), G2, and finally M (mitosis where the duplicated and paired chromosomes are pulled apart into two nuclei and the cytoplasm is divided into two new cells which are copies of the original). This simple system is under very strict control by many factors both internal and external to the cell. The process is triggered by cyclin and cyclin-dependent kinase (Cdk) complexes that phosphorylate and thereby deactivate the retinoblastoma protein (Rb) and release E2F transcription factors. Cdks are only functional when coupled with their partner cyclin which is expressed at specific times in the cell cycle (undergoing a cyclic synthesis and degradation each cell cycle), and also when Cdk inhibitory proteins (CKIs) are inactivated. In addition, there are multiple checkpoints within the cell cycle where specific conditions must be met before the cycle is allowed to continue and progress towards mitosis.

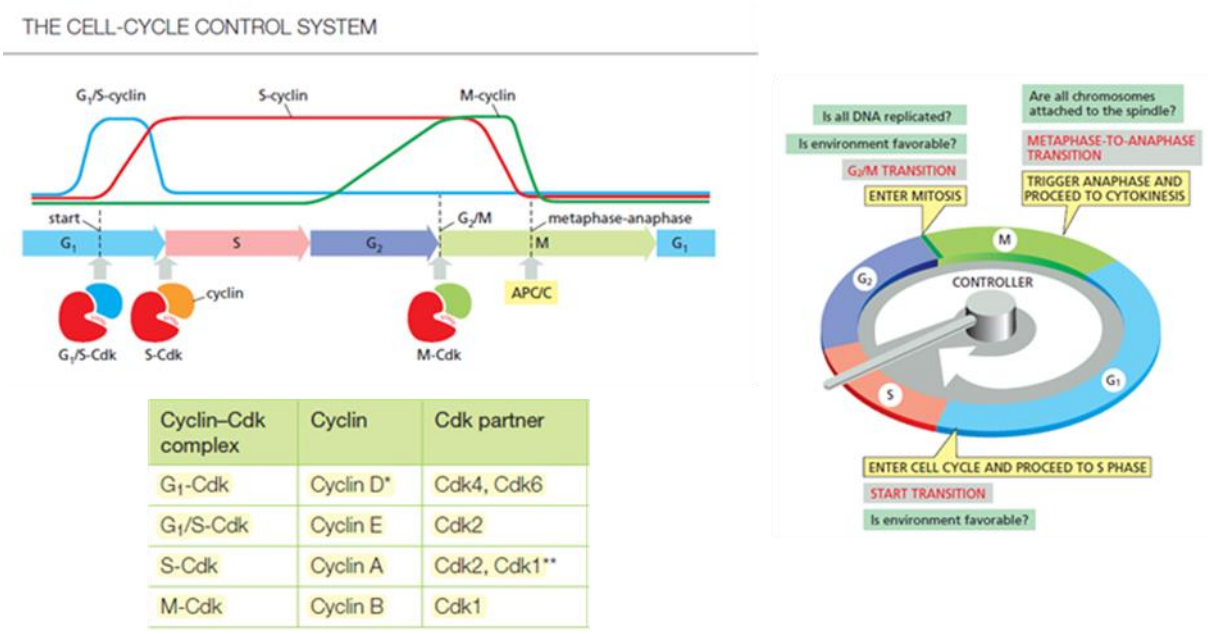

Cyclin–Cdk complex	Cyclin	Cdk partner
G_1-Cdk	Cyclin D*	Cdk4, Cdk6
G_1/S-Cdk	Cyclin E	Cdk2
S-Cdk	Cyclin A	Cdk2, Cdk1**
M-Cdk	Cyclin B	Cdk1

Figure 77: The cell cycle control system is primarily controlled by cyclical pairings of specific cyclins with their partner cyclin-dependent kinases. The cyclins are only available for specific times during the cell cycle so the kinases can only affect other proteins at these times. Numerous activating and inhibitory molecules are also involved to finely tune the system. Finally, there are 3 major "checkpoints" that need to be passed in order for the cycle to progress. Taken from *"Molecular Biology of the Cell"* (Alberts 2015)

However, this basic system (Figure 77) is much more complicated in cardiomyocytes and there are a few cell cycle variants operating as the cells mature. Polyploidy may occur through modifications in the cell cycle machinery that controls karyokinesis and/or cytokinesis. As illustrated in Figure 78, this is referred to as endomitosis or endoreplication and usually involves multiple rounds of DNA replication without fully completing mitosis, or if mitosis does complete, then cytokinesis does not, leading to cells with multiple nuclei with various amounts of DNA (Bergmann, Zdunek et al. 2011, Patterson, Barske et al. 2017, Auchampach, Han et al. 2022). The contractile apparatus of the cardiomyocytes and their physiological requirements as part of an actively beating myocardium place tight restrictions on their ability to divide even when all the mitotic factors promoting this are in place. It becomes notoriously difficult to determine true and complete cell division where one functioning CM undergoes DNA replication once followed by nuclear and then cytoplasmic division into two functioning CM. This is extensively reviewed elsewhere (Broughton and Sussman 2019, Hashmi and Ahmad 2019, Auchampach, Han et al. 2022, Zhu, Sun et al. 2022, Zhu, Yuan et al. 2024).

CM cell cycle activity diminishes shortly after birth with the downregulated expression of cyclins and cyclin-dependent kinases, which are all highly expressed during embryonic cardiac development. Cyclins A and B (which are active in cell cycle phases G2 and M) are found in embryonic and neonatal hearts but not later, while cyclins D and E (G1 and S) are present in

neonatal and young hearts. Similarly, CDKs 2 and 4 are present from embryonic to neonatal but reduced in young and adult hearts. Simultaneously, cyclin inhibitors are upregulated to promote cell cycle exit (Kang, Kim et al. 1997, Haubner, Adamowicz-Brice et al. 2012, Hashmi and Ahmad 2019). Cell cycle arrest is influenced by other factors such as increased ROS production and DNA damage, maturing contractile apparatus hindering cell division, centrosome disassembly, activation/inhibition of various molecular pathways and many more (Verbon, Post et al. 2012, Puente, Kimura et al. 2014, Aguilar-Sanchez, Michael et al. 2018, Broughton and Sussman 2019).

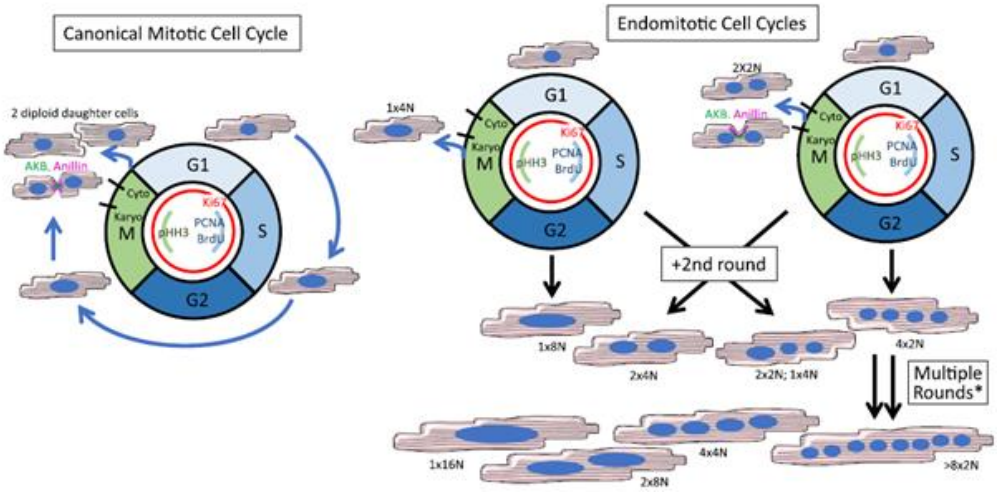

Figure 78: An alternative cell cycle occurs in some maturing cardiomyocytes which results in more than one round of DNA duplication and/or multiple nuclear divisions without actual cytokinesis. This results in cells that have nuclei with more than the standard diploid set of chromosomes as well as more than one nucleus. These variations may contribute to the lack of straightforward cell division of these cardiomyocytes. Taken from *"*Measuring cardiomyocyte cell-cycle activity and proliferation in the age of heart regeneration*"* (Auchampach, Han et al. 2022)

Effect of cardiomyocyte ploidy on regenerative potential

In all species including zebrafish, amphibians, mice and humans, developmentally early CM are mononuclear and diploid but in mammals this changes with maturation when the majority of CM become bi- or multi-nucleated and polyploid to different degrees. The timing of this ploidy switch also changes between species with it occurring in mice after one week (coinciding with the closing of the regenerative window discussed previously) (Soonpaa, Kim et al. 1996, Poss, Wilson et al. 2002, Porrello, Mahmoud et al. 2011, Zhu, Sun et al. 2022). Even among different strains of mice, the number of mononuclear diploid CM varies greatly and, most interestingly, strains that have a higher number of these cells correlate positively with better CM proliferation and functional recovery after heart injury (Patterson, Barske et al. 2017). The precise timing in humans is still unclear with some studies indicating it happens before birth and others quoting up to three months

after birth or even into adolescence and early adulthood (Xavier-Vidal and Mandarim-de-Lacerda 1995, Mollova, Bersell et al. 2013, Ye, Qiu et al. 2016)

5.1.2 HUMAN INDUCED PLURIPOTENT STEM CELL CARDIOMYOCYTES

The use of human induced pluripotent stem cells (hiPSCs) has benefitted cardiac research by providing a human model that may be more clinically relevant than animal models, especially in the areas of disease modelling and drug testing. Despite an extensive amount of research (Eschenhagen and Weinberger 2024), there are many aspects of hiPSC-CM physiology that are not thoroughly investigated. This chapter also looks at these cells under different maturation conditions and how they respond to stresses such as hypoxia and acidity that would be present after ischaemic injury.

Use of hiPSC-CM to mitigate damage after MI injury

Despite many early studies proposing the idea, it is now generally accepted that the postnatal mammalian heart has no indigenous stem cell population (Barile, Messina et al. 2007, Sultana, Zhang et al. 2015, Santini, Forte et al. 2016, Kretzschmar, Post et al. 2018) and only a very low rate of CM renewal derived from a few existing CM that are able to undergo cell cycling. After MI, with the resulting loss of massive numbers of CM, transplantation of new CM derived from IPSCs may help mitigate some of the damage. Although retention of direct intramyocardial injected IPSC-CMs is very low (estimated to be approximately 10% in best cases with most cells almost immediately lost due to leakage back through the injection channel or transported out of the area via adjacent venous and lymphatic vessels), some do remain for extended periods of time, even maturing and integrating into existing myocardium: 12 weeks to 3 months in some nonhuman primate studies (Chong, Yang et al. 2014, Shiba, Gomibuchi et al. 2016, Liu, Chen et al. 2018). New CM incorporated into gels or patches (engineered heart tissue) are more successful (2-6 times more efficient, some lasting up to 32 weeks with vascularisation occurring after 4 weeks) but still have a low success rate (Eschenhagen, Ridders et al. 2022). Some examples of engrafted cells are shown in Figure 79. Cell death is probably due to the inhospitable environment of the myocardium after infarct with lack of blood supply and resulting hypoxia and extracellular fibrosis being key factors in apoptosis. Also, these grafts are still relatively small compared to the area of initial damage so cannot provide complete recovery of muscular function. Much work is being done to

improve IPSC-CM cell survival and retention such as co-injection with hydrogels, improved injection techniques, protocols to stimulate proliferation of injected cells with increased vascularisation and pro-survival cocktails of compounds to reduce apoptosis and necrosis (Fernandes, Naumova et al. 2010, Nakajima, Fujita et al. 2015, Mitsutake, Pyun et al. 2017). Another important aspect of using injected cells is the need for long-term immunosuppression to prevent rejection by the patient's immune system. While essential and acceptable for whole organ transplantation protocols, the negative aspects are harder to justify for smaller, less invasive amounts of cells or grafts. The use of patient-derived hiPSC-CM is desirable as immune suppression is no longer needed, but it's also very costly and inefficient, so research into a hypoimmunogenic "universal donor" is underway (Meissner, Schulze et al. 2022, Simpson, Hewitt et al. 2023).

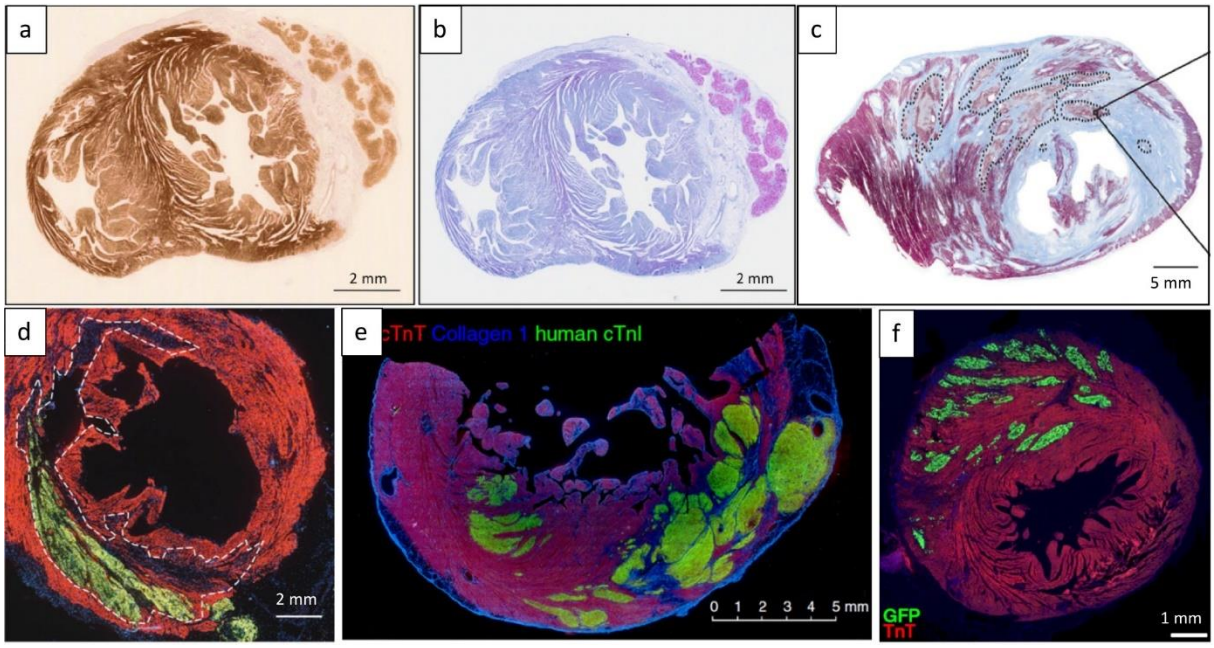

Figure 79: Remuscularisation with pluripotent stem cell derived cardiomyocytes. A,B: patch transplant; C-F: injected cells, GFP-labelled in D-F. Injected cell sources: A-C are hiPSC-CM, D-E are hESC-CM and F is cynomolgus PSC-CM. Recipient hearts: A-B are cryo-injured guinea pig, C is ischaemia-reperfusion MI pig, D-F are ischaemia-reperfusion nonhuman primate (so A-E are xenogeneic and F is allogeneic). Images A-B from Querdel et al. 2021, C from Romagnuolo et al. 2019, D from Chong et al. 2016, E from Liu et al. 2018 and F from Shiba et al. 2016. This panel *from "How to repair a broken heart with pluripotent stem-cell derived cardiomyocytes" 2022* (Eschenhagen, Ridders et al. 2022)

Cell cycling of transplanted IPSC-CM

An interesting observation within these grafts was some evidence of active cell cycling, with one study showing 24.5% of cells positive for Ki67 after 1 week, which dropped to 14.5% after 4 weeks (Laflamme, Gold et al. 2005). Other studies gave values from <1% up to 15% (Riegler, Tiburcy et al. 2015, Weinberger, Breckwoldt et al. 2016, Liu, Chen et al. 2018, Querdel, Reinsch et al. 2021).

Although this marker more accurately reflects levels of DNA replication rather than actual cell division, other studies have confirmed selective proliferation and clonal expansion of some Brainbow-labelled cells in vitro as well as after engraftment after transplantation. The size of the surviving cells has also increased by 75% in two weeks which indicates they are maturing in situ (El-Nachef, Bugg et al. 2021). This cell cycling activity was explored further in studies that used hiPSC-CM which stably express CCND2, a cell cycle activator cyclin. These cells were injected through the epicardium of mouse and pig hearts and formed larger grafts with greater functional benefits than control cells. They also had higher expression of Ki67 (22% rather than 5% in controls) (Zhu, Zhao et al. 2018, Zhao, Nakada et al. 2021).

IPSC-CM maturity

Although hiPSC-CM are an invaluable research tool that is already being used to test cardiotoxicity during drug development, they remain immature in traditional 2D culture even after long-term culture and their responses may not represent adult CM in vivo. Briefly, immature cells have different morphology with fewer and less organised sarcomeric structures which affect contractility, their membrane structures have different electrophysiological properties and they have foetal – neonatal metabolism with fewer, more immature mitochondria (Kehat, Gepstein et al. 2002, Bhute, Bao et al. 2017, Lopez, Al-Siddiqi et al. 2021). For therapeutic injection, their immature status also poses a problem, mostly as their variable electrophysiological properties due to differences in gap junction and sarcolemma proteins distribution, immature Ca^{+2} handling and lack of T-tubules leading to slower contraction signal conduction which may cause arrhythmia within the host myocardium. Their small size and different shape may also be problematic with integration (Chen, Kim et al. 2009). This situation has improved recently because of better differentiation and screening protocols for IPSC-CM increasing their maturity but it remains a concern (Tan and Ye 2018, Feyen, McKeithan et al. 2020). However, some research indicates that this immature status may also be a benefit to cell survival and engraftment as mature CM are too fragile to tolerate injection (Laflamme, Gold et al. 2005).

There are many strategies for maturing hiPSC-CM including 3D cultures, engineered heart tissue grown on scaffolds, modulating ECM, external mechanical and electrical stimulation, pharmacological and genetic manipulations, co-culture with other cardiac cell types and extended culture, reviewed elsewhere (Tan and Ye 2018, Ottaviani, Ter Huurne et al. 2023). While our study did not attempt to improve the maturity of hiPSC-CMs beyond that previously done in our lab (Malandraki-Miller, Lopez et al. 2018, Lopez, Al-Siddiqi et al. 2021), we compared cells of two

levels of maturity grown as monolayers in their cell cycle response to hypoxia and acidity. One cohort of differentiated CM was cultured in high glucose media as traditional cell culture protocols dictate, and the second had lower glucose with added fatty acids to encourage a more mature metabolic profile. Even though both cohorts were far less mature than even the P1 Fucci cells from our last study, we hoped to show some differences between the two hiPSC-CM groups, as we did between early and late neonatal mouse cardiomyocytes.

5.1.3 HYPOXIA AND ACIDITY IN CULTURED CELLS

Hypoxia in the cell

Hypoxic conditions are known to affect cell cycling by changing levels of specific transcription factors that respond to low oxygen levels, thus altering gene expression to promote conservation of energy and cell survival in these adverse conditions. Cell cycling mechanisms and their control are high energy processes and hypoxia can cause arrest in G1 or even S phase to save resources. Hypoxia Inducible Factor (HIF) is one of the main molecules responsible for the cellular response to hypoxia. This heterodimer of HIFα and HIFβ acts as a cellular oxygen sensor to manage hypoxic stress. One of the two subunits, HIFβ, is continuously present in the cell cytoplasm. The other, HIFα, has an oxygen-dependent domain (ODD) which leads to destruction of this subunit in the presence of normal cellular levels of oxygen by enzymes called prolyl hydroxylases (PHDs). For these enzymes to function, they need cofactors α-ketoglutarate, iron and molecular oxygen. The PHDs hydroxylate HIFα which creates a binding site for an E3 ligase complex which leads to polyubiquitylation and subsequent degradation via the proteosome. However, in hypoxia, the lack of oxygen allows HIFα to remain intact and bind to HIFβ, and together they translocate to the nucleus and affect HIF target genes by binding to hypoxia responsive elements (HRE) (Ortmann, Druker et al. 2014). These target genes are involved in metabolism, angiogenesis and cell proliferation, and other effects such as autophagy and apoptosis.

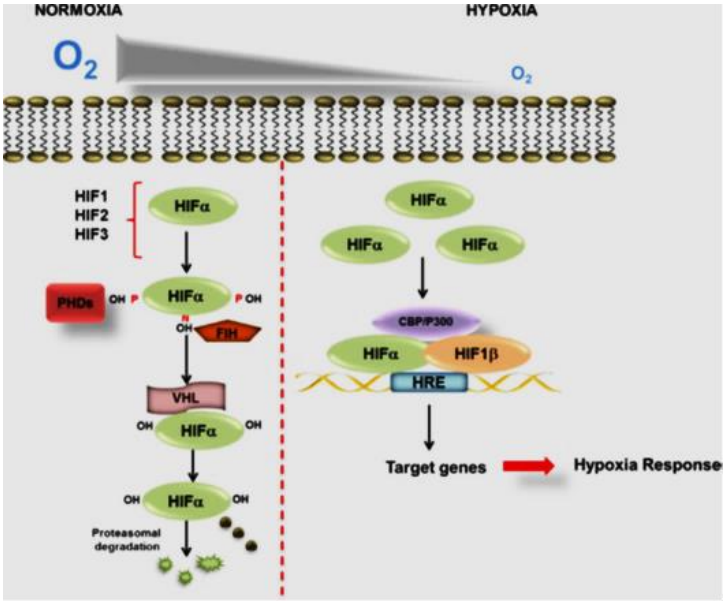

Figure 80: Hypoxia response in cells is dependent on the intracellular level of HIFα. In normoxia, it is degraded by the action of PHD enzymes which use molecular oxygen as a cofactor. The hydroxylated HIFα is targeted by the proteosome for destruction. In hypoxic conditions, the lack of oxygen allows HIFα to accumulate and bind to its partner HIFβ, enter the nucleus and affect gene transcription. *Taken from "Cell cycle progression in response to oxygen levels"* (Ortmann, Druker et al. 2014).

Hypoxia in experimental conditions

Cell culture in hypoxic conditions is usually performed in a designated incubator designed to have different levels of oxygen, nitrogen and carbon dioxide gases pumped into the sealed and humidified chamber. Standard cell culture conditions usually have approximately 20% O_2 and 5% CO_2 but a hypoxic chamber uses added N_2 gas to reduce the O_2 levels to 0.5% -5% as required. In our hiPSC-CM experiments, we used 2% O_2 levels to provide a hypoxic environment. Hypoxia can also be induced without modulating environmental gases by adding hypoxia-mimetics to the cell culture media. Dimethyloxaloylglycine (DMOG) is widely used in research models of cell culture as well as in vivo animal models to induce similar effects to physiological hypoxia that can be maintained outside a hypoxic incubator. DMOG is a cell permeable prolyl hydroxylase inhibitor, which upregulates HIF by preventing degradation of HIF-1α. However, results should be treated with some caution as DMOG also inhibits other α-ketoglutarate hydroxylases, such as the β2-adrenergic receptor (Bino, Kucera et al. 2016, Stoehr, Yang et al. 2016).

Acidity in experimental conditions

Variations in pH are larger and occur faster in cell/tissue culture conditions than in vivo as there is usually less perfusion and dynamic buffering. Cells are very sensitive to these changes which effect normal growth and function, with pH fluctuations adding stress to the system. Cellular

metabolism releases acids (mostly lactic acid via glycolysis but there are others) into the media which accumulate and reduce the environmental pH, so the media composition is critical and using appropriate buffering strategies can help maintain equilibrium. Acidity levels also depend on other conditions such as the gas mixture in the incubator, temperature, humidity and time between media changes. It is essential to closely monitor pH in cell culture experiments to produce reproducible and valid data especially when other variables are changed and compared between groups (Michl, Park et al. 2019). In these experiments, as with the Fucci cells where we varied pH between the groups, we used a combination of CO_2/HCO_3^- and HEPES buffers in custom-mixed media, with half the chamber volume replaced daily.

5.2 OVERALL AIMS

Since the second research chapter examined tissue sections across the entire heart using Fucci mice to monitor cell cycle activity after MI surgery and pHLIP to check acidic areas during development and after cryoinfarct MI, we wanted to set up a model to observe cycling activity in individual cells in more detail. Cell culture systems can be subjected to controlled variations in media composition and atmosphere, providing a more tractable system than surgery to study cell cycling in cardiomyocytes.

5.2.1 P1 VS P7 CARDIOMYOCYTES IN CULTURE

Using the Fucci mouse model, we wanted to culture primary cells from P1 and P7 hearts in a monolayer for ease of imaging to determine if there are any obvious differences in cell cycle activity over a time course of 7 days, and see if this can be influenced by environmental changes in hypoxia and/or pH.

5.2.2 hiPSC-CM RESPONSES TO HYPOXIA AND pH VARIATIONS

The final aim of my thesis was to see if hiPSC-CM of different maturity levels have any similarities to primary cardiomyocytes isolated from P1 and P7 mouse hearts with respect to cell cycling activity under hypoxic and/or acidic conditions.

5.3 METHOD DEVELOPMENT AND RESULTS

5.3.1 EXPERIMENTAL DESIGN (Part 1): ISOLATED AND CULTURED CARDIOMYOCYTES FROM P1 AND P7 FUCCI MOUSE HEARTS

The intact heart is not ideal for studying cellular responses to controlled interventions, so we implemented a cell culture model that allows monitoring of cell cycle stages with manipulation of extracellular conditions. The red and green Fucci nuclei are clearly visible in a monolayer culture system. Litters of Fucci pups at P1 and P7 were genotyped using the light torch and goggles method described previously and Fucci positive hearts were digested to yield individual cardiomyocytes which were plated for culture in 8-well plates. On consecutive days, cells in one well were co-stained with Hoechst 33342 and 20 images taken on a confocal microscope, giving a time course of 7 days. Experimental conditions tested media with or without addition of DMOG to mimic hypoxia, and also different pH levels to check responses to acidity (Figure 81).

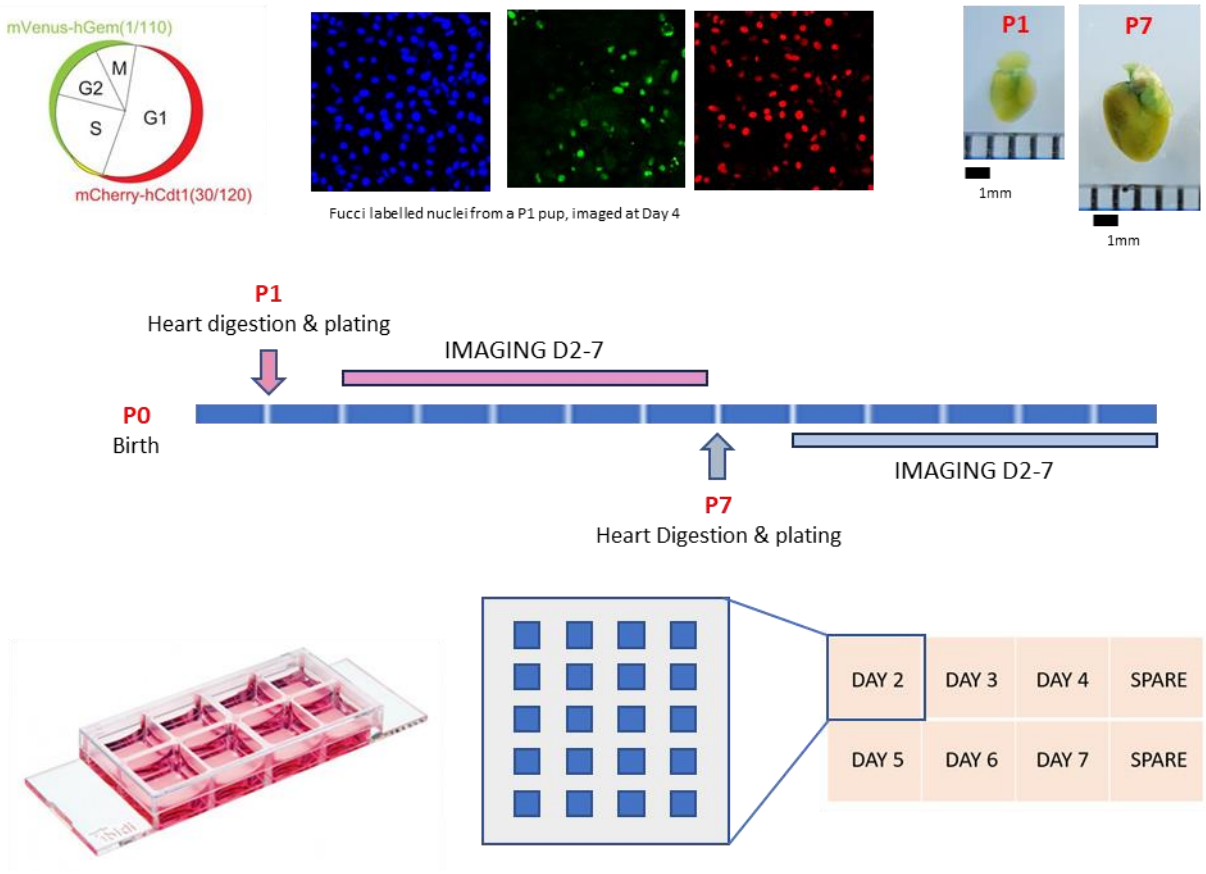

Figure 81: Experimental design for Fucci isolated cells assay. Top row L-R: Fucci fluorescence emissions during the cell cycle; confocal images of nuclei from a P1 dissociated heart showing Fucci fluorescence at Day 4; P1 and P7 hearts to show difference in size (to scale). Middle row: Experimental timeline of digestion and imaging; Bottom row: Ibidi 8-well imaging plate where the dissociated cardiomyocytes were cultured for a week; imaging pattern for one well each day (20 images).

5.3.2 FUCCI CELL ISOLATION AND CULTURE FROM P1 AND P7 NEONATAL MOUSE PUPS

Cardiomyocytes were isolated from P1 or P7 Fucci-positive mouse pup hearts removed after Schedule 1. The hearts were rinsed in ice-cold PBS buffer and trimmed to remove atria and outflow tract tissue. They were kept in fresh PBS over ice in sterile conditions until digestion. Two digestion protocols were tested – the first manual method is based on the neonatal rat heart digestion protocol that the lab used regularly to generate NRVMs, and the second was an automated, commercially available method. These are summarised below, with full details in the Appendices.

Manual digestion:

The hearts were chopped into 1mm^3 pieces and divided equally between 2 falcon tubes. The PBS was removed and replaced with 5mL of an enzyme mix of collagenase A and pancreatin. The tissue was digested with gentle stirring for 5 mins in a 37°C water bath, briefly left to settle and the supernatant (which will contain mostly cell debris) discarded. 8mL of fresh enzyme mix was added to the tissue and digested as above for 20 mins. This supernatant, now containing viable dissociated cells, was removed to another falcon tube and centrifuged to pellet the cells. After removing the supernatant with the digestive enzymes, the pellet was resuspended in culture buffer and stored in the incubator. Fresh enzyme mix was added to the remaining tissue in the first tubes and the process repeated until all the tissue was digested (Figure 82).

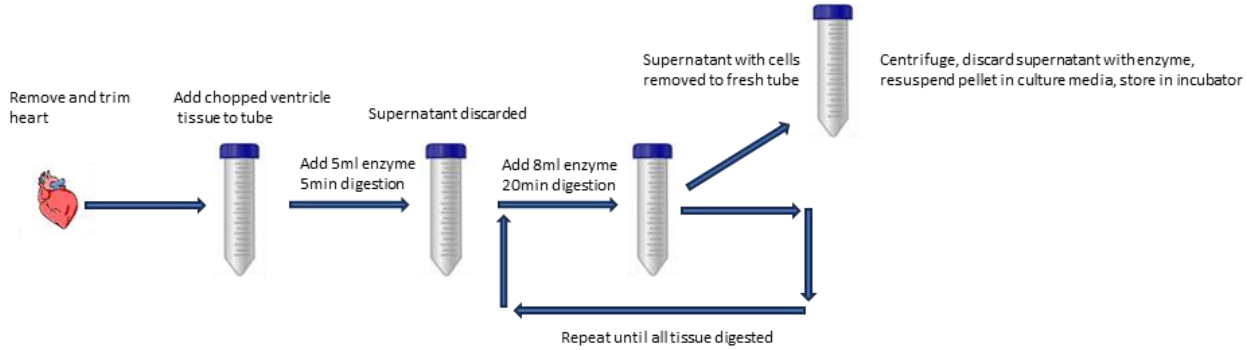

Figure 82: Manual method of heart digestion using cycles of enzymatic digestion and cell removal.

Automated digestion:

For this method we used the Neonatal Heart Dissociation Kit and the gentleMACS Octo Dissociator with Heater instrument from Miltenyi Biotec (Figure 83). This system combines mechanical dissociation with a proprietary enzyme mix for degradation of the extracellular matrix

to yield a sterile mixture of heart cell types which is suitable for cell culture or further processing such as FACS. The hearts were chopped as above and added to the C-Tubes with the enzyme mix and dissociated by a pre-set programme "37C_mr_NHDK_1" (56 minutes of stirring periods at 37°C). The C-Tubes were then centrifuged, supernatant removed and the cell pellet resuspended in M2 culture media as above.

Figure 83: Single cell dissociation of P1 and P7 neonatal mouse hearts was performed on the gentleMACS Octo Dissociator platform (left). Close up view of C-Tubes, used in the digestion process, showing the agitator cap. The tubes are positioned in the dissociator with the blue cap down so the tissue pieces are thoroughly mixed with the enzyme solution (right).

Both methods - final steps:

The cell mix was pre-plated onto tissue-culture treated 100mm cell culture plates without additional coatings for 2 hours in an incubator set at 37°C, 5% CO_2. This allowed the cardiac fibroblasts and endothelial cells to settle and attach to the surface of the plate while the cardiomyocytes remain in suspension. This suspension was carefully removed, centrifuged and resuspended in fresh culture medium. The cardiomyocytes were plated at a density of 50,000 cells per well (200,000 cells/mL) on fibronectin coated 8-well Ibidi cell culture plates and left to settle for one day. The cells were cultured in DMEM including 5% FBS, 10% HS, 20% M199, 1% P/S with 250µL per well under standard conditions: 37°C, 5% CO_2.

Comparison of the two methods and final protocol:

There are multiple factors which may contribute to variability in cell numbers using the manual digestion protocol, including precise timings of the individual digestion steps, collection of cells for each round of digestion and the need for fresh enzyme mix each day (the automated system enzymes are premixed for uniformity). Using the automated gentleMACS cell isolation system we isolated 6.57 million cardiomyocytes (0.25 million per P1 heart) from 26 P1 pups. The manual isolation method could be more productive and give up to 0.63 million per P1 heart but became inconsistent for older hearts such as P3 (0.24 – 0.52 million cells/heart) or P7 (0.27 – 0.58 million

cells/heart). For experimental consistency we decided to use the automated protocol for all the isolations for these experiments which gave an average of 0.25 (P1) and 0.37 (P7) million cells/heart. The trimmed mass of the P1 hearts averaged 12mg while the P7 hearts averaged 28mg – more than twice the ventricular mass but without twice the number of isolated CMs.

Previous cell culture studies in our lab had been developed for fast growing cancer cell lines which were seeded for short-term culture. Here we wanted to observe slower growing primary cardiomyocytes over 7 days, so we tested a range of cell seeding densities of 20,000 to 100,000 per well (80,000 – 400,000 cells/mL). We also checked a variety of coatings for the wells to see if that changed their growth characteristics: collagen (0.1% gelatine), fibronectin, laminin and the base Ibidi-Coat (manufacturers coating). The conclusion from these test protocols was that 50,000 cells per well (200,000 cells/mL density) on a fibronectin precoat maintained the cells in good condition and proliferating as expected over the 7-day observation period, so these were the conditions chosen for the rest of this study. Neonatal cardiomyocytes are glycolytic and generate large amounts of lactate but we did not want to completely replace the media as that might remove any growth factors that the cells may be releasing and thus affect the overall division rate. Therefore, we replaced half the volume of media with fresh media every second day.

Culturing cells in a hypoxic environment

Hypoxia was mimicked in our Fucci cell culture media by the addition of DMOG rather than atmospheric reduction of oxygen levels because we needed to remove the cells from the incubator for 1 hour of daily imaging. If we had used a hypoxic incubator, HIF levels would have dropped rapidly during imaging due to the presence of oxygen, which does not occur if HIF is elevated due to addition of DMOG. We did not want this daily cyclic change over six days of imaging, so we opted for the less ideal but more practical method of media supplementation. For P1 pups, DMOG was added to all the solutions used for the cell isolation including the PBS for initial heart collection, the digestive enzyme mix, and pre-plating medium at a concentration of 1uM (equivalent to 0.4% DMOG solution). Note that for the P1 pups, this was much closer to the time of birth (a relatively hypoxic in utero environment) than for the P7 pups. For P7, as it was a return to hypoxic conditions after a week of normoxia, we only added DMOG after the dissociation process at the time of cell plating. The control cells had the same volume of DMSO added instead of DMOG (as this is the solvent for the DMOG).

Culturing cells in an acidic environment

We wanted to test how this cell assay model would respond to differences in media pH which mimic extracellular acidity in the developing heart or resulting from reduced perfusion in cardiac tissue that is compromised by MI. Isolated cells from P1 and P7 Fucci pups were plated and imaged as before but with media at neutral (7.4 control) or acidic pH (6.6 – 6.7). For the P1 cells cultured in acidic media there were three separate isolations whereas for the P7 cells we were only able to use cells from two isolations due to the Covid restrictions to animal breeding facilities. However, we plated two assays from the last isolation to give a total of three assays (i.e. two of the three assays originated from the same litter of pups).

	Medium pH		Medium pH
P1 isolation #1	6.7 & 7.5	P7 isolation #1	6.7 & 7.5
P1 isolation #2	6.6 & 7.4	P7 isolation #2	6.6 & 7.4
P1 isolation #3	6.7 & 7.5	P7 isolation #2	6.7 & 7.5

5.3.3 FUCCI CELL IMAGING AND ANALYSIS MACRO DEVELOPMENT

Image collection started on Day 2, and continued daily to Day 7, the experimental endpoint. Under sterile conditions, Hoeschst 33342 was added to one well of the Ibidi plate to counterstain the nuclei – 0.3µL from stock bottle (concentration 10mg/mL) into media volume 250 – 300µL (approximately x1000 dilution). After incubating for 15 minutes, the media was removed and replaced by Hepes-buffered RPMI. Imaging was performed on a Zeiss 700 LSM confocal microscope (see Chapter 2 General Methods - Imaging) with a fixed set of parameters for each channel throughout the experiment to ensure imaging consistency and enable direct comparison of results.

A focal plane was chosen to encompass as many nuclei as possible and which was just above the plate surface to minimise green auto-fluorescence (Figure 84). Three channels were imaged sequentially for each image, and the cell images from all 20 areas in each well shown in Figure 81 were combined to give a total cell count per day. These were sorted by a custom-written image analysis Matlab macro into four categories representing the main phases of the cell cycle: Red = G1, Yellow = G1/S transition, Green = S/G2/M and Black = Late M/G0. Briefly, Channel 1 with all nuclei stained with Hoechst was used to make a mask of the areas to be analysed; then the

nuclei were checked for size, excluding those outside a set range (the larger nuclei tend to be fibroblasts in this culture mix, the smaller likely endothelial cells).

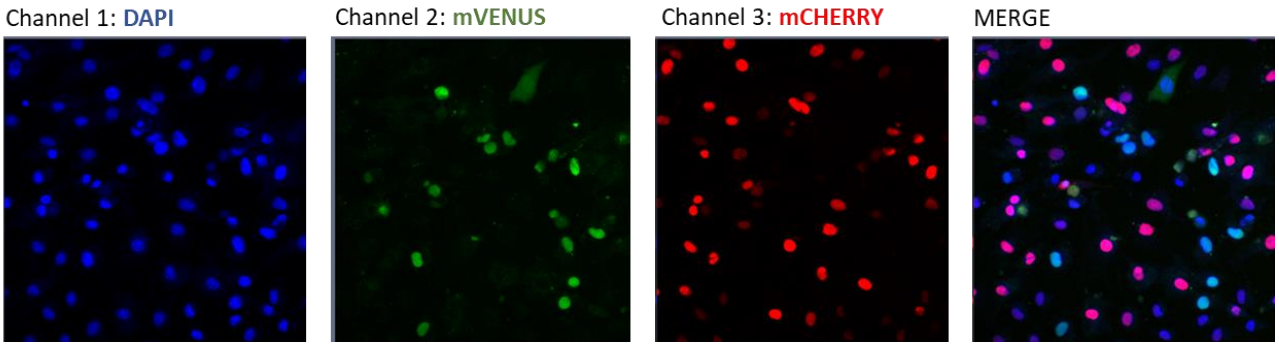

Figure 84: Sample images from one area of a single well of a P1 culture, at Day 3. 20 such images were taken from this well and added together to give a total cell count for each day.

The images were then analysed for the intensity of red and green in each selected area, with the results for each nucleus plotted on a 2-dimensional graph. The graphs for all six days of imaging were pooled and cluster analysis performed to provide a best fit division of the cells into the four categories (Figure 85). This same best fit division was then retrospectively applied to each day individually to give the daily count of cells in each cell cycle phase (Figure 86).

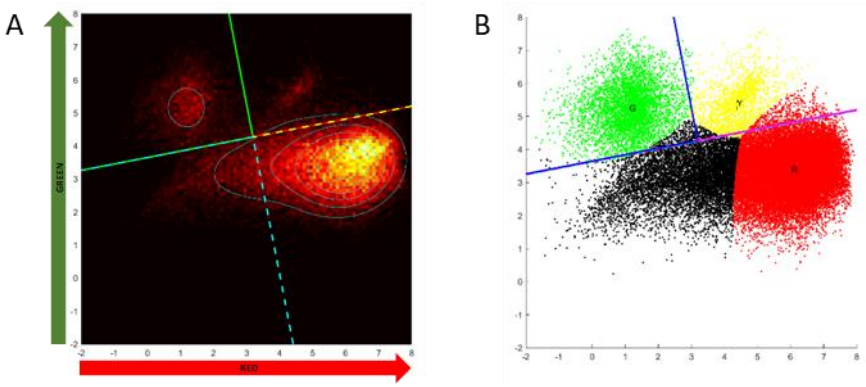

Figure 85: Cluster analysis of Fucci cells into 4 groups, each colour representing a specific cell cycle phase: Red = G1; Yellow = G1/S transition; Green = S/G2/M; Black = late M/G0.

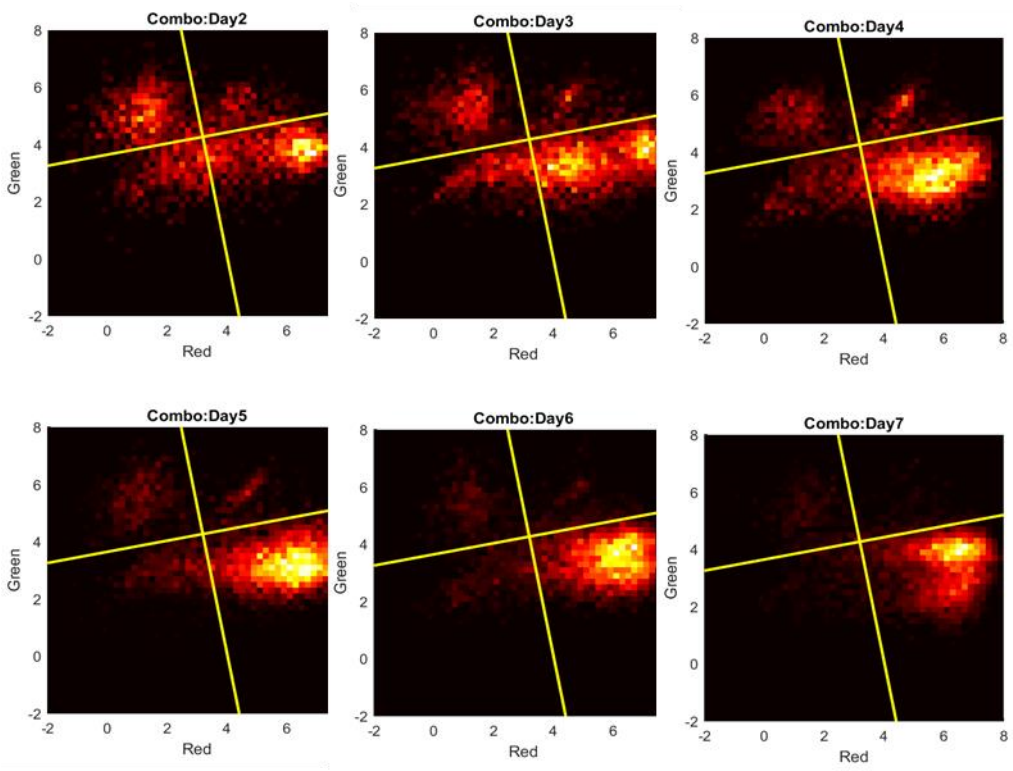

Figure 86: Cluster analysis applied to 6-day time course (Days 2-7) of cell nuclei isolated from a P1 mouse. Cell numbers in each cluster were plotted per day. There were at least three separate isolations of P1 and P7 pups which gave a minimum total of 60 images per day (some experiments had 5 isolations, while the last set with double treatment of both DMOG and low pH only had 1 isolation of P1 and 1 of P7).

The fraction of each cluster was graphed for each day as per Figure 87 discussed below.

5.3.4 FUCCI ISOLATED CELLS: P1 VS P7 WITH NO TREATMENT (BASELINE)

The first set of experiments looked at untreated cells from P1 and P7 hearts across the week of culture (Figure 87 and Table 5.1).

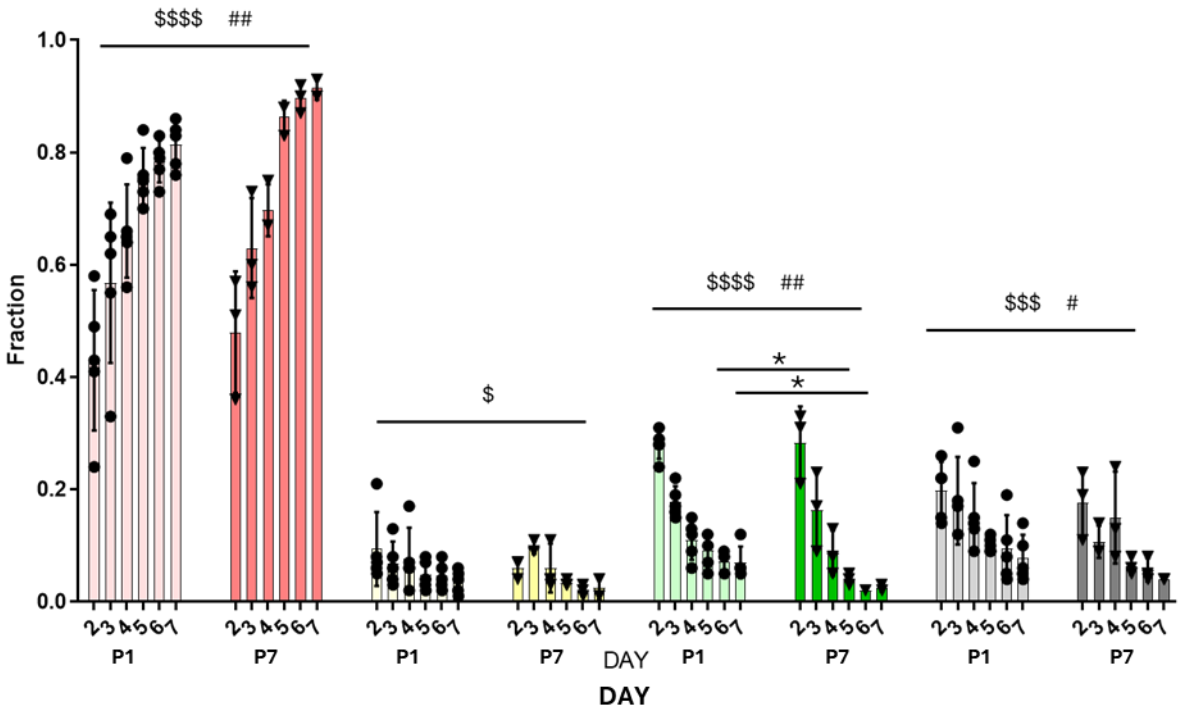

Figure 87: Daily comparison of P1 and P7 baseline cell cycle assays (P1: n=5; P7: n=3 isolations). Data for each colour (red = G1; yellow = G1/S; green = S/G2/M; black = G0) were analysed with a two-way ANOVA with Tukey post-hoc comparison; $-$$$$ indicates significant effect of time, #-## indicates significant effect of p1 vs P7 on all data; * p < 0.05 for P1 vs P7 post-hoc signficiance.

Table 5.1: Post-hoc analysis between days of culture

		Day 3	Day 4	Day 5	Day 6	Day 7
P 1	G1 Day 2	ns	**	****	****	****
	G1 Day 3	n/a	ns	*	**	***
P 7	G1 Day 2	ns	*	****	****	****
	G1 Day 3	n/a	ns	*	**	**
P 1	S/G2/M Day 2	***	****	****	****	****
	S/G2/M Day 3	n/a	*	**	***	***
P 7	S/G2/M Day 2	**	****	****	****	****
	S/G2/M Day 3	n/a	ns	**	***	**
P 1	Late M/G0 Day 2	ns	ns	ns	*	*
	Late M/G0 Day 3	n/a	ns	ns	ns	*
P 7	Late M/G0 Day 2	ns	ns	ns	ns	ns
	Late M/G0 Day 3	n/a	ns	ns	ns	ns

When the data from all four groups were analysed as a mixed effects ANOVA, there was no effect of time due to the opposing effect on the cells in G1 against those in S/G2/M but there was a significant effect of group ($p<0.0001$) and a significant interaction of time and group ($p<0.0001$). Both P1 and P7 cell populations had just under 50% of cells in G1 on Day 2, which increased to 80-90% after Day 5. Analysis of each phase of cell cycling separately, using a two-way ANOVA, showed that there was a significant effect of time for each phase although this was more significant for G1 ($p<0.0001$) and for S/G2/M ($p<0.0001$) than for late M/G0 ($p<0.001$) or G1/S ($p<0.05$). There was a significant effect of cell cohort (P1 or P7) for cells in G1 ($p<0.04$), S/G2/M ($p<0.01$), and late M/G0 ($p<0.05$) but not for cells in G1/S. Post hoc analysis showed that for cells in G1 there was a significant increase in cell fraction between day 2 and days 3-7, and between day 3 and days 4-7 for P1 cells, and between day 2 and days 4-7 and day 3 and days 5-7 for P7 cells. For cells in S/G2/M there was a significant decrease in cell fraction between day 2 and days 3-7, and between day 3 and days 4-7 for P1 cells and between day 2 and days 3-7 and between day 3 and days 5-7 for P7 cells. For cells in late M/G0 the was a small decrease in cell fraction between day 2 and days 6-7 for P1 cells. There was no significant difference in cell fraction for any groups of cells in G1/S.

In summary, over time there was in increase in cells in G1 and a decrease in cells in other phases of the cell cycle for both P1 and P7 cells. This started more quickly in P1 cells (although the difference in significance is very slight) and happened to a greater extent in the P7 cells, although this was not significant in the post-hoc analysis except for at days 5 and 6 for cells in S/G2/M. (Supplemental information Figure S-6: This data was initially analysed as a one-way ANOVA comparing P1 vs P7 for each phase for each day separately, with the fractions plotted as columns above but also as a series of line graphs: although it is not technically correct to connect the dots on these lines, it does give a good overview of the data and how the two cohorts compare over the week.

5.3.5 FUCCI ISOLATED CELLS: P1 VS P7 – HYPOXIC ENVIRONMENT

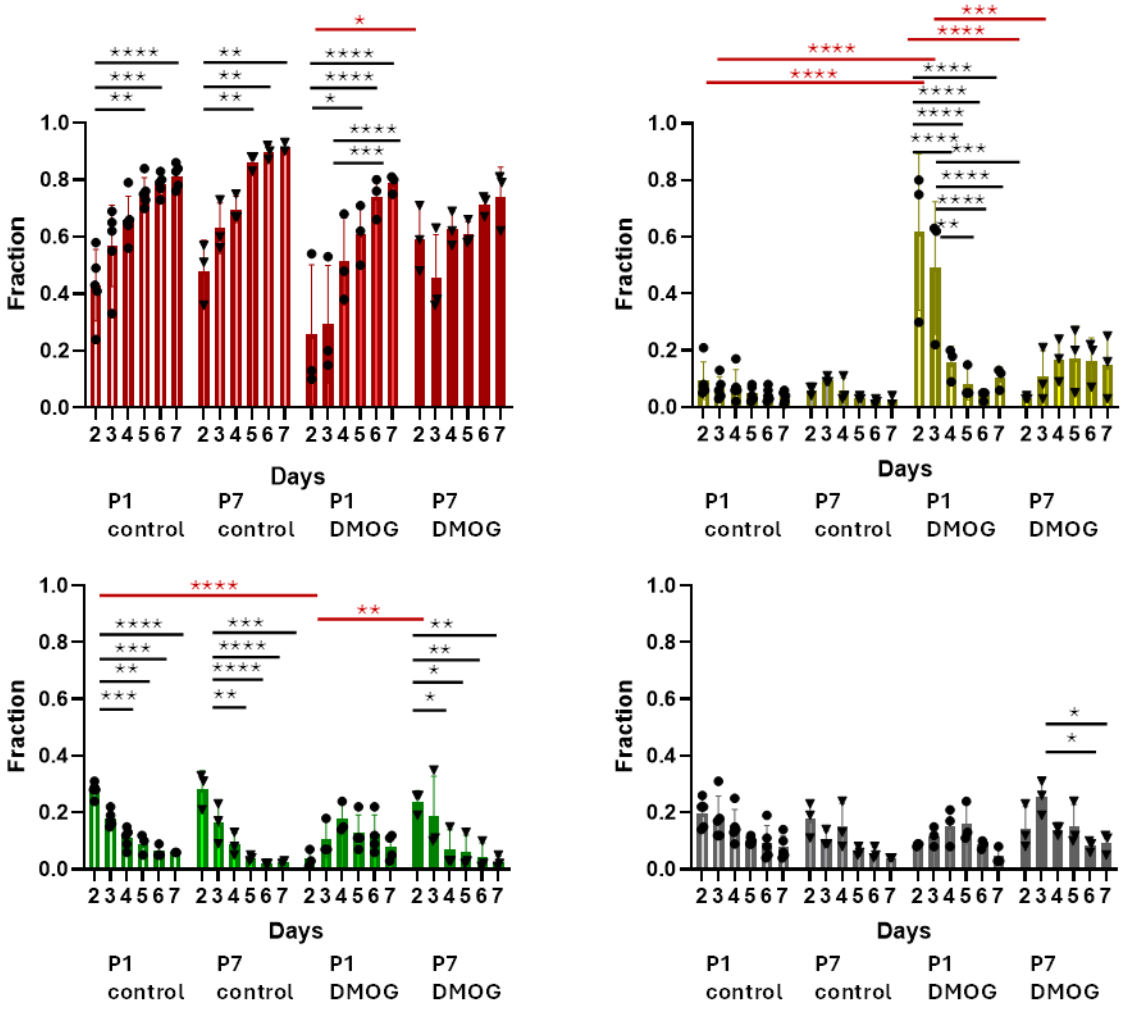

Figure 88: DMOG-induced hypoxia: Time course of the cell cycle in cultured neonatal Fucci mice cells comparing cells isolated at P1 vs P7 under DMOG treatment. n = 3 separate isolations for each group (P1 or P7). Analysed with a three-way ANOVA with Tukey's multiple comparisons test; *P<0.05, **P<0.01, ***P<0.001, ****P<0.0001, Significances between groups shown in red while within groups are in black.

Treatment of P1 cells with DMOG caused a dramatic increase in the number of cells in G1/S which was not seen with the P7 cells. The data for each phase of the cell cycle were analysed using a three-way ANOVA with a Tukey post-hoc test (Figure 88). There was a significant effect of time in all groups ($p<.0001$). For cells in G1 and G1/S, there was a significant effect of DMOG ($p<0.0001$ for both groups) and P1 vs P7 ($p<0.001$ for G1, $p<0.01$ for G1/S); for cells in S/G2/M and those in late M/G0 there was a significant effect of time ($p<0.0001$) but not of DMOG or P1 vs P7. Post-hoc analysis indicated that there was an increase in cells in G1 from day 2 to days 5-7 in both control groups and the P1 DMOG group but not the P7 DMOG group. There was also a significant difference in cells in G1 between P1 and P7 DMOG-treated cells on day 2. There was a significant decrease in cells in G1/S from days 2 and 3 to days 5-7 in the P1 DMOG treated cells but not the other groups. There was a significant increase in the fraction of cells in G1/S between

P1 control and P1 DMOG-treated cells and a decrease between the P1 and P7 DMOG-treated cells on days 2 and 3. The fraction of cells in S/G2/M decreased with time in the control cells and the P7 DMOG-treated cells but not those at P1. There was a significant difference in the fraction of cells in S/G2/M between the P1 DMOG-treated cells and both the P1 control cells and the P7 DMOG treated cells on day 2. There were few changes in the fraction of cells in late M/G0 between groups or over time. In summary, addition of DMOG initially appeared to arrest P1 cells in S-phase and prevent the transition to G2. However, this affect was lost over time such that by day 7 the level of DMOG-treated P1 cells matched that in the other groups. In contrast, DMOG treatment of P7 cells blunted the increase in cells in G1 with time.

5.3.6 FUCCI ISOLATED CELLS: P1 VS P7 CELLS - ACIDIC ENVIRONMENT

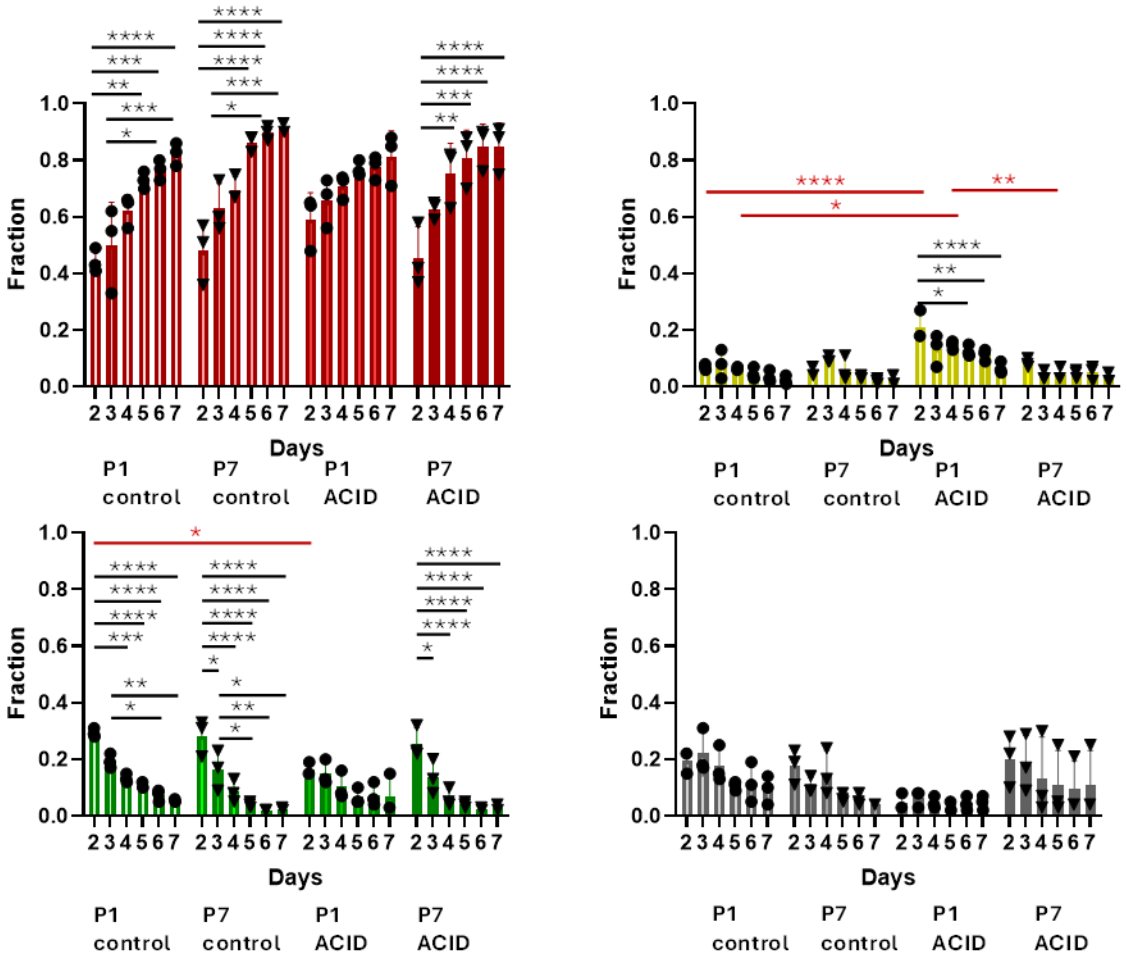

Figure 89: Time course of the cell cycle in cultured neonatal Fucci mice cells comparing cells isolated at P1 vs P7 in control or acidic media. n = 3 separate isolations for each group (P1 or P7). Analysed with a three-way ANOVA with Tukey's multiple comparisons test; *P<0.05, **P<0.01, ***P<0.001, ****P<0.0001, Significances between groups shown in red

Culture of the cells in acidic media had a similar effect to that seen with DMOG, although to a lesser extent. The data for each phase of the cell cycle were analysed using a three-way ANOVA with a Tukey post-hoc test (Figure 8). There was a significant effect of time in all groups ($p<0.05$ for late M/G0, $p<0.0001$ for all other groups). For cells in G1, there was a significant effect of pH ($p<0.01$) but not of P1 vs P7; for cells in G1/S there was a significant effect of pH ($p<0.0001$) and P1 vs P7 ($p<0.0001$); for cells in S/G2/M there was a significant effect of pH ($p<0.01$) and P1 vs P7 ($p<0.01$) but for in late M/G0 there was no effect of pH or of P1 vs P7. Post-hoc analysis indicated that there was an increase in cells in G1 from day 2 and 3 to days 5-7 in both control groups and the P7 acid group but not the P1 acid group. There was no difference in cell fraction between treatment groups. There was a significant decrease in cells in G1/S from days 2 and 3 to days 5-7 in the P1 acid-treated cells but not the other groups. There was a significant increase in the fraction of cells in G1/S between P1 control and P1 acid-treated cells at day 2 and 3 and a decrease between the P1 and P7 acid-treated cells at day 3. The fraction of cells in S/G2/M decreased with time in both the control groups and the acid-treated cells at p7 but not at P1. There was a significant difference in the fraction of cells in S/G2/M between the P1 control and acid-treated cells at day 2 but not for P7. There were few changes in the fraction of cells in late M/G0 between groups or over time. In summary, the increase in the fraction of cells in G1 and the decrease in those in S/G2/M was seen in acid-treated cells at P7 but not at P1. The increase in P1 cells at G1/S that was seen with DMOG-treatment was also seen with acid.

A parallel study in our group looked at isolated P1 Fucci CM at a single timepoint for a range of pH values. The cells were isolated as before and left to settle for 3 days. Then the media was changed to one of the 6 pH values listed below for 48 hours before imaging. The results for 7 isolations are consolidated and shown in Figure 90. This particular section of work was done with Dr. Alzbetka Hulikova.

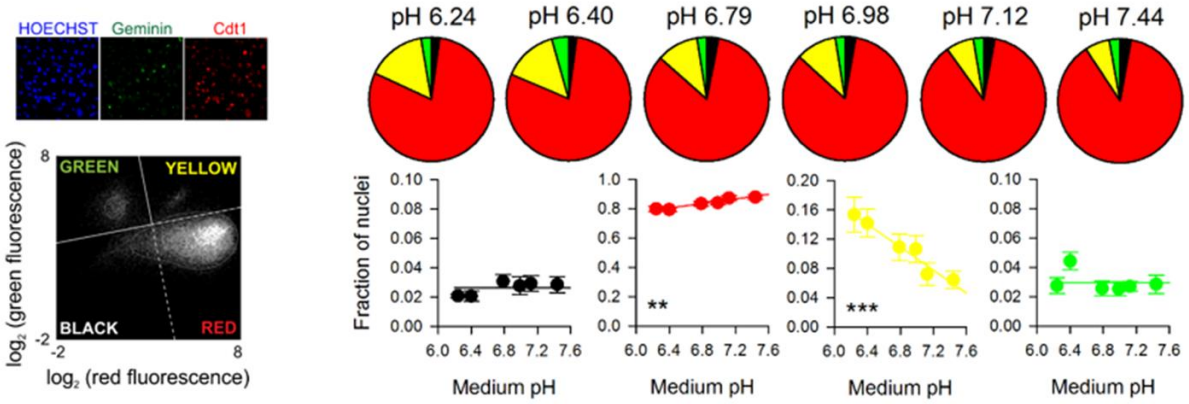

Figure 90: Fucci CM from P1 neonatal mouse pups are cultured for 48 hours in media with pH values of 6.24, 6.40, 6.79, 6.98, 7.12 and 7.44. The pie charts show the fractions of cells in each group at each pH level, and each phase is graphed below. Fraction of red/yellow nuclei was pH sensitive (**p<0.01 and ***p<0.001, one-way ANOVA).

5.3.7 FUCCI ISOLATED CELLS: P1 VS P7 WITH ACIDIC MEDIA AND HYPOXIA

In conditions of disease and cell stress such as after MI, areas of ischaemic cardiac tissue can be both hypoxic and acidic at the same time – these are two separate but related environmental situations. We wanted a final experimental situation where both of these were altered together and the combined effect on cell cycle activity monitored. Unfortunately, this set of experiments was limited to only one biological repeat due to the Covid restrictions mentioned earlier. Presented here for a brief observation are the outcomes of this single assay.

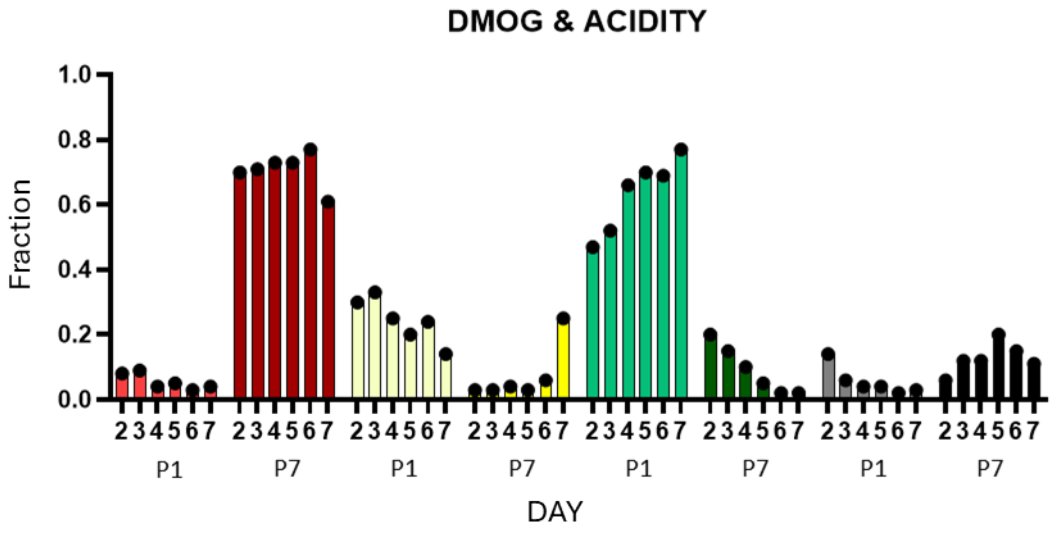

Figure 91: P1 vs P7 isolated nuclei subjected to both hypoxia (via DMOG) and acidity simultaneously. There is a dramatic response to these conditions in the P1 cells with an increase in nuclei in the last G2/M stages of cell division (green). There is no such immediate response in the P7 group but there does appear to be a very delayed increase in

cells entering S (with a matching drop in G1) after 7 days of exposure. We could not do statistics on this graph as we only had one repeat (n = 1) due to loss of the Fucci line.

There is an obvious increase in cell cycling activity for the P1 cells when the environmental conditions mimicking hypoxia and acidity are encountered together. There is a large increase in the cells in both G1/S (yellow) and this time, continuing onto G2 (green). This is the only situation observed so far where the fraction of cells in G1 (red) is low. To confirm this outcome, I checked the original heat plots of the data generated by the analysis macro (summary Figure 92 and daily breakdown Figure 93) and the result was very clear- the shift in P1 cells from Day 2 progressed daily from G1/S (yellow) to mostly G2 (green). In the P7 situation we see the cells in G1 fairly constant for the first 5 days and then a sudden drop as the fraction in G1/S finally starts to increase. This does not translate to more cells in G2, at least during this time frame.

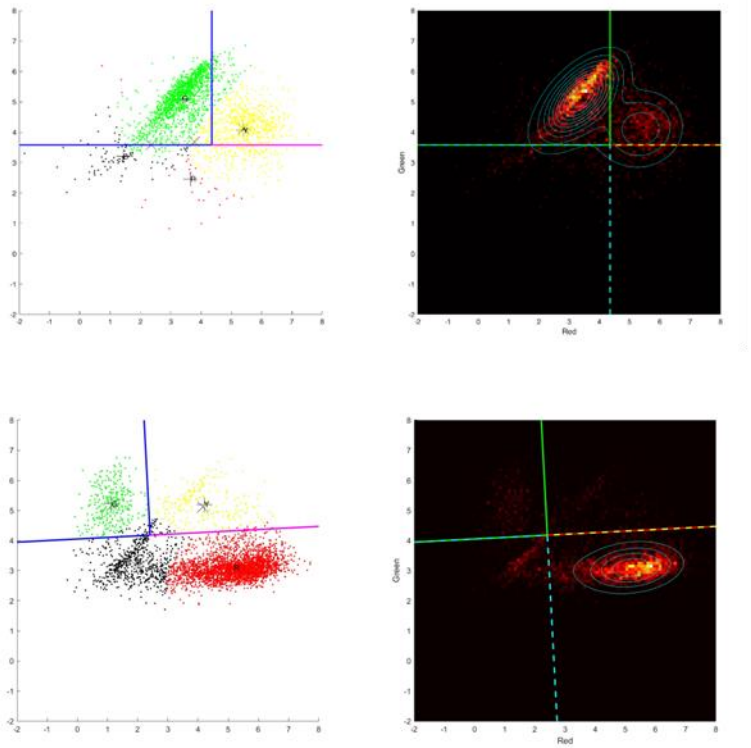

Figure 92: Cluster analysis for the P1 cells (top row) showing a clear shift to green G2/M nuclei which is not the case with the P7 cells (bottom row).

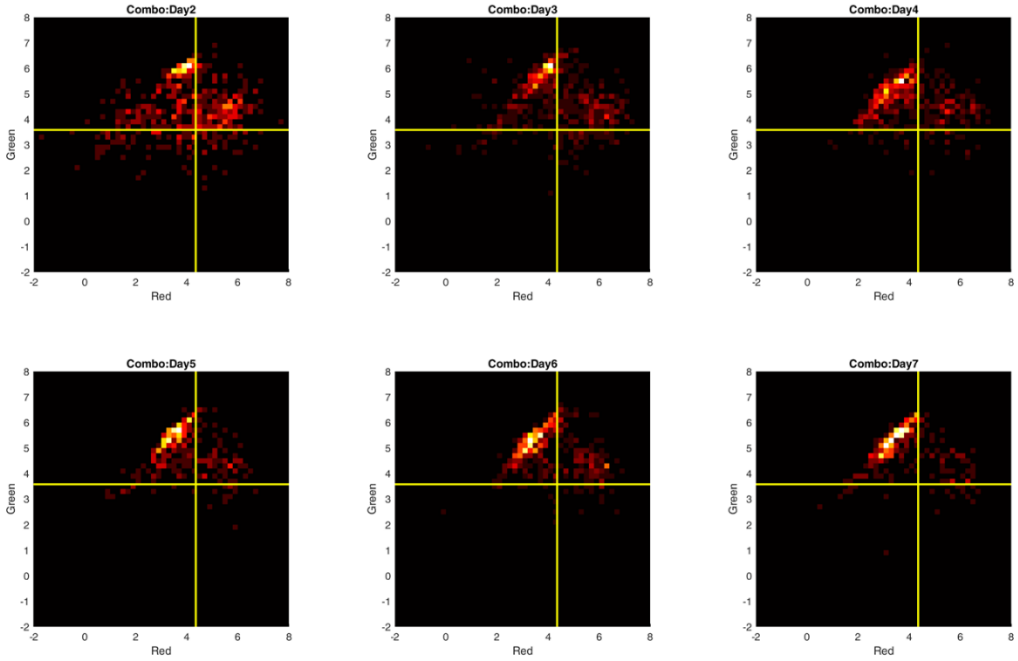

Figure 93: Cluster analysis plots (Day 2 through to 7) for the P1 cells grown in acidic and hypoxic conditions. This can be compared to Figure 86 for a P1 time course under normal conditions of pH and oxygen levels.

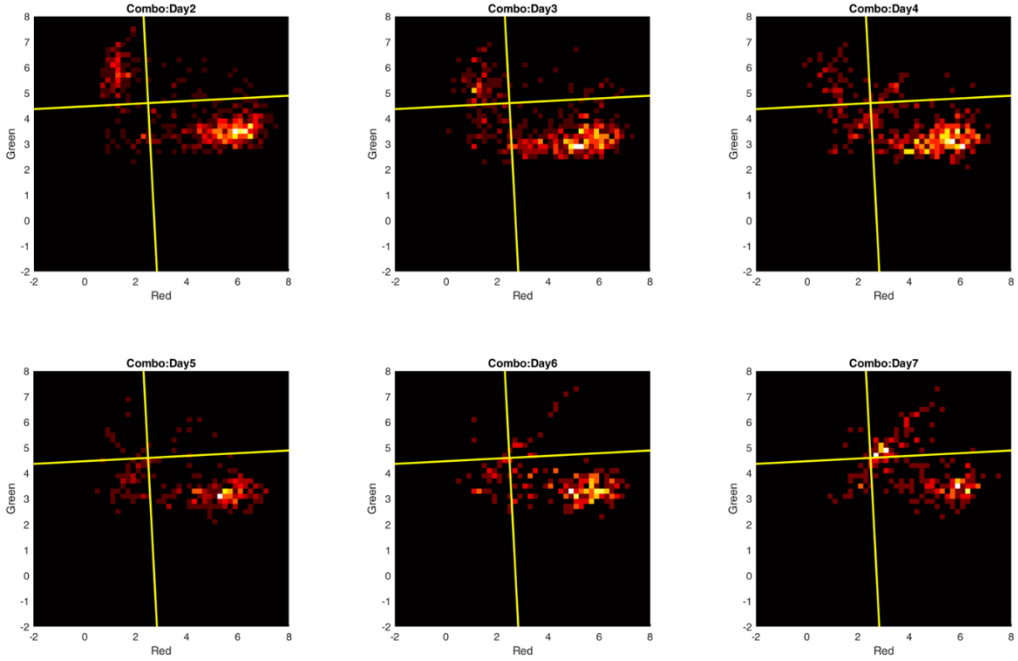

Figure 94: Cluster analysis plots (Day 2 through to 7) for the P7 cells grown in acidic and hypoxic conditions.

5.3.8 EXPERIMENTAL DESIGN (Part 2): Human induced pluripotent stem cell derived cardiomyocytes

Human induced pluripotent stem cells derived from embryonic lung fibroblasts were differentiated into beating cardiomyocytes via a precisely timed induction of the Wnt pathway (detailed below). After differentiation, the CM were either matured by addition of oleic acid to the cell culture medium or left in glucose media for a week (Lopez, Al-Siddiqi et al. 2021). Then combinations of normoxia/hypoxia and pH media were used for either 12, 18 or 24 hours, at which point the cells were fixed for immunofluorescent staining and imaging or harvested for RNA (Figure 95).

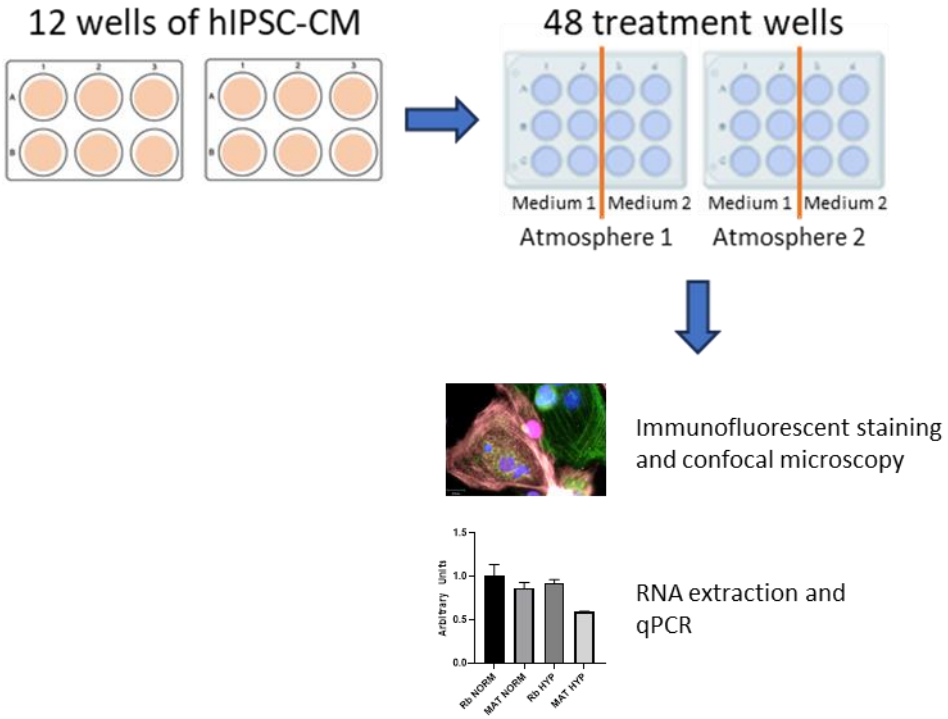

Figure 95: Layout of experimental culture wells for hIPSC-CM testing. 12 wells (each 9.6cm^2) of differentiated hIPSC-CM were replated into 48 experimental wells (each 3.5cm$^{2)}$ on 2 plates. Medium 1 = Rb$^+$ (cell culture media with high glucose); Medium 2 = MAT (maturation media containing low glucose and high fatty acids). Some experiments used Matrigel coated coverslips for IF staining and imaging, others had cells harvested for RT-qPCR assays.

5.3.9 hiPSC CULTURE AND MAINTENANCE

The hiPSC-CMs used in these experiments were differentiated from the foetal lung fibroblast cell line IMR90 which is derived from a 16-week old Caucasian female foetus (originally created by Dr James Thomson at WiCell, University of Wisconsin and given to our lab by Prof. Sian Harding,

Imperial College London). We follow a protocol based on that of Lian et al. (Lian, Zhang et al. 2013) with modifications developed in our lab to induce metabolic maturation (Lopez, Al-Siddiqi et al. 2021). Complete protocols are listed in Appendix 5, with standard stem cell culture techniques described in Chapter 2: General Methods.

5.3.10 DIFFERENTIATION OF hiPSCs INTO CARDIOMYOCYTES

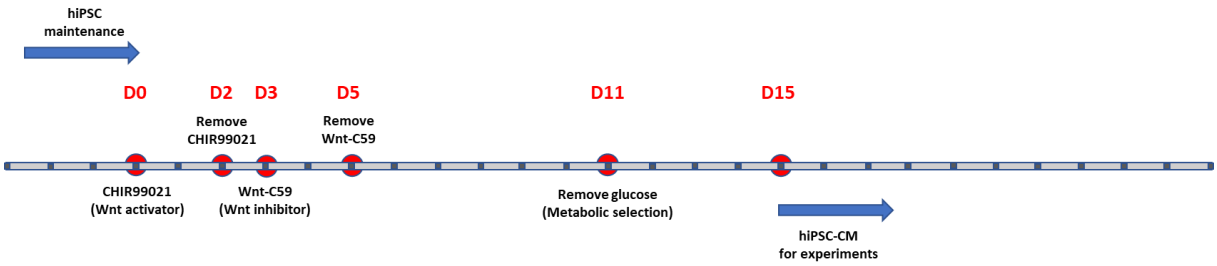

Figure 96: Differentiation timeline from IPSC to beating cardiomyocytes using timed Wnt activation. After 15 days, the cells are moved to fresh plates to mature and settle for another week, with an additional final week in either glucose or fatty acid media before use for these experiments.

The confluent wells of stem cells were differentiated into beating cardiomyocytes by adding Wnt pathway activator CHIR99021 (concentration 6μM) in Rb^- media (RPMI with 11mM glucose, 1% B27 minus insulin) on Day 0. On Day 2, this media was replaced with fresh Rb^- without any additional supplements. On Day 3, Wnt-C59 was added to Rb^- media, concentration 2.5μM, to inhibit further activation of the Wnt pathway and left for two days. On Day 5, the cells were fed with fresh Rb^- media which was replaced every second day until Day 11 when metabolic selection is performed: Met^- medium (RPMI without glucose, 1% B27 minus insulin) was used to starve contaminating fibroblasts that have not differentiated into cardiomyocytes. On Day 15, the live CMs were lifted from the 6-well plates and replated into fresh experimental 12-well Matrigel coated plates (plating concentration 1.0 – 1.5 x 10^6 cells/well). They were allowed to settle down for another 7 days in Rb^+ media (RPMI with 11mM glucose supplemented with 1% B27 plus insulin), with media changes every second day. For the immunostaining experiments, a sterile 13mm coverslip was added into each of the wells prior to coating with Matrigel and plating the cells. See Figure 96 for a timeline overview and Appendix 5 for details of the 15-day differentiation protocol.

5.3.11 PREPARING THE CARDIOMYOCYTES FOR TESTING IN DIFFERENT CONDITIONS

After this week to settle the differentiated cardiomyocytes, we prepared different experimental conditions for the two plates with combinations of the following protocols:

Maturation of cardiomyocytes by addition of fatty acids

We compared cells cultured for another week in standard Rb^+ media containing 11mM glucose with those cultured for the same time in maturation media ("Mat") containing the fatty acid oleic acid (400μM) to increase the developmental age of these cardiomyocytes by providing a metabolic stimulus. The 12-well plates were divided into two halves: Medium 1 = Rb^+ and Medium 2 = Mat (Figure 95).

Exposure to different media pH

After 7 days of either standard or maturation media, the wells were again divided into two further subgroups with either neutral pH 7.4 or acidic pH 6.4 compositions of Rb^+ or Mat medium for an additional 12, 18 or 24 hours culture. See experimental plate layout in Figure 97.

Exposure to different atmospheric conditions

In addition, one plate was left in the normoxic (20% oxygen) cell culture incubator and the other was moved to a hypoxic incubator for exactly 12 or 24 hours. The hypoxia level was 2% oxygen maintained by addition of extra nitrogen. In another set of experiments, hypoxia was mimicked by the addition of 1mM DMOG for 18 hours with cells remaining in the normoxic incubator as for the Fucci cells.

CONDITION	MEDIUM	ENVIRONMENT	PLATE #
1	Rb^+ (pH 7.4)	Normoxia	1 (3 wells)
2	Rb^+ (pH 6.4)	Normoxia	1 (3 wells)
3	Mat (pH 7.4)	Normoxia	1 (3 wells)
4	Mat (pH 6.4)	Normoxia	1 (3 wells)
5	Rb^+ (pH 7.4)	Hypoxia	1 (3 wells)
6	Rb^+ (pH 6.4)	Hypoxia	1 (3 wells)
7	Mat (pH 7.4)	Hypoxia	1 (3 wells)
8	Mat (pH 6.4)	Hypoxia	1 (3 wells)

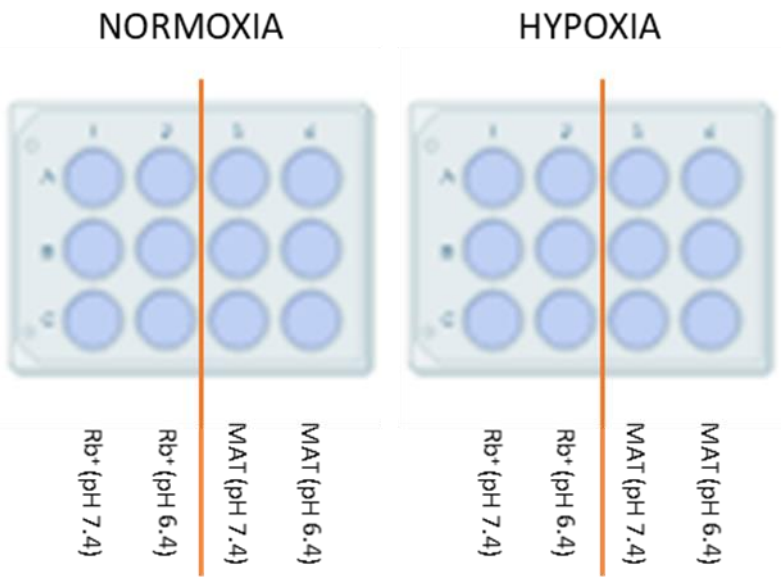

Figure 97: Graphical layout of a 12 well cell culture plates. Each plate was divided into two halves so that representative wells of each of the two media types could be on the same plate (6 wells of each type per plate). For some experiments, this was further divided into normal or acidic pH conditions (3 wells of each type). One plate remained in normoxia while the other went into hypoxic conditions for the designated period.

5.3.12 hiPSC-CM: HYPOXIA VS NORMOXIA IMMUNOFLUORESCENT STAINING

Quantifying levels of cardiac contractile proteins

Cells grown on coverslips in Rb^+ and Mat media were subjected to either 12 or 24 hours of atmospheric hypoxia or maintained in normoxia for an equal time and then stained for sarcomeric α-actinin (labels sarcomeres in muscle cells, specifically where actin filaments are connected to the Z lines), Tnni3 (labels cardiac troponin I type 3), and Ki-67 (labels cells that are actively cycling from cell cycle phase G1 through to mitosis but not those that are quiescent, i.e. G0). Hoechst was added to label cell nuclei. Please refer to General Methods – Immunofluorescent Staining for staining details.

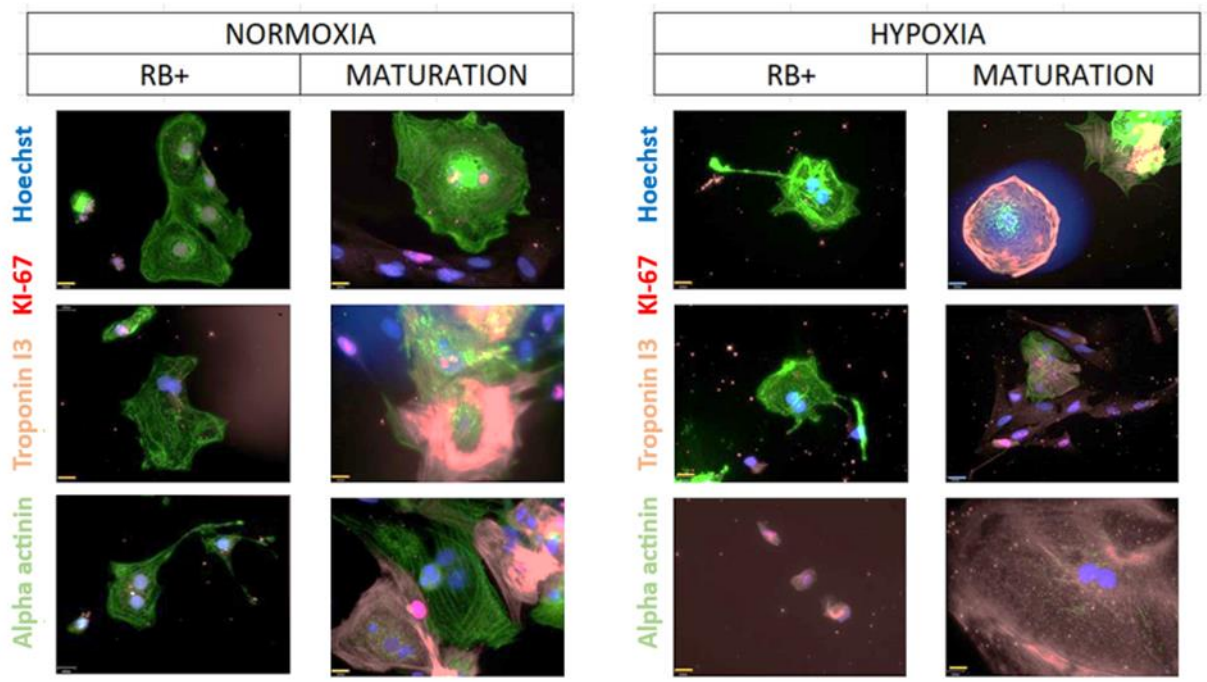

Figure 98: High magnification images of hiPSC-CM cultured for 24 hrs in Rb^+ (glucose) compared to Mat (with added oleic acid) media. While sarcomeric structures are evident in both cultures with clear α-actinin stripes visible, there is a large increase in the amount of troponin I3 fibres in the Mat cultures. This is quantified in later staining. Green=sarcomeric α-actinin; Red=Ki-67 (nuclear staining only); Magenta=cardiac troponin I type 3; Blue=Hoechst. Scale bar=16 µm (lower left corner of image).

Sarcomeric structures were visible in all four conditions, with clear striations and long fibres extending across the cells. However, as expected due to the increased maturity, there was a large increase in the amount of troponin I3 in the cells cultured in maturation media - there is an isomeric switch from troponin I1 to I3 as they mature. (Bandman 1992, Gomes, Guzman et al. 2002, Racca, Klaiman et al. 2016, Lopez, Al-Siddiqi et al. 2021).

To get a quantitative evaluation of the number of cells and their maturity, we set up a standardised imaging protocol for all the coverslips as we did for the Fucci cell quantification analysis. Each coverslip was imaged at a low magnification of 10X to get as large a field of view as possible with the channels set as follows:

CHANNEL	EMISSION COLOUR	EXPOSURE TIME	ELECTRONIC GAIN	FILTER CUBE
1	DAPI (blue)	50 ms	50	D (DAPI)
2	FITC (green)	500 ms	50	F (FITC)
3	TRITC (red)	500 ms	50	T (TRITC)
4	Far Red (magenta)	500 ms	50	FR (Far Red)

A total of nine images were taken from the same approximate locations on each coverslip to minimise bias by choosing the "best" areas:

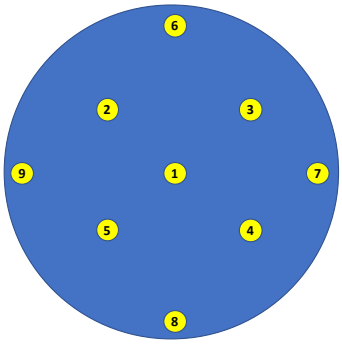

Figure 99: Layout of 9 image areas across a 13mm glass coverslip. Note the size of the yellow location spots is not to scale with the blue coverslip.

These nine images were analysed by ImageJ image analysis functions embedded in a Matlab script. Running the image analysis script to calculate the integrated density of each of the channels across all the images allowed us to compare and quantify the relative amounts of each cell marker across the different conditions (Figure 100).

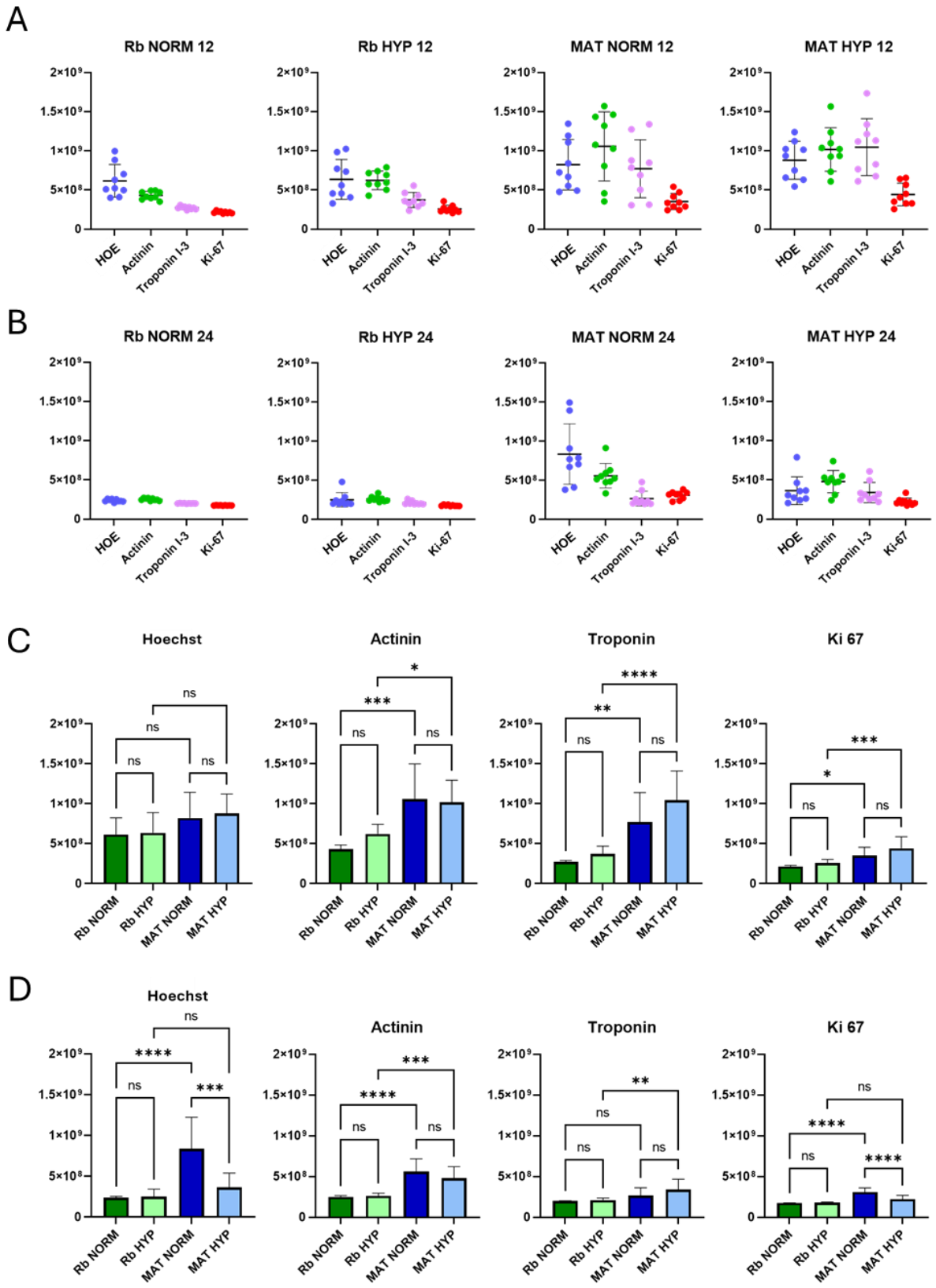

Figure 100: Comparing integrated density (Y axis) for each channel between normoxic and hypoxic culture conditions in Rb^+ or Mat media with quantification and comparison of each marker for all 4 conditions after 12 (A, C) or 24 (B, D) hours. One-way ANOVA with Tukey's multiple comparisons, **** p<0.0001; *** p<0.001; ** p<0.01; * p<0.05.

Comparing normoxia with hypoxia after 12 and 24 hours:

Cells were cultured in Rb^+ or maturation media for one week and then either kept in normoxia or transferred to hypoxia for 12 or 24 hours. Confocal analysis confirmed that a week in maturation medium increased the expression of the contractile proteins α-actinin and Tnni3 and this was not affected after 12 or 24 hours of culture under hypoxia. Ki-67 fluorescence was also higher in cells cultured in maturation medium under normoxia ($p < 0.0001$), but this increase was lost after 24 hours in hypoxia. There were more nuclei in the group cultured in the maturation media under normoxia in the 24 hour group, however, this increase was lost when cells were cultured in hypoxia for 24 hours ($p = 0.0003$). This is summarised below:

	Mat medium higher than Rb medium Normoxia higher hypoxia		
		12 hours	24 hours
HOE	Rb Norm vs Rb Hyp	ns	ns
	Mat Norm vs Mat Hyp	ns	***
	Rb Norm vs Mat Norm	ns	****
	Rb Hyp vs Mat Hyp	ns	ns
Actinin	Rb Norm vs Rb Hyp	ns	ns
	Mat Norm vs Mat Hyp	ns	ns
	Rb Norm vs Mat Norm	***	****
	Rb Hyp vs Mat Hyp	*	***
Troponin I3	Rb Norm vs Rb Hyp	ns	ns
	Mat Norm vs Mat Hyp	ns	ns
	Rb Norm vs Mat Norm	**	ns
	Rb Hyp vs Mat Hyp	****	**
Ki67	Rb Norm vs Rb Hyp	ns	ns
	Mat Norm vs Mat Hyp	ns	****
	Rb Norm vs Mat Norm	*	****
	Rb Hyp vs Mat Hyp	***	ns
Significance:	(**** p<0.0001; *** p<0.005; ** p<0.01; * p<0.05)		

Figure 101: Summary of differences in expression of contractile proteins and Ki67 in Rb^+ or Mat media for 12 or 24 hours.

Comparing individiual dividing/non-dividing cardiomyocytes

An interesting check of individual CMs expressing Ki67 in their nuclei showed that the surrounding cytoplasm had less troponin I3 than in cells not expressing Ki67, while having similar levels of α-actinin. Using high magnification images of cells in Maturation media in normoxic conditions, and zooming into individual cells that expressed Ki67, a circular area of fixed size was

drawn centred around the nucleus, only selecting cells that were surrounded by α-actinin. Within this area, the integrated density of the four channels was recorded. We could see that these cells had significantly less troponin I3 than cells without Ki67 expression.

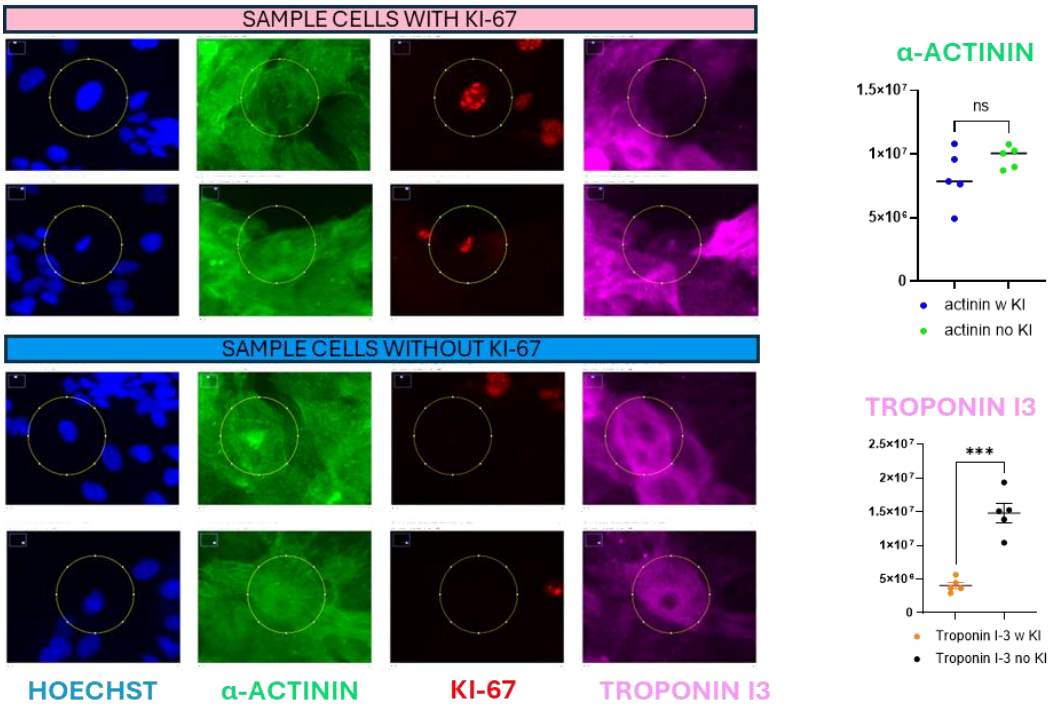

Figure 102: Integrated intensity analysis of Troponin I3 comparing cells with Ki-67 to those without it (Maturation media, normoxic environment). Sample cells from each category are shown, and the analysis area is outlined with a yellow circle. While the cells contained similar levels of a-actinin, there was significantly less troponin I3 in cells that were actively cycling. Unpaired t-test with n=5 for both groups; p<0.001.

5.3.13 FIBROBLAST CONTAMINATION OF hiPSC-CM CULTURES

The differentiation protocol to convert IMR90 pluripotent stem cells to cardiomyocytes contains a metabolic selection step to remove contaminating fibroblasts. Although this step does kill off most of the undifferentiated fibroblasts and leave a well of approximately 90-95% beating cardiomyocytes remaining immediately afterwards, continued culture for the following days in fresh high glucose media (with or without added fatty acids), allows any surviving FB to proliferate. This can be seen as areas of non-beating cells in the growing cultures and after fixation, by absence of staining with either α-actinin or troponin I3 as outlined in Figure 103. As one of my experimental assays was cell proliferation of cardiomyocytes within the different media and their responses to hypoxia and acidity, I wanted to investigate the extent of this fibroblast contamination.

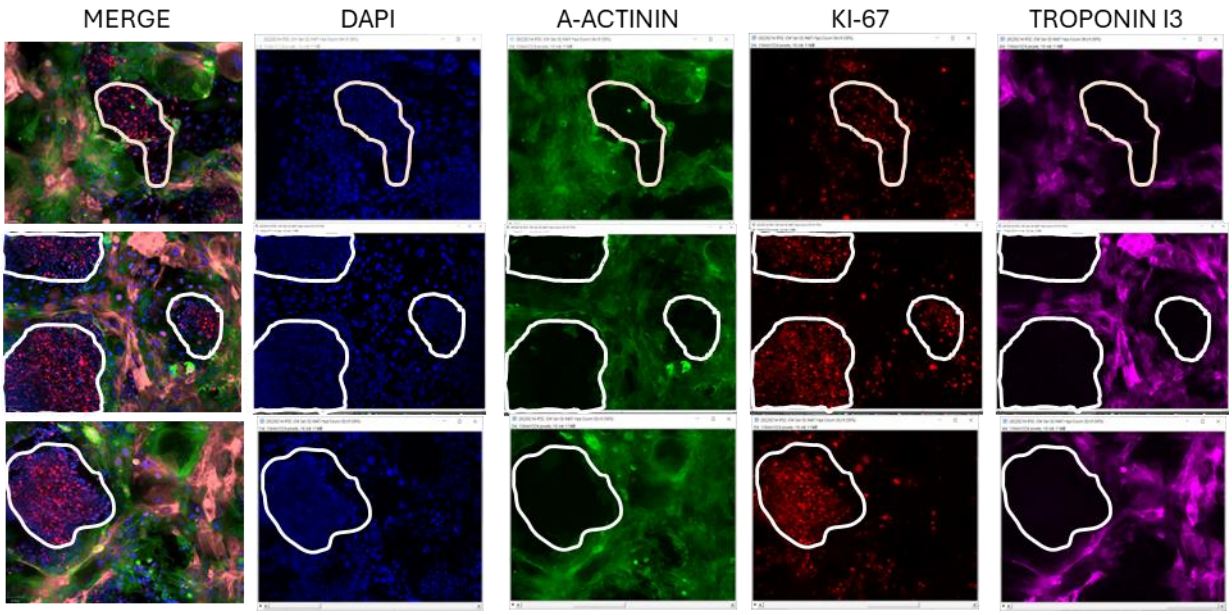

Figure 103: Sample areas outlined in white without α-actinin or troponin I3 staining that contain nuclei of actively dividing cells as labelled by KI-67. These areas may be fibroblasts. This culture is in Mat media with 12 hours of hypoxia.

Another set of coverslips from the same experimental batch that underwent hypoxia for 12 hours was stained with Hoechst, α-actinin and KI-67 as before, but now with vimentin to stain fibroblasts.

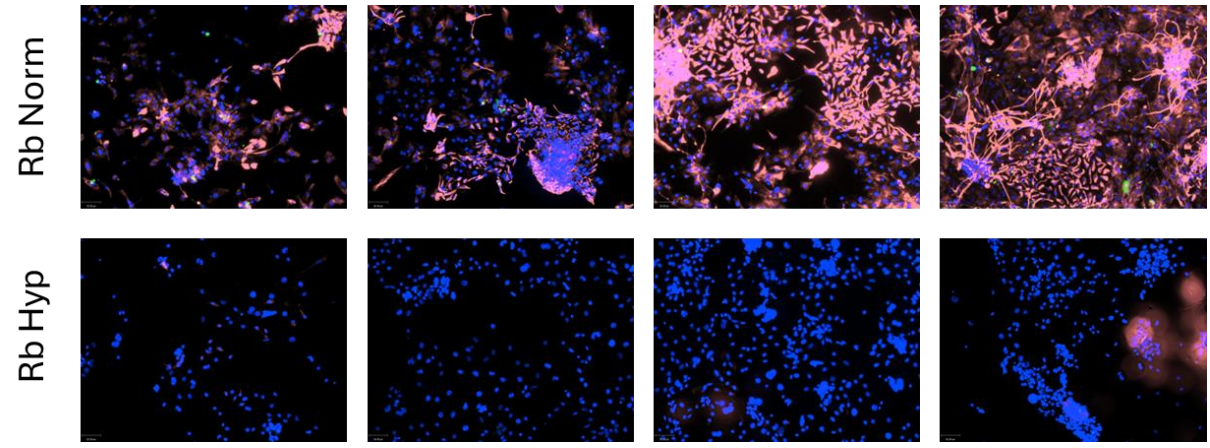

Figure 104: Sample IPSC-CM cultures grown in Rb^{+} medium in a normoxic (top row) and hypoxic (bottom row) atmospheres exhibit various degrees of fibroblast contamination. The normoxic set showed mild (left two images) to severe (right two images) fibroblast contamination, while the amounts in hypoxia were much less. This difference was not observed for cultures in Mat media. Blue=Hoechst; Magenta=Vimentin.

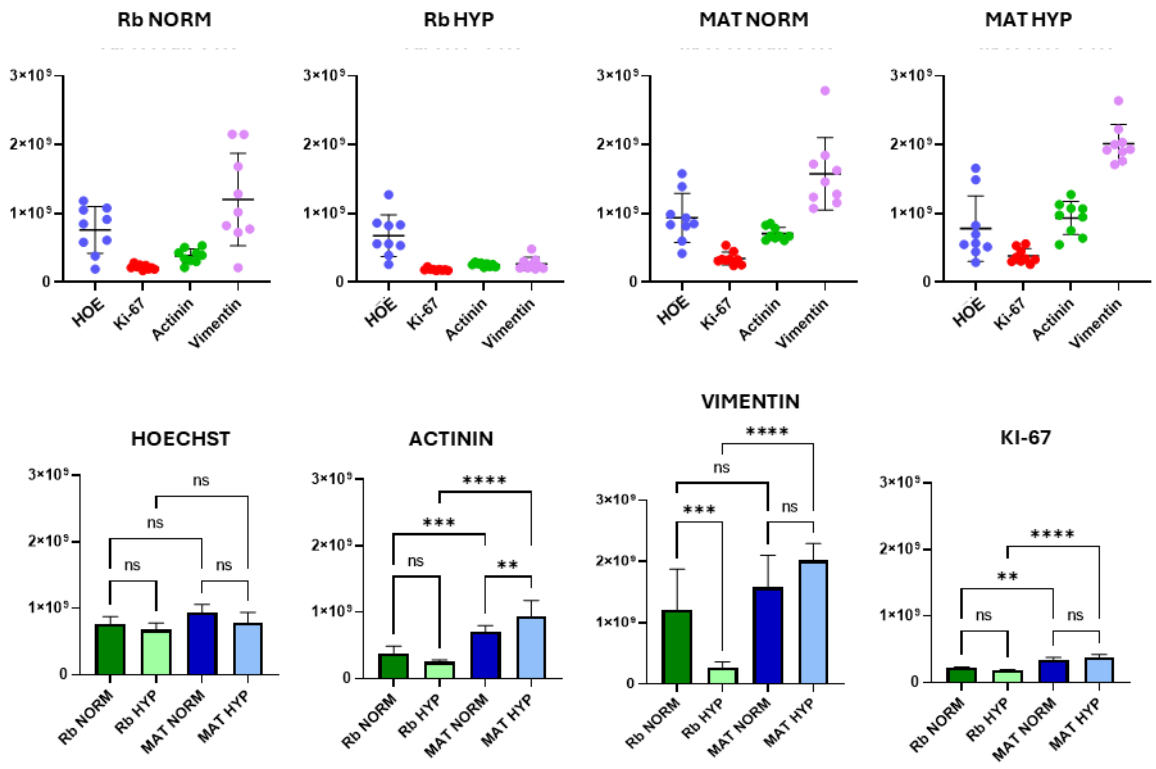

Figure 105: Integrated density quantification of fibroblasts in Rb^+ or Mat media, hypoxia (12 hours) or normoxia. In Rb^+ media, hypoxia reduces the amount of vimentin staining from FB but increases it in Mat media. One-way ANOVA with Tukey's multiple comparisons, **** p<0.0001; *** p<0.001; ** p<0.01; * p<0.05.

As with the previous staining set for 12 hours above (Figure 100C), there was no significant difference in the number of cells in each condition with comparisons for α-actinin and Ki67 very similar (here we do see more α-actinin in the Mat Hyp condition than Mat Norm which we did not observe before but that is within experimental variation). We can see how the effect of hypoxia on the fibroblast population with significantly less FB in Rb^+ compared to Rb^+ normoxia, (although there was a lot of variability among the 9 images for normoxia and very little variability in hypoxia) and interestingly significantly more FB in Mat media than Rb^+ in hypoxia. Ki67 values were higher for Mat than Rb^+ in normoxia and highest in Mat hypoxia.

5.3.14 HYPOXIA AND ACIDITY EFFECTS ON hiPSC-CM CULTURES EVALUATED BY qPCR

Checking levels of cardiac contractile proteins after 12 hours of hypoxia

In addition to immunofluorescent staining for cardiac contractile proteins, we examined messenger RNA levels using qPCR from the same batches of differentiated CMs treated with 12 hours of hypoxia or normoxia, and another batch treated with acidic media (kept in normoxic conditions).

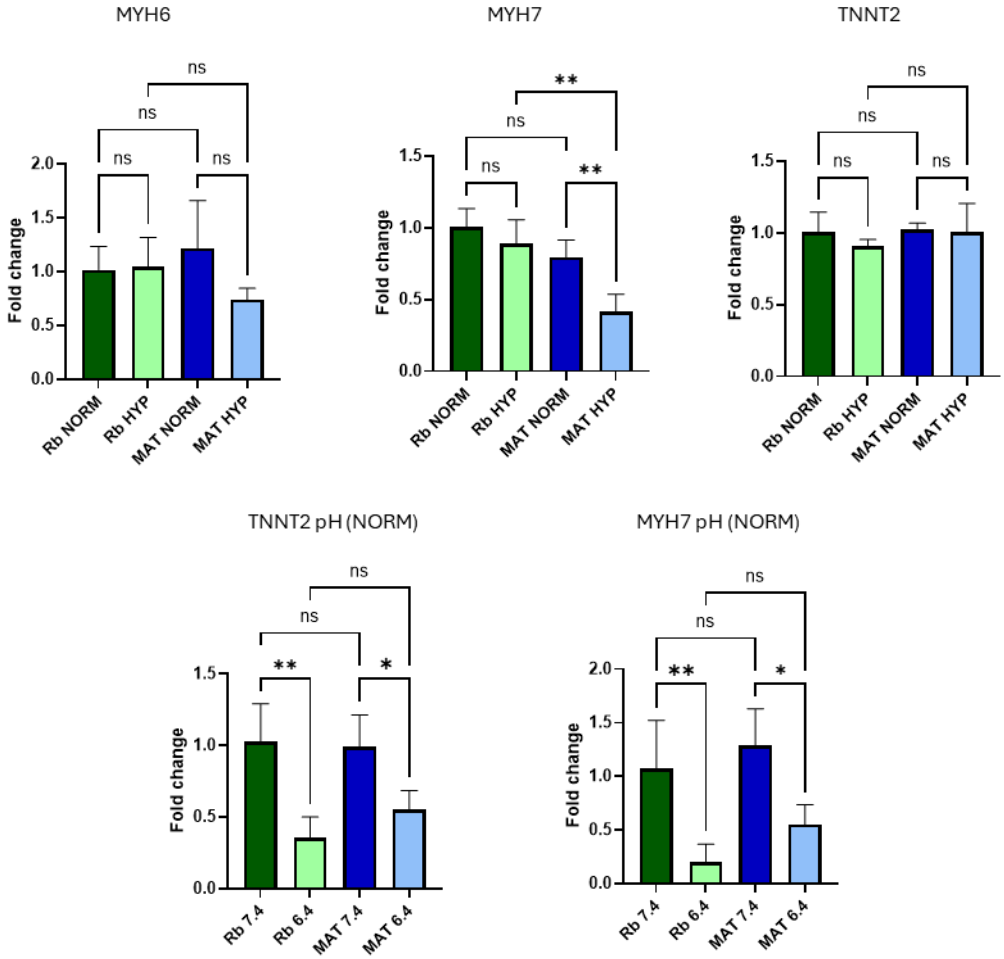

Figure 106: qPCR results for cultures grown in Rb^+ or Maturation media for 7 days with a final 12 hours in hypoxia or continued normoxia (top row). Of the three contractile protein levels of mRNA tested, only MYH7 dropped under hypoxia but only for the maturation media cultures. In low pH media under normoxic conditions (bottom row), both TNNT2 and MYH7 were significantly reduced. (**** p<0.0001; *** p<0.005; ** p<0.01; * p<0.05; 2-way ANOVA, n=3 for all data sets).

Hypoxia had no effect on mRNA levels of MYH6 or TNNT2 but it significantly lowered levels of MYH7 for the cultures grown in maturation media: $p<0.01$ less comparing normoxia with hypoxia directly, and also comparing maturation with Rb^+ media (where there was no difference in

normoxia). In Rb^+ and maturation media, acidity caused levels of both MYH7 and TNNT2 to decrease ($p<0.01$ and $p<0.05$ respectively) with similar results for both contractile proteins.

Effects on cell cycling by hypoxia and acidity

We wanted to study cell cycling under different conditions of hypoxia and acidity with the hiPSC-CMs to see if we would get similar results to those seen with the Fucci cells. Cells were cultured in Rb^+ media or maturation media for 7 days and then placed in media at pH 7.4 or pH 6.4 under normoxia or hypoxia for 12 hours. Primers for CCND2, CCNE1, CCNA2, and CCNB1 (representative cyclins from each main cell cycle phase) were designed using NCBI Primer-Blast as detailed in Chapter 2: General Methods. Additionally, we also tried AURKA and CDC7.

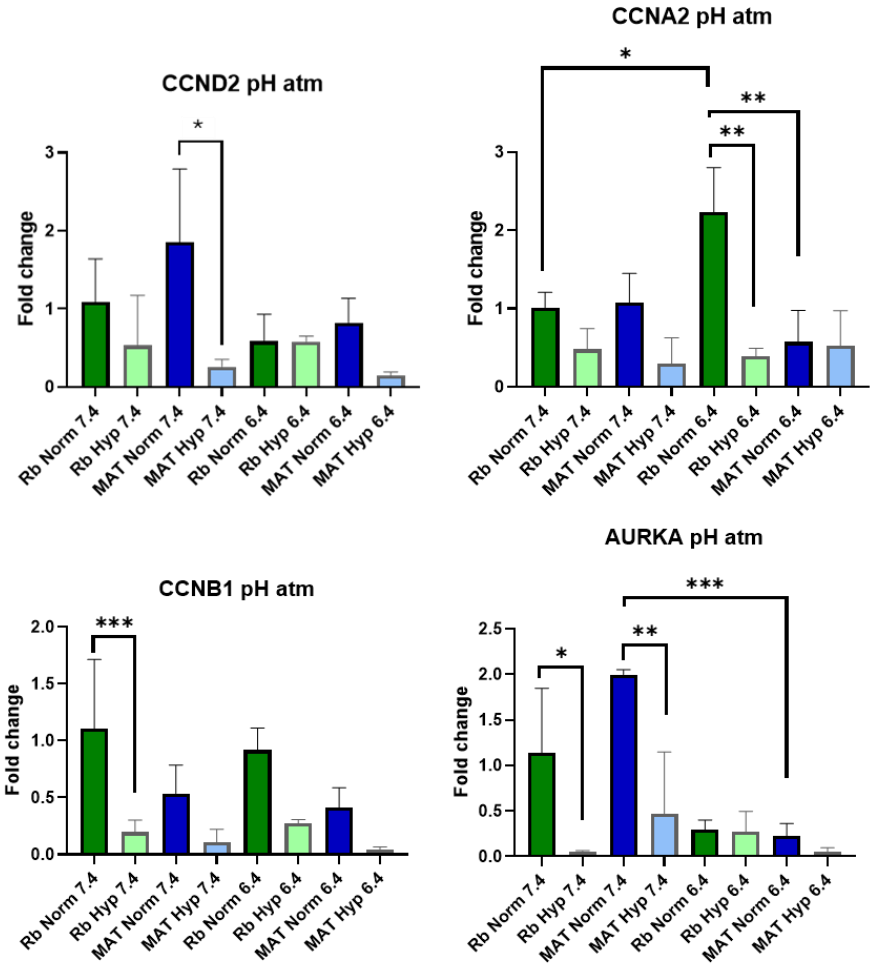

Figure 107: Cell cycle markers cyclins CCND2, CCNA2, CCNB1 and mitotic marker AURKA effects in hypoxia and pH combinations. (CCND2 n=2 for maturation, hypoxia and pH 7.4 & 6.4, CCNA2 n=2 for Rb^+ hypoxia and pH 6.4, AURKA n=2 for maturation, normoxia and pH 7.4: Mixed-effects analysis with Šídák's multiple comparisons test; CCNB1 n=2 for Rb^+ and maturation media in hypoxia at pH 6.4: 3-way ANOVA.)

Culture at under hypoxia had a detrimental effect on the cells such that we only had an n of 2 for some genes. Statistical analysis showed that there was a significant effect of hypoxia on expression of CCND2 ($p < 0.05$), CCNA2 ($p < 0.01$), CCNB1 ($p < 0.01$) and AURKA ($p < 0.01$). There was a significant effect of maturation on expression of CCNA2 and of pH on AURKA. Data for CCNE1 expression was too variable between technical repeats to be included. Post-hoc analysis showed a significant difference in CCND2 expression for cells cultured in maturation medium at pH 7.4 between hypoxia and normoxia. There was no effect of pH on cells cultured in either medium. Expression of CCNA2 was higher in cells cultured in RB^+ media at pH 6.4 than any other condition, although this was only statistically significant when compared to cells in RB^+ media under normoxia at pH 7.4, in RB^+ media under hypoxia at pH 6.4 and cells in maturation media under normoxia at pH 6.4 ($p<0.05$). CCNB1 was only significantly affected by hypoxia in Rb^+ media at pH 7.4 ($p < 0.001$). AURKA levels were reduced by culture in hypoxia for cells in RB^+ media or in maturation media at pH 7.4 ($p<0.05$ or < 0.01 respectively). The change in pH level also resulted in a significant decrease in AURKA levels for cells cultured in maturation media under normoxia ($p<0.001$).

Comparing atmospheric hypoxia with DMOG-induced hypoxia

As the hypoxic Fucci cell imaging over the experimental time course of one week was performed using DMOG to mimic hypoxia rather than atmospheric hypoxia, we wanted to run a series of direct comparisons between these two on the hiPSC-CMs. Using cell cycling as a measure, we cultured a batch of cells either in the hypoxic chamber or with 1mM DMOG added to the media and incubated for 18 hours - this time period was used to replicate the protocol in a reference protocol (Stoehr, Yang et al. 2016). As above, we were only able to get reliable results from 2 repeats for some genes.

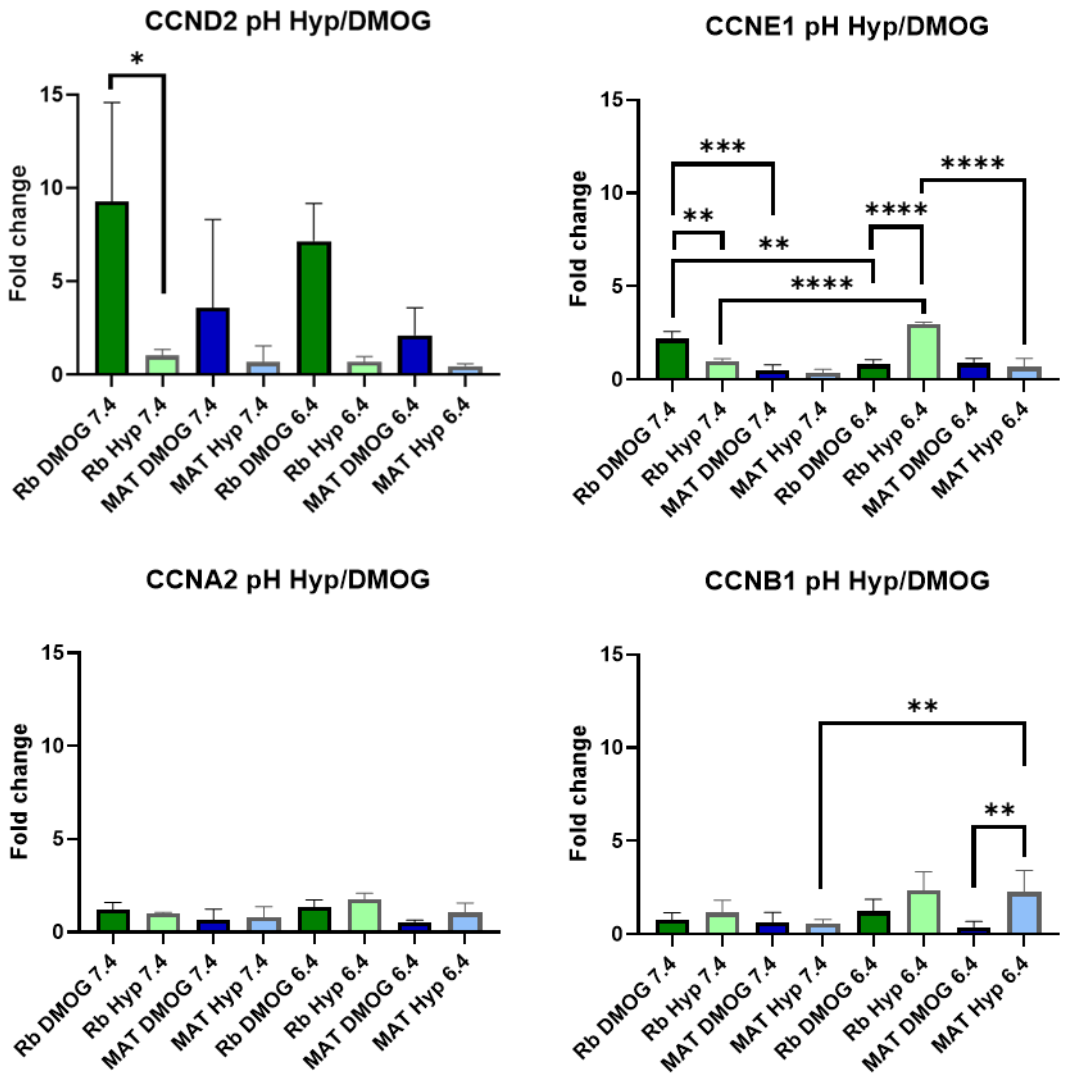

Figure 108: The same groups of hiPSC-CM with Rb^+ or Mat media in neutral or acidic pH and subjected to atmospheric hypoxia (2% O_2) or DMOG-induced hypoxia. Mixed-effects analysis with Šídák's multiple comparisons test; 3-way ANOVA.

Mixed effect analysis showed that there was a significant difference in expression of CCND2 and CCNB1 when cultured under hypoxia or with DMOG ($p < 0.01$). There was also a significant effect of maturation on expression of CCND2 and CCNB1 ($p < 0.05$). Finally there was a significant effect of pH on expression of CCNB1 ($p < 0.01$). Post hoc analysis showed that CCND2 expression in RB^+ cells at pH 7.4 were much higher with DMOG than at atmospheric hypoxia ($p<0.01$). CCNB1 expression was significantly higher in cells in maturation medium at pH 6.4 under hypoxia than in those at pH 7.4 ($p < 0.01$) or those at pH 6.4 with DMOG ($p < 0.01$).

5.3.15 STUDY LIMITATIONS

There are a number of limitations to the work presented in this chapter.

As already discussed, there was a wide variability in the number of cells isolated as cardiomyocytes are sensitive to the isolation procedure and this sensitivity increases with cell maturity. It is likely that the cell isolation protocol pre-selected for the less mature cardiomyocytes and that this would clearly have affected the results. We could have attempted to quantify the number of dead cells in the isolated fraction, such as by staining using Trypan Blue or Sytox Orange in a fraction of each isolate (which was done only to measure cell density for culture plating), however some cells are ruptured and lost during the digestion process and cannot be tracked. In addition, although we included a pre-plating step to remove fibroblasts this does not remove all fibroblasts and those remaining will proliferate through subsequent cell culture steps, although steps were taken to disregard the larger fibroblast nuclei in culture during the automated counting macro. Similarly, although the differentiation of iPS cells to iPSC-CM includes a glucose-depletion step to select for cardiomyocytes, some partially differentiated cells may survive and become fibroblasts which will continue to proliferate.

5.4 DISCUSSION & CONCLUSIONS

5.4.1 FUCCI CELL ASSAYS

Using isolated cardiomyocytes from P1 and P7 Fucci-positive mouse pups, we performed a series of cell counting assays under different environmental conditions and used a custom written Matlab macro to sort cell nuclei into 4 different categories based on their cell cycle phase: G1 (red), G1/S (yellow), S/G2/M (green) with a small percentage of cells in very late mitosis or that have exited the cell cycle (G0, black). The conditions tested were (1) baseline (no additional stresses); (2) hypoxia induced by DMOG; (3) acidity changes with different media compositions; and (4) hypoxia and acidity combined.

Fucci isolated P1 vs P7 cardiomyocytes without any treatment

Surprisingly, we did not observe many significant differences in the number of cells in each phase of the cell cycle between the P1 and P7 baseline groups over the course of the seven days. We were expecting to see more cells in the yellow (G1/S) or green (S/G2/M) phases for the P1 cells but both cell populations had <50% of cells in G1 on Day 2, which increased to 80-90% after Day 5. We expected the P1 cells to be more proliferative throughout the week of culture than the P7 cells, however this was not the case. This may be explained by the inherent limitations of the cell isolation procedure – the enzymatic digestion of the ventricular tissue, whether by the manual protocol or the more automated procedure, seems less destructive for more immature cells in that they seem more tolerant of the process. More mature and differentiated cells seem to be increasingly sensitive and we may be losing a lot more of these during the cell dissociation step. The number of viable cells for the more mature hearts does not rise linearly with the heart weight, so we may be "pre-selecting" for the more immature cardiomyocytes from the P7 cohort, thus reducing the differences between the two groups, and explaining why the plot of fractions in each cell cycle phase over the seven days appears almost identical despite knowing that P1 cells are more proliferative than P7. This is not a trivial problem and many groups have been researching methods to achieve improved heart cell isolations since the 1960's with various levels of success. One lab has tried to produce a method that works reliably for different ages but they also had reduced viability and fewer numbers of CM as the hearts aged as shown in Figure 109 (Nicks, Holman et al. 2022). Cells grown in culture also behave differently to those in vivo which may contribute to these unexpected results. Growing P1-P2 neonatal mouse CM in standard culture conditions of 20% O_2 and comparing to those grown in 3% O_2 (equivalent to 21mm Hg which is the estimated pO_2 in adult hearts in situ) showed those in 3% expressed higher amounts of Ki67 and Aurora B staining as well as more mRNA coding for cyclin A2 and B2 (Bon-Mathier, Rignault-Clerc et al. 2020)

Cardiomyocyte (CM) yield after the isolation and purification steps.

Age	CM number after isolation	Viability (%)	Rod-shaped (%)	n	CM number after purification	n
Neonate (P2)	$1.56 \pm 0.48 \times 10^6$	100	53 (~30–85)	72	$1.03 \pm 0.33 \times 10^6$	56
Infant (P10)	$1.62 \pm 0.39 \times 10^6$	70 (~60–90)	70 (~60–90)	69	$0.96 \pm 0.29 \times 10^6$	44
Infant (P13)	$1.65 \pm 0.44 \times 10^6$	70 (~60–90)	70 (~60–90)	25	$0.8 \pm 0.21 \times 10^6$	25
Adult (P70)	$2.21 \pm 0.36 \times 10^6$	72 (~60–90)	72 (~60–90)	27	$1.6 \pm 0.29 \times 10^6$	19

Mean ± SD; P, postnatal day. Rod-shaped *vs* round-shaped CMs (%). Note: Only infant and adult cardiomyocytes with >60% viability [16] were used in this study.

Figure 109: A recent study in the Graham lab developed a standardised method for CM isolation from mouse hearts of different ages. Note that the viability of isolated cardiomyocytes goes down between P2 and P10. Taken from *"Standardised method for cardiomyocyte isolation and purification from individual murine neonatal, infant and adult hearts"* (Nicks, Holman et al. 2022).

An interesting analysis would be to standardise the numbers in each cycle to the total number of cardiomyocytes at each age in an intact heart, however, this would be difficult to determine accurately as CMs undergo hypertrophy and the cell populations of different types within the developing heart also changes (Bergmann, Zdunek et al. 2015).

Fucci isolated P1 vs P7 cardiomyocytes in hypoxia and acidity

However, in a system stressed by hypoxia mimetic DMOG treatment, the situation was very different, with the two cohorts behaving quite distinctly. There was a large initial increase in the G1/S fraction of P1 cells which was not observed with the P7 cells. The P1 G1/S fraction at Day 2 was nearly six times higher than at baseline, and the G1, S/G2/M and G0 fractions reduced at first but increasing from Day 4 so they resembled baseline by Day 7. Many of P1 cells in G1/S in DMOG may be "stuck" in that phase as the increase in S/G2/M was less than the increase in G1/S though there was a slight rise from Day 4. There were changes with the P7 cohort as well but not as dramatic. The G1/S fraction at Day 2 was similar to P7 baseline but interestingly it rose during the time course to 0.14 at Day 7 (peaking at 0.18 at Day 4) so these cells seem to be responding less and more slowly to DMOG but with an extended effect than the P1 cells. We did not see any increase in S/G2/M but there were more cells in G0 with fewer in G1 indicating possible exit from the cell cycle.

When P1 and P7 CM were cultured in acidic media (pH 6.6-6.7), we saw some similarities to the hypoxic response. Again, the P1 acidic cells had an increased G1/S (not as large as the hypoxic increase but it seemed to be present until Day 7) and reduced S/G2/M fraction. Interestingly there were fewer cells in the P1 G0 fraction than at baseline. The P7 acidic cells did not respond as strongly but here there seems to be more G0 cells than baseline.

The final experiment combined hypoxia and acidity together to mimic possible conditions after MI injury. Although we were only able to try this once, a very interesting result was observed over the week of imaging. In this situation, the P1 cells had a large increase in G1/S and S/G2/M fractions with a correspondingly large decrease in the G1 fraction. The P7 cohort had an increase in G1/S at the very end of the week with a drop in G1 but no translation to S/G2/M within this timeframe. It appears that the combination of hypoxia and acidity promotes true P1 cell proliferation but obviously it would need to be repeated many times and further tested before any firm conclusions could be drawn.

Previous studies have also shown that CM progressing through the cell cycle after injury appear to stop at the G1/S stage where DNA synthesis starts, also known traditionally as the restriction point, (Figure 110A) (Pardee 1974, Alvarez, Wang et al. 2019, Broughton and Sussman 2019). Alvarez used the Fucci-Tg strain of mouse to claim up to 95% of adult CM are stuck in G1/S rather than G1 or G0 but other studies align more closely with our results of cells tending to G1 over time (Hashimoto, Yuasa et al. 2014, Hashimoto, Yuasa et al. 2015). A recent study in the Bergmann group using TNNT2-Fucci hiPSC-CM in culture tracked single CM over 72 hours and showed that 90% did not show any cell cycle activity, 5% actually underwent cytokinesis and cell division, 3% became binucleated and 1.4% underwent polyploidisation. They did not see any binucleated or polyploid nuclei go through cell division, supporting the idea that only mononucleated diploid nuclei are capable of this. Detailed observation of these last 3 cycling populations had an average duration of S/G2/M phase of 16-17 hours whereas the polyploid cells had a different pattern which suggested arrest in G2 with a longer period of mVenus expression lasting 24.5 hours on average (Figure 110B) (Murganti, Derks et al. 2022).

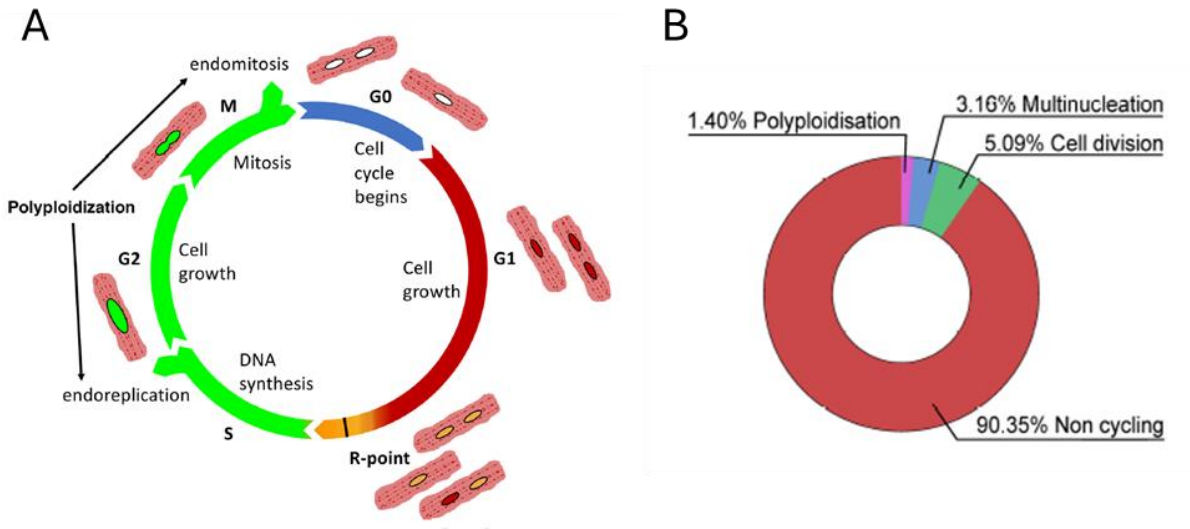

Figure 110: (A) Adult mammalian cardiomyocytes have two places to stop progressing through the cell cycle: either R (restriction point or start of S, referred to as G1/S – yellow for the Fucci reporter system) or later due to polyploidy. *Taken from "Adult cardiomyocyte cell cycle detour: off-ramp to quiescent destinations"* (Broughton and Sussman 2019). (B) Another study shows that of the 3 groups of CM active in the cell cycle only 5% actually go through division while 3% become multinucleated and 1.4% become polyploid. From *"Fucci*-based live imaging platform reveals cell cycle dynamics and identifies pro-proliferative compounds in hiPSC-*CM"* (Murganti, Derks et al. 2022)

5.4.2 hiPSC-CM ASSAYS

It's been 30 years since the first experiments to inject foetal mouse cardiomyocytes into adult mouse hearts showed successful survival and maturation of the injected cells as well as their integration into the myocardium with new intercalated discs (Soonpaa, Koh et al. 1994). hiPSC-CM therapies have now reached the stage of clinical trials but much remains to be done to optimise these procedures and increase the potential benefits that this technology offers. We performed a series of assays to determine how hypoxia and acidity affected the maturity and cell cycling functions of these cells at two levels of maturation. We also checked for culture contamination by fibroblasts.

Contractile protein staining to verify maturation status of hiPSC-CM in Rb^+ vs Mat media

In Rb^+ or Mat media-grown cultures exposed to either normoxia (20% O_2) or hypoxia (2% O_2) for 12 or 24 hours, we stained for α-actinin and troponin I3 as well as the cell cycle activity marker Ki-67 with Hoechst to label nuclei. The cells grown in Rb^+ showed no difference in Hoechst intensity between normoxia and 12 or 24hrs of hypoxia, implying they did not die under hypoxic conditions. This contrasted with the Mat cells which showed a significant decrease in cell numbers after 24 but not 12 hours in hypoxia suggesting increased sensitivity to hypoxia in these more mature cells. These results are consistent with a recent study that performed a similar assay and also showed that the relatively more immature cells grown in Rb^+ media did not experience increased cell death after 24 hours of hypoxia but more mature cells grown in Mat media increased the percentage of apoptotic cells from 12% to 40% (Peters, Maas et al. 2022). We also saw an increase in α-actinin and troponin I3 in Mat media over Rb^+ when comparing a similar cell count as they did, however we had more Ki-67 expression in Mat media compared to Rb^+ while they had less (all measured in normoxia). Lopez et.al also saw an increase in α-actinin after the addition of oleic acid, i.e. Mat media (Lopez, Al-Siddiqi et al. 2021).

Comparing individual dividing/non-dividing cardiomyocytes

We examined some individual cells expressing Ki-67 cultured in Mat media in normoxia under high magnification and showed these cells had significantly less troponin I3 in a fixed-size area centred around the nucleus, even though the amount of α-actinin remained similar. This may be an indication that cells actively in the G1 to S/G2/M phases labeled by Ki-67 may be de-differentiating to prepare for cell division or endoreplication.

Fibroblast contamination of hiPSC-CM cultures

The need for pure cultures of the desired cell type for transplantation is obvious, especially as cells other than CMs may proliferate uncontrollably and result in teratomas. Despite including the recommended metabolic starvation step in our CM differentiation protocol, a few fibroblasts survived the glucose starvation period and proceeded to divide during the following weeks. To quantify the degree of fibroblast contamination in our cultures, we stained for vimentin in both types of media with/without hypoxia. Although vimentin is a common marker for mesenchymal cells and not specific to only fibroblasts (it is also expressed in endothelial and smooth muscle cells among others), it clearly labelled non-myocytes which was the main intention. In Rb^+, hypoxic culture had significantly less vimentin staining, while in Mat media there was no difference between normoxia and hypoxia. In normoxia there was no difference between Rb^+ and Mat vimentin levels, however in hypoxia, Mat cultures had significantly more. This emphasises the need for further steps to prevent mesenchymal cell contamination such as longer or repeated glucose starvation steps or an additional FACS isolation before final experimental plating.

Hypoxia and acidity effects on hiPSC-CM cultures assessed with qPCR

To complement the IF staining, we compared mRNA levels of some other cardiac contractile proteins in cells treated with hypoxia and acidity with both types of media. We did not see any differences between cells (from the same batch) in Rb^+/Mat with/without 12hrs of hypoxia for TNNT2 and a slight (insignificant) drop in MYH6 but did see significantly reduced MYH7 cells grown in Mat media with hypoxia. MYH7 is expressed in more mature CM so this could show there were less of these mature cells that survived hypoxia which matches the IF results above which showed fewer CM surviving Mat hypoxia after 24hrs but not 12hrs – the cells may be producing less MYH7 mRNA but still be surviving at 12hrs. From the IF results, all these groups had similar numbers of cells (as measured by Hoechst intensity) so this drop also could be due to increased FB contamination in the aliquot of total mRNA as seen by the increased vimentin IF intensity, however this is counteracted by all groups having similar levels of TNNT2. With acidic media of pH 6.4 in normoxia, both TNNT2 and MYH7 levels dropped significantly indicating a sensitivity to low pH for both Rb^+ and Mat media.

We performed qPCR on the 4 groups with Rb^+/Mat with/without 12hrs of hypoxia, and added pH as another variable. We looked at CCND2, CCNE1, CCNA2 and CCNB1 as well as AURKA. The results even within some groups were quite variable so checking for significant differences

was problematic, with some experimental results needing to be excluded due to difficult experimental situations with inconsistent and possibly erroneous values. As expected, hypoxia reduced expression of CCND2, CCNA2, CCNB2 and AURKA in the same media at the same pH with both neutral and acidic conditions affected. Acidity increased levels of CCNA2 (S/G2/M cyclin) for Rb^+ normoxia but that was lost if hypoxia was added. Generally, the low pH situations had less expression of these cell cycle markers than neutral pH, which again is not surprising for cardiomyocytes.

Comparing atmospheric hypoxia with DMOG-induced hypoxia

Like many other research groups, we used DMOG as a hypoxia mimetic for some imaging experiments such as the Fucci cell cycling assay. One final experiment was to directly compare results between the addition of DMOG to the culture media with atmospheric hypoxia (2% O_2) induced by increased nitrogen in the incubator using the hiPSC-CMs qPCR cell cycling assay. CCND2 had consistently higher expression with DMOG for both media types and both pH levels, but there was no effect at all for CCNA2, while DMOG reduced CCNB1 in acidic Mat media. It is widely known that DMOG has other effects in addition to inducing a hypoxia-like environment. It's direct inhibition of PHDs also affects degradation and synthesis of other proteins. One study found 167 proteins that were affected by adding DMOG to hiPSC-CM, including those involved with RNA splicing, and changes to protein translation of cytoskeletal and sarcomeric proteins (Stoehr, Yang et al. 2016). Another slightly less relevant study in cancer cells found DMOG significantly altered metabolites such as serine, ornithine and homomethionine, in addition to reducing fatty acid levels and affecting energy metabolism (Imran Khan 2022). An early effect of DMOG is inhibition of mitochondrial function (Zhdanov, Okkelman et al. 2015). Therefore, the differences to amounts of cyclin mRNA between true atmospheric hypoxia and DMOG should not be unexpected, and DMOG used with these differences taken into consideration when interpreting results.

5.4.3 SUMMARY DISCUSSION: HYPOXIA AND ACIDITY EFFECTS IN CULTURED CARDIOMYOCYTES

Hypoxia's role in CM cell cycle regulation has been controversial and difficult to determine. Different levels of O_2 deprivation at different times in the maturation of these cells induce different results. There is little doubt that hypoxia during MI is harmful, causing cell death and tissue

damage, but afterwards, it may promote regenerative pathways and potentially help with repair and recovery (Haubner, Adamowicz-Brice et al. 2012). An intriguing population study based in Switzerland concluded that living at a higher altitude had a protective effect on coronary heart disease (and stroke), with CHD mortality decreasing by 22% for every 1000m altitude (Faeh, Gutzwiller et al. 2009). During mammalian development, the foetal heart exists in a hypoxic environment (2-5% O_2 in utero) with poor capillary perfusion which is conducive to CM hyperplasia. Initially, HIF signalling is extensive in the heart until E9.5 but later becomes limited to certain areas as the coronary vasculature develops. Mutations that cause loss of normal HIF-1α functioning result in multiple heart defects and lethality by E11 caused by excessive CM hyperplasia in inappropriate locations (Iyer, Kotch et al. 1998, Ahuja, Sdek et al. 2007, Dunwoodie 2009). The later stages of heart development occur as the environment becomes normoxic and fully perfused. In zebrafish the two-chambered heart leads to mixing of arterial and venous blood resulting in a hypoxemic circulation and the ability to regenerate damaged myocardium after ischaemic injury (Hashmi and Ahmad 2019, Zhu, Sun et al. 2022, Zhu, Yuan et al. 2024). Several studies have identified hypoxia as a stimulus for heart regeneration in adult mice. The Sadek group found that gradual exposure to hypoxaemia with 7% O2 inhibits oxidative metabolism, decreases mitochondrial cristae density, reduces ROS production and thus DNA damage and leads to reactivation of CM mitosis after 2 weeks (Kimura, Nakada et al. 2017, Nakada, Canseco et al. 2017), they also found the heart weight to body weight ratio increased with both RV and LV weights significantly increased in hypoxic hearts. Interestingly, CM size measurements showed increases in the RV but not in the LV, possibly due to the decreased mitochondrial mass and changes to sarcomeres (RV hypertrophy is also associated with hypoxia due to pulmonary hypertension (Zhu, Zhang et al. 2017)). LV functional measurements by echocardiography showed improved systolic function and smaller fibrotic scar size. After fixation and enzymatic digestion, they saw increased numbers of rod and round CMs with more mononucleated and fewer binucleated cells. These cells also had 8x increase in BrdU incorporation and importantly, increased Aurora B kinase localised to the cleavage furrow (although this does not guarantee progression to complete cell division). These cells were mostly located in remote regions which matched the results we saw in our Fucci slice studies in the previous chapter which noted that the older mice had cell cycle activation in the remote regions.

Acidity without hypoxia is not as well researched in cardiomyocytes but earlier studies indicate that it can cause reduced contractility and adverse Ca^{+2} (and other ion) handling and lead to metabolic stress (Steenbergen, Deleeuw et al. 1977, Garlick, Radda et al. 1979). Despite this, acidity can also

help recovery of contraction upon reoxygenation after periods of hypoxia, thus conferring a protective effect (Bing, Brooks et al. 1973), possibly by conserving energy during the hypoxic period. Cardiomyocytes have some resistance to low levels of chronic hypoxia but the combination of hypoxia and acidosis as present after prolonged ischemia has been reported to cause necrosis and apoptosis of CM and is probably the main cause of their loss after MI injury. Acidity is caused by increased glycolysis and lactic acid production, and it may stabilise members of the Bcl-2 family of apoptosis-regulating proteins, and also increase their association with mitochondria opening the permeability pore without caspase activation. Hypoxia can also induce expression of these proteins, thus exacerbating the situation (Kubasiak, Hernandez et al. 2002, Graham, Frazier et al. 2004). Hypoxia-acidosis has also been shown to fragment CM DNA. Acidosis also contributes to necrotic pathways which are also involved in tissue damage, causing disruption to membrane ion transporters, loss of membrane integrity and triggering inflammatory responses. This can lead to arrythmia in the heart (Vaughan-Jones, Spitzer et al. 2009).

5.5 FUTURE WORK

The Fucci isolated cells assays would benefit from the use of one of the newer variations of Fucci that label only cardiomyocyte nuclei to avoid the need to screen for and eliminate those outside than expected CM size range. Also, access to integrated culture and imaging would negate the need to use DMOG rather than atmospheric hypoxia, which may produce more physiologically accurate results. Automated imaging would reduce the technical workload.

The hiPSC-CM assays need to be more comprehensive with a wider range of markers used in the IF staining, especially to identify contaminating cells. Similarly for the qPCR cell cycle experiments, more repeats would have reduced the variability of the results. Studying an extended panel of cyclins in association with IF confocal analysis to quantify levels of multinucleation and myocyte size would help determine whether true cell division was occurring. Use of an additional FACS protocol step to further purify the cultures would be beneficial before prolonged culture and experimentation.

Finally, replicating our Fucci cell assays using the new TNNT2-Fucci-labelled hiPSC-CM would be very interesting.

CHAPTER 6

Discussion summary and Concluding remarks

Discussions of research results are presented in full at the end of Chapters 3, 4 and 5. We discussed how our results compared to published studies and also noted possible future work to advance each project. Here we briefly recap the main findings and highlight innovative outcomes from our experiments.

6.1 Longitudinal neonate MRI shows regeneration with tissue replacement and functional recovery after MI injury in P1 hearts but not in P7

Research innovations and main findings

- Adult mouse MRI scanning protocols can be adapted to image pups immediately after birth with full recovery allowing for longitudinal imaging;
- Repeated inhalation anaesthesia may affect body development at these young age points
- Functional heart parameters were monitored from P1 to P28 revealing developmental progression of ejection fraction (from EDV and ESV), LVM/BM and heart rate in detail and from an earlier time point (P1) than previously published studies;
- The same distinct sinusoidal pattern of heart rates was observed for all four experimental groups (2 ages x 2 surgery protocols) – they all had a significant slowing of heart rate around P14;
- Different outcomes after MI injury by LAD ligation were observed for the cohort having surgery at P1 (regenerative) compared to P7 (reparative), and also compared to age-matched sham injury;
- Mouse hearts injured at P1 can regenerate the damaged tissue and show functional recovery but this ability was not observed if injury was performed at P7. The P7 injury cohort showed permanent injury with scarring and ventricular remodelling;
- *This study was published in Circulation (2018) "Magnetic Resonance Imaging of the Regenerating Neonatal Mouse Heart" (first author).*

This work presented in the first chapter of this thesis intended to resolve the ongoing controversy of whether neonate mammals actually have the regenerative potential reported in some studies but disputed in others, and, if they do, to determine how long they retain this ability using our model system of MI in neonatal mice. Infarct studies vary considerably in the extent of initial damage as each surgery is different and causes diverse degrees of ischaemia in each heart, whether that difference is intentional (for example, a larger or smaller section of tissue resected by design, or

the ligation suture deliberately placed higher or lower on the LAD artery) or simply caused by technical variation between researchers or even between specimens while attempting to keep these factors consistent. This variance leads to difficulties in interpreting surgical outcomes and has contributed to the controversy. We re-engineered some aspects of the adult mouse MRI scanning procedure to facilitate repeated imaging of the same pup from baseline at either P1 or P7 through 4 follow-up scans at Days 4, 7, 14 and 21 post surgery. After confirming injury at Day 4 by visualising akinesis of the left ventricular wall where the LAD suture was ligated, we saw functional recovery and tissue regeneration in the P1 cohort which did not occur for the P7 cohort. P7 pups had sustained loss of ejection fraction caused by increased EDV and ESV due to ventricular remodelling which started as soon as Day 4 post surgery.

Having shown that recovery or continuing damage progression could be monitored, this novel platform may be used to test new treatments and therapies to determine if we can extend the period of recovery to older mice. This work is being further developed by Professor Jurgen Scheider at the Institute of Cardiovascular and Metabolic Medicine's clinical imaging facility at the University of Leeds.

6.2 P1 and P7 Fucci2 neonates show different areas and degrees of cell cycle activation across the myocardium after MI injury

Research innovations and main findings:

- Fucci positive neonatal mouse pups (<P3 age) can be quickly and easily identified using a bright LED coloured light source in combination with filter goggles for rapid and noninvasive genotyping immediately after birth;
- Fucci positive pups did not have any different outcome after myocardial infarction surgery when compared with Fucci negative controls;
- Comprehensive mapping of Fucci labelled cell cycle activity across 21 areas of the heart showed almost no significant differences at P5 and P11 in uninjured hearts;
- Significantly different levels and locations of cell cycling activity between P5 and P11 hearts were observed 4 days after MI injury, with P5 hearts showing increased cell cycling in the LV wall and the septum as well as in the atria.

We noticed that for a limited time period, Fucci positive pups could be accurately genotyped using the light torch/goggles method used extensively for other fluorescence-emitting animals such as GFP/YFP mice (but those are much brighter with a strong fluorescence). This had not been tried with Fucci before, with researchers needing to genotype using the traditional method of PCR. Previously, if positive pups were needed for surgery at P1, the entire litter had to be done with genotypes confirmed by tail clip when the hearts were harvested, with the negative pups wasting time and resources.

With an examination of 21 fixed points in the heart (5 points in RV, IVS and LV walls, 2 in each atria and 1 each in the base and apex), we mapped exactly where cell cycling activity was occurring in neonatal hearts by using the R26p-Fucci2 model system. We counted red cell nuclei that were in the G1 phase against those that are green and have entered S, are in G2 or starting mitosis (although not necessarily completing the process). P5 pups with or without MI surgery at P1 were directly compared, as were P11 with/without surgery at P7. Looking at P5 and P11 without injury showed one area that differed significantly: the P11 mid-LV showed an increase in cycling activity as indicated by a drop in the fraction of cells in G1. This might be related to the reported thyroid hormone surge at this age which some studies suggest indicates a second period of CM proliferation. Interestingly, this coincided with our observed dip in heart rate around P14 in the neonate MRI study.

The P5 MI group showed significantly more activity along the LV and IVS compared to the P5 shams, indicating cell cycle activation in response to injury. The P11 response was more muted and in different locations, having less activation close to the injury site but some in remote areas in the IVS, RV and LA. We did not have time to investigate reasons for this cell cycling in remote regions but it would be interesting to look at in more detail in the future.

6.3 pHLIP acidity marker in the developing heart and after adult injury

Research innovations and main findings:

- We showed that pHLIP could successfully be used to label areas of acidic myocardium in mice ranging in age from P1 through to adult with no adverse effects and high reproducibility, making this the first application to a developmental study of a marker

dye previously only used in cancer tumour research. *This is listed on the phlipinc.com/imaging website;*

- pHLIP signal was stable with minimal fluorescent signal reduction in frozen sections of heart or kidney tissue up to four months after initial imaging;
- We demonstrated that P1 and P7 neonatal mouse hearts have consistent areas of acidic myocardium along the inner ventricle walls and atria, which dissipates by P21 and is not present at all in adult mice. *This finding was published in Basic Research in Cardiology (2022) "Alkaline nucleoplasm facilitates contractile gene expression in the mammalian heart" (second author – joint);*
- We also saw how areas with damaged myocardium were labelled acidic with pHLIP after cryo-infarct surgery in adult rats. *This was published in Cardiovascular Research (2022) "Acidic environments trigger intracellular H+-sensing FAK proteins to re-balance sarcolemmal acid-base transporters and auto-regulate cardiomyocyte pH".*

We examined the developing heart (P1, P7, P21, Adult) with pHLIP and noted acidic niches in the endocardium and atria at different stages. They were present in P1 and P7 neonates but they had mostly dissipated by P21 and not appear in the adult, indicating a maturing cardiac vasculature that improves perfusion throughout the myocardium. In a cryoinfarct model of MI injury in adult rats, the area surrounding the site of ischaemic injury was clearly labelled by pHLIP, illustrating the acidity caused by disrupted blood flow and resultant tissue damage. The intensity of the signal depended on the extent of the injury. Establishing pH as a factor in maturing myocardium may present new opportunities to modulate this in the injured adult situation.

Immunofluorescent staining for cardiac contractile proteins TnnT2 and Crip2 showed reduced intensity in the damaged tissue areas, coinciding with pHLIP staining. There may possibly be reduced contractile proteins in areas where cell cycling in response to this injury may be triggered but this would require more investigation before any conclusions could be made.

6.4 P1 and P7 Fucci isolated cells cultured in different environmental conditions

Research innovations and main findings:

- We developed an automated, non-biased cluster analysis protocol to sort imaged Fucci nuclei into 4 categories (representing cell cycle phases G1, G1/S, S/G2/M and G0) based on their relative fluorescent emissions of red and green;
- There were no apparent differences between CM isolated from P1 and P7 pups when cultured under baseline conditions;
- Significant differences between these groups appeared when the cells were stressed by a hypoxia-mimetic – the P1 cells had a large and immediate response while the P7 cells did not react as strongly initially but may have a small response later in the week;
- The situation was similar when the cells were stressed by acidity, with P1 showing a significant response (although not as strong as that to hypoxia) while the P7 cells seemed to stop cycling;
- A preliminary study of hypoxia and acidity together caused the P1 cells to dramatically start proliferating, the P7 cells again responded more slowly and with less change (this result will need to be repeated).

The first isolated cells assay would lead us to believe that there were no differences between P1 and P7 cardiomyocytes in standard culture conditions of 20% atmospheric oxygen and neutral pH, however when stressors such as hypoxia (induced chemically by DMOG) and acidity were added to the system, significant differences became apparent. We attributed the similarities in the baseline groups to the limitations of the enzymatic digestion procedure that may be "pre-selecting" more immature cells from within the P7 isolation output because the more mature ones do not survive as well. Although these P7 cells appear to be similar to the P1 cells, they clearly do have differences which manifest under hypoxic and/or acidic conditions. The P1 cells treated with DMOG respond with a rapid increase in G1/S cell number as cell cycle activity begins. They do not necessarily follow through into complete cell division though, and many seem to "get stuck" in this phase and do not progress further. A smaller response was seen when they were cultured in low pH media. The P7 cells responded much more slowly, taking a few days to show any effects, and when this finally happened, it was more muted. Hypoxia and acidity together may cause the younger P1 cells to undergo genuine proliferation as we saw a strong response with nuclei in the S/G2/M green phase throughout the week of measurements (with a concurrent drop in G1 cells) but this result needs verification.

6.5 hiPSC-CM grown in different media and subjected to hypoxia and/or acidity

Research innovations and main findings:

- We confirmed that hiPSC-CM grown in media containing fatty acids ("maturation or Mat media") were more mature than those grown in standard high glucose media ("Rb") by imaging increased intensity of staining for Tnni3 in the Mat cultures. This was not affected by culture under hypoxia;
- hiPSC-CM in Mat media were more sensitive to hypoxia than Rb cultures as indicated by a drop in cell numbers under 2% O_2 for 24 hrs compared to 20% O_2; (note that we did not see this after 12 hrs of hypoxia);
- In normoxia, higher Ki-67 expression was observed with Mat media cultures having a similar cell count to Rb cultures;
- We noted that for individual cells expressing Ki-67, there was less TnnI3 in a fixed area around the nucleus than in cells not expressing Ki-67, even though levels of α-actinin remained similar;
- With acidic media of pH 6.4 in normoxia, both TNNT2 and MYH7 mRNA expression dropped significantly in both Rb and Mat media;
- We checked cell cycle indicators for both media with/without hypoxia and noted hypoxia reduced expression of CCND2, CCNA2, CCNB2 and AURKA for both media and normal as well as acidic pH; acidity increased the S/G2/M cyclin for Rb normoxic but not hypoxic conditions;
- We also noted significant differences between these measurements when hypoxia was induced by directly reducing O_2 levels or chemically induced with DMOG;
- Finally, the issue of unaccounted amounts of fibroblast contamination in supposedly purified hiPSC-CM cultures remains problematic and needs to taken into consideration when analysing experimental data.

Taken together, these results show that longer periods of hypoxia (24 hours) have detrimental effects on Mat media matured hiPSC-CM compared to those grown in standard Rb^+ media, though they were tolerant to shorter 12 hour exposures. Levels of some contractile proteins expressed in more mature cells (MYH7) were reduced under hypoxia while others (α-actinin, TNNI3) were unaffected. Hypoxia reduced expression of cell cycle markers (CCND2, CCNA2, CCNB1, AURKA) in both media. Interestingly, using chemically-induced hypoxia with DMOG, we saw

consistently higher expression of CCND2 but variable effects on the others, confirming its use as a hypoxia-mimetic should be treated with caution.

These studies also confirmed an ongoing issue with contamination of hiPSC-CM cultures even after steps are taken to purify them during the differentiation process. Glucose starvation removed most but not all remaining FBs, leaving a few to proliferate over the course of continued culture. A final FACS step to distil CM before qPCR studies would improve data quality.

6.6 Concluding remarks

The consensus used to be that the adult mammalian heart was post-mitotic and thus incapable of CM renewal (Lam and Sadek 2018). After a heart attack, a fibrotic scar is laid down to prevent rupture of the ventricle wall (where ischaemia causes the loss of billions of cardiomyocytes) which further limits normal pumping action across the syncytium. The remaining viable myocardium remodels with enlarged EDV and ESV but EF is reduced and ultimately heart failure is expected. Recent studies have shown that there remains a very small degree of cardiomyocyte proliferation as the heart ages, but the vast majority of CMs do not divide and have exited the cell cycle (Bergmann, Bhardwaj et al. 2009, Bergmann and Braun 2016, Graham and Bergmann 2017). During development and maturation of the heart, most of the CM become bi- or multi-nucleated and/or polyploid after several cycles of endoreplication, causing complications with the traditional cell cycling process (Auchampach, Han et al. 2022, Huang, Huang et al. 2023). Another complication is linked to the complex ultrastructure of these cells. The contractile apparatus constituting the sarcomeres is a rigid hinderance to cell division. There is evidence that a small percentage of adult cardiomyocytes remain mononucleated and diploid, and that these can undergo cell division by dedifferentiating to a less mature state which results in partial disassembly of some of the sarcomeric structure allowing mitosis to proceed. One of the reasons for mature CM exiting the cell cycle is the abrupt switch from the relatively hypoxic environment of the womb to the oxygen-rich one at birth (Breckwoldt, Weinberger et al. 2016). The increased oxygen levels allow the cardiomyocytes to use oxidative phosphorylation over glycolysis to meet the increased requirement for ATP to fuel the heart muscle as body demands intensify postnatally. The high levels of fatty acids now available in the bloodstream provide a suitable substrate for OXPHOS. A result of this is increased ROS produced by mitochondrial activity which may induce DNA damage and help push the CM out of the cell cycle. If these maturing cardiomyocytes remain in a

hypoxic environment, cell cycling continues for a longer period of time and this prolongs the regenerative window (Kimura, Nakada et al. 2017, Nakada, Canseco et al. 2017, Nakada and Sadek 2021).

Both P1 and P7 Fucci slices after MI injury showed increased cell cycling activity compared to age-matched shams implying injury increases cell cycling. As LAD ligation causes an ischaemic injury to the surrounding and downstream tissue with reduced blood (and therefore oxygen) flow, areas of relative hypoxia are induced. However, ischaemia also causes acidity in affected tissues by returning them to a more glycolytic metabolism which releases lactate into the cells, and reduced vascular perfusion to remove waste products. We mimicked acidity by using media with a pH of 6.4, and again saw the P1 CM had a slightly increased fraction of cells in G1/S but they did not proceed further (the response was much less than the DMOG response). The combination of DMOG-induced hypoxia and acidity (representing tissue conditions after ischaemic injury) showed a dramatic increase in S/G2/M cells in the P1 cultures, where CMs were actually progressing through the cell cycle to mitosis. This did not happen for the P7 cultures, but we did see a step towards it by the end of the week. Finally, we tested the combination of hypoxia and acidity in an hiPSC-CM 2D model with two levels of maturity, where cells grown in Rb^+ (glucose) media were compared to cells grown in Maturation (fatty acid) media. We saw the mature hiPSC-CMs were more sensitive to hypoxia with cell numbers dropping and showing less cell cycle activity whereas those grown in Rb^+ were tolerant of hypoxia. The idea of dedifferentiating CM in preparation for cell cycling was verified by comparing levels of Tnni3 staining in a fixed area around a nucleus that was expressing Ki-67, and we observed less Tnni3 in these cells than in those that did not have Ki-67 in their nucleus (while noting that α-actinin intensity was similar in both groups). Acidic media caused mRNA levels of TNNT2 and MYH7 to drop in Rb^+ and Mat media cells and hypoxia reduced expression of cyclins D, A and B (the results for cyclin E were too mixed to draw any conclusions). Using DMOG to mimic hypoxia produced different results to using a low-O2 incubator with a high expression of CCND2 with DMOG.

In conclusion, we confirmed regeneration by longitudinal neonatal MRI after MI injury in P1 mouse hearts, which did not occur in P7 hearts. We studied where increased cell cycling was appearing after injury at these time points across heart slices in detailed immunofluorescence assays and used a biopeptide marker developed for cancer research in a developmental study to map acidic regions across the maturing myocardium from P1 to adult. Lastly, linking hypoxia and acidity with cell cycling in tractable cell culture models of primary mouse cardiomyocytes and human

induced pluripotent stem cell-derived cardiomyocytes, we noted how differing cell maturity levels responded to combinations of low oxygen levels (atmospheric and chemically-induced) and media of different pH values, conditions which mimic those in a heart after ischaemic injury.

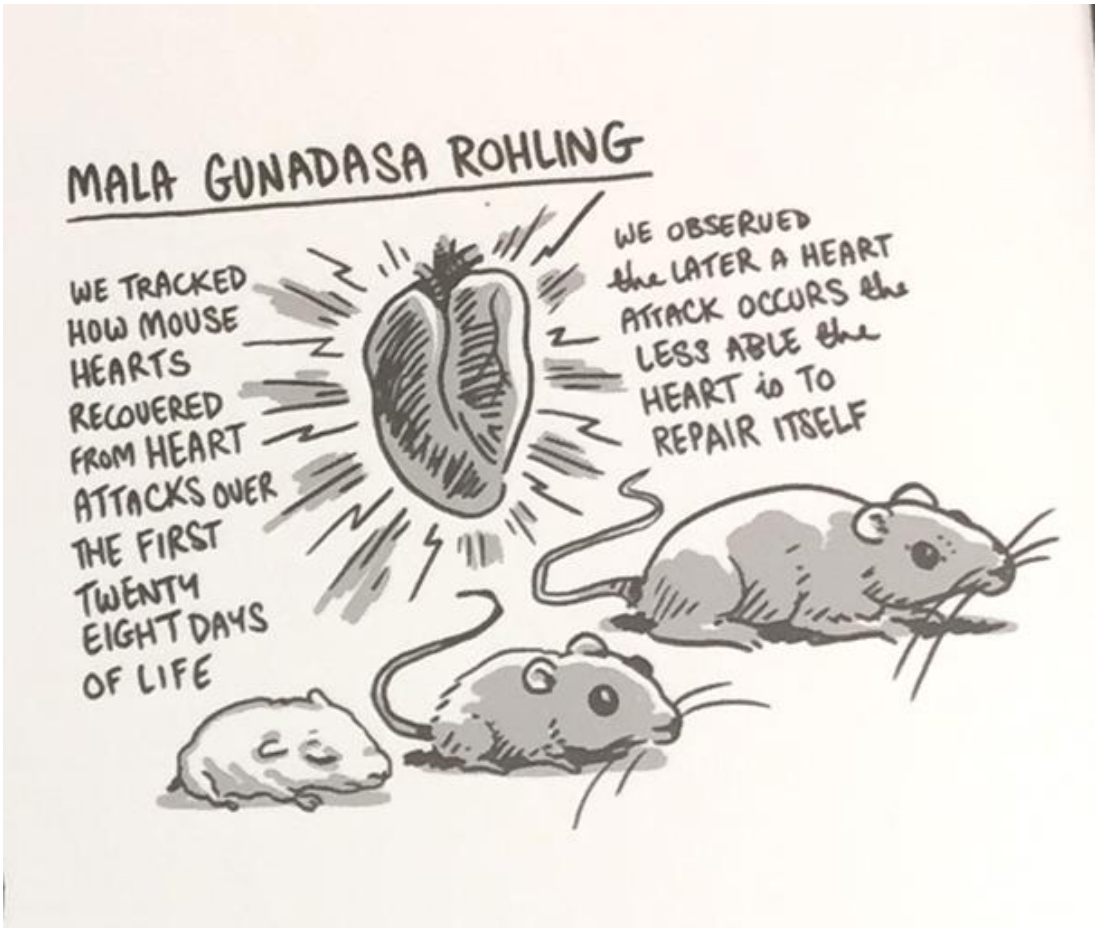

Drawn by Jack Brougham, 2018

Maybe one day this will no longer be true…

APPENDICES & SUPPLEMENTAL FIGURES

APPENDIX 1: Circulation paper (p1\3)

Circulation

RESEARCH LETTER

Magnetic Resonance Imaging of the Regenerating Neonatal Mouse Heart

Mala Gunadasa-Rohling, BSc
Megan Masters, BSc, MSc, PhD
Mahon L. Maguire, MA, MSci, PhD
Sean C. Smart, BSc, MSc, PhD
Jürgen E. Schneider, PhD
Paul R. Riley, BSc, PhD

After myocardial infarction (MI), the human heart is unable to regenerate lost tissue, leading to scarring, pathological remodeling, and progression to heart failure. The study of animal models that can intrinsically regenerate the heart, therefore, offers therapeutic insight into targeting tissue restoration. In 2011, the first evidence of mammalian heart regeneration was reported by Porrello et al.[1] After surgical resection of ≈15% of the left ventricle apex of a postnatal day 1 (P1) neonatal mouse, the heart fully regenerated by 21 days after injury, whereas if the procedure was repeated 1 week later on a P7 mouse heart, fibrosis and scarring ensued, recapitulating the adult wound-healing response. The mechanism of regeneration observed involved proliferation of resident cardiomyocytes, which is analogous to that described in the adult zebrafish heart.[2] Since the original study, others have described neonatal myocardial regeneration after alternative insults, such as MI.[3] However, controversy also surrounds the extent of heart regeneration during the first weeks of life, whereby it was reported that regeneration did not occur in the P1 heart and was replaced by long-term fibrosis (180 days) with extensive cardiac remodeling.[4]

The major issue to date with all of these studies is that they are based on sacrificing individual animals at specific time points after injury, followed by histological assessment of the heart. This provides no insight into the extent of the initial injury, whether the heart was indeed injured from the outset or the regenerative process over time. Moreover, an important question remains as to how the regenerating mammalian heart copes in terms of functional output and remodeling during scar resolution and tissue restoration, as is directly relevant to human patients with ischemic heart disease subjected to regenerative therapies. To address both of these key issues, we developed noninvasive MRI, which enabled tracking of individual newborn mice after MI. Although MRI is well established for quantifying and monitoring cardiac function in adult mice, its longitudinal application in neonates requires significant refinement and has not been reported at the early P1 time point or after injury.[5]

We measured left-ventricular function at baseline (before surgery, day 0) and days 4, 7, 14, and 21 after MI for P1 and P7 age groups versus matched sham-operated controls. We assessed left-ventricular end-diastolic volume, end-systolic volume, ejection fraction, stroke volume, heart rate, and left-ventricular mass/body mass index (Figure; stroke volume and heart rate not shown). Representative images at days 4 and 21 after MI revealed extensive growth of the heart and apparent maintenance of wall thickness in P1 injured hearts versus sham controls, compared to left-ventricular dilation and wall thinning after injury at P7 (Figure, A and B). End-diastolic volume for the P7 MI group was significantly higher than in sham controls at most time points after injury (Figure, C), which is consistent with chamber dilation and remodeling. For the P1 group, there was no difference immediately after injury, but a rise in end-diastolic volume in the injury group was observed,

Key Words: cardiac output
■ magnetic resonance imaging
■ myocardial infarction

https://www.ahajournals.org/journal/circ

APPENDIX 1: Circulation paper (p2\3)

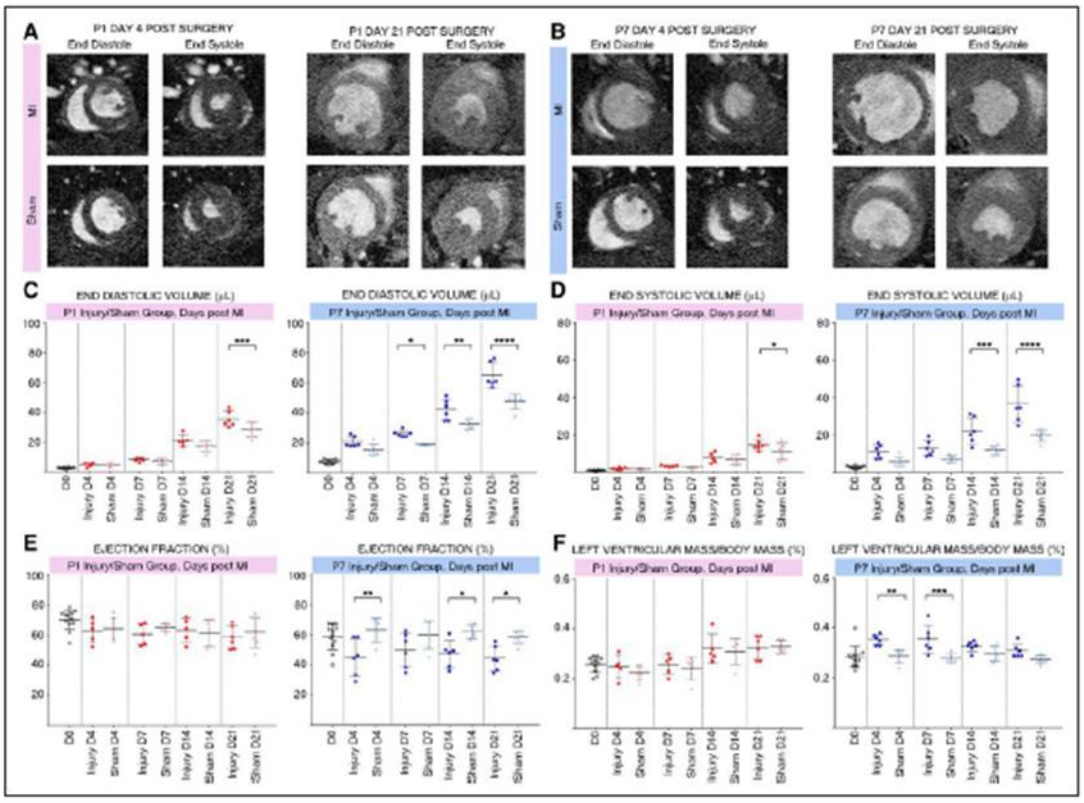

Figure. Functional MRI parameters at baseline and days 4, 7, 14, and 21 after MI and sham-operated P1 versus P7 mice.
A and **B**, Midventricular short-axis cine-MRI frames for P1 (**A**) and P7 (**B**) hearts in diastole and systole at days 4 and 21 after MI. **C** through **F**, MRI values for end diastolic volume (**C**), end systolic volume (**D**), ejection fraction (**E**), and left ventricular mass to body mass ratio (**F**) are indicated. Each time point shows a comparison between the injury and sham groups within each P1 and P7 cohort across the duration of study. One-way ANOVA with Sidak's multiple comparisons test. Significant differences between injury and sham cohorts are indicated as **P*<0.05, ***P*<0.01, ****P*<0.001, and *****P*<0.0001; N=5 or 6 for all groups. MI indicates myocardial infarction; MRI, magnetic resonance imaging; and P, postnatal day.

which became significant by day 21 (Figure, C), inferring that regeneration may be incomplete in contrast to previous reports.[3] End-systolic volume values for the P7 injured group were also significantly higher across later time points (Figure, D). The P1 injured group revealed small increases in end-systolic volume, which were significant only by day 21 (Figure, D). The ejection fraction was significantly lower for the P7 injury group, compared with controls, for most of the time points analyzed (Figure, E): there was a decrease in ejection fraction immediately after MI, an apparent recovery at day 7, followed by further significant decreases in ejection fraction through days 14 and 21, suggesting impaired recovery of normal heart function over time. In contrast, the P1 group revealed no significant differences in ejection fraction between injured and sham hearts at all time points (Figure, E. Moreover, ejection fraction was maintained at ≈60% as previously reported for intact neonatal mice.[5] Maintenance of function coincides with the regenerative response at P1 and is likely linked to the compensatory growth of the heart from this stage and throughout the analyses. Stroke volume increased linearly for both P1 and P7 hearts as the mice aged, with a significant increase in the P1 MI group at day 14 (not shown). There were no significant differences in heart rate across all groups (not shown). The left-ventricular mass/body mass index was significantly increased in the P7 group at days 4 and 7 and remained elevated until end point after injury (Figure, F), which is consistent with an adult cardiomyocyte hypertrophy response, whereas no significant differences were observed at P1 (Figure, F).

Collectively, these data reveal compensatory changes in cardiac function with the restoration of tissue and resolution of injury for P1 neonates and sustained injury responses for the P7 cohort. This study resolves the controversy surrounding neonatal mouse heart regeneration and establishes a functional platform for live capture of the regenerative process and for future testing of genetic or therapeutic interventions.

Circulation. 2018;138:2439–2441. DOI: 10.1161/CIRCULATIONAHA.118.036086

APPENDIX 1: Circulation paper (p3\3)

All animal experiments were carried out according to the UK Home Office project license PPL30/2987 compliant with the UK Animals (Scientific Procedures) Act 1986 and approved by the local Biological Services Ethical Review Process.

ARTICLE INFORMATION

The data, analytical methods, and study materials will be made available to other researchers for purposes of reproducing the results or replicating the procedure. These are available on request from paul.riley@dpag.ox.ac.uk and J.E.Schneider@leeds.ac.uk.

Correspondence

Paul R. Riley, BSc, PhD, Department of Physiology, Anatomy and Genetics Sherrington Bldg, University of Oxford, South Parks Rd, Oxford OX1 3PT, United Kingdom; or Jürgen E. Schneider, PhD, Division of Biomedical Imaging, Leeds Institute of Cardiovascular and Metabolic Medicine, LIGHT Laboratories, Clarendon Way, University of Leeds, Leeds LS2 9JT, United Kingdom. Email paul.riley@dpag.ox.ac.uk or J.E.Schneider@leeds.ac.uk

Affiliations

Department of Physiology, Anatomy and Genetics, British Heart Foundation, Oxbridge Centre of Regenerative Medicine, University of Oxford, UK (M.G.-R., M.M., J.E.S., P.R.R.). British Heart Foundation, Experimental Magnetic Resonance Unit, Wellcome Trust Centre for Human Genetics, Roosevelt Dr, Oxford, UK (M.L.M., J.E.S.). RDM Cardiovascular Medicine, John Radcliffe Hospital, Headley Way, Headington, Oxford UK (M.L.M., J.E.S.). Department of Oncology, Cancer Research UK, Medical Research Council, Oxford Institute for Radiation Oncology, University of Oxford, UK (S.C.S.). Division of Biomedical Imaging, Leeds Institute of Cardiovascular and Metabolic Medicine, LIGHT Laboratories, Clarendon Way, University of Leeds, UK (J.E.S.).

Acknowledgments

The authors thank the late Victoria Thornton for supporting the MRI work and Dr Tobias Wech (University of Würzburg, Germany) for providing the optimized compressed sensing sampling schemes. The authors also appreciate the technical and administrative support from Lee-Anne Stork and Aude Vernet during the surgery and scanning procedures.

Sources of Funding

This work was generously supported by the British Heart Foundation via a chair award (CH/11/1/28798; PRR), senior fellowship (FS/11/50/29038; JES), and through the British Heart Foundation Oxbridge Regenerative Medicine Center (RM/13/3/30159; MGR, JES, and PRR.); and a European Union Seventh Framework Program Initial Training Network: CardioNet (#289600; MM). PRR and JES conceived of and designed the original study. MM carried out pilot MRI studies. MLM, SCS, and JES designed and built the custom hardware for neonate MRI scanning. JES developed the data acquisition method and image analysis software. MGR performed the neonate surgeries and MRI scanning with MLM. MGR analyzed the data and prepared it for publication. The manuscript was written by PRR and edited by MGR and JES. All authors approved the final version of the manuscript.

Disclosures

PRR is cofounder and equity holder in OxStem Cardio, an Oxford University spin-out that seeks to exploit therapeutic strategies stimulating endogenous repair in cardiovascular regenerative medicine.

REFERENCES

1. Porrello ER, Mahmoud AI, Simpson E, Hill JA, Richardson JA, Olson EN, Sadek HA. Transient regenerative potential of the neonatal mouse heart. *Science*. 2011;331:1078–1080. doi: 10.1126/science.1200708
2. Kikuchi K, Holdway JE, Werdich AA, Anderson RM, Fang Y, Egnaczyk GF, Evans T, Macrae CA, Stainier DY, Poss KD. Primary contribution to zebrafish heart regeneration by gata4(+) cardiomyocytes. *Nature*. 2010;464:601–605. doi: 10.1038/nature08804
3. Porrello ER, Mahmoud AI, Simpson E, Johnson BA, Grinsfelder D, Canseco D, Mammen PP, Rothermel BA, Olson EN, Sadek HA. Regulation of neonatal and adult mammalian heart regeneration by the miR-15 family. *Proc Natl Acad Sci U S A*. 2013;110:187–192. doi: 10.1073/pnas.1208863110
4. Andersen DC, Jensen CH, Baun C, Hvidsten S, Zebrowski DC, Engel FB, Sheikh SP. Persistent scarring and dilated cardiomyopathy suggest incomplete regeneration of the apex resected neonatal mouse myocardium: a 180 days follow up study. *J Mol Cell Cardiol*. 2016;90:47–52. doi: 10.1016/j.yjmcc.2015.11.031
5. Wiesmann F, Ruff J, Hiller KH, Rommel E, Haase A, Neubauer S. Developmental changes of cardiac function and mass assessed with MRI in neonatal, juvenile, and adult mice. *Am J Physiol Heart Circ Physiol*. 2000;278:H652–H657. doi: 10.1152/ajpheart.2000.278.2.H652

APPENDIX 2: Table of values for grouped results of functional parameters

Functional parameters of cardiac function with and without MI infarction surgery as measured by MRI. One-way ANOVA results are shown comparing MI to sham groups for the P1 and P7 cohorts (significant differences between injury and sham cohorts are indicated as *P < 0.05; **P < 0.01; ***P < 0.001 and ****P < 0.0001; n=5 or 6 for all groups).

	P1 MI		P1 Sham			P7 MI		P7 Sham		
	END DIASTOLIC VOL		END DIASTOLIC VOL			END DIASTOLIC VOL		END DIASTOLIC VOL		
	Mean	SD	Mean	SD		Mean	SD	Mean	SD	
D1 - P1	2.56 ± 0.44					7.51 ± 1.32				
D4 - P5	4.92	1.17	4.82	0.99	ns	20.89	3.13	15.81	3.28	ns
D7 - P8	8.291	1.14	7.167	1.76	ns	26.36	2.00	19.1	0.70	*
D14 - P15	21.25	3.47	17.38	3.04	ns	42.25	6.33	32.77	3.06	**
D21 - P22	35.58	4.69	28.49	4.44	***	65.19	7.53	47.99	4.58	****
	P1 MI		P1 Sham			P7 MI		P7 Sham		
	END SYSTOLIC VOL		END SYSTOLIC VOL			END SYSTOLIC VOL		END SYSTOLIC VOL		
	Mean	SD	Mean	SD		Mean	SD	Mean	SD	
D1 - P1	0.75 ± 0.17					3.04 ± 0.63				
D4 - P5	1.882	0.72	1.68	0.39	ns	11.52	3.24	6.005	2.50	ns
D7 - P8	3.204	0.47	2.513	0.68	ns	13.33	3.73	7.561	1.55	ns
D14 - P15	7.864	2.40	6.813	2.29	ns	22.63	6.49	12.38	2.17	***
D21 - P22	14.59	2.73	11.13	4.10	*	36.68	9.01	19.79	2.86	****
	P1 MI		P1 Sham			P7 MI		P7 Sham		
	EJECTION FRACTION		EJECTION FRACTION			EJECTION FRACTION		EJECTION FRACTION		
	Mean	SD	Mean	SD		Mean	SD	Mean	SD	
D1 - P1	70.58 ± 6.31					59.05 ± 8.33				
D4 - P5	63.25	7.08	64.52	6.50734	ns	45.32	11.32	63.25	7.43	**
D7 - P8	60.85	6.25	65.1	2.33	ns	50.1	10.46	60.28	8.66	ns
D14 - P15	63.6	7.18	61.79	8.01	ns	47.44	8.15	62.42	4.20	*
D21 - P22	58.74	6.88	62.2	9.14	ns	44.5	7.61	58.84	3.92	*
	P1 MI		P1 Sham			P7 MI		P7 Sham		
	STROKE VOL		STROKE VOL			STROKE VOL		STROKE VOL		
	Mean	SD	Mean	SD		Mean	SD	Mean	SD	
D1 - P1	1.82 ± 0.40					4.48 ± 1.12				
D4 - P5	3.042	0.53	3.135	0.77	ns	9.363	2.20	9.801	1.09	ns
D7 - P8	5.087	1.06	4.653	1.12	ns	13.03	2.05	11.54	1.86	ns
D14 - P15	13.38	1.82	10.57	1.51	**	19.62	1.93	19	3.73	ns
D21 - P22	19.33	1.87	17.36	1.44	ns	28.51	2.40	28.2	3.04	ns
	P1 MI		P1 Sham			P7 MI		P7 Sham		
	HEART RATE		HEART RATE			HEART RATE		HEART RATE		
	Mean	SD	Mean	SD		Mean	SD	Mean	SD	
D1 - P1	408.58 ± 26.30					408.92 ± 58.32				
D4 - P5	463.4	11.22	475.8	24.83	ns	430.2	23.26	411.8	26.77	ns
D7 - P8	388.6	47.70	400.4	21.67	ns	349	56.66	336.3	60.14	ns
D14 - P15	292.8	33.34	279	28.91	ns	420.3	54.15	444	32.96	ns
D21 - P22	460	33.74	461.5	14.58	ns	494	16.65	474.2	22.27	ns
	P1 MI		P1 Sham			P7 MI		P7 Sham		
	LVM / BM		LVM / BM			LVM / BM		LVM / BM		
	Mean	SD	Mean	SD		Mean	SD	Mean	SD	
D1 - P1	0.26 ± 0.03					0.28 ± 0.04				
D4 - P5	0.248	0.04	0.224	0.03	ns	0.3533	0.02	0.2867	0.02	**
D7 - P8	0.256	0.04	0.242	0.04	ns	0.355	0.05	0.2783	0.02	***
D14 - P15	0.32	0.05	0.308	0.05	ns	0.3267	0.02	0.2983	0.03	ns
D21 - P22	0.325	0.04	0.3283	0.02	ns	0.31	0.03	0.2733	0.01	ns

APPENDIX 3: NEONATE MRI GRANT APPLICATION NOTES 2022

BHF CRM Development of advanced MR imaging techniques for the regenerating mouse heart
Applicants: Prof Jurgen E Schneider (PI), Dr Nadira Yuldasheva (both University of Leeds); Prof Paul R Riley (University of Oxford)) to deliver solutions to some of these concerns identified below:

Hardware development:
One key step to obtain more consistent, easier to analyse images is to include ECG measurements during the scan which can be used to check the MR images as the scan is being performed, and to negate the need for retrospective gating. We would like to develop a system to reliably derive ECG signals from the pups by utilising our recently established collaboration with an expert in this field, Dr FN Guerrero, who has experience obtaining these from various organisms, some as small as fruit flies. He will attempt to deliver an electrode that will be suitable for safe and repeated scanning of neonatal mouse pups from P1 size and for use within the MRI scanner. The respiratory signals we obtained from the pressure pad were used only to monitor the pup's breathing during the scan, but if we can use a live ECG signal, we may also be able to use the signal for more sophisticated imaging sequencing techniques. Ideally, cradles could be designed in a modular fashion with a much finer gradation of sizes to adapt to the growing pup. These would have anaesthesia delivery and integrated heating to minimise space and also include the optimal ECG monitoring equipment.

Software development:
We would like to increase the current 2D compressed sensing sequence to 3D to increase the speed of the scan further and improve the resolution of the slices at the same time. This may also help to reduce image artefacts and increase the signal-to-noise ratio of the output. We would like to be able to quantify the extent of initial injury during the scan after the surgery to provide additional evidence for injury along with visual akinesis (and thus solidify the claim of regeneration). This may require further exploration of the injection of contrast agents into these young pups. And finally, we would attempt to automate the data analysis process using advanced machine learning protocols to segment the functional MRI data by training the system on data sets of both healthy and damaged, infarcted hearts that have been previously manually segmented. This would be in a further collaboration with Dr T. Wech who has contributed to fundamental advancements in the analysis and development of MRI scanning for smaller subjects (Wech, Lemke et al. 2011).

APPENDIX 4: pHLIP INJECTIONS

pHLIP dose and injection methods for the developmental mice and cryo-infarcted rat studies

MOUSE AGE	AVG BODY MASS	2mM pHILP-Cy5.5 STOCK VOLUME	HOECHST STOCK VOLUME	PBS BUFFER VOLUME	VOL OF WORKING SOLUTION	CONCENTRATION OF WORKING SOLN	FINAL INJECTION VOLUME	INJECTION METHOD	TIME BEFORE HARVEST
P1	2.18 g	4 µl		96 µL	100 µL	80 µM	20 µL	SUBCUTANEOUS	24 hrs
P7	6.59 g	12 µl		88 µL	100 µL	240 µM	20 µL	SUBCUTANEOUS	24 hrs
P21	14 g	12 µl		88 µL	100 µL	240 µM	40 µL	INTERPERITONEAL	24 hrs
ADULT	25 g	4 µl		96 µL	100 µL	80 µM	200 µL	SUBCUTANEOUS	24 hrs
ADULT	25 g	4 µl		96 µL	100 µL	80 µM	200 µL	INTRAPERITONEAL	24 hrs
ADULT	25 g	4 µl		96 µL	100 µL	80 µM	100 µL	INTRAVENOUS	5 hrs
P1	2.18 g	4 µl	2 µl	94 µL	100 µL	80 µM	20 µL	SUBCUTANEOUS	24 hrs
P7	6.59 g	12 µl	6 µl	82 µL	100 µL	240 µM	20 µL	SUBCUTANEOUS	24 hrs
P21	14 g	12 µl	14 µl	74 µL	100 µL	240 µM	40 µL	INTRAPERITONEAL	24 hrs
ADULT	25 g	4 µl	25 µl	71 µL	100 µL	80 µM	100 µL	INTRAVENOUS	5 hrs
RAT AGE	AVG BODY MASS	2mM pHILP-Cy5.5 STOCK VOLUME	HOECHST STOCK VOLUME	PBS BUFFER VOLUME	VOL OF WORKING SOLUTION	CONCENTRATION OF WORKING SOLN	FINAL INJECTION VOLUME	INJECTION METHOD	TIME BEFORE HARVEST
ADULT	200 g	32 µl	200 µl	168 µL	400 µL	160 µM	400 µL	INTRAPERITONEAL	24 hrs
ADULT	260 - 298 g	32 µl	200 µl	168 µL	400 µL	160 µM	400 µL	INTRAVENOUS	5 hrs

APPENDIX 5: (1/3) DIFFERENTIATION PROTOCOL OVERVIEW FOR hiPSC BEATING CARDIOMYOCYTES

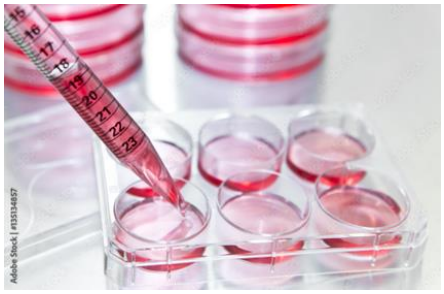

Media changes:

1. iPSC maintenance in mTeSR
2. Day 0 – RPMI with glucose + B27 minus insulin + CHIR99021
3. Day 2 – RPMI with glucose + B27 minus insulin
4. Day 3 - RPMI with glucose + B27 minus insulin + Wnt-C59
5. Day 5 - RPMI with glucose + B27 minus insulin
6. Day 11 - RPMI without glucose + B27 minus insulin
7. Day 15 - RPMI with glucose + B27 with insulin

TIMELINE:

DAY 0 - 12 wells: Differentiation: Rb- + CHIR99029 (4ml/well)	Wnt pathway initiation
DAY 1: Leave cells alone	
DAY 2: media change: Rb- (3ml/well)	
DAY 3: Rb- + Wnt-C59 (4ml/well)	Wnt pathway inhibition
DAY 4: Leave cells alone	
DAY 5: media change: Rb- (4ml/well)	
DAY 6: Leave cells alone	
DAY 7: media change: Rb- (4ml/well)	
DAY 8: Leave cells alone	
DAY 9: media change: Rb- (4ml/well)	
DAY 10: Leave cells alone	
DAY 11: media change: Rb- without glucose (Met-) (4ml/well)	Metabolic maturation of CM; loss of other cells
DAY 11: media change: Rb- without glucose (Met-) (4ml/well)	
DAY 12: Leave cells alone	
DAY 13: media change: Rb- without glucose (Met-) (4ml/well)	
DAY 14: Leave cells alone	
DAY 15: media change: RPMI supplemented with B27 complete	

APPENDIX 5: (2/3) DIFFERENTIATION PROTOCOL DETAILS

DAY 0 – Start differentiation process by stimulating Wnt pathway

- Use Rb^- medium:
    - RPMI Medium 1640 (+ L-Glutamine)
    - B-27 Minus Insulin (10ml supplement)
- Add CHIR99021 concentration = 1:2000
- Ex: For 12 wells to differentiate
    - 4ml Rb^- media per well = 48 ml total (for 2 plates x 6 wells)
    - Add 24ul CHIR99021
- Remove mTeSr, add Rb^- + CHIR (4ml per well)

DAY 1

- No action needed, leave cells alone for first day

DAY 2 – Remove Wnt stimulus

- Remove media, add 4mL Rb^- medium

DAY 3 – Inhibit further Wnt action by blocking endogenous production

- Cells currently in 2 x 6 well plates (12 wells total)
- Media: Rb^- 48ml
  C59 12ul (1:4000 dilution)
- Remove Rb^- media; Add 4ml Rb^- + Wnt-C59 per well to terminate differentiation

DAYS 4 - 10 – Continued differentiation of iPSC to beating cardiomyocytes

- Every second day, remove old Rb^- medium and add fresh Rb^- (leave cells alone between media changes)

DAYS 11-14 – Metabolic selection of cardiomyocytes and reduction of undifferentiated fibroblasts

- Use Met^- medium:
    - RPMI Basal Medium (without Glucose)
    - B-27 Minus Insulin (10ml supplement)
- Change medium every second day

DAY 15 – Differentiation complete, hiPSC-CM culture

- Use Rb^+ medium:
    - RPMI Medium 1640 (+ L-Glutamine)
    - B-27 Complete with Insulin (10ml supplement)

APPENDIX 5: (3/3) DIFFERENTIATION PROTOCOL DETAILS

IPSC CULTURE MEDIA

Product	**Company**	**Catalogue number**
mTeSR™1 Complete Kit: mTeSR™1 Basal Medium, 400 mL mTeSR™1 5X Supplement, 100 mL	STEMCELL Technologies	85850
TeSR™-E8™ Kit for hESC/hiPSC Maintenance TeSR™-E8™ Basal Medium, 480 mL TeSR™-E8™ 25X Supplement, 20 mL	STEMCELL Technologies	05990
ReLeSR™	STEMCELL Technologies	05872
Rock Inhibitor (Y-27632)	MERCK	SCM075
Matrigel	CORNING	356234
RF-Matrigel	CORNING	354230
RPMI 1640	ThermoFisher Scientific	11875085
RPMI 1640, no glucose	ThermoFisher Scientific	11879020
B27 minus insulin	ThermoFisher Scientific	A1895601
B27 complete	ThermoFisher Scientific	17504044
CHIR99021	TOCRIS	4423
Wnt-C59	TOCRIS	5148

(A) Stem cell (IPSC) culture and maintenance

(B) IPSC to IPSC-Cardiomyocyte differentiation protocol

(C) IPSC-Cardiomyocyte maintenance and maturation media

(i) Rb^{+}

(II) Maturation

SUPPLEMENTAL FIGURE S1: (1/2) Functional parameters of the neonatal heart after MI injury – End Diastolic Volume, End Systolic Volume, Ejection Fraction

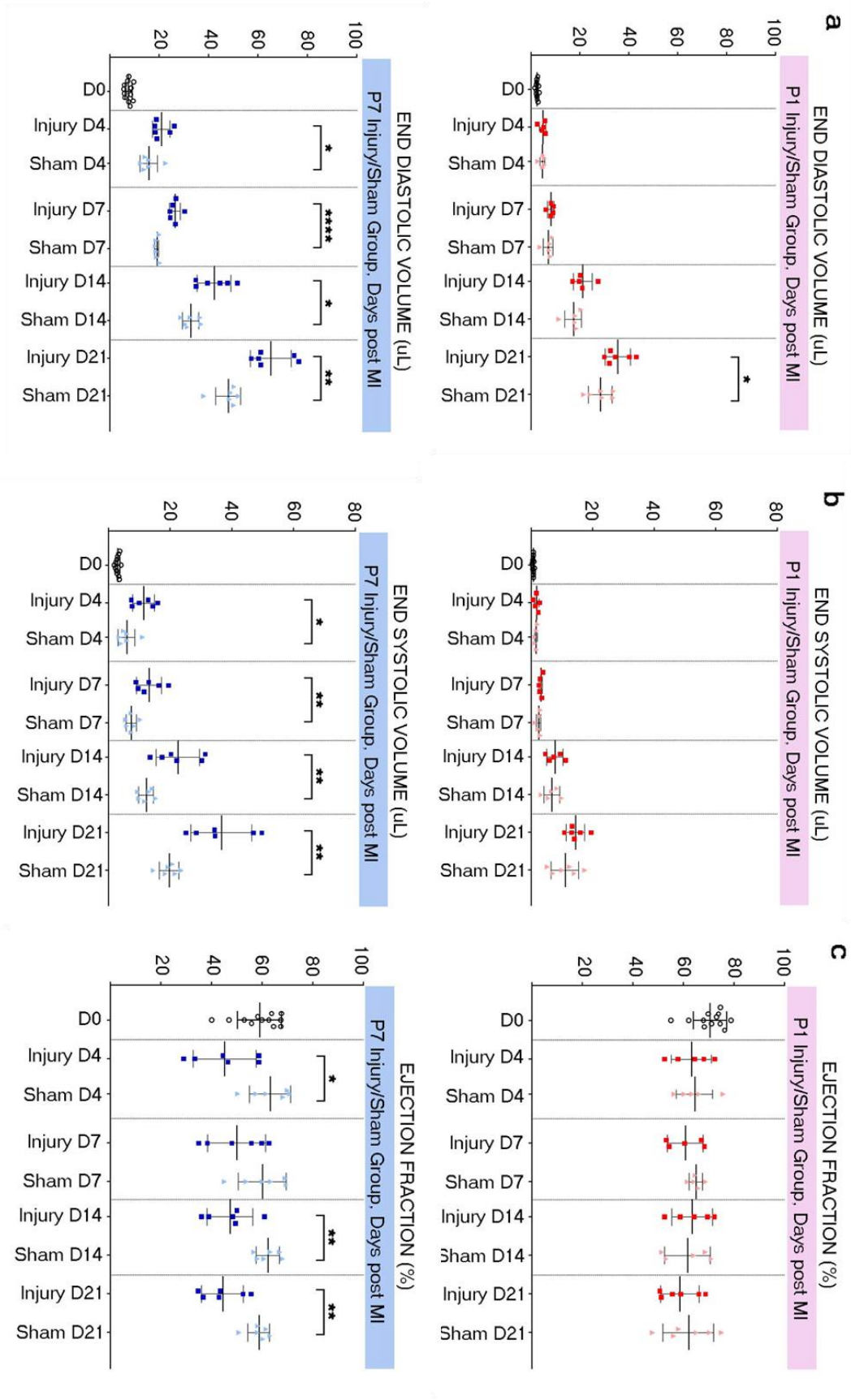

SUPPLEMENTAL FIGURE S1: (2/2) Functional parameters of the neonatal heart after MI injury – Stroke Volume, Heart Rate, Left Ventricular Mass/Body Mass ratio

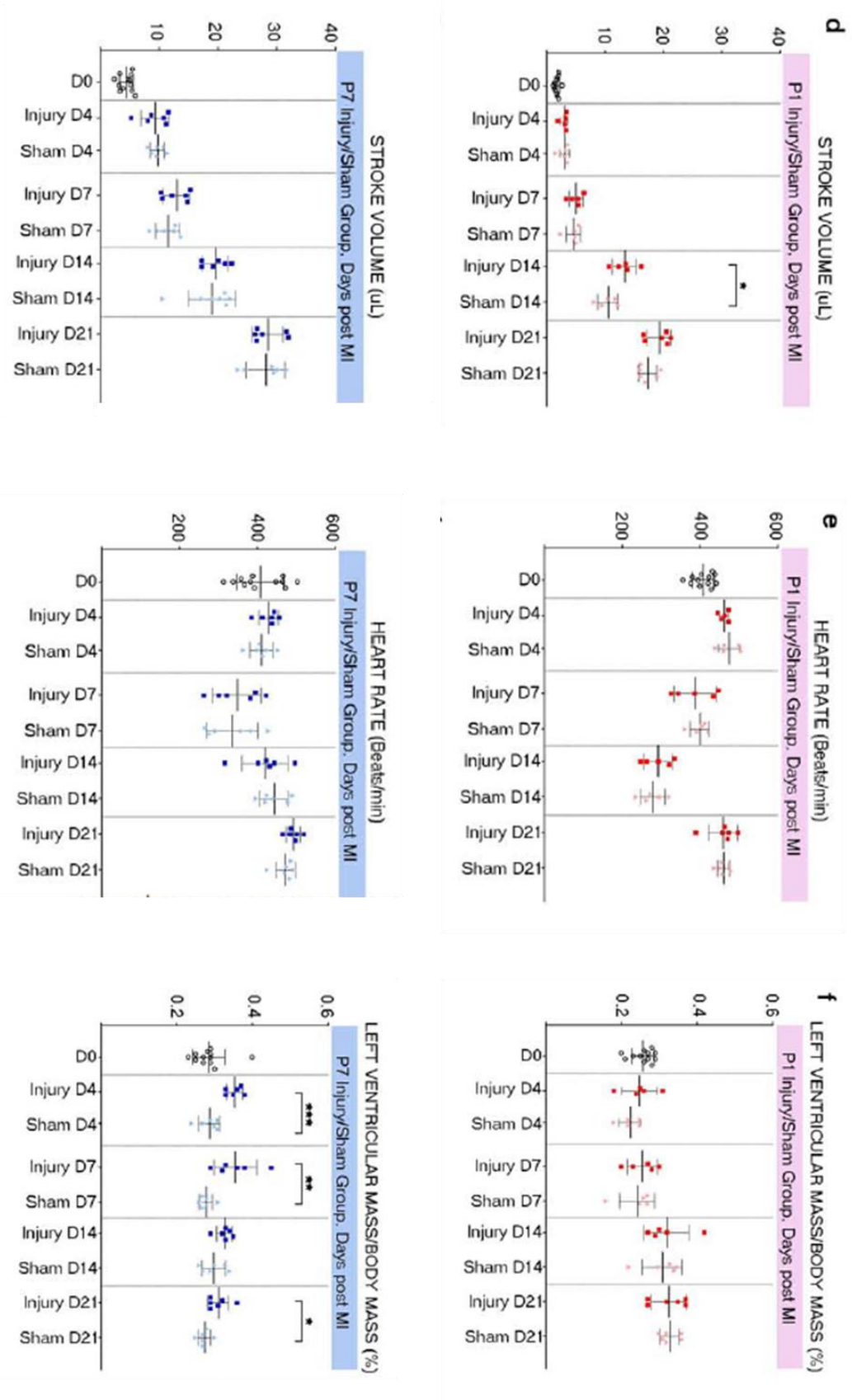

SUPPLEMENTAL FIGURE S2: Longitudinal analysis of 3xP1 and 3xP7 pups after MI/sham injury

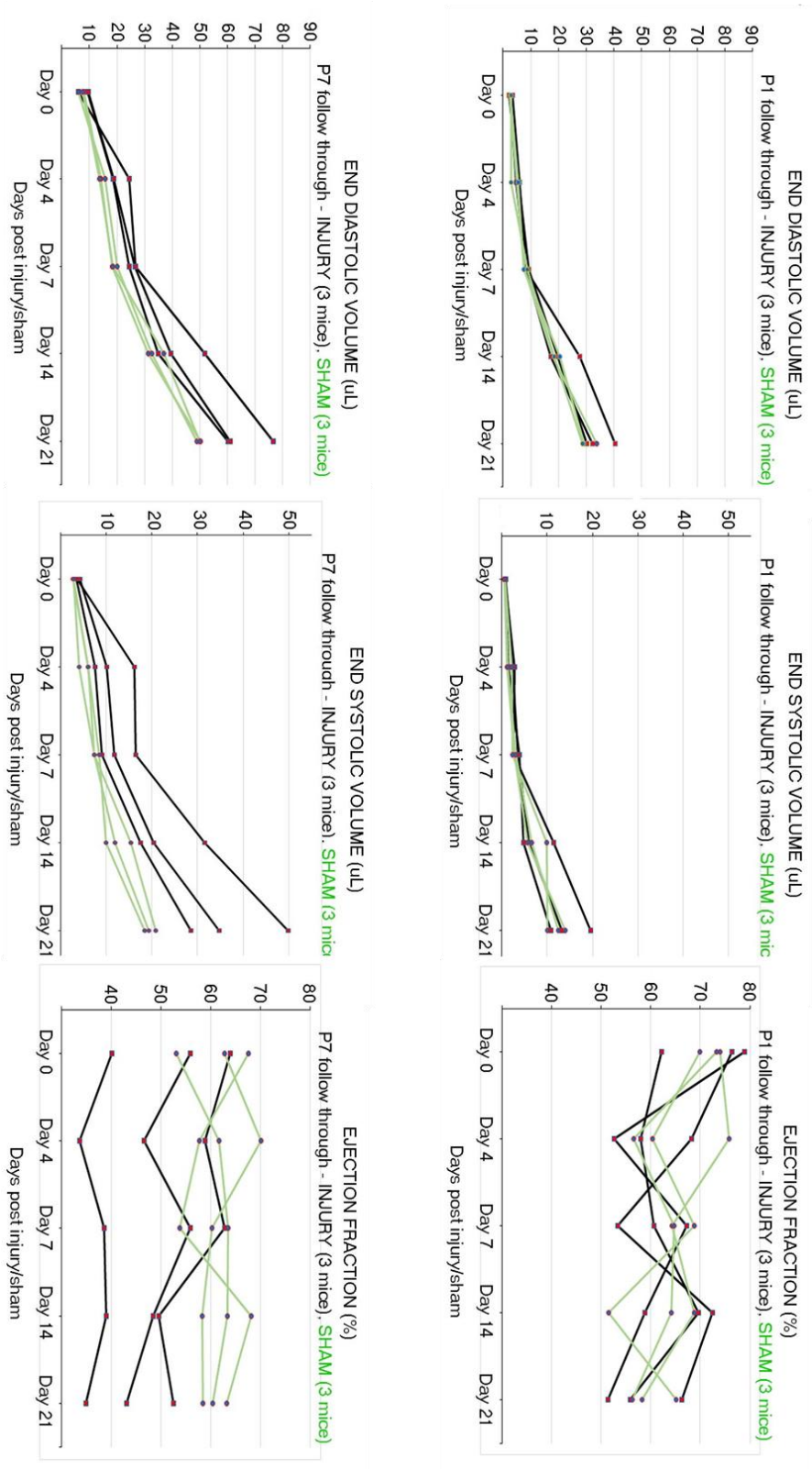

SUPPLEMENTAL FIGURE S3: (1/2) Fucci slice assay of cycling cells across the P5 (injured at P1) and P11 (injured at P7) hearts.

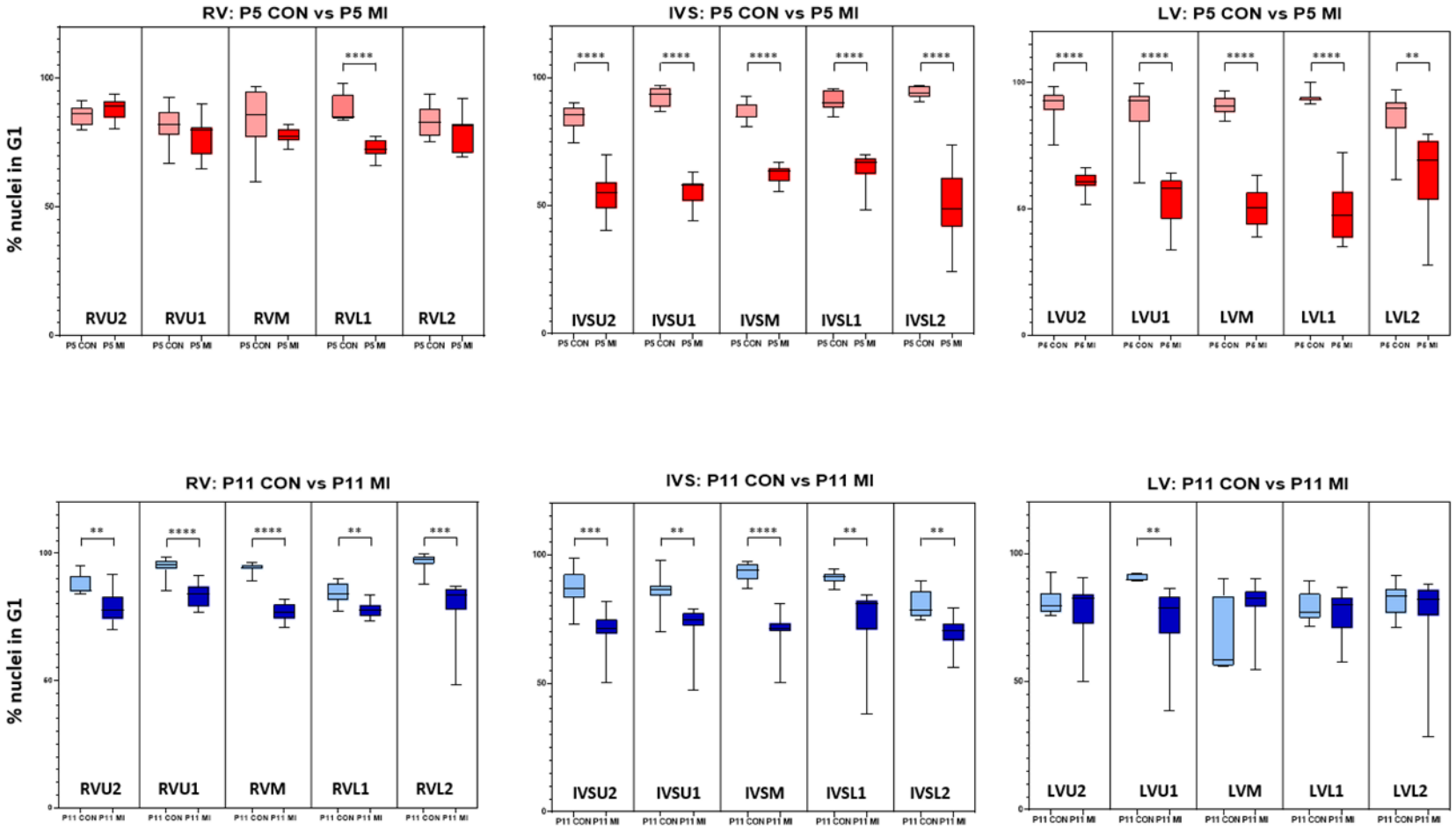

Regions of cell cycling activity along the heart walls: The lower this value, the higher is the implied number of nuclei more actively cycling into S, G2 and M phases. For injury at P1 and response measured 4 days later (P5), there are strong areas of cell cycle activation along the full length of the LV and IVS whereas for the P7 situation, the main response is more remote: also in the IVS but extending to the RV. There is almost nothing in the LV close to the initial injury at all. N = 3 hearts in each group (3 slices per heart), unpaired t-test, *P < 0.05; **P < 0.01; ***P < 0.001 and ****P < 0.0001;

SUPPLEMENTAL FIGURE S3: (2/2) Fucci slice assay of cycling cells across the P5 (injured at P1) and P11 (injured at P7) hearts.

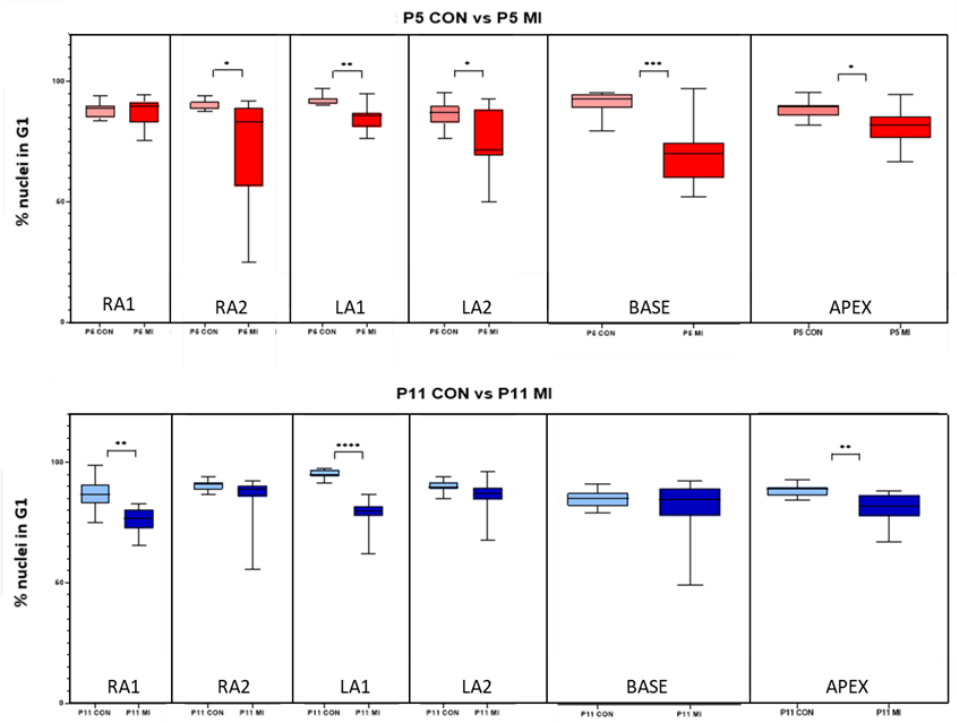

Regions of cell cycling activity in other regions of the heart: Right and Left Atria, Base and Apex. N = 3 hearts in each group (3 slices per heart), unpaired t-test, *P < 0.05; **P < 0.01; ***P < 0.001 and ****P < 0.0001;

SUMMARY OF AREAS OF GREATEST SIGNIFICANCE

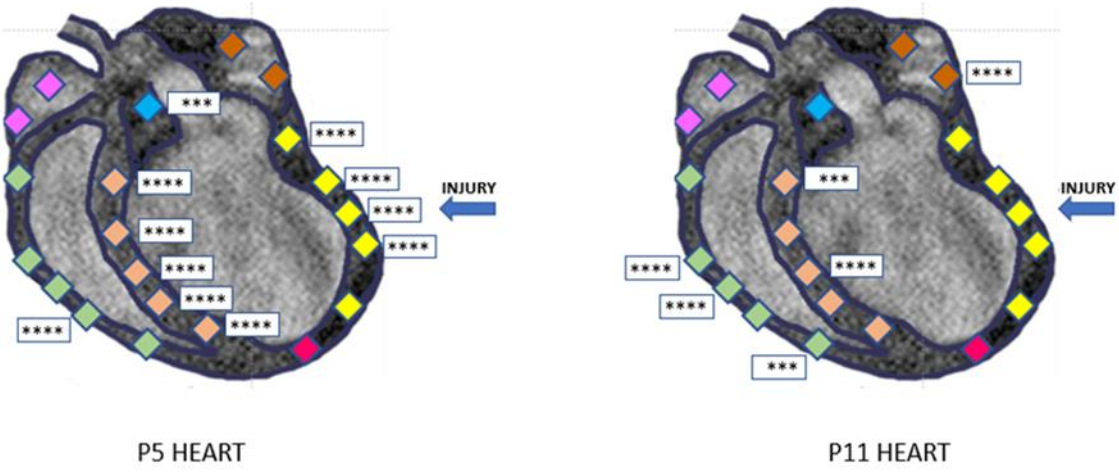

Summary graphic: regions of greatest cell cycling activity after MI injury in P5 and P11 hearts. The P5 heart shows cell cycle activation along the left ventricle and intraventricular septum whereas the P11 heart has activation in more remote regions including the right ventricle. The significance values are from Figs. 20 and 21 above with only areas where ***P < 0.001 and ****P < 0.0001 are mapped directly onto an outline of the heart.

SUPPLEMENTAL FIGURE S4: Un-injected P1 and P7 hearts showing no signal without pHLIP

We needed another set of controls for P1 and P7 hearts that had no injections of pHLIP but were sectioned and imaged using the same settings as for the treated hearts. We could see a very small amount of autofluorescence in the P7 sample (right image) as the cardiac tissue matures, with more in the vessels entering and exiting the heart, but most of the image was dark. There was no fluorescence visible in the P1 images (left image).

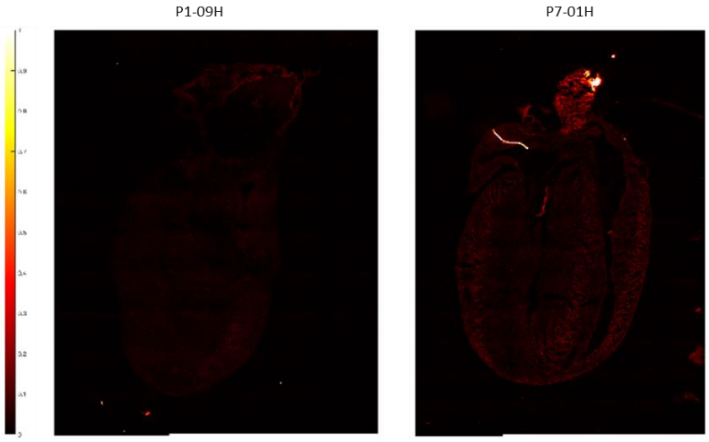

SUPPLEMENTAL FIGURE S5: Additional P1, P7, P21 and Adult injected with pHLIP

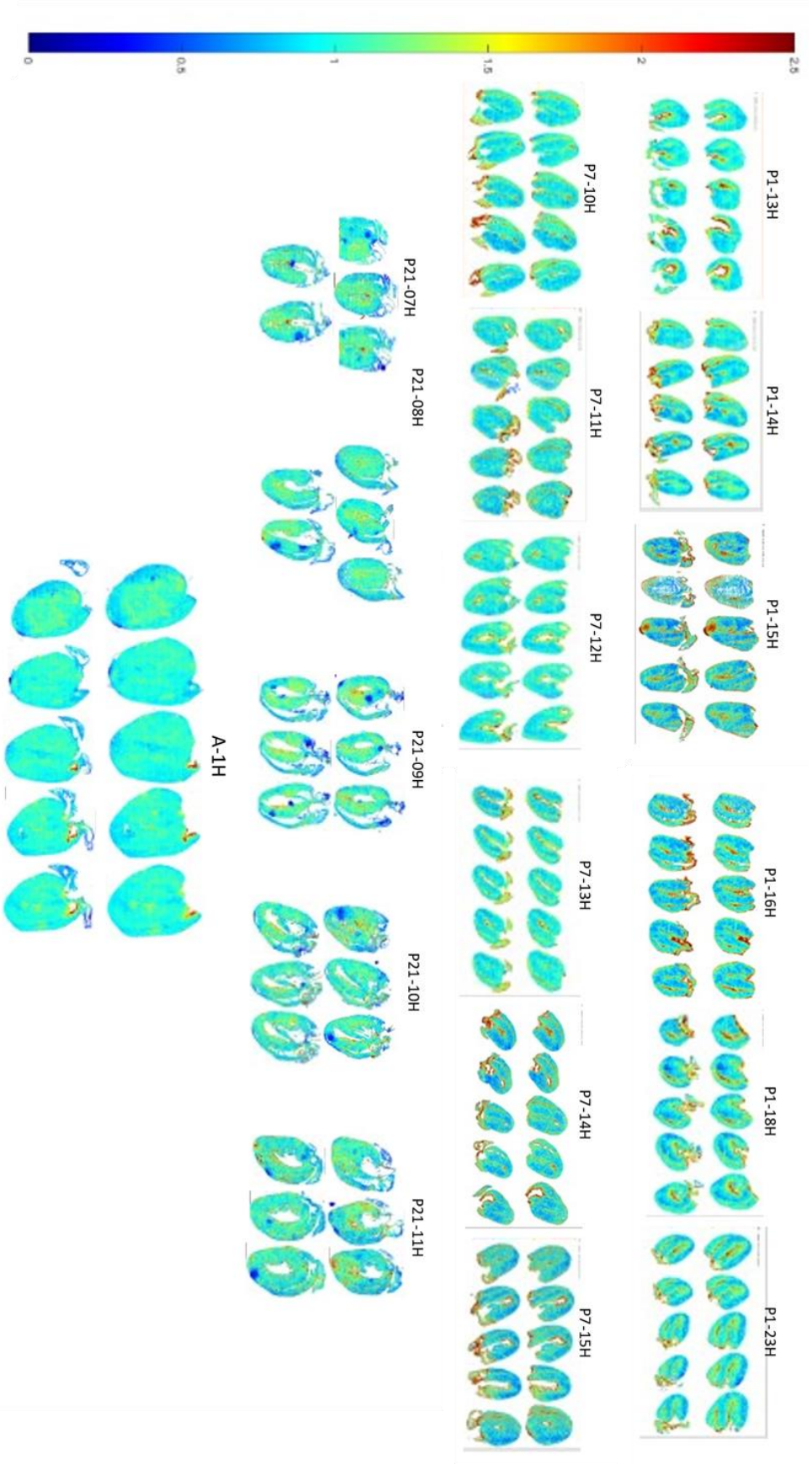

SUPPLEMENTAL FIGURE S6: (1/4) Fucci isolated cells timecourse shows cell cycling patterns changing for different conditions

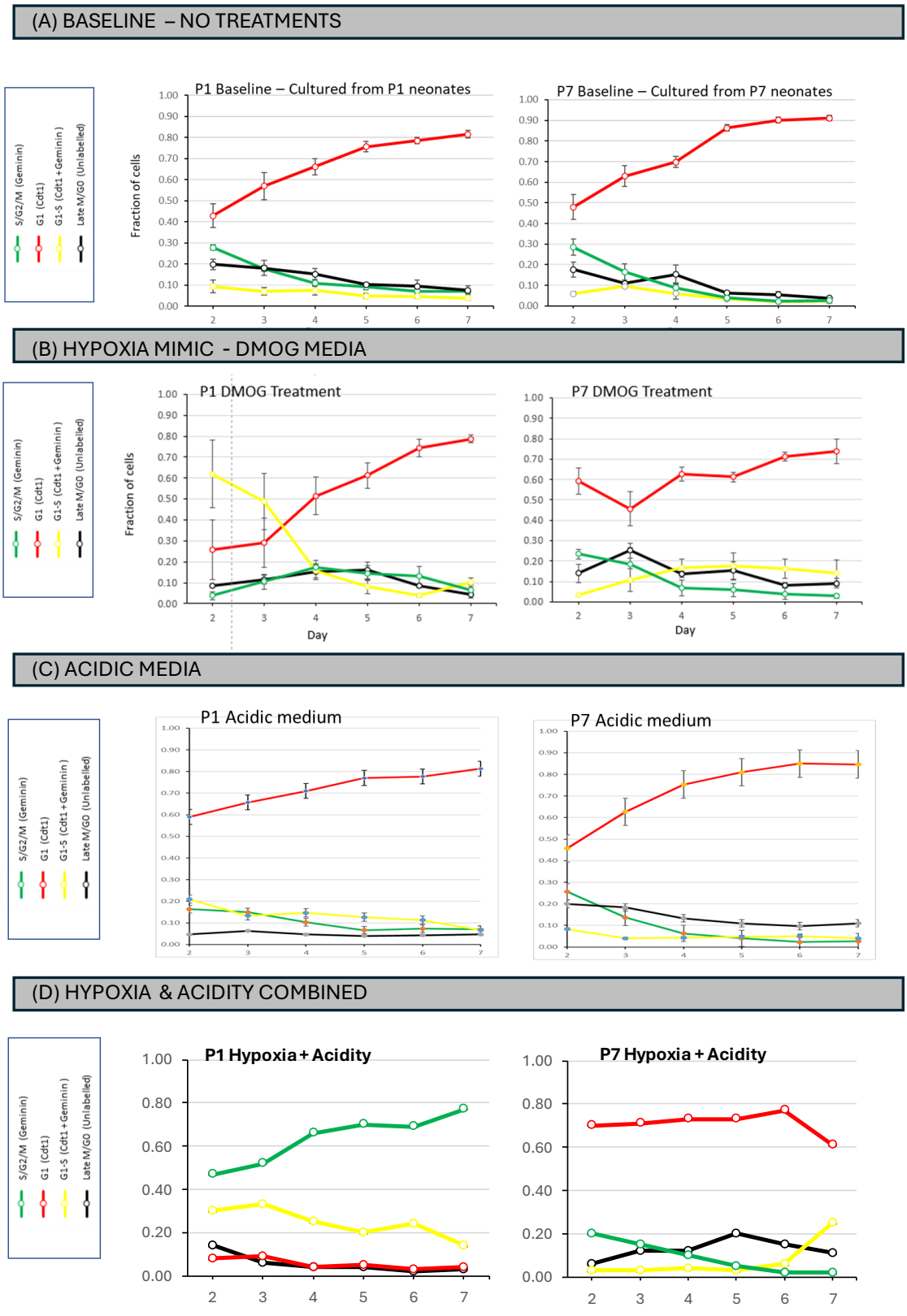

SUPPLEMENTAL FIGURE S6: (2/4) Fucci isolated cells P1 vs P7 cells at Baseline

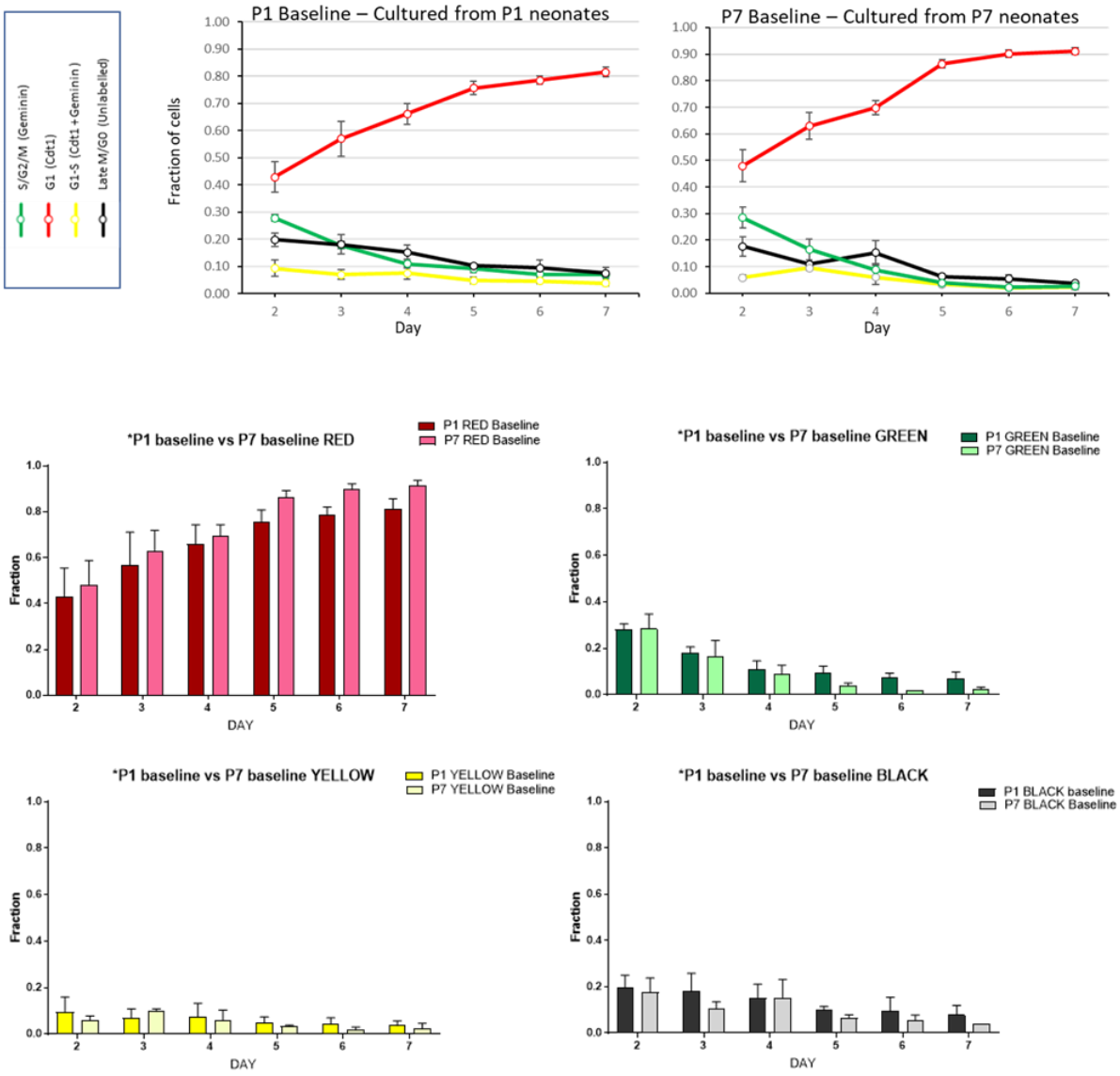

Supplemental Figure S6: Baseline time course of the cell cycle in cultured neonatal Fucci mice cells comparing cells isolated at postnatal day 1 (P1) vs P7. Top row: Fraction of cells in each category plotted against time, left graph is P1 and right graph is P7; the fraction is the sum of the 20 images per well per day, and (n = 3 separate isolations for each age group). Middle & Bottom rows: Direct comparison on day 2 – 7 for each category. Note there was no statistical difference between each cell cycle phase (n=3, One-way ANOVA with Sidak's multiple comparisons test).

SUPPLEMENTAL FIGURE S6: (3/4) Fucci isolated cells P1 vs P7 cells with hypoxia (DMOG)

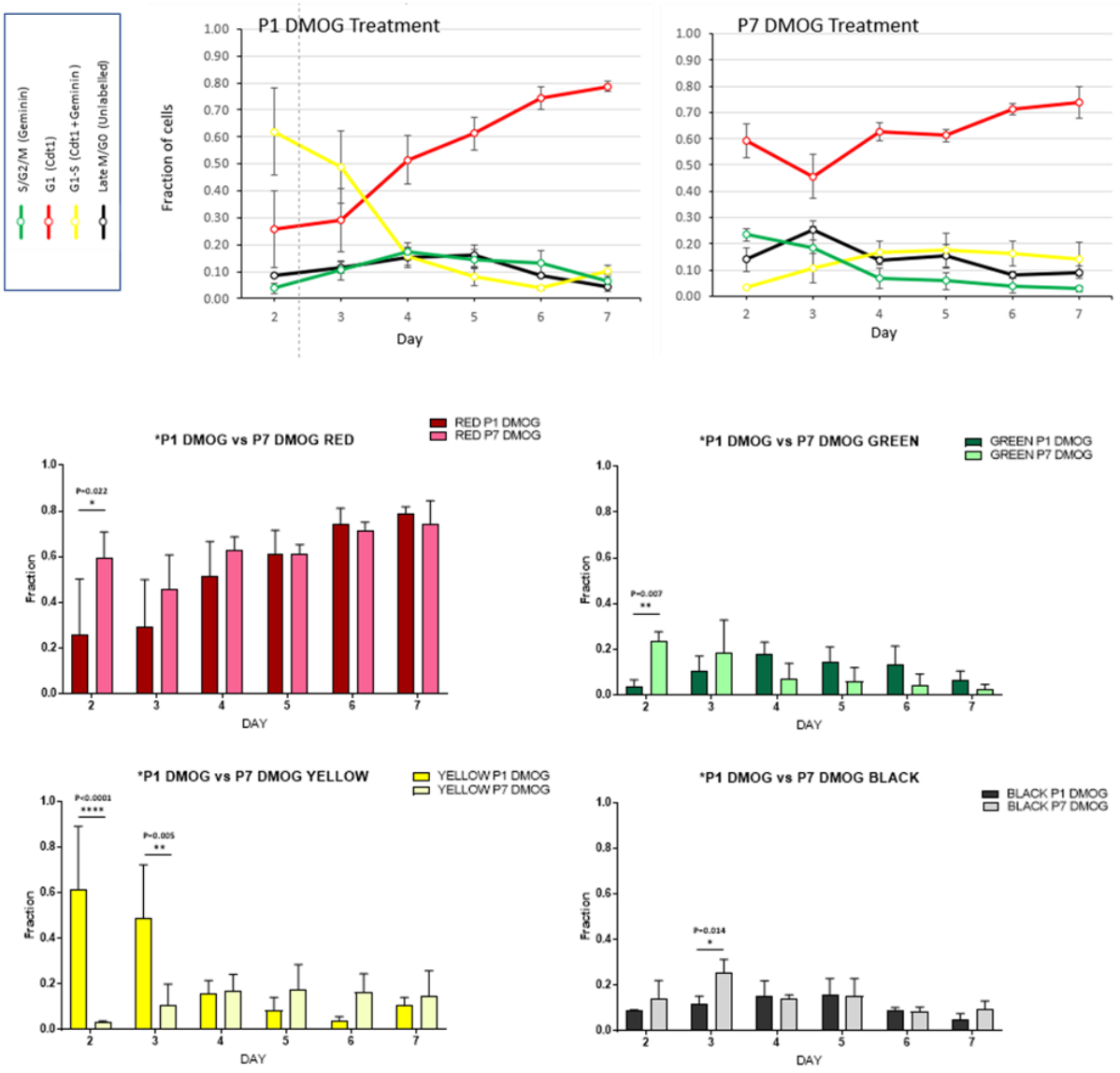

Supplemental Figure 5-2: Time course of the cell cycle in cultured neonatal Fucci mice cells comparing cells isolated at P1 vs P7 under hypoxic conditions. Top row: Fraction of cells in each category plotted against time, left graph is P1 and right graph is P7; n = 3 separate isolations for each group (P1 or P7). Middle & Bottom rows: Direct comparison day 2 – 7 for each category. (One-way ANOVA with Sidak's multiple comparisons test; *P<0.05, **P<0.01, ***P<0.001, ****P<0.0001).

SUPPLEMENTAL FIGURE S6: (4/4) Fucci isolated cells P1 vs P7 cells with acidity

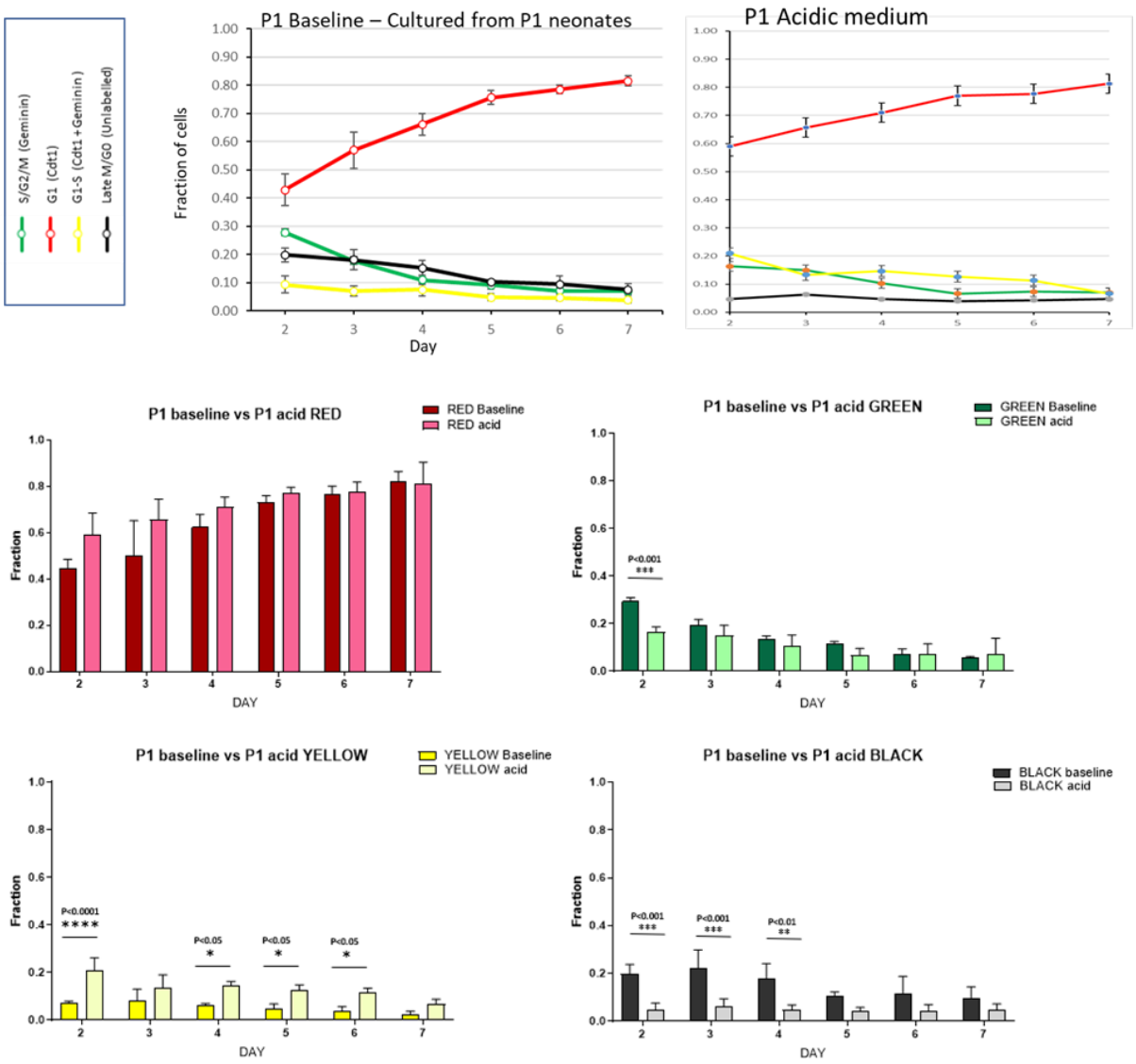

Supplemental Figure 5-3: Breakdown of the P1 assay by cell cycle phase, directly comparing normal pH media with acidic media. (One-way ANOVA with Sidak's multiple comparisons test; *P<0.05, **P<0.01, ***P<0.001, ****P<0.0001).

NOTE: We could not do this statistical analysis for the combined hypoxia and acidity data as there was only an n = 1.

REFERENCES

Abe, T., A. Sakaue-Sawano, H. Kiyonari, G. Shioi, K. Inoue, T. Horiuchi, K. Nakao, A. Miyawaki, S. Aizawa and T. Fujimori (2013). "Visualization of cell cycle in mouse embryos with Fucci2 reporter directed by Rosa26 promoter." Development **140**(1): 237-246.

Aggeli, I. K., C. Gaitanaki, A. Lazou and I. Beis (2001). "Activation of multiple MAPK pathways (ERKs, JNKs, p38-MAPK) by diverse stimuli in the amphibian heart." Mol Cell Biochem **221**(1-2): 63-69.

Aguilar-Sanchez, C., M. Michael and S. Pennings (2018). "Cardiac Stem Cells in the Postnatal Heart: Lessons from Development." Stem Cells Int **2018**: 1247857.

Ahuja, P., P. Sdek and W. R. MacLellan (2007). "Cardiac myocyte cell cycle control in development, disease, and regeneration." Physiol Rev **87**(2): 521-544.

Alberts, B. (2015). Molecular Biology of the Cell, Garland Science.

Alkass, K., J. Panula, M. Westman, T. D. Wu, J. L. Guerquin-Kern and O. Bergmann (2015). "No Evidence for Cardiomyocyte Number Expansion in Preadolescent Mice." Cell **163**(4): 1026-1036.

Allukian, M., 3rd, J. Xu, M. Morris, R. Caskey, W. Dorsett-Martin, T. Plappert, M. Griswold, J. H. Gorman, 3rd, R. C. Gorman and K. W. Liechty (2013). "Mammalian cardiac regeneration after fetal myocardial infarction requires cardiac progenitor cell recruitment." Ann Thorac Surg **96**(1): 163-170.

Alvarez, R., Jr., B. J. Wang, P. J. Quijada, D. Avitabile, T. Ho, M. Shaitrit, M. Chavarria, F. Firouzi, D. Ebeid, M. M. Monsanto, N. Navarrete, M. Moshref, S. Siddiqi, K. M. Broughton, B. A. Bailey, N. A. Gude and M. A. Sussman (2019). "Cardiomyocyte cell cycle dynamics and proliferation revealed through cardiac-specific transgenesis of fluorescent ubiquitinated cell cycle indicator (FUCCI)." J Mol Cell Cardiol **127**: 154-164.

Anderson, M., A. Moshnikova, D. M. Engelman, Y. K. Reshetnyak and O. A. Andreev (2016). "Probe for the measurement of cell surface pH in vivo and ex vivo." Proc Natl Acad Sci U S A **113**(29): 8177-8181.

Andreev, O. A., A. D. Dupuy, M. Segala, S. Sandugu, D. A. Serra, C. O. Chichester, D. M. Engelman and Y. K. Reshetnyak (2007). "Mechanism and uses of a membrane peptide that targets tumors and other acidic tissues in vivo." Proc Natl Acad Sci U S A **104**(19): 7893-7898.

Andreev, O. A., D. M. Engelman and Y. K. Reshetnyak (2009). "Targeting acidic diseased tissue: New technology based on use of the pH (Low) Insertion Peptide (pHLIP)." Chim Oggi **27**(2): 34-37.

Andreev, O. A., D. M. Engelman and Y. K. Reshetnyak (2014). "Targeting diseased tissues by pHLIP insertion at low cell surface pH." Front Physiol **5**: 97.

Anversa, P., A. Leri and J. Kajstura (2006). "Cardiac regeneration." J Am Coll Cardiol **47**(9): 1769-1776.

Apaydin, O., A. Altaikyzy, A. Filosa and S. Sawamiphak (2023). "Alpha-1 adrenergic signaling drives cardiac regeneration via extracellular matrix remodeling transcriptional program in zebrafish macrophages." Dev Cell **58**(22): 2460-2476 e2467.

Atout, S., S. Shurrab and C. Loveridge (2022). "Evaluation of the Suitability of RNAscope as a Technique to Measure Gene Expression in Clinical Diagnostics: A Systematic Review." Mol Diagn Ther **26**(1): 19-37.

Auchampach, J., L. Han, G. N. Huang, B. Kuhn, J. W. Lough, C. C. O'Meara, A. Y. Payumo, N. A. Rosenthal, H. M. Sucov, K. E. Yutzey and M. Patterson (2022). "Measuring cardiomyocyte cell-cycle activity and proliferation in the age of heart regeneration." Am J Physiol Heart Circ Physiol **322**(4): H579-H596.

Baark, F., E. C. T. Waters, T. R. Eykyn and R. Southworth (2024). "Characterization and Validation of Radiotracer Kinetics Using the Langendorff Isolated Perfused Heart." Methods Mol Biol **2729**: 251-267.

Badea, C. T., L. W. Hedlund, J. F. Mackel, L. Mao, H. A. Rockman and G. A. Johnson (2007). "Cardiac micro-computed tomography for morphological and functional phenotyping of muscle LIM protein null mice." Mol Imaging **6**(4): 261-268.

Bandman, E. (1992). "Contractile protein isoforms in muscle development." Dev Biol **154**(2): 273-283.

Bargehr, J., L. P. Ong, M. Colzani, H. Davaapil, P. Hofsteen, S. Bhandari, L. Gambardella, N. Le Novere, D. Iyer, F. Sampaziotis, F. Weinberger, A. Bertero, A. Leonard, W. G. Bernard, A. Martinson, N. Figg, M. Regnier, M. R. Bennett, C. E. Murry and S. Sinha (2019). "Epicardial cells derived from human embryonic stem cells augment cardiomyocyte-driven heart regeneration." Nat Biotechnol **37**(8): 895-906.

Barile, L., E. Messina, A. Giacomello and E. Marban (2007). "Endogenous cardiac stem cells." Prog Cardiovasc Dis **50**(1): 31-48.

Baudouy, D., J. F. Michiels, A. Vukolic, K. D. Wagner and N. Wagner (2017). "Echocardiographic and Histological Examination of Cardiac Morphology in the Mouse." J Vis Exp(128).

Bell, R. M., M. M. Mocanu and D. M. Yellon (2011). "Retrograde heart perfusion: the Langendorff technique of isolated heart perfusion." J Mol Cell Cardiol **50**(6): 940-950.

Bergmann, O. (2019). "Clearing up the mist: cardiomyocyte renewal in human hearts." Eur Heart J **40**(13): 1037-1038.

Bergmann, O., R. D. Bhardwaj, S. Bernard, S. Zdunek, F. Barnabe-Heider, S. Walsh, J. Zupicich, K. Alkass, B. A. Buchholz, H. Druid, S. Jovinge and J. Frisen (2009). "Evidence for cardiomyocyte renewal in humans." Science **324**(5923): 98-102.

Bergmann, O. and T. Braun (2016). "Caught Red-Handed: Cycling Cardiomyocytes." Circ Res **118**(1): 3-5.

Bergmann, O., S. Zdunek, K. Alkass, H. Druid, S. Bernard and J. Frisen (2011). "Identification of cardiomyocyte nuclei and assessment of ploidy for the analysis of cell turnover." Exp Cell Res **317**(2): 188-194.

Bergmann, O., S. Zdunek, A. Felker, M. Salehpour, K. Alkass, S. Bernard, S. L. Sjostrom, M. Szewczykowska, T. Jackowska, C. Dos Remedios, T. Malm, M. Andra, R. Jashari, J. R. Nyengaard, G. Possnert, S. Jovinge, H. Druid and J. Frisen (2015). "Dynamics of Cell Generation and Turnover in the Human Heart." Cell **161**(7): 1566-1575.

Bergmann, O., S. Zdunek, J. Frisen, S. Bernard, H. Druid and S. Jovinge (2012). "Cardiomyocyte renewal in humans." Circ Res **110**(1): e17-18; author reply e19-21.

Berry, C. J., D. R. Thedens, K. Light-McGroary, J. D. Miller, W. Kutschke, K. A. Zimmerman and R. M. Weiss (2009). "Effects of deep sedation or general anesthesia on cardiac function in mice undergoing cardiovascular magnetic resonance." J Cardiovasc Magn Reson **11**(1): 16.

BHF (2024). "Global Factsheet September 2024."

BHF. (2024). "UK Factsheet September 2024."

Bhute, V. J., X. Bao, K. K. Dunn, K. R. Knutson, E. C. McCurry, G. Jin, W. H. Lee, S. Lewis, A. Ikeda and S. P. Palecek (2017). "Metabolomics Identifies Metabolic Markers of Maturation in Human Pluripotent Stem Cell-Derived Cardiomyocytes." Theranostics **7**(7): 2078-2091.

Bing, O. H., W. W. Brooks and J. V. Messer (1973). "Heart muscle viability following hypoxia: protective effect of acidosis." Science **180**(4092): 1297-1298.

Bino, L., J. Kucera, K. Stefkova, L. Svihalkova Sindlerova, M. Lanova, J. Kudova, L. Kubala and J. Pachernik (2016). "The stabilization of hypoxia inducible factor modulates differentiation status and inhibits the proliferation of mouse embryonic stem cells." Chem Biol Interact **244**: 204-214.

Blin, G., D. Nury, S. Stefanovic, T. Neri, O. Guillevic, B. Brinon, V. Bellamy, C. Rucker-Martin, P. Barbry, A. Bel, P. Bruneval, C. Cowan, J. Pouly, S. Mitalipov, E. Gouadon, P. Binder, A. Hagege, M. Desnos, J. F. Renaud, P. Menasche and M. Puceat (2010). "A purified population of multipotent cardiovascular progenitors derived from primate pluripotent stem cells engrafts in postmyocardial infarcted nonhuman primates." J Clin Invest **120**(4): 1125-1139.

Böhm, A. M., Dirsch, O., Oberhuber, A. (2022). "Cardiac magnetic resonance imaging in small animals: Basic concepts and applications in translational research." Cells **11**(5): 857.

Bollini, S., J. M. Vieira, S. Howard, K. N. Dube, G. M. Balmer, N. Smart and P. R. Riley (2014). "Re-activated adult epicardial progenitor cells are a heterogeneous population molecularly distinct from their embryonic counterparts." Stem Cells Dev **23**(15): 1719-1730.

Bon-Mathier, A. C., S. Rignault-Clerc, C. Bielmann and N. Rosenblatt-Velin (2020). "Oxygen as a key regulator of cardiomyocyte proliferation: New results about cell culture conditions!" Biochim Biophys Acta Mol Cell Res **1867**(3): 118460.

Bouwman, M., D. E. M. de Bakker, H. Honkoop, A. E. Giovou, D. Versteeg, A. R. Boender, P. D. Nguyen, M. Slotboom, D. Colquhoun, M. Vigil-Garcia, L. Kooijman, R. Janssen, I. B. Hooijkaas, M. Gunthel, K. J. Visser, M. Klerk, L. Zentilin, M. Giacca, J. Kaslin, G. J. J. Boink, E. van Rooij, V. M. Christoffels and J. Bakkers (2025). "Cross-species comparison reveals that Hmga1 reduces H3K27me3 levels to promote cardiomyocyte proliferation and cardiac regeneration." Nat Cardiovasc Res.

Breckwoldt, K., F. Weinberger and T. Eschenhagen (2016). "Heart regeneration." Biochim Biophys Acta **1863**(7 Pt B): 1749-1759.

Broughton, K. M. and M. A. Sussman (2019). "Adult Cardiomyocyte Cell Cycle Detour: Off-ramp to Quiescent Destinations." Trends Endocrinol Metab **30**(8): 557-567.

Buijtendijk, M. F. J., P. Barnett and M. J. B. van den Hoff (2020). "Development of the human heart." Am J Med Genet C Semin Med Genet **184**(1): 7-22.

Caillat, C. and A. Perrakis (2012). "Cdt1 and geminin in DNA replication initiation." Subcell Biochem **62**: 71-87.

Camacho, P., H. Fan, Z. Liu and J. Q. He (2016). "Large Mammalian Animal Models of Heart Disease." J Cardiovasc Dev Dis **3**(4).

Camacho, P., H. Fan, Z. Liu and J. Q. He (2016). "Small mammalian animal models of heart disease." Am J Cardiovasc Dis **6**(3): 70-80.

Camelliti, P., S. A. Al-Saud, R. T. Smolenski, S. Al-Ayoubi, A. Bussek, E. Wettwer, N. R. Banner, C. T. Bowles, M. H. Yacoub and C. M. Terracciano (2011). "Adult human heart slices are a multicellular system suitable for electrophysiological and pharmacological studies." J Mol Cell Cardiol **51**(3): 390-398.

Canseco, D. C., W. Kimura, S. Garg, S. Mukherjee, S. Bhattacharya, S. Abdisalaam, S. Das, A. Asaithamby, P. P. Mammen and H. A. Sadek (2015). "Human ventricular unloading induces cardiomyocyte proliferation." J Am Coll Cardiol **65**(9): 892-900.

Carey, C. M., H. L. Hollins, A. V. Schmid and J. A. Gagnon (2024). "Distinct features of the regenerating heart uncovered through comparative single-cell profiling." Biol Open **13**(4).

Cassidy, P. J., J. E. Schneider, S. M. Grieve, C. Lygate, S. Neubauer and K. Clarke (2004). "Assessment of motion gating strategies for mouse magnetic resonance at high magnetic fields." J Magn Reson Imaging **19**(2): 229-237.

Castillo-Casas, J. M., S. Cano-Carrillo, C. Sanchez-Fernandez, D. Franco and E. Lozano-Velasco (2023). "Comparative Analysis of Heart Regeneration: Searching for the Key to Heal the Heart-Part I: Experimental Injury Models to Study Cardiac Regeneration." J Cardiovasc Dev Dis **10**(8).

Chablais, F., J. Veit, G. Rainer and A. Jazwinska (2011). "The zebrafish heart regenerates after cryoinjury-induced myocardial infarction." BMC Dev Biol **11**: 21.

Chen, H. S., C. Kim and M. Mercola (2009). "Electrophysiological challenges of cell-based myocardial repair." Circulation **120**(24): 2496-2508.

Chen, W. C., Z. Wang, M. A. Missinato, D. W. Park, D. W. Long, H. J. Liu, X. Zeng, N. A. Yates, K. Kim and Y. Wang (2016). "Decellularized zebrafish cardiac extracellular matrix induces mammalian heart regeneration." Sci Adv **2**(11): e1600844.

Chen, Y. C., G. Zheng, D. G. Donner, D. K. Wright, J. P. Greenwood, T. H. Marwick and J. R. McMullen (2024). "Cardiovascular magnetic resonance imaging for sequential assessment of cardiac fibrosis in mice: technical advancements and reverse translation." Am J Physiol Heart Circ Physiol **326**(1): H1-H24.

Cheng, Y. C., M. L. Hsieh, C. J. Lin, C. M. C. Chang, C. Y. Huang, R. Puntney, A. Wu Moy, C. Y. Ting, D. Z. Herr Chan, M. W. Nicholson, P. J. Lin, H. C. Chen, G. C. Kim, J. Zhang, J. Coonen, P. Basu, H. A. Simmons, Y. W. Liu, T. A. Hacker, T. J. Kamp and P. C. H. Hsieh (2023). "Combined Treatment of Human Induced Pluripotent Stem Cell-Derived Cardiomyocytes and Endothelial Cells Regenerate the Infarcted Heart in Mice and Non-Human Primates." Circulation **148**(18): 1395-1409.

Chong, J. J., X. Yang, C. W. Don, E. Minami, Y. W. Liu, J. J. Weyers, W. M. Mahoney, B. Van Biber, S. M. Cook, N. J. Palpant, J. A. Gantz, J. A. Fugate, V. Muskheli, G. M. Gough, K. W. Vogel, C. A. Astley, C. E. Hotchkiss, A. Baldessari, L. Pabon, H. Reinecke, E. A. Gill, V. Nelson, H. P. Kiem, M. A. Laflamme and C. E. Murry (2014). "Human embryonic-stem-cell-derived cardiomyocytes regenerate non-human primate hearts." Nature **510**(7504): 273-277.

Clancy, C. E. and L. F. Santana (2024). "Advances in induced pluripotent stem cell-derived cardiac myocytes: technological breakthroughs, key discoveries and new applications." J Physiol **602**(16): 3871-3892.

Clark, D. P. and C. T. Badea (2021). "Advances in micro-CT imaging of small animals." Phys Med **88**: 175-192.

Clark, S. J. (2006). "Understanding cardiac troponin T in the newborn period." Am J Respir Crit Care Med **173**(7): 816-817; author reply 817.

Clark, S. J., P. Newland, C. W. Yoxall and N. V. Subhedar (2004). "Concentrations of cardiac troponin T in neonates with and without respiratory distress." Arch Dis Child Fetal Neonatal Ed **89**(4): F348-352.

Cobbe, S. M. and P. A. Poole-Wilson (1980). "Tissue acidosis in myocardial hypoxia." J Mol Cell Cardiol **12**(8): 761-770.

Compernolle, V., K. Brusselmans, D. Franco, A. Moorman, M. Dewerchin, D. Collen and P. Carmeliet (2003). "Cardia bifida, defective heart development and abnormal neural crest migration in embryos lacking hypoxia-inducible factor-1alpha." Cardiovasc Res **60**(3): 569-579.

Daiou, A., K. Petalidou, G. Siokatas, E. I. Papadopoulos and K. E. Hatzistergos (2022). "Developmental and regenerative biology of cardiomyocytes." Int J Dev Biol **66**(1-2-3): 59-75.

Dall'Armellina, E., S. K. Piechnik, V. M. Ferreira, Q. L. Si, M. D. Robson, J. M. Francis, F. Cuculi, R. K. Kharbanda, A. P. Banning, R. P. Choudhury, T. D. Karamitsos and S. Neubauer (2012). "Cardiovascular magnetic resonance by non contrast T1-mapping allows assessment of severity of injury in acute myocardial infarction." J Cardiovasc Magn Reson **14**(1): 15.

Dark, N., M. V. Cosson, L. I. Tsansizi, T. J. Owen, E. Ferraro, A. J. Francis, S. Tsai, C. Bouissou, A. Weston, L. Collinson, N. Abi-Gerges, P. E. Miller, K. T. MacLeod, E. Ehler, R. Mitter, S. E. Harding, J. C. Smith and A. S. Bernardo (2023). "Generation of left ventricle-like cardiomyocytes with improved structural, functional, and metabolic maturity from human pluripotent stem cells." Cell Rep Methods **3**(4): 100456.

Davidson, S. M., T. Padro, S. Bollini, G. Vilahur, D. J. Duncker, P. C. Evans, T. Guzik, I. E. Hoefer, J. Waltenberger, J. Wojta and C. Weber (2021). "Progress in cardiac research: from rebooting cardiac regeneration to a complete cell atlas of the heart." Cardiovasc Res **117**(10): 2161-2174.

de Boer, B. A., G. van den Berg, P. A. de Boer, A. F. Moorman and J. M. Ruijter (2012). "Growth of the developing mouse heart: an interactive qualitative and quantitative 3D atlas." Dev Biol **368**(2): 203-213.

De Falco, M., G. Cobellis and A. De Luca (2009). "Proliferation of cardiomyocytes: a question unresolved." Front Biosci (Elite Ed) **1**: 528-536.

Dimasi, C. G., J. R. T. Darby and J. L. Morrison (2023). "A change of heart: understanding the mechanisms regulating cardiac proliferation and metabolism before and after birth." J Physiol **601**(8): 1319-1341.

Doppler, S. A., R. Lange, K. L. Laugwitz and M. Krane (2017). "Cardiac development: from current understanding to new regenerative concepts." J Thorac Dis **9**(Suppl 1): S1-S4.

Doyle, M. J., J. L. Lohr, C. S. Chapman, N. Koyano-Nakagawa, M. G. Garry and D. J. Garry (2015). "Human Induced Pluripotent Stem Cell-Derived Cardiomyocytes as a Model for Heart Development and Congenital Heart Disease." Stem Cell Rev Rep **11**(5): 710-727.

Dunwoodie, S. L. (2009). "The role of hypoxia in development of the Mammalian embryo." Dev Cell **17**(6): 755-773.

DuPont, M., H. Visca, A. Moshnikova, D. M. Engelman, Y. K. Reshetnyak and O. A. Andreev (2022). "Tumor treatment by pHLIP-targeted antigen delivery." Front Bioeng Biotechnol **10**: 1082290.

Easwaran, H. P., H. Leonhardt and M. C. Cardoso (2005). "Cell cycle markers for live cell analyses." Cell Cycle **4**(3): 453-455.

El-Nachef, D., D. Bugg, K. M. Beussman, S. Steczina, A. M. Martinson, C. E. Murry, N. J. Sniadecki and J. Davis (2021). "Engrafted Human Induced Pluripotent Stem Cell-Derived Cardiomyocytes Undergo Clonal Expansion In Vivo." Circulation **143**(16): 1635-1638.

Eschenhagen, T., R. Bolli, T. Braun, L. J. Field, B. K. Fleischmann, J. Frisen, M. Giacca, J. M. Hare, S. Houser, R. T. Lee, E. Marban, J. F. Martin, J. D. Molkentin, C. E. Murry, P. R. Riley, P. Ruiz-Lozano, H. A. Sadek, M. A. Sussman and J. A. Hill (2017). "Cardiomyocyte Regeneration: A Consensus Statement." Circulation **136**(7): 680-686.

Eschenhagen, T., K. Ridders and F. Weinberger (2022). "How to repair a broken heart with pluripotent stem cell-derived cardiomyocytes." J Mol Cell Cardiol **163**: 106-117.

Eschenhagen, T. and F. Weinberger (2024). "Challenges and perspectives of heart repair with pluripotent stem cell-derived cardiomyocytes." Nat Cardiovasc Res **3**(5): 515-524.

Faeh, D., F. Gutzwiller, M. Bopp and G. Swiss National Cohort Study (2009). "Lower mortality from coronary heart disease and stroke at higher altitudes in Switzerland." Circulation **120**(6): 495-501.

Farah, E. N., R. K. Hu, C. Kern, Q. Zhang, T. Y. Lu, Q. Ma, S. Tran, B. Zhang, D. Carlin, A. Monell, A. P. Blair, Z. Wang, J. Eschbach, B. Li, E. Destici, B. Ren, S. M. Evans, S. Chen, Q. Zhu and N. C. Chi (2024). "Spatially organized cellular communities form the developing human heart." Nature **627**(8005): 854-864.

Fernandes, S., A. V. Naumova, W. Z. Zhu, M. A. Laflamme, J. Gold and C. E. Murry (2010). "Human embryonic stem cell-derived cardiomyocytes engraft but do not alter cardiac remodeling after chronic infarction in rats." J Mol Cell Cardiol **49**(6): 941-949.

Feyen, D. A. M., W. L. McKeithan, A. A. N. Bruyneel, S. Spiering, L. Hormann, B. Ulmer, H. Zhang, F. Briganti, M. Schweizer, B. Hegyi, Z. Liao, R. P. Polonen, K. S. Ginsburg, C. K. Lam, R. Serrano, C. Wahlquist, A. Kreymerman, M. Vu, P. L. Amatya, C. S. Behrens, S. Ranjbarvaziri, R. G. C. Maas, M. Greenhaw, D. Bernstein, J. C. Wu, D. M. Bers, T. Eschenhagen, C. M. Metallo and M. Mercola (2020). "Metabolic Maturation Media Improve Physiological Function of Human iPSC-Derived Cardiomyocytes." Cell Rep **32**(3): 107925.

Fine, B. (2019). "Heart regeneration in mouse and human: a bioengineering perspective." Current Opinion in Physiology.

Fleming, S., M. Thompson, R. Stevens, C. Heneghan, A. Pluddemann, I. Maconochie, L. Tarassenko and D. Mant (2011). "Normal ranges of heart rate and respiratory rate in children from birth to 18 years of age: a systematic review of observational studies." Lancet **377**(9770): 1011-1018.

Foglia, M. J. and K. D. Poss (2016). "Building and re-building the heart by cardiomyocyte proliferation." Development **143**(5): 729-740.

French, B. A. a. E., F.H. (2008). "Magnetic resonance imaging of mouse models of cardiomyopathy." Current Cardiovascular Imaging Reports **1**(2): 108-117.

Fukuda, R., A. Aharonov, Y. T. Ong, O. A. Stone, M. El-Brolosy, H. M. Maischein, M. Potente, E. Tzahor and D. Y. Stainier (2019). "Metabolic modulation regulates cardiac wall morphogenesis in zebrafish." Elife **8**.

Gaitanaki, C., T. Kalpachidou, I. K. Aggeli, P. Papazafiri and I. Beis (2007). "CoCl2 induces protective events via the p38-MAPK signalling pathway and ANP in the perfused amphibian heart." J Exp Biol **210**(Pt 13): 2267-2277.

Galdos, F. X., Y. Guo, S. L. Paige, N. J. VanDusen, S. M. Wu and W. T. Pu (2017). "Cardiac Regeneration: Lessons From Development." Circ Res **120**(6): 941-959.

Garlick, P. B., G. K. Radda and P. J. Seeley (1979). "Studies of acidosis in the ischaemic heart by phosphorus nuclear magnetic resonance." Biochem J **184**(3): 547-554.

Gemberling, M., T. J. Bailey, D. R. Hyde and K. D. Poss (2013). "The zebrafish as a model for complex tissue regeneration." Trends Genet **29**(11): 611-620.

Gerweck, L. E. and K. Seetharaman (1996). "Cellular pH gradient in tumor versus normal tissue: potential exploitation for the treatment of cancer." Cancer Res **56**(6): 1194-1198.

Giffen, K. P., H. Liu, K. L. Kramer and D. Z. He (2019). "Expression of Protein-Coding Gene Orthologs in Zebrafish and Mouse Inner Ear Non-sensory Supporting Cells." Front Neurosci **13**: 1117.

Gladka, M. M., A. K. Z. Johansen, S. J. van Kampen, M. M. C. Peters, B. Molenaar, D. Versteeg, L. Kooijman, L. Zentilin, M. Giacca and E. van Rooij (2023). "Thymosin beta4 and prothymosin alpha promote cardiac regeneration post-ischaemic injury in mice." Cardiovasc Res **119**(3): 802-812.

Godwin, J. W., R. Debuque, E. Salimova and N. A. Rosenthal (2017). "Heart regeneration in the salamander relies on macrophage-mediated control of fibroblast activation and the extracellular landscape." NPJ Regen Med **2**.

Godwin, J. W. and N. Rosenthal (2014). "Scar-free wound healing and regeneration in amphibians: immunological influences on regenerative success." Differentiation **87**(1-2): 66-75.

Goldberg, M. A., S. P. Dunning and H. F. Bunn (1988). "Regulation of the erythropoietin gene: evidence that the oxygen sensor is a heme protein." Science **242**(4884): 1412-1415.

Gomes, A. V., G. Guzman, J. Zhao and J. D. Potter (2002). "Cardiac troponin T isoforms affect the Ca2+ sensitivity and inhibition of force development. Insights into the role of troponin T isoforms in the heart." J Biol Chem **277**(38): 35341-35349.

Gonzalez-Rosa, J. M., C. E. Burns and C. G. Burns (2017). "Zebrafish heart regeneration: 15 years of discoveries." Regeneration (Oxf) **4**(3): 105-123.

Graham, E. and O. Bergmann (2017). "Dating the Heart: Exploring Cardiomyocyte Renewal in Humans." Physiology (Bethesda) **32**(1): 33-41.

Graham, R. M., D. P. Frazier, J. W. Thompson, S. Haliko, H. Li, B. J. Wasserlauf, M. G. Spiga, N. H. Bishopric and K. A. Webster (2004). "A unique pathway of cardiac myocyte death caused by hypoxia-acidosis." J Exp Biol **207**(Pt 18): 3189-3200.

Grandi, E., M. F. Navedo, J. J. Saucerman, D. M. Bers, N. Chiamvimonvat, R. E. Dixon, D. Dobrev, A. M. Gomez, O. F. Harraz, B. Hegyi, D. K. Jones, T. Krogh-Madsen, W. L. Murfee, M. A. Nystoriak, N. G. Posnack, C. M. Ripplinger, R. Veeraraghavan and S. Weinberg (2023). "Diversity of cells and signals in the cardiovascular system." J Physiol **601**(13): 2547-2592.

Grant, G. D., K. M. Kedziora, J. C. Limas, J. G. Cook and J. E. Purvis (2018). "Accurate delineation of cell cycle phase transitions in living cells with PIP-FUCCI." Cell Cycle **17**(21-22): 2496-2516.

Gray, G. A., I. S. Toor, R. Castellan, M. Crisan and M. Meloni (2018). "Resident cells of the myocardium: more than spectators in cardiac injury, repair and regeneration." Curr Opin Physiol **1**: 46-51.

Gunadasa-Rohling, M., M. Masters, M. L. Maguire, S. C. Smart, J. E. Schneider and P. R. Riley (2018). "Magnetic Resonance Imaging of the Regenerating Neonatal Mouse Heart." Circulation **138**(21): 2439-2441.

Gunthel, M., P. Barnett and V. M. Christoffels (2018). "Development, Proliferation, and Growth of the Mammalian Heart." Mol Ther **26**(7): 1599-1609.

Guo, Q. Y., J. Q. Yang, X. X. Feng and Y. J. Zhou (2023). "Regeneration of the heart: from molecular mechanisms to clinical therapeutics." Mil Med Res **10**(1): 18.

Hashimoto, H., S. Yuasa, H. Tabata, S. Tohyama, N. Hayashiji, F. Hattori, N. Muraoka, T. Egashira, S. Okata, K. Yae, T. Seki, T. Nishiyama, K. Nakajima, A. Sakaue-Sawano, A. Miyawaki and K. Fukuda (2014). "Time-lapse imaging of cell cycle dynamics during development in living cardiomyocyte." J Mol Cell Cardiol **72**: 241-249.

Hashimoto, H., S. Yuasa, H. Tabata, S. Tohyama, T. Seki, T. Egashira, N. Hayashiji, F. Hattori, D. Kusumoto, A. Kunitomi, M. Takei, S. Kashimura, G. Yozu, M. Shimojima, C. Motoda, N. Muraoka, K. Nakajima, A. Sakaue-Sawano, A. Miyawaki and K. Fukuda (2015). "Analysis of

cardiomyocyte movement in the developing murine heart." Biochem Biophys Res Commun **464**(4): 1000-1007.

Hashmi, S. and H. R. Ahmad (2019). "Molecular switch model for cardiomyocyte proliferation." Cell Regen **8**(1): 12-20.

Haubner, B. J., M. Adamowicz-Brice, S. Khadayate, V. Tiefenthaler, B. Metzler, T. Aitman and J. M. Penninger (2012). "Complete cardiac regeneration in a mouse model of myocardial infarction." Aging (Albany NY) **4**(12): 966-977.

Hiba, B., N. Richard, M. Janier and P. Croisille (2006). "Cardiac and respiratory double self-gated cine MRI in the mouse at 7 T." Magn Reson Med **55**(3): 506-513.

Hirai, M., P. Cattaneo, J. Chen and S. M. Evans (2016). "Revisiting Preadolescent Cardiomyocyte Proliferation in Mice." Circ Res **118**(6): 916-919.

Hirai, M., J. Chen and S. M. Evans (2016). "Tissue-Specific Cell Cycle Indicator Reveals Unexpected Findings for Cardiac Myocyte Proliferation." Circ Res **118**(1): 20-28.

Hu, T., M. Malek Mohammadi, F. Ebach, M. Hesse, M. I. Kotlikoff and B. K. Fleischmann (2024). "Right ventricular cardiomyocyte expansion accompanies cardiac regeneration in newborn mice after large left ventricular infarcts." JCI Insight **9**(5).

Huang, H., G. N. Huang and A. Y. Payumo (2023). "Two decades of heart regeneration research: Cardiomyocyte proliferation and beyond." WIREs Mech Dis: e1629.

Huang, N. F., R. E. Sievers, J. S. Park, Q. Fang, S. Li and R. J. Lee (2006). "A rodent model of myocardial infarction for testing the efficacy of cells and polymers for myocardial reconstruction." Nat Protoc **1**(3): 1596-1609.

Hulikova, A., K. C. Park, A. A. Loonat, M. Gunadasa-Rohling, M. K. Curtis, Y. J. Chung, A. Wilson, C. A. Carr, A. W. Trafford, M. Fournier, A. Moshnikova, O. A. Andreev, Y. K. Reshetnyak, P. R. Riley, N. Smart, T. A. Milne, N. T. Crump and P. Swietach (2022). "Alkaline nucleoplasm facilitates contractile gene expression in the mammalian heart." Basic Res Cardiol **117**(1): 17.

Hunt, J. F., P. Rath, K. J. Rothschild and D. M. Engelman (1997). "Spontaneous, pH-dependent membrane insertion of a transbilayer alpha-helix." Biochemistry **36**(49): 15177-15192.

Ihnat, C. L., H. Zimmerman, J. G. Copeland, F. J. Meaney, R. E. Sobonya, B. T. Larsen, B. Blair, D. Lax and B. J. Barber (2011). "Left ventricular assist device support as a bridge to recovery in young children." Congenit Heart Dis **6**(3): 234-240.

Imran Khan, M. (2022). "Exploration of metabolic responses towards hypoxia mimetic DMOG in cancer cells by using untargeted metabolomics." Saudi J Biol Sci **29**(10): 103426.

Iyer, N. V., L. E. Kotch, F. Agani, S. W. Leung, E. Laughner, R. H. Wenger, M. Gassmann, J. D. Gearhart, A. M. Lawler, A. Y. Yu and G. L. Semenza (1998). "Cellular and developmental control of O2 homeostasis by hypoxia-inducible factor 1 alpha." Genes Dev **12**(2): 149-162.

Jensen, V. S., T. Porsgaard, J. Lykkesfeldt and H. Hvid (2016). "Rodent model choice has major impact on variability of standard preclinical readouts associated with diabetes and obesity research." Am J Transl Res **8**(8): 3574-3584.

Jesty, S. A., M. A. Steffey, F. K. Lee, M. Breitbach, M. Hesse, S. Reining, J. C. Lee, R. M. Doran, A. Y. Nikitin, B. K. Fleischmann and M. I. Kotlikoff (2012). "c-kit+ precursors support postinfarction myogenesis in the neonatal, but not adult, heart." Proc Natl Acad Sci U S A **109**(33): 13380-13385.

Jewhurst, K. and K. A. McLaughlin (2015). "Beyond the Mammalian Heart: Fish and Amphibians as a Model for Cardiac Repair and Regeneration." J Dev Biol **4**(1).

Jonker, S. S., S. Louey, G. D. Giraud, K. L. Thornburg and J. J. Faber (2015). "Timing of cardiomyocyte growth, maturation, and attrition in perinatal sheep." FASEB J **29**(10): 4346-4357.

Jopling, C., E. Sleep, M. Raya, M. Marti, A. Raya and J. C. Izpisua Belmonte (2010). "Zebrafish heart regeneration occurs by cardiomyocyte dedifferentiation and proliferation." Nature **464**(7288): 606-609.

Kang, J., J. Hu, R. Karra, A. L. Dickson, V. A. Tornini, G. Nachtrab, M. Gemberling, J. A. Goldman, B. L. Black and K. D. Poss (2016). "Modulation of tissue repair by regeneration enhancer elements." Nature **532**(7598): 201-206.

Kang, M. J., J. S. Kim, S. W. Chae, K. N. Koh and G. Y. Koh (1997). "Cyclins and cyclin dependent kinases during cardiac development." Mol Cells **7**(3): 360-366.

Karamitsos, T. D. and S. Neubauer (2011). "Cardiovascular magnetic resonance in heart failure." Curr Cardiol Rep **13**(3): 210-219.

Karamitsos, T. D. and S. Neubauer (2011). "Cardiovascular magnetic resonance: a powerful diagnostic and prognostic tool in modern cardiology." Prog Cardiovasc Dis **54**(3): 179-180.

Kehat, I., A. Gepstein, A. Spira, J. Itskovitz-Eldor and L. Gepstein (2002). "High-resolution electrophysiological assessment of human embryonic stem cell-derived cardiomyocytes: a novel in vitro model for the study of conduction." Circ Res **91**(8): 659-661.

Kemi, O. J., I. Arbo, M. A. Hoydal, J. P. Loennechen, U. Wisloff, G. L. Smith and O. Ellingsen (2006). "Reduced pH and contractility in failing rat cardiomyocytes." Acta Physiol (Oxf) **188**(3-4): 185-193.

Khan, M. A., Mueller, C.E. (2016). Pharmacological and Toxicological Methods.

Kim, H. D., D. J. Kim, I. J. Lee, B. J. Rah, Y. Sawa and J. Schaper (1992). "Human fetal heart development after mid-term: morphometry and ultrastructural study." J Mol Cell Cardiol **24**(9): 949-965.

Kimura, W., Y. Nakada and H. A. Sadek (2017). "Hypoxia-induced myocardial regeneration." J Appl Physiol (1985) **123**(6): 1676-1681.

Kimura, W., F. Xiao, D. C. Canseco, S. Muralidhar, S. Thet, H. M. Zhang, Y. Abderrahman, R. Chen, J. A. Garcia, J. M. Shelton, J. A. Richardson, A. M. Ashour, A. Asaithamby, H. Liang, C. Xing, Z. Lu, C. C. Zhang and H. A. Sadek (2015). "Hypoxia fate mapping identifies cycling cardiomyocytes in the adult heart." Nature **523**(7559): 226-230.

Kloner, R. A. (2020). "Stunned and Hibernating Myocardium: Where Are We Nearly 4 Decades Later?" J Am Heart Assoc **9**(3): e015502.

Kolwicz, S. C., Jr., S. Purohit and R. Tian (2013). "Cardiac metabolism and its interactions with contraction, growth, and survival of cardiomyocytes." Circ Res **113**(5): 603-616.

Konfino, T., N. Landa, T. Ben-Mordechai and J. Leor (2015). "The type of injury dictates the mode of repair in neonatal and adult heart." J Am Heart Assoc **4**(1): e001320.

Koth, J., M. L. Maguire, D. McClymont, L. Diffley, V. L. Thornton, J. Beech, R. K. Patient, P. R. Riley and J. E. Schneider (2017). "High-Resolution Magnetic Resonance Imaging of the Regenerating Adult Zebrafish Heart." Sci Rep **7**(1): 2917.

Koth, J., X. Wang, A. C. Killen, W. T. Stockdale, H. G. Potts, A. Jefferson, F. Bonkhofer, P. R. Riley, R. K. Patient, B. Gottgens and M. T. M. Mommersteeg (2020). "Runx1 promotes scar deposition and inhibits myocardial proliferation and survival during zebrafish heart regeneration." Development **147**(8).

Kretzschmar, K., Y. Post, M. Bannier-Helaouet, A. Mattiotti, J. Drost, O. Basak, V. S. W. Li, M. van den Born, Q. D. Gunst, D. Versteeg, L. Kooijman, S. van der Elst, J. H. van Es, E. van Rooij, M. J. B. van den Hoff and H. Clevers (2018). "Profiling proliferative cells and their progeny in damaged murine hearts." Proc Natl Acad Sci U S A **115**(52): E12245-E12254.

Kubasiak, L. A., O. M. Hernandez, N. H. Bishopric and K. A. Webster (2002). "Hypoxia and acidosis activate cardiac myocyte death through the Bcl-2 family protein BNIP3." Proc Natl Acad Sci U S A **99**(20): 12825-12830.

Kubin, T., J. Poling, S. Kostin, P. Gajawada, S. Hein, W. Rees, A. Wietelmann, M. Tanaka, H. Lorchner, S. Schimanski, M. Szibor, H. Warnecke and T. Braun (2011). "Oncostatin M is a major mediator of cardiomyocyte dedifferentiation and remodeling." Cell Stem Cell **9**(5): 420-432.

Laflamme, M. A., J. Gold, C. Xu, M. Hassanipour, E. Rosler, S. Police, V. Muskheli and C. E. Murry (2005). "Formation of human myocardium in the rat heart from human embryonic stem cells." Am J Pathol **167**(3): 663-671.

Lam, N. T. and H. A. Sadek (2018). "Neonatal Heart Regeneration: Comprehensive Literature Review." Circulation **138**(4): 412-423.

Lau, A. Z., J. J. Miller, M. D. Robson and D. J. Tyler (2017). "Simultaneous assessment of cardiac metabolism and perfusion using copolarized [1-(13) C]pyruvate and (13) C-urea." Magn Reson Med **77**(1): 151-158.

Lau, A. Z., J. J. Miller and D. J. Tyler (2017). "Mapping of intracellular pH in the in vivo rodent heart using hyperpolarized [1-13C]pyruvate." Magn Reson Med **77**(5): 1810-1817.

Lawrence, E. and C. H. Wilson (2024). "Turning back time: the promise of cardiac regeneration." Nat Rev Cardiol **21**(12): 846.

Lazar, E., H. A. Sadek and O. Bergmann (2017). "Cardiomyocyte renewal in the human heart: insights from the fall-out." Eur Heart J **38**(30): 2333-2342.

Leinonen, J. V., A. K. Emanuelov, Y. Platt, Y. Helman, Y. Feinberg, C. Lotan and R. Beeri (2013). "Left atrial appendages from adult hearts contain a reservoir of diverse cardiac progenitor cells." PLoS One **8**(3): e59228.

Leone, M., A. Magadum and F. B. Engel (2015). "Cardiomyocyte proliferation in cardiac development and regeneration: a guide to methodologies and interpretations." Am J Physiol Heart Circ Physiol **309**(8): H1237-1250.

Lewis, A. J. M., J. J. Miller, A. Z. Lau, M. K. Curtis, O. J. Rider, R. P. Choudhury, S. Neubauer, C. H. Cunningham, C. A. Carr and D. J. Tyler (2018). "Noninvasive Immunometabolic Cardiac Inflammation Imaging Using Hyperpolarized Magnetic Resonance." Circ Res **122**(8): 1084-1093.

Li, M. and J. C. Izpisua Belmonte (2016). "Mending a Faltering Heart." Circ Res **118**(2): 344-351.

Li, Y., Z. Lv, L. He, X. Huang, S. Zhang, H. Zhao, W. Pu, Y. Li, W. Yu, L. Zhang, X. Liu, K. Liu, J. Tang, X. Tian, Q. D. Wang, K. O. Lui and B. Zhou (2019). "Genetic Tracing Identifies Early Segregation of the Cardiomyocyte and Nonmyocyte Lineages." Circ Res **125**(3): 343-355.

Lian, X., J. Zhang, S. M. Azarin, K. Zhu, L. B. Hazeltine, X. Bao, C. Hsiao, T. J. Kamp and S. P. Palecek (2013). "Directed cardiomyocyte differentiation from human pluripotent stem cells by modulating Wnt/beta-catenin signaling under fully defined conditions." Nat Protoc **8**(1): 162-175.

Lindsey, M. L., Z. Kassiri, J. A. I. Virag, L. E. de Castro Bras and M. Scherrer-Crosbie (2018). "Guidelines for measuring cardiac physiology in mice." Am J Physiol Heart Circ Physiol **314**(4): H733-H752.

Liu, N. and E. N. Olson (2022). "CRISPR Modeling and Correction of Cardiovascular Disease." Circ Res **130**(12): 1827-1850.

Liu, X., W. Pu, L. He, Y. Li, H. Zhao, Y. Li, K. Liu, X. Huang, W. Weng, Q. D. Wang, L. Shen, T. Zhong, K. Sun, R. Ardehali, B. He and B. Zhou (2021). "Cell proliferation fate mapping reveals

regional cardiomyocyte cell-cycle activity in subendocardial muscle of left ventricle." Nat Commun **12**(1): 5784.

Liu, Y. W., B. Chen, X. Yang, J. A. Fugate, F. A. Kalucki, A. Futakuchi-Tsuchida, L. Couture, K. W. Vogel, C. A. Astley, A. Baldessari, J. Ogle, C. W. Don, Z. L. Steinberg, S. P. Seslar, S. A. Tuck, H. Tsuchida, A. V. Naumova, S. K. Dupras, M. S. Lyu, J. Lee, D. W. Hailey, H. Reinecke, L. Pabon, B. H. Fryer, W. R. MacLellan, R. S. Thies and C. E. Murry (2018). "Human embryonic stem cell-derived cardiomyocytes restore function in infarcted hearts of non-human primates." Nat Biotechnol **36**(7): 597-605.

Livak, K. J. and T. D. Schmittgen (2001). "Analysis of relative gene expression data using real-time quantitative PCR and the 2(-Delta Delta C(T)) Method." Methods **25**(4): 402-408.

Lopez, C. A., H. Al-Siddiqi, U. Purnama, S. Iftekhar, A. A. N. Bruyneel, M. Kerr, R. Nazir, M. da Luz Sousa Fialho, S. Malandraki-Miller, R. Alonaizan, F. Kermani, L. C. Heather, J. Czernuszka and C. A. Carr (2021). "Physiological and pharmacological stimulation for in vitro maturation of substrate metabolism in human induced pluripotent stem cell-derived cardiomyocytes." Sci Rep **11**(1): 7802.

Lukasik, V. M. and R. J. Gillies (2003). "Animal anaesthesia for in vivo magnetic resonance." NMR Biomed **16**(8): 459-467.

Lupu, I. E., S. De Val and N. Smart (2020). "Coronary vessel formation in development and disease: mechanisms and insights for therapy." Nat Rev Cardiol **17**(12): 790-806.

Macholl, S., M. S. Morrison, P. Iveson, B. E. Arbo, O. A. Andreev, Y. K. Reshetnyak, D. M. Engelman and E. Johannesen (2012). "In vivo pH imaging with (99m)Tc-pHLIP." Mol Imaging Biol **14**(6): 725-734.

Mahmoud, A. I., E. R. Porrello, W. Kimura, E. N. Olson and H. A. Sadek (2014). "Surgical models for cardiac regeneration in neonatal mice." Nat Protoc **9**(2): 305-311.

Majesky, M. W. (2018). "Vascular Development." Arterioscler Thromb Vasc Biol **38**(3): e17-e24.

Malandraki-Miller, S., C. A. Lopez, H. Al-Siddiqi and C. A. Carr (2018). "Changing Metabolism in Differentiating Cardiac Progenitor Cells-Can Stem Cells Become Metabolically Flexible Cardiomyocytes?" Front Cardiovasc Med **5**: 119.

Maloney, S. E., C. M. Yuede, C. E. Creeley, S. L. Williams, J. N. Huffman, G. T. Taylor, K. N. Noguchi and D. F. Wozniak (2019). "Repeated neonatal isoflurane exposures in the mouse induce apoptotic degenerative changes in the brain and relatively mild long-term behavioral deficits." Sci Rep **9**(1): 2779.

Marques, I. J., E. Lupi and N. Mercader (2019). "Model systems for regeneration: zebrafish." Development **146**(18).

Meissner, T. B., H. S. Schulze and S. M. Dale (2022). "Immune Editing: Overcoming Immune Barriers in Stem Cell Transplantation." Curr Stem Cell Rep **8**(4): 206-218.

Menendez-Montes, I., B. Escobar, B. Palacios, M. J. Gomez, J. L. Izquierdo-Garcia, L. Flores, L. J. Jimenez-Borreguero, J. Aragones, J. Ruiz-Cabello, M. Torres and S. Martin-Puig (2016). "Myocardial VHL-HIF Signaling Controls an Embryonic Metabolic Switch Essential for Cardiac Maturation." Dev Cell **39**(6): 724-739.

Michl, J., K. C. Park and P. Swietach (2019). "Evidence-based guidelines for controlling pH in mammalian live-cell culture systems." Commun Biol **2**: 144.

Miller, J. R., T. S. Lancaster and P. Eghtesady (2015). "Current approaches to device implantation in pediatric and congenital heart disease patients." Expert Rev Cardiovasc Ther **13**(4): 417-427.

Mitsutake, Y., W. B. Pyun, D. Rouy, C. W. P. Foo, S. H. Stertzer, P. Altman and F. Ikeno (2017). "Improvement of Local Cell Delivery Using Helix Transendocardial Delivery Catheter in a Porcine Heart." Int Heart J **58**(3): 435-440.

Mollova, M., K. Bersell, S. Walsh, J. Savla, L. T. Das, S. Y. Park, L. E. Silberstein, C. G. Dos Remedios, D. Graham, S. Colan and B. Kuhn (2013). "Cardiomyocyte proliferation contributes to heart growth in young humans." Proc Natl Acad Sci U S A **110**(4): 1446-1451.

Moorhouse, C. P., B. Halliwell, M. Grootveld and J. M. Gutteridge (1985). "Cobalt(II) ion as a promoter of hydroxyl radical and possible 'crypto-hydroxyl' radical formation under physiological conditions. Differential effects of hydroxyl radical scavengers." Biochim Biophys Acta **843**(3): 261-268.

Murganti, F., W. Derks, M. Baniol, I. Simonova, P. Trus, K. Neumann, S. Khattak, K. Guan and O. Bergmann (2022). "FUCCI-Based Live Imaging Platform Reveals Cell Cycle Dynamics and Identifies Pro-proliferative Compounds in Human iPSC-Derived Cardiomyocytes." Front Cardiovasc Med **9**: 840147.

Nahrendorf, M., F. K. Swirski, E. Aikawa, L. Stangenberg, T. Wurdinger, J. L. Figueiredo, P. Libby, R. Weissleder and M. J. Pittet (2007). "The healing myocardium sequentially mobilizes two monocyte subsets with divergent and complementary functions." J Exp Med **204**(12): 3037-3047.

Nakada, Y., D. C. Canseco, S. Thet, S. Abdisalaam, A. Asaithamby, C. X. Santos, A. M. Shah, H. Zhang, J. E. Faber, M. T. Kinter, L. I. Szweda, C. Xing, Z. Hu, R. J. Deberardinis, G. Schiattarella, J. A. Hill, O. Oz, Z. Lu, C. C. Zhang, W. Kimura and H. A. Sadek (2017). "Hypoxia induces heart regeneration in adult mice." Nature **541**(7636): 222-227.

Nakada, Y. and H. A. Sadek (2021). "Experimental Hypoxia as a Model for Cardiac Regeneration in Mice." Methods Mol Biol **2158**: 337-344.

Nakajima, K., J. Fujita, M. Matsui, S. Tohyama, N. Tamura, H. Kanazawa, T. Seki, Y. Kishino, A. Hirano, M. Okada, R. Tabei, M. Sano, S. Goto, Y. Tabata and K. Fukuda (2015). "Gelatin Hydrogel Enhances the Engraftment of Transplanted Cardiomyocytes and Angiogenesis to Ameliorate Cardiac Function after Myocardial Infarction." PLoS One **10**(7): e0133308.

Naqvi, N., M. Li, J. W. Calvert, T. Tejada, J. P. Lambert, J. Wu, S. H. Kesteven, S. R. Holman, T. Matsuda, J. D. Lovelock, W. W. Howard, S. E. Iismaa, A. Y. Chan, B. H. Crawford, M. B. Wagner, D. I. Martin, D. J. Lefer, R. M. Graham and A. Husain (2014). "A proliferative burst during preadolescence establishes the final cardiomyocyte number." Cell **157**(4): 795-807.

Neff, A. W., A. E. Dent and J. B. Armstrong (1996). "Heart development and regeneration in urodeles." Int J Dev Biol **40**(4): 719-725.

Nguyen, P. D., I. Gooijers, G. Campostrini, A. O. Verkerk, H. Honkoop, M. Bouwman, D. E. M. de Bakker, T. Koopmans, A. Vink, G. E. M. Lamers, A. Shakked, J. Mars, A. A. Mulder, S. Chocron, K. Bartscherer, E. Tzahor, C. L. Mummery, T. P. de Boer, M. Bellin and J. Bakkers (2023). "Interplay between calcium and sarcomeres directs cardiomyocyte maturation during regeneration." Science **380**(6646): 758-764.

Nguyen, T., M. Rosa-Garrido, H. Sadek, D. J. Garry and J. J. Zhang (2024). "Promoting cardiomyocyte proliferation for myocardial regeneration in large mammals." J Mol Cell Cardiol **188**: 52-60.

Nicks, A. M., S. R. Holman, A. Y. Chan, M. Tsang, P. E. Young, D. T. Humphreys, N. Naqvi, A. Husain, M. Li, N. J. Smith, S. E. Iismaa and R. M. Graham (2022). "Standardised method for cardiomyocyte isolation and purification from individual murine neonatal, infant, and adult hearts." J Mol Cell Cardiol **170**: 47-59.

Ortmann, B., J. Druker and S. Rocha (2014). "Cell cycle progression in response to oxygen levels." Cell Mol Life Sci **71**(18): 3569-3582.

Ottaviani, D., M. Ter Huurne, D. A. Elliott, M. Bellin and C. L. Mummery (2023). "Maturing differentiated human pluripotent stem cells in vitro: methods and challenges." Development **150**(11).

Ou, Q., Z. Jacobson, R. R. E. Abouleisa, X. L. Tang, S. M. Hindi, A. Kumar, K. N. Ivey, G. Giridharan, A. El-Baz, K. Brittian, B. Rood, Y. H. Lin, S. A. Watson, F. Perbellini, T. A. McKinsey, B. G. Hill, S. P. Jones, C. M. Terracciano, R. Bolli and T. M. A. Mohamed (2019). "Physiological Biomimetic Culture System for Pig and Human Heart Slices." Circ Res **125**(6): 628-642.

Ouyang, Q., R. Xu, Q. Lin, J. Yan, L. Zhang and H. Zhao (2024). "Multimodal ultrasound imaging of a rat model with ischemic heart failure and its relationship to histopathology." Am J Transl Res **16**(9): 4589-4600.

Pardee, A. B. (1974). "A restriction point for control of normal animal cell proliferation." Proc Natl Acad Sci U S A **71**(4): 1286-1290.

Park, K. C., D. C. Gaze, P. O. Collinson and M. S. Marber (2017). "Cardiac troponins: from myocardial infarction to chronic disease." Cardiovasc Res **113**(14): 1708-1718.

Patterson, M., L. Barske, B. Van Handel, C. D. Rau, P. Gan, A. Sharma, S. Parikh, M. Denholtz, Y. Huang, Y. Yamaguchi, H. Shen, H. Allayee, J. G. Crump, T. I. Force, C. L. Lien, T. Makita, A.

J. Lusis, S. R. Kumar and H. M. Sucov (2017). "Frequency of mononuclear diploid cardiomyocytes underlies natural variation in heart regeneration." Nat Genet **49**(9): 1346-1353.

Peters, J. M. (1998). "SCF and APC: the Yin and Yang of cell cycle regulated proteolysis." Curr Opin Cell Biol **10**(6): 759-768.

Peters, M. C., R. G. C. Maas, I. van Adrichem, P. A. M. Doevendans, M. Mercola, T. Saric, J. W. Buikema, A. van Mil, S. A. J. Chamuleau, J. P. G. Sluijter, A. P. Hnatiuk and K. Neef (2022). "Metabolic Maturation Increases Susceptibility to Hypoxia-induced Damage in Human iPSC-derived Cardiomyocytes." Stem Cells Transl Med **11**(10): 1040-1051.

Pinto, A. R., A. Ilinykh, M. J. Ivey, J. T. Kuwabara, M. L. D'Antoni, R. Debuque, A. Chandran, L. Wang, K. Arora, N. A. Rosenthal and M. D. Tallquist (2016). "Revisiting Cardiac Cellular Composition." Circ Res **118**(3): 400-409.

Piquereau, J. and R. Ventura-Clapier (2018). "Maturation of Cardiac Energy Metabolism During Perinatal Development." Front Physiol **9**: 959.

Porrello, E. R., A. I. Mahmoud, E. Simpson, J. A. Hill, J. A. Richardson, E. N. Olson and H. A. Sadek (2011). "Transient regenerative potential of the neonatal mouse heart." Science **331**(6020): 1078-1080.

Porrello, E. R. and E. N. Olson (2014). "A neonatal blueprint for cardiac regeneration." Stem Cell Res **13**(3 Pt B): 556-570.

Poss, K. D., L. G. Wilson and M. T. Keating (2002). "Heart regeneration in zebrafish." Science **298**(5601): 2188-2190.

Potts, H. G., W. T. Stockdale and M. T. M. Mommersteeg (2021). "Unlocking the Secrets of the Regenerating Fish Heart: Comparing Regenerative Models to Shed Light on Successful Regeneration." J Cardiovasc Dev Dis **8**(1).

Price, E. L., J. M. Vieira and P. R. Riley (2019). "Model organisms at the heart of regeneration." Dis Model Mech **12**(10).

Puente, B. N., W. Kimura, S. A. Muralidhar, J. Moon, J. F. Amatruda, K. L. Phelps, D. Grinsfelder, B. A. Rothermel, R. Chen, J. A. Garcia, C. X. Santos, S. Thet, E. Mori, M. T. Kinter, P. M. Rindler, S. Zacchigna, S. Mukherjee, D. J. Chen, A. I. Mahmoud, M. Giacca, P. S. Rabinovitch, A. Aroumougame, A. M. Shah, L. I. Szweda and H. A. Sadek (2014). "The oxygen-rich postnatal environment induces cardiomyocyte cell-cycle arrest through DNA damage response." Cell **157**(3): 565-579.

Quaife-Ryan, G. A., C. B. Sim, M. Ziemann, A. Kaspi, H. Rafehi, M. Ramialison, A. El-Osta, J. E. Hudson and E. R. Porrello (2017). "Multicellular Transcriptional Analysis of Mammalian Heart Regeneration." Circulation **136**(12): 1123-1139.

Querdel, E., M. Reinsch, L. Castro, D. Kose, A. Bahr, S. Reich, B. Geertz, B. Ulmer, M. Schulze, M. D. Lemoine, T. Krause, M. Lemme, J. Sani, A. Shibamiya, T. Studemann, M. Kohne, C. V. Bibra, N. Hornaschewitz, S. Pecha, Y. Nejahsie, I. Mannhardt, T. Christ, H. Reichenspurner, A. Hansen, N. Klymiuk, M. Krane, C. Kupatt, T. Eschenhagen and F. Weinberger (2021). "Human Engineered Heart Tissue Patches Remuscularize the Injured Heart in a Dose-Dependent Manner." Circulation **143**(20): 1991-2006.

Racca, A. W., J. M. Klaiman, J. M. Pioner, Y. Cheng, A. E. Beck, F. Moussavi-Harami, M. J. Bamshad and M. Regnier (2016). "Contractile properties of developing human fetal cardiac muscle." J Physiol **594**(2): 437-452.

Reshetnyak, Y. K., O. A. Andreev, U. Lehnert and D. M. Engelman (2006). "Translocation of molecules into cells by pH-dependent insertion of a transmembrane helix." Proc Natl Acad Sci U S A **103**(17): 6460-6465.

Riegler, J., M. Tiburcy, A. Ebert, E. Tzatzalos, U. Raaz, O. J. Abilez, Q. Shen, N. G. Kooreman, E. Neofytou, V. C. Chen, M. Wang, T. Meyer, P. S. Tsao, A. J. Connolly, L. A. Couture, J. D. Gold, W. H. Zimmermann and J. C. Wu (2015). "Human Engineered Heart Muscles Engraft and Survive Long Term in a Rodent Myocardial Infarction Model." Circ Res **117**(8): 720-730.

Riley, P. R. and N. Smart (2009). "Thymosin beta4 induces epicardium-derived neovascularization in the adult heart." Biochem Soc Trans **37**(Pt 6): 1218-1220.

Riley, P. R. and N. Smart (2011). "Vascularizing the heart." Cardiovasc Res **91**(2): 260-268.

Roberts, T. A., A. N. Price, L. H. Jackson, V. Taylor, A. L. David, M. F. Lythgoe and D. J. Stuckey (2017). "Direct comparison of high-temporal-resolution CINE MRI with Doppler ultrasound for assessment of diastolic dysfunction in mice." NMR Biomed **30**(10).

Rosenholm, M., E. Paro, H. Antila, V. Voikar and T. Rantamaki (2017). "Repeated brief isoflurane anesthesia during early postnatal development produces negligible changes on adult behavior in male mice." PLoS One **12**(4): e0175258.

Ruff, J., F. Wiesmann, K. H. Hiller, S. Voll, M. von Kienlin, W. R. Bauer, E. Rommel, S. Neubauer and A. Haase (1998). "Magnetic resonance microimaging for noninvasive quantification of myocardial function and mass in the mouse." Magn Reson Med **40**(1): 43-48.

Rumyantsev, P. P. (1991). Growth and Hyperplasia of Cardiac Muscle Cells, Harwood Academic Publisher**:** 70-199.

Saikia, D. and B. Mahanta (2019). "Cardiovascular and respiratory physiology in children." Indian J Anaesth **63**(9): 690-697.

Sakaue-Sawano, A., T. Hoshida, M. Yo, R. Takahashi, K. Ohtawa, T. Arai, E. Takahashi, S. Noda, H. Miyoshi and A. Miyawaki (2013). "Visualizing developmentally programmed endoreplication in mammals using ubiquitin oscillators." Development **140**(22): 4624-4632.

Sakaue-Sawano, A., H. Kurokawa, T. Morimura, A. Hanyu, H. Hama, H. Osawa, S. Kashiwagi, K. Fukami, T. Miyata, H. Miyoshi, T. Imamura, M. Ogawa, H. Masai and A. Miyawaki (2008). "Visualizing spatiotemporal dynamics of multicellular cell-cycle progression." Cell **132**(3): 487-498.

Sakaue-Sawano, A., K. Ohtawa, H. Hama, M. Kawano, M. Ogawa and A. Miyawaki (2008). "Tracing the silhouette of individual cells in S/G2/M phases with fluorescence." Chem Biol **15**(12): 1243-1248.

Saleh, M. G., S. K. Sharp, A. Alhamud, B. S. Spottiswoode, A. J. van der Kouwe, N. H. Davies, T. Franz and E. M. Meintjes (2012). "Long-term left ventricular remodelling in rat model of nonreperfused myocardial infarction: sequential MR imaging using a 3T clinical scanner." J Biomed Biotechnol **2012**: 504037.

Santini, M. P., E. Forte, R. P. Harvey and J. C. Kovacic (2016). "Developmental origin and lineage plasticity of endogenous cardiac stem cells." Development **143**(8): 1242-1258.

Schmid, G. and P. Pfitzer (1985). "Mitoses and binucleated cells in perinatal human hearts." Virchows Arch B Cell Pathol Incl Mol Pathol **48**(1): 59-67.

Schoen, F. J. a. M., R.N. (2021). High frequency echocardiography in mice and rats. Pathologic Basis of Disease. P. A. C. Robbins, Elsevier.

Semenza, G. L. (2007). "Life with oxygen." Science **318**(5847): 62-64.

Shah, S., E. D. Chryssos and H. Parker (2009). "Magnetic resonance imaging: a wealth of cardiovascular information." Ochsner J **9**(4): 266-277.

Shan, L. (2004). Cy5.5-labeled pH low insertion peptide (pHLIP). Molecular Imaging and Contrast Agent Database (MICAD). Bethesda (MD).

Sharma, B., A. Chang and K. Red-Horse (2017). "Coronary Artery Development: Progenitor Cells and Differentiation Pathways." Annu Rev Physiol **79**: 1-19.

Shiba, Y., T. Gomibuchi, T. Seto, Y. Wada, H. Ichimura, Y. Tanaka, T. Ogasawara, K. Okada, N. Shiba, K. Sakamoto, D. Ido, T. Shiina, M. Ohkura, J. Nakai, N. Uno, Y. Kazuki, M. Oshimura, I. Minami and U. Ikeda (2016). "Allogeneic transplantation of iPS cell-derived cardiomyocytes regenerates primate hearts." Nature **538**(7625): 388-391.

Simoes, F. C., T. J. Cahill, A. Kenyon, D. Gavriouchkina, J. M. Vieira, X. Sun, D. Pezzolla, C. Ravaud, E. Masmanian, M. Weinberger, S. Mayes, M. E. Lemieux, D. N. Barnette, M. Gunadasa-Rohling, R. M. Williams, D. R. Greaves, L. A. Trinh, S. E. Fraser, S. L. Dallas, R. P. Choudhury, T. Sauka-Spengler and P. R. Riley (2020). "Macrophages directly contribute collagen to scar formation during zebrafish heart regeneration and mouse heart repair." Nat Commun **11**(1): 600.

Simoes, F. C. and P. R. Riley (2018). "The ontogeny, activation and function of the epicardium during heart development and regeneration." Development **145**(7).

Simoes, F. C. and P. R. Riley (2022). "Immune cells in cardiac repair and regeneration." Development **149**(8).

Simpson, A., A. W. Hewitt and K. A. Fairfax (2023). "Universal cell donor lines: A review of the current research." Stem Cell Reports **18**(11): 2038-2046.

Singh Angom, R., Y. Wang, E. Wang, S. K. Dutta and D. Mukhopadhyay (2023). "Conditional, Tissue-Specific CRISPR/Cas9 Vector System in Zebrafish Reveals the Role of Nrp1b in Heart Regeneration." Arterioscler Thromb Vasc Biol **43**(10): 1921-1934.

Singleman, C. and N. G. Holtzman (2012). "Analysis of postembryonic heart development and maturation in the zebrafish, Danio rerio." Dev Dyn **241**(12): 1993-2004.

Smart, N., S. Bollini, K. N. Dube, J. M. Vieira, B. Zhou, S. Davidson, D. Yellon, J. Riegler, A. N. Price, M. F. Lythgoe, W. T. Pu and P. R. Riley (2011). "De novo cardiomyocytes from within the activated adult heart after injury." Nature **474**(7353): 640-644.

Smith, K. A., S. A. Hill, A. C. Begg and J. Denekamp (1988). "Validation of the fluorescent dye Hoechst 33342 as a vascular space marker in tumours." Br J Cancer **57**(3): 247-253.

Soonpaa, M. H., K. K. Kim, L. Pajak, M. Franklin and L. J. Field (1996). "Cardiomyocyte DNA synthesis and binucleation during murine development." Am J Physiol **271**(5 Pt 2): H2183-2189.

Soonpaa, M. H., G. Y. Koh, M. G. Klug and L. J. Field (1994). "Formation of nascent intercalated disks between grafted fetal cardiomyocytes and host myocardium." Science **264**(5155): 98-101.

Soonpaa, M. H., S. P. Reuter, P. F. Castelluccio and L. J. Field (2023). "Musings on intrinsic cardiomyocyte cell cycle activity and myocardial regeneration." J Mol Cell Cardiol **182**: 86-91.

Sosunov, E. A., E. P. Anyukhovsky, A. A. Sosunov, A. Moshnikova, D. Wijesinghe, D. M. Engelman, Y. K. Reshetnyak and O. A. Andreev (2013). "pH (low) insertion peptide (pHLIP) targets ischemic myocardium." Proc Natl Acad Sci U S A **110**(1): 82-86.

Spannbauer, A., J. Mester-Tonczar, D. Traxler, N. Kastner, K. Zlabinger, E. Hasimbegovic, M. Riesenhuber, N. Pavo, G. Goliasch and M. Gyongyosi (2020). "Large Animal Models of Cell-Free Cardiac Regeneration." Biomolecules **10**(10).

Stathopoulou, K., C. Gaitanaki and I. Beis (2006). "Extracellular pH changes activate the p38-MAPK signalling pathway in the amphibian heart." J Exp Biol **209**(Pt 7): 1344-1354.

Steenbergen, C., G. Deleeuw, T. Rich and J. R. Williamson (1977). "Effects of acidosis and ischemia on contractility and intracellular pH of rat heart." Circ Res **41**(6): 849-858.

Steinhauser, M. L. and R. T. Lee (2011). "Regeneration of the heart." EMBO Mol Med **3**(12): 701-712.

Stockdale, W. T., M. E. Lemieux, A. C. Killen, J. Zhao, Z. Hu, J. Riepsaame, N. Hamilton, T. Kudoh, P. R. Riley, R. van Aerle, Y. Yamamoto and M. T. M. Mommersteeg (2018). "Heart Regeneration in the Mexican Cavefish." Cell Rep **25**(8): 1997-2007 e1997.

Stoehr, A., Y. Yang, S. Patel, A. M. Evangelista, A. Aponte, G. Wang, P. Liu, J. Boylston, P. H. Kloner, Y. Lin, M. Gucek, J. Zhu and E. Murphy (2016). "Prolyl hydroxylation regulates protein degradation, synthesis, and splicing in human induced pluripotent stem cell-derived cardiomyocytes." Cardiovasc Res **110**(3): 346-358.

Stuckey, D. J., C. A. Carr, D. J. Tyler and K. Clarke (2008). "Cine-MRI versus two-dimensional echocardiography to measure in vivo left ventricular function in rat heart." NMR Biomed **21**(7): 765-772.

Sultana, N., L. Zhang, J. Yan, J. Chen, W. Cai, S. Razzaque, D. Jeong, W. Sheng, L. Bu, M. Xu, G. Y. Huang, R. J. Hajjar, B. Zhou, A. Moon and C. L. Cai (2015). "Resident c-kit(+) cells in the heart are not cardiac stem cells." Nat Commun **6**: 8701.

Sylva, M., M. J. van den Hoff and A. F. Moorman (2014). "Development of the human heart." Am J Med Genet A **164A**(6): 1347-1371.

Tan, C. M. J. and A. J. Lewandowski (2020). "The Transitional Heart: From Early Embryonic and Fetal Development to Neonatal Life." Fetal Diagn Ther **47**(5): 373-386.

Tan, S. H. and L. Ye (2018). "Maturation of Pluripotent Stem Cell-Derived Cardiomyocytes: a Critical Step for Drug Development and Cell Therapy." J Cardiovasc Transl Res **11**(5): 375-392.

Tang, J. L. Y., Y. Guo, W. T. Stockdale, K. Rana, A. C. Killen, M. T. M. Mommersteeg and Y. Yamamoto (2018). "The developmental origin of heart size and shape differences in Astyanax mexicanus populations." Dev Biol **441**(2): 272-284.

Thackeray, J. T. and F. M. Bengel (2016). "Translational Molecular Nuclear Cardiology." Cardiol Clin **34**(1): 187-198.

Tian, J., M. F. Smith, P. Chinnadurai, V. Dilsizian, A. Turgeman, A. Abbo, K. Gajera, C. Xu, D. Plotnick, R. Peters, M. Saba, S. Shorofsky and T. Dickfeld (2009). "Clinical application of PET/CT fusion imaging for three-dimensional myocardial scar and left ventricular anatomy during ventricular tachycardia ablation." J Cardiovasc Electrophysiol **20**(6): 567-604.

Tian, X., T. Hu, H. Zhang, L. He, X. Huang, Q. Liu, W. Yu, L. He, Z. Yang, Y. Yan, X. Yang, T. P. Zhong, W. T. Pu and B. Zhou (2014). "Vessel formation. De novo formation of a distinct coronary vascular population in neonatal heart." Science **345**(6192): 90-94.

Tyser, R. C., A. M. Miranda, C. M. Chen, S. M. Davidson, S. Srinivas and P. R. Riley (2016). "Calcium handling precedes cardiac differentiation to initiate the first heartbeat." Elife **5**.

Vaughan-Jones, R. D., K. W. Spitzer and P. Swietach (2009). "Intracellular pH regulation in heart." J Mol Cell Cardiol **46**(3): 318-331.

Vavere, A. L., G. B. Biddlecombe, W. M. Spees, J. R. Garbow, D. Wijesinghe, O. A. Andreev, D. M. Engelman, Y. K. Reshetnyak and J. S. Lewis (2009). "A novel technology for the imaging of acidic prostate tumors by positron emission tomography." Cancer Res **69**(10): 4510-4516.

Velayutham, N., C. M. Alfieri, E. J. Agnew, K. W. Riggs, R. S. Baker, S. R. Ponny, F. Zafar and K. E. Yutzey (2020). "Cardiomyocyte cell cycling, maturation, and growth by multinucleation in postnatal swine." J Mol Cell Cardiol **146**: 95-108.

Velayutham, N. and K. E. Yutzey (2022). "Porcine Models of Heart Regeneration." J Cardiovasc Dev Dis **9**(4).

Verbon, E. H., J. A. Post and J. Boonstra (2012). "The influence of reactive oxygen species on cell cycle progression in mammalian cells." Gene **511**(1): 1-6.

Virani, S. S., A. Alonso, E. J. Benjamin, M. S. Bittencourt, C. W. Callaway, A. P. Carson, A. M. Chamberlain, A. R. Chang, S. Cheng, F. N. Delling, L. Djousse, M. S. V. Elkind, J. F. Ferguson, M. Fornage, S. S. Khan, B. M. Kissela, K. L. Knutson, T. W. Kwan, D. T. Lackland, T. T. Lewis, J. H. Lichtman, C. T. Longenecker, M. S. Loop, P. L. Lutsey, S. S. Martin, K. Matsushita, A. E. Moran, M. E. Mussolino, A. M. Perak, W. D. Rosamond, G. A. Roth, U. K. A. Sampson, G. M. Satou, E. B. Schroeder, S. H. Shah, C. M. Shay, N. L. Spartano, A. Stokes, D. L. Tirschwell, L. B. VanWagner, C. W. Tsao, E. American Heart Association Council on, C. Prevention Statistics and S. Stroke Statistics (2020). "Heart Disease and Stroke Statistics-2020 Update: A Report From the American Heart Association." Circulation **141**(9): e139-e596.

Walsh, S., A. Ponten, B. K. Fleischmann and S. Jovinge (2010). "Cardiomyocyte cell cycle control and growth estimation in vivo--an analysis based on cardiomyocyte nuclei." Cardiovasc Res **86**(3): 365-373.

Wang, H., M. J. Paulsen, C. E. Hironaka, H. S. Shin, J. M. Farry, A. D. Thakore, J. Jung, H. J. Lucian, A. Eskandari, S. Anilkumar, M. A. Wu, M. C. Cabatu, A. N. Steele, L. M. Stapleton, Y. Zhu and Y. J. Woo (2020). "Natural Heart Regeneration in a Neonatal Rat Myocardial Infarction Model." Cells **9**(1).

Wang, J., D. Panakova, K. Kikuchi, J. E. Holdway, M. Gemberling, J. S. Burris, S. P. Singh, A. L. Dickson, Y. F. Lin, M. K. Sabeh, A. A. Werdich, D. Yelon, C. A. Macrae and K. D. Poss (2011). "The regenerative capacity of zebrafish reverses cardiac failure caused by genetic cardiomyocyte depletion." Development **138**(16): 3421-3430.

Wang, L. (2005). "A primer on rodent identification methods." Lab Anim (NY) **34**(4): 64-67.

Wang, X., I. Yokoi, J. Liu and A. Mori (1993). "Cobalt(II) and nickel(II) ions as promoters of free radicals in vivo: detected directly using electron spin resonance spectrometry in circulating blood in rats." Arch Biochem Biophys **306**(2): 402-406.

Watson, S. A., C. M. Terracciano and F. Perbellini (2019). "Myocardial Slices: an Intermediate Complexity Platform for Translational Cardiovascular Research." Cardiovasc Drugs Ther **33**(2): 239-244.

Wech, T., A. Lemke, D. Medway, L. A. Stork, C. A. Lygate, S. Neubauer, H. Kostler and J. E. Schneider (2011). "Accelerating cine-MR imaging in mouse hearts using compressed sensing." J Magn Reson Imaging **34**(5): 1072-1079.

Weinberger, F. (2019). "Heart regeneration: from mouse to human." Current Opinion in Physiology.

Weinberger, F., K. Breckwoldt, S. Pecha, A. Kelly, B. Geertz, J. Starbatty, T. Yorgan, K. H. Cheng, K. Lessmann, T. Stolen, M. Scherrer-Crosbie, G. Smith, H. Reichenspurner, A. Hansen and T. Eschenhagen (2016). "Cardiac repair in guinea pigs with human engineered heart tissue from induced pluripotent stem cells." Sci Transl Med **8**(363): 363ra148.

Wessels, A. and D. Sedmera (2003). "Developmental anatomy of the heart: a tale of mice and man." Physiol Genomics **15**(3): 165-176.

Wiesmann, F., J. Ruff, C. Dienesch, A. Leupold, E. Rommel, A. Haase and S. Neubauer (2000). "Cardiovascular phenotype characterization in mice by high resolution magnetic resonance imaging." MAGMA **11**(1-2): 10-15.

Wiesmann, F., J. Ruff, K. H. Hiller, E. Rommel, A. Haase and S. Neubauer (2000). "Developmental changes of cardiac function and mass assessed with MRI in neonatal, juvenile, and adult mice." Am J Physiol Heart Circ Physiol **278**(2): H652-657.

Wilson, A. D., M. A. Richards, M. K. Curtis, M. Gunadasa-Rohling, S. Monterisi, A. A. Loonat, J. J. Miller, V. Ball, A. Lewis, D. J. Tyler, A. Moshnikova, O. A. Andreev, Y. K. Reshetnyak, C. Carr and P. Swietach (2022). "Acidic environments trigger intracellular H+-sensing FAK proteins to re-balance sarcolemmal acid-base transporters and auto-regulate cardiomyocyte pH." Cardiovasc Res **118**(14): 2946-2959.

Wu, Y. and E. X. Wu (2009). "MR study of postnatal development of myocardial structure and left ventricular function." J Magn Reson Imaging **30**(1): 47-53.

Wyatt, L. C., A. Moshnikova, T. Crawford, D. M. Engelman, O. A. Andreev and Y. K. Reshetnyak (2018). "Peptides of pHLIP family for targeted intracellular and extracellular delivery of cargo molecules to tumors." Proc Natl Acad Sci U S A **115**(12): E2811-E2818.

Xavier-Vidal, R. and C. A. Mandarim-de-Lacerda (1995). "Cardiomyocyte proliferation and hypertrophy in the human fetus: quantitative study of the myocyte nuclei." Bull Assoc Anat (Nancy) **79**(246): 27-31.

Yang, X. P., Y. H. Liu, N. E. Rhaleb, N. Kurihara, H. E. Kim and O. A. Carretero (1999). "Echocardiographic assessment of cardiac function in conscious and anesthetized mice." Am J Physiol **277**(5): H1967-1974.

Ye, L., G. D'Agostino, S. J. Loo, C. X. Wang, L. P. Su, S. H. Tan, G. Z. Tee, C. J. Pua, E. M. Pena, R. B. Cheng, W. C. Chen, D. Abdurrachim, J. Lalic, R. S. Tan, T. H. Lee, J. Zhang and S. A. Cook (2018). "Early Regenerative Capacity in the Porcine Heart." Circulation **138**(24): 2798-2808.

Ye, L., L. Qiu, H. Zhang, H. Chen, C. Jiang, H. Hong and J. Liu (2016). "Cardiomyocytes in Young Infants With Congenital Heart Disease: a Three-Month Window of Proliferation." Sci Rep **6**: 23188.

Ye, Q., J. Jo, C. Y. Wang, H. Oh, J. Zhan, T. J. Choy, K. I. Kim, A. D'Alessandro, Y. K. Reshetnyak, S. Y. Jung, Z. Chen, S. P. Marrelli and H. K. Lee (2024). "Astrocytic Slc4a4 regulates blood-brain barrier integrity in healthy and stroke brains via a CCL2-CCR2 pathway and NO dysregulation." Cell Rep **43**(5): 114193.

Yeo, J. M., V. Tse, J. Kung, H. Y. Lin, Y. T. Lee, J. Kwan, B. P. Yan and G. Tse (2017). "Isolated heart models for studying cardiac electrophysiology: a historical perspective and recent advances." J Basic Clin Physiol Pharmacol **28**(3): 191-200.

Zgheib, C., M. W. Allukian, J. Xu, M. W. Morris, Jr., R. C. Caskey, B. J. Herdrich, J. Hu, J. H. Gorman, 3rd, R. C. Gorman and K. W. Liechty (2014). "Mammalian fetal cardiac regeneration after myocardial infarction is associated with differential gene expression compared with the adult." Ann Thorac Surg **97**(5): 1643-1650.

Zhao, M., Y. Nakada, Y. Wei, W. Bian, Y. Chu, A. V. Borovjagin, M. Xie, W. Zhu, T. Nguyen, Y. Zhou, V. Serpooshan, G. P. Walcott and J. Zhang (2021). "Cyclin D2 Overexpression Enhances the Efficacy of Human Induced Pluripotent Stem Cell-Derived Cardiomyocytes for Myocardial Repair in a Swine Model of Myocardial Infarction." Circulation **144**(3): 210-228.

Zhdanov, A. V., I. A. Okkelman, F. W. Collins, S. Melgar and D. B. Papkovsky (2015). "A novel effect of DMOG on cell metabolism: direct inhibition of mitochondrial function precedes HIF target gene expression." Biochim Biophys Acta **1847**(10): 1254-1266.

Zheng, J. (2012). "Energy metabolism of cancer: Glycolysis versus oxidative phosphorylation (Review)." Oncol Lett **4**(6): 1151-1157.

Zhou, P. and W. T. Pu (2016). "Recounting Cardiac Cellular Composition." Circ Res **118**(3): 368-370.

Zhou, Y. Q., F. S. Foster, B. J. Nieman, L. Davidson, X. J. Chen and R. M. Henkelman (2004). "Comprehensive transthoracic cardiac imaging in mice using ultrasound biomicroscopy with anatomical confirmation by magnetic resonance imaging." Physiol Genomics **18**(2): 232-244.

Zhu, C., T. Yuan and J. Krishnan (2024). "Targeting cardiomyocyte cell cycle regulation in heart failure." Basic Res Cardiol **119**(3): 349-369.

Zhu, T. T., W. F. Zhang, P. Luo, Z. X. Qian, F. Li, Z. Zhang and C. P. Hu (2017). "LOX-1 promotes right ventricular hypertrophy in hypoxia-exposed rats." Life Sci **174**: 35-42.

Zhu, W., J. Sun, S. P. Bishop, H. Sadek and J. Zhang (2022). "Turning back the clock: A concise viewpoint of cardiomyocyte cell cycle activation for myocardial regeneration and repair." J Mol Cell Cardiol **170**: 15-21.

Zhu, W., M. Zhao, S. Mattapally, S. Chen and J. Zhang (2018). "CCND2 Overexpression Enhances the Regenerative Potency of Human Induced Pluripotent Stem Cell-Derived Cardiomyocytes: Remuscularization of Injured Ventricle." Circ Res **122**(1): 88-96.